Adaptation of the Artificial Compressibility Formulation for Free Surface Flows with Applications in Ship & Marine Hydrodynamics

by
Dimitris Ntouras

A dissertation submitted to the National Technical University of Athens
in partial fulfilment of the requirements for the degree of Doctor of Engineering

October 2023
Athens, Greece

National Technical University of Athens
School of Naval Architecture & Marine Engineering

Adaptation of the Artificial Compressibility Formulation for Free Surface Flows with Applications in Ship & Marine Hydrodynamics

Dimitris Ntouras

Examination Committee:

1. K. Belibassakis*
   Professor, School of Naval Architecture & Marine Engineering, NTUA
2. K. Giannakoglou
   Professor, School of Mechanical Engineering, NTUA
3. G. Papadakis (Supervisor)*
   Assistant Professor, School of Naval Architecture & Marine Engineering, NTUA
4. C. Papadopoulos
   Associate Professor, School of Naval Architecture & Marine Engineering, NTUA
5. K. Spyrou
   Professor, School of Naval Architecture & Marine Engineering, NTUA
6. G. Tzabiras
   Professor Emeritus, School of Naval Architecture & Marine Engineering, NTUA
7. S. Voutsinas*
   Professor, School of Mechanical Engineering, NTUA

**Members of the Advisory Committee*

Ευρωπαϊκή Ένωση
European Social Fund

Operational Programme
Human Resources Development,
Education and Lifelong Learning
Co-financed by Greece and the European Union

ΕΣΠΑ 2014-2020
ανάπτυξη - εργασία - αλληλεγγύη

This page intentionally left blank

Acknowledgments

I would like to thank the people that have contributed, with one way or the other, in the completion of the present thesis.

First and foremost, I would like to express my sincere gratitude to my supervisor, professor G. Papadakis, for his constant support and encouragement through all these years. His invaluable guidance and dedication were the most significant ingredients for completing this project. Furthermore, I would like to extend my appreciations to professors S. Voutsinas and K. Belibassakis, members of the advisory committee, for their insightful comments and suggestions to proceed with this thesis. Apart from the members of the advisory committee, I would like to also thank professor V. Riziotis for his support and cooperation.

During the past five years, I had the honor to meet and work with amazing people from both schools of Mechanical Engineering and Naval Architecture & Marine Engineering. Firstly, I would like to thank the experimentalists of the Laboratory of Ship and Marine Hydrodynamics (LMSH), and especially Dr. D. Liarokapis, for providing me with detailed experimental data (see Sec. 5.1 and 5.3) essential for the validation process of the proposed numerical solver. From the Aerodynamics Lab of NTUA, I'm extremely grateful to have worked with Dr. D. Manolas, a tireless researcher who had always been there to discuss ideas with me and new topics of research. Also from Aerodynamics lab, I would like to thank Dr. J. Prospathopoulos for sharing his knowledge on aerodynamic flows and on computer clusters. Of course all these years would be different if were not for my colleagues and friends. I would like to thank Ch. Backirzoglou, D. Vlastos, N. Spyropoulos, G. Serafeim, Dr. T. Andronikos and Dr. K. Diakakis, as well as the newly added members to our group, S. Zafeiris and A. Alexandris, for easing my timing in NTUA.

Furthermore, I would like to thank BETA CAE Systems for providing to our Lab the Ansa meshing software, as well as, the Ship Design Lab of NTUA and especially Dr. A. Kanellopoulou for granting us the license for the Hexpress software.

Last but not least, I could not thank enough my parents and my sisters for supporting me and encouraging me at every step I take. I would not have got this far without their support.

This research was partially supported by SEATECH H2020 project funded by the European Union's Horizon 2020 research and innovation program under the grant agreement No 857840, and by Greece and the European Union (European Social Fund–ESF) through the Operational Programme Human Resources Development, Education and Lifelong Learning in the context of the project "Strengthening Human Resources Research Potential via Doctorate Research – 2nd Cycle" (MIS-5000432), implemented by the State Scholarships Foundation (IKY).

D. Ntouras,
October 2023

This page intentionally left blank

Abstract

Computational Fluid Dynamics (CFD) has enabled the design process in many engineering applications. Advancements in computing power have allowed for the extension of CFD methods in multi–phase flows. This category of methods can be directly applied in the field of Ship & Marine Hydrodynamics. Multi–phase modeling can be used to study the interaction of the two–immiscible fluids (air/water). A methodology can be formulated to address problems such as wave propagation, viscous effects close to surface piercing boundaries and wave–structure interaction.

This thesis investigates the extension of the Artificial Compressibility (AC) method in free surface flows in conjunction with the Volume of Fluid (VoF) approach. The objective is to formulate a complete CFD methodology for the hydrodynamic analysis of ship hulls and offshore platforms. A thorough validation and verification process is followed. Carefully designed numerical experiments are conducted and results are compared against analytical, experimental and other numerical results. The capabilities, limitations and potential enhancements of the method are outlined. The methodology is implemented as an extension to the compressible URANS solver *MaPFlow*, developed at NTUA.

In the following chapters, initially, the theoretical background of the coupled AC/VoF methodology is discussed. Afterwards, the numerical formulation of the Unsteady Reynolds Averaged Navier Stokes (URANS) equations for free surface flows is given in detail. The equations are discretized using the finite volume method in unstructured polyhedral grids. Since the structure can move in space, cell can motion and deformation is also consider in the discretization process. Focus is further given on introducing waves in a computational domain. Waves are introduced and absorbed using source terms that drive the flowfield to a target solution. The linear theory of Airy and the Stream Function theory of Fenton are used as basis for the numerical wave generation. Additionally, the problem of turbulence overproduction near the free surface is faced. Existing options are examined and further guidelines are given. Fluid–Structure Interaction (FSI) problems are at the core of the validation test cases. For these purposes, a 6 Degrees of Freedom (DoFs) rigid body solver is developed and coupled with the URANS solver. In order to effectively move the rigid body inside the computational mesh, deformation algorithms are utilized.

A series of validation test cases are conducted inspired from the domain of Ship & Marine Hydrodynamics. Firstly, simplified 2–dimensional (2D) flows are considered. The specifics of generation and propagation, wave interaction with variable bathymetry and wave–induced motion of floating platforms are examined. Taken advantage of the simplifications arising from the 2D approximation, parametric studies are conducted regarding the influence of the AC parameter $-\beta-$, as well as, the parameters for wave generation and absorption. The method is generalized in the 3–dimensional space (3D). Comments are made on the challenge of maintaining the hydrostatic equilibrium in 3D applications, especially for polyhedral cell elements. The validation process continues by considering more realistic applications. The developed numerical methodology is used as a tool to assess the efficiency of a propeller in deep water, the resistance and the dynamic trim of two ship hulls and the response of floating structures in regular and irregular head waves conditions.

As indicated by the comparisons, the method performs well in all cases. A fine agreement between the results is found, proving that the developed coupled AC/VoF numerical methodology can compete against already existing State–of–the–Art numerical tools and contribute to the further advancement of the CFD tools.

This page intentionally left blank

Περίληψη

Η μέθοδος της Υπολογιστικής Ρευστομηχανικής έχει συμβάλλει καθοριστικά στην διαδικασία του σχεδιασμού σε όλα τα επίπεδα της επιστήμης του μηχανικού. Η ανάπτυξη της διαθέσιμης υπολογιστικής ισχύος έχει επιτρέψει την επέκταση των μεθόδων αυτών σε ροές με περισσότερες από μία φάσεις. Σε αυτήν την κατηγορία μεθόδων εντάσσονται και προβλήματα Ναυτικής & Θαλάσσιας Υδροδυναμικής. Τα μοντέλα πολυφασικών ροών μπορούν να προσαρμοστούν για την διφασική μοντελοποίηση των άμμεικτων ρευστών, του νερού και του αέρα. Η προκύπτουσα μεθοδολογία μπορεί να χρησιμοποιηθεί για την ανάλυση προβλημάτων κυματικής διάδοσης, συνεκτικών φαινομένων κοντά σε στερεά τοιχώματα που βρίσκονται κοντά ή τέμνουν την ελεύθερη επιφάνεια, αλλά και να μοντελοποιήσει την αλληλεπίδραση κυμάτων με πλωτές κατασκευές.

Η παρούσα διατριβή μελετά την επέκταση την μεθόδου της Τεχνητής Συμπιεστότητας σε ροές με ελεύθερη επιφάνεια, συζευγμένη με την μέθοδο του κλασματικού όγκου. Ο σκοπός της εργασίας είναι να δημιουργήσει μια πλήρη μεθοδολογία υπολογιστικής ρευστομηχανικής για την υδροδυναμική ανάλυση πλοίων και πλωτών κατασκευών. Σε αυτά τα πλαίσια παρουσιάζεται η ενδελεχής πιστοποίηση της προτεινόμενης μεθοδολογίας. Η εργασία παρουσιάζει προσεκτικά σχεδιασμένα υπολογιστικά πειράματα, τα αποτελέσματα των οποίων συγκρίνονται με αναλυτικές λύσεις, πειραματικά δεδομένα αλλά και με διαθέσιμα υπολογιστικά αποτελέσματα. Σκιαγραφούνται οι δυνατότητες, οι περιορισμοί και οι πιθανές βελτιώσεις της μεθόδου. Η προτεινόμενη μεθοδολογία υλοποιήθηκε ως επέκταση σε προ–υπάρχον λογισμικό υπολογιστικής ρευστομηχανικής που αναπτύσσεται στον Εθνικό Μετσόβιο Πολυτεχνείο. Ο υπολογιστικός κώδικας MaPFlow επιλύει τις μη–μόνιμες, σταθμισμένες κατά Reynolds, συμπιεστές εξισώσεις Navier Stokes.

Αρχικά, στην εργασία παρουσιάζεται το θεωρητικό υπόβαθρο της συζευγμένης μεθοδολογίας Τεχνητής Συμπιεστότητας και κλασματικού όγκου. Μετέπειτα, αναλύεται η αριθμητική διατύπωση των μη—μόνιμων τυρβώδων εξισώσεων Navier Stokes για ροές με ελεύθερη επιφάνεια. Οι εξισώσεις ροής διακριτοποιούνται κάνοντας χρήση της μεθόδου των πεπερασμένων όγκων σε τυχαίους πολυεδρικούς όγκους. Η διακριτοποίηση των εξισώσεων ροής θεωρεί τόσο την κίνηση και όσο και την παραμόρφωση των όγκων ελέγχου. Κύματα ελεύθερης επιφάνειας εισάγονται και αποσβένονται από την υπολογιστική δεξαμενή εισάγοντας κατάλληλους όρους πηγής. Στόχος είναι να οδηγηθεί μέσω αυτών η υπολογιστική λύση στο εξωτερικώς επιβαλλόμενο πεδίο ροής. Η κυματική θεωρία του Airy για γραμμικούς κυματισμούς και η μη–γραμμική θεωρία της Ροϊκής Συνάρτησης του Fenton χρησιμοποιούνται ως βάση για την διαδικασία της κυματογέννησης. Επιπρόσθετα, η αύξηση της τυρβώδους συνεκτικότητας κοντά στην ελεύθερη επιφάνεια αντιμετωπίζεται επιτυχώς. Εξετάζονται λύσεις που προτείνονται από την βιβλιογραφία και δίδονται περαιτέρω οδηγίες για την επιτυχή αντιμετώπιση της. Στο επίκεντρο της μελέτης βρίσκονται τα προβλήματα αλληλεπίδρασης στερεού ρευστού. Σε αυτά τα πλαίσια, αναπτύσσεται ένας δυναμικός επιλύτης στερεού σώματος 6 βαθμών ελευθερίας και πραγματοποιείται η σύζευξη του με τον ρευστομηχανικό επιλύτη. Η μετακίνηση του στερεού σώματος μέσα στο υπολογιστικό χωρίο πραγματοποιείται κάνοντας χρήση αλγορίθμων παραμόρφωσης πλέγματος.

Αναφορικά με την διαδικασία πιστοποίησης του επιλύτη, διεξάγονται μια σειρά από υπολογιστικά πειράματα που άπτονται στο πεδίο της Ναυτικής & Θαλάσσιας υδροδυναμικής. Σε πρώτο επίπεδο, θεωρούνται απλοποιημένες 2-διάστατες (2Δ) ροές, όπου παρουσιάζονται προβλήματα γέννησης και διάδοσης κυματισμών, αλληλεπίδρασης κυμάτων με μεταβλητή βαθυμετρία αλλά και η απόκριση πλωτών κατασκευών. Εκμεταλλευόμενοι τις απλοποιήσεις που εγείρονται από την 2Δ προσέγγιση, διεξάγονται παραμετρικές μελέτες για την ανάλυση υπολογιστικών παραμέτρων όπως για την σταθερά –β– της Τεχνητής Συμπιεστότητας, αλλά και για τις σταθερές ελέγχου της διαδικασίας γέννησης και απόσβεσης κυματισμών. Η μέθοδος γενικεύεται σε 3–διάστατες (3Δ) ροές. Έμφαση δίνεται στην διατήρηση της υδροστατικής ισορροπίας σε μη– δομημένα πλέγματα με πολυεδρικούς όγκους ελέγχου. Η διαδικασία πιστοποίησης επεκτείνεται σε πιο ρεαλιστικές εφαρμογές. Η παρούσα μεθοδολογία χρησιμοποιείται ως εργαλείο για την πρόλεξη της απόδοσης προπέλας σε ελεύθερη ροή, της αντίστασης και της δυναμικής διαγωγής πλοίων σε ήρεμο νερό και τέλος της απόκρισης πλωτών κατασκευών σε κανονικούς και τυχαίους κυματισμούς.

Βάσει των συγκρίσεων, τα αποτελέσματα της μεθόδου κρίνονται ικανοποιητικά σε όλες τις περιπτώσεις. Η πλειοψηφία των αποτελεσμάτων βρίσκεται σε καλή συμφωνία με τα υπόλοιπα διαθέσιμα αποτελέσματα. Συμπερασματικά θεωρείται ότι, η προτεινόμενη μεθοδολογία μπορεί να ανταγωνιστεί άλλες σύγχρονες υλοποιήσεις και να συμβάλει με την σειρά της στην περαιτέρω ανάπτυξη της υπολογιστικής ρευστομηχανικής.

Contents

1 Introduction **1**
- 1.1 Motivation & Objectives . . . 1
- 1.2 Literature Review . . . 5
- 1.3 Present Contributions . . . 12
- 1.4 Structure of Thesis . . . 13

2 Theoretical Background **15**
- 2.1 Governing Equations of Two–Phase Flows . . . 15
- 2.2 Arbitrary Lagrangian–Eulerian Form . . . 20
- 2.3 Relative Frame of Reference . . . 21
- 2.4 Turbulence Modeling . . . 22
  - 2.4.1 Closure . . . 23
  - 2.4.2 Initial & Boundary Conditions . . . 24
  - 2.4.3 Turbulence Overproduction in Surface Wave Flows . . . 25
- 2.5 Water Waves Theory . . . 26
  - 2.5.1 Linear Airy Wave Theory . . . 27
  - 2.5.2 Stream–Function Theory . . . 28
  - 2.5.3 Irregular Waves . . . 29
- 2.6 Motion of Rigid Body . . . 29

3 Numerical Framework **33**
- 3.1 Definition of a Control Volume . . . 33
- 3.2 Finite Volume Method . . . 34
- 3.3 Spatial Discretization . . . 35
  - 3.3.1 Evaluation of Inviscid Fluxes . . . 35
  - 3.3.2 Evaluation of Viscous Fluxes . . . 42
  - 3.3.3 Flux Correction for Non–Planar Vertices . . . 42
- 3.4 Temporal Discretization . . . 45
- 3.5 Boundary Conditions of the Flow Equations . . . 47
- 3.6 Linearization & Matrix Assembly . . . 50
- 3.7 Discretization of the Turbulence Model . . . 52
- 3.8 Numerical Wave Generation & Absorption . . . 52
- 3.9 Coupling Algorithm for Fluid–Structure Interaction problems . . . 54
- 3.10 Deforming Grids . . . 56
  - 3.10.1 Exponential Damping . . . 56
  - 3.10.2 Radial Basis Functions . . . 56

4 Applications in Two–Dimensional Flows **61**
- 4.1 Free Surface Waves in Constant Bathymetry . . . 61
  - 4.1.1 Cnoidal Wave . . . 61
  - 4.1.2 3^{rd} Order Stokes Wave . . . 70

4.2 Wave Interaction with Variable Bathymetry . . . 72
4.3 Moonpool–Type Floater . . . 75

5 Applications in Three–Dimensional Flows 81
5.1 Evaluation of Propeller in Open Water Tests . . . 81
5.1.1 Numerical Setup . . . 83
5.1.2 Systematic Evaluation of the Propeller . . . 85
5.2 KRISO Container Ship . . . 87
5.2.1 Numerical Setup . . . 88
5.2.2 Fixed Conditions . . . 94
5.2.3 Dynamic Trim & Sinkage . . . 96
5.2.4 Evaluation in Regular Head Waves . . . 98
5.3 Ship Bow Dynamics . . . 106
5.3.1 Numerical Setup . . . 107
5.3.2 Dynamic Trim & Sinkage of the Bare Hull . . . 109
5.3.3 Resistance of the Full Configuration . . . 111
5.3.4 Effect of Foil Inclination in Calm Water Conditions . . . 113
5.3.5 Effect of Wing in Presence of Regular Waves . . . 115
5.4 Semi–Submersible Platform . . . 120
5.4.1 Numerical Setup . . . 123
5.4.2 Decay Tests . . . 130
5.4.3 Response under Irregular Wave Excitation . . . 134

6 Conclusions & Future Work 141
6.1 Thesis Conclusions . . . 141
6.2 Suggestions for Future Work . . . 143
6.3 Publications . . . 144
6.3.1 Journal Papers . . . 145
6.3.2 Conference Papers . . . 145

A δ–formulation of Rigid Body Equations 147

B Numerical Solution of Dynamic System of Equations 149

C Eigenstructure of the Hyperbolic Two–Phase Problem 151

D Characteristic Boundary Conditions 153

E KCS – Comparison with Other Numerical Codes 157

Bibliography 176

Chapter 1

Introduction

This introductory chapter explores the various challenges encountered in modern marine engineering applications. The various techniques used for hydrodynamic analysis are described, as well as State–of–the–Art numerical methods. Additionally, a thorough literature survey on the main computational tools is conducted and the goals of the proposed numerical method are set. Lastly, the structure of the thesis is given.

1.1 Motivation & Objectives

The harsh and unpredictable nature of the marine environment itself is one of the key challenges in marine engineering. Offshore structures, such as marine vessels and platforms, operate and interact with wind, waves, currents and eventually intense turbulence. All these aspects impact on design, operation and safety of offshore structures. A detailed and carefully planned design process should be followed in order to include the various aspects and challenges of the environmental conditions. Furthermore, the ecological impact of marine structures should be taken into account. Managing the noise generated by underwater operations and reducing emissions to ensure sustainable practices are also aspects to be considered during the evaluation of a design concept. It is imperative to create methods that will help improve the efficiency of the ships and the structural integrity of offshore structures. The main objective of the thesis is to create a robust numerical formulation, which will facilitate the marine engineer to overcome these challenges.

A distinguishable feature of the marine environment is the presence of the interfacial boundary between air and water. Due to the large density difference of the two fluids, the free surface term is commonly adopted. Within a theoretical framework, free surface flows can be viewed as two–phase flows, characterized by the simultaneous presence of two immiscible fluids, air and water. The free surface deforms under a pressure field (wind, presence of a moving vehicle close to the free surface), gravity tries to restore equilibrium and wave patterns are created, which propagate away from the source. Propagating waves change the local flow characteristics (pressure and velocity), absorb energy and play a critical role in various offshore structures, including ships, offshore platforms and underwater vehicles operating close to the free surface. Accurate modeling of the free surface is crucial in many applications in order to assess various performance aspects of marine structures, ranging from resistance calculations and maneuvering trials, to the response of ship hulls under wave excitation and optimization the design of platforms for supporting offshore wind turbines.

As a ship moves through water, a well–recognizable pattern is created, as shown in Figure 1.1a. Divergent waves propagate away from the bow of the ship, while an unsteady turbulent wake is forming at the stern of the ship. Hydrodynamic assessment of a ship typically begins with resistance calculations. During this test, the force required to tow the ship is computed. Resistance calculations involve predictions about turbulent boundary layer formation around

the hull, flow separation at the stern of the ship, accurate capturing of the wave system generated from the motion of the ship, wave elevation and possible breaking on the surface of the hull. This is a fundamental step in ship design process, providing crucial information for assessing the power requirements and fuel efficiency of vessels.

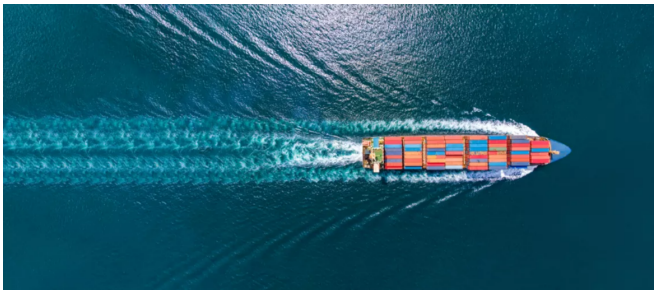

(a) Wake of a container ship in calm water[1]

(b) Propeller of a merchant ship[2]

Figure 1.1: Pictures of two technological aspects in marine engineering

Additionally, modern applications, apart from the hydrodynamic evaluation of the structure, aim to understand the motion of the structure under the flow excitation using a multi–disciplinary approach. Fluid–Structure Interaction (FSI) process considers more than one physical aspects. In naval architecture, it is crucial to understand interaction between the hull and the surrounding fluid even in simple straight ahead conditions in calm waters, and further, analyze its dynamic behavior when subjected to incident waves. To this end, the FSI procedure is utilized that incorporates both body and flow dynamics. A thorough understanding of the coupled dynamics is important for the assessment of stability, structural integrity, and motion characteristics of ships, leading to the optimization of vessel design and the enhancement of passengers comfort and safety.

Another engineering aspect, that lies within the scope of the present thesis, is the assessment of the propulsion systems. Typically, a bladed–propeller design is adopted for the propulsion of large vessels, as shown in Figure 1.1b. The development of accurate methods for propeller evaluation can provide valuable insights into the interaction between the propeller and the surrounding fluid. Detailed modeling of the flow around the propeller blades, the assessment of the propeller is enabled in terms of its performance, efficiency, and even cavitation behavior. This information is crucial for optimizing the propulsion system of vessels, resulting in improved fuel efficiency, reduced emissions and enhanced maneuverability.

The growing interest in renewable energy has pushed forward the development of offshore wind farms. In the early days of offshore technology, the deployment of wind turbines (WT) was limited to shallow waters where fixed structures, such as jackets and monopiles, were used as foundation. The high wind potential in open seas, far from the shore, created the need for alternative designs, in order to deploy WTs in greater depths. For deep sea applications, construction and maintenance costs of the fixed structures increase drastically. Alternatively, a floating platform design is preferred to support the tower of WTs. Among the various concepts, the semi–submersible platform has gained the attention of researchers. This platform uses a catenary mooring line system to hold it in place and prevent it from drifting. The main source of restoring force, in the pitch and heave direction, is the buoyancy force that acts on the surface of the floater. In Figure 1.2 two concepts of semi–submersible floaters are presented. Both concepts are further discussed later and used as validation test cases in this thesis. In Figure 1.2a, the platform UMaine VolturnUs [1] is shown. This is a reference platform for 15–megawatt (MW) wind turbine, developed by International Energy Agency (IEA). The platform consists of a main column to support the WT's tower and three more radial columns that add support

[1]Photo Credit: GreenOak/Shutterstock https://www.shutterstock.com
[2]https://wikipedia.org

and increase the displacement of the platform. The second concept is shown in Figure 1.2b. This platform is distinguished by an opening in the middle, where water oscillates freely and interacts with the platform. This concept has been proposed and commercialized by Ideol, and the objective of the *moonpool* is to reduce the structure motions. The previous concepts were facilitated by detailed assessment of the hydrodynamic and aerodynamic loads that act on the platform. These calculations added to the optimization of the platform's structural design and optimized its performance, ensuring its stability under extreme environmental conditions.

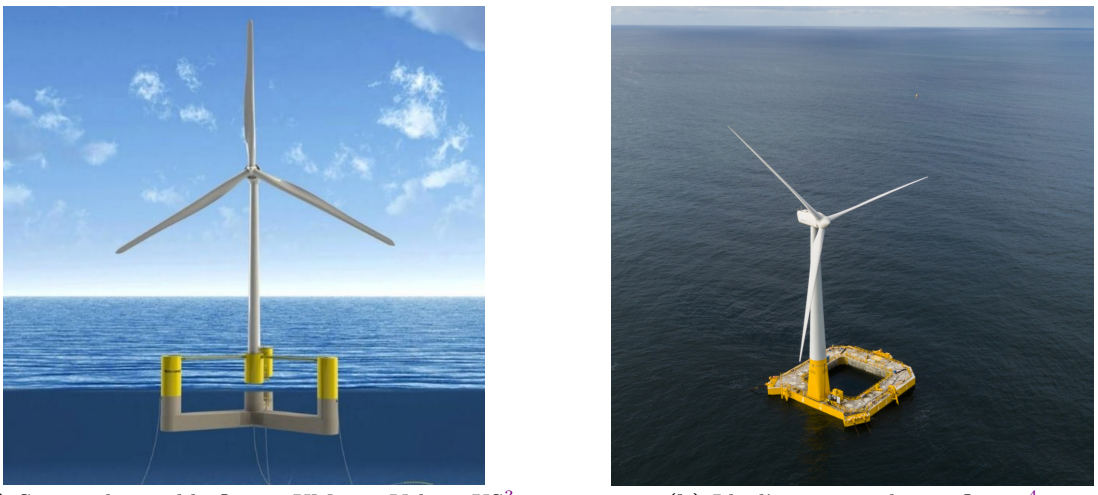

(a) Semi–submersible floater UMaine–VolturnUS[3] **(b)** Ideol's moonpool type floater[4]

Figure 1.2: Two modern semi–submersible concepts for the deployment of offshore wind turbines in great depths.

It becomes clear that unique set of challenges are posed in the aquatic environment that need to be faced by engineers. A variety of specialized techniques to capture FSI under the specific environmental considerations encountered in the aquatic environment have been developed over the past years. One approach to analyze the behavior of structures excited by a flowfield, involves the implementation of detailed experiments. While real–world, full scale experiments provide the advantage of accurate predictions, their costs are relatively high, resulting in a constraint on the number of experiments that can be conducted. Typically, experiments are conducted in laboratory tanks for scaled models. Again, expensive and specialized equipment is required, yet the environmental conditions are easily monitored and more detailed measurements can be taken. However, the inclusion of the free surface introduces scaling effects. In model scale experiments, it is unfeasible to achieve similarity in both Reynolds and Froude numbers. In order to compare results with full scale models, empirical correlations methods are typically introduced.

Apart from experiments, traditionally, engineers relied on analytical models to gain insights into fluid dynamics. Analytical methods are based on simplified assumptions and incorporate experimental observations for fast and approximate calculations. With the increase of computing power, computational methods became a standard procedure for approximating fluid phenomena. Engineers formulated numerical methods that can account for more physical aspects. Over the years, a series of computational tools, of varying fidelity, have been developed. Boundary element methods (BEM) based on the potential formulation of the velocity field have been widely used in the literature to model non–linear phenomena, including propagation of free surface waves [2]. They can provide sufficiently accurate results at small computational cost [3] and can be easily coupled with other numerical frameworks [4, 5]. More sophisticated models have been also developed [6] reducing the problem size and consequently the computational

[3] https://umaine.edu
[4] https://bw-ideol.com

cost. However, potential methods do not account for viscosity and a remedy is to apply viscous corrections on the results [7]. When viscous effects become significant, the usual approach is to employ a Computational Fluid Dynamics (CFD) framework. Space is discretized using structured/unstructured grids and often the Reynolds Averaged Navies-Stokes (RANS) equations are solved on the underlying mesh.

CFD methods have emerged as a powerful tool in the field of engineering, leveraging the analysis process of fluid flows and enabling design. In recent years, CFD has witnessed significant advancements due to the remarkable increase in computing power and the development of sophisticated numerical methods. CFD is cost–effective, efficient and allows for a faster design process. It provides detailed flow information that is not easily measurable in experiments, enabling engineers to gain insight into complex flow phenomena. This flexibility and versatility make CFD an indispensable tool for engineering purposes, in research as well as in industry. CFD reduces significantly time and cost associated with physical experiments, enables extensive parametric studies, facilitating exploration of design alternatives and their impact on performance.

While CFD is a powerful tool for simulating fluid flows, it is worth comparing it with reduced order models commonly used in engineering. Compared to simplified analytical models, CFD offers naturally a higher level of accuracy by solving the governing equations directly. However, it is important to note that CFD can be computationally expensive, particularly for large scale and time dependent problems, which may limit its applicability in certain scenarios. On the other hand, reduced order models, such as semi–analytical linear or non–linear methods, as well as BEM solvers, offer computational efficiency and fast results. Therefore, the choice between CFD and reduced order models depends on the specific requirements of the engineering problem, considering each time the trade–off between accuracy and computational cost. Noticeably, there are several works [8] proposing a hybrid potential/CFD, combining efficiency and accurate representation of viscous phenomena.

Nowadays, State–of–the–art CFD tools, in conjunction with the constantly increasing High Performance Computing (HPC) capabilities, offers significant advancements in the field of ocean engineering and in the hydrodynamic evaluation of offshore structures. Some of the features that modern computational practices have lied their attention ar, the difficulties that arise from the incompressibility constraint, accurate representation of the free surface, effective capturing of small scale turbulence, while at the same time considering the dynamics of the structure. In case of free surface flows, usually the incompressible Navier–Stokes equations (conservation of mass and momentum) are adopted to predict flow motion, although in some cases compressibility effects are considered in the air phase [9, 10] as well. Research in this area has been systematically conducted since the mid–60s and a variety of methods have been developed that can be alternatively used.

Specifically for the free surface modeling, which has been greatly favored by the increase of the computational power, the perplexities introduced to the flowfield, increase drastically the computational cost. Research is focused on developing methods for the accurate tracking of the free surface. Some of the most well known methods are discussed in the next section. Tracking the motion of an interface has been troubling researches even beyond marine engineering applications. Multi–phase flows have gained the attention of the scientific community due to their applicability in a range of applications. Apart from free surface flows, similar modeling can be applied for reacting flows and cavitating flows, as well as for bubble dynamics [11].

Turbulence has always been a main topic of discussion in the fluid dynamics community. The most common approach is to model the main effects of turbulence, such as increased diffusion and mixing, by introducing the Reynolds Averaged approximation. Nowadays, advanced turbulence models have shifted towards more accurate turbulence representations. Emphasis has been given to resolve smaller turbulence scales, especially when analyzing sheared flows or the wake of a structure. Large Eddy Simulation (LES) and Detached Eddy Simulation (DES) are

the most famous approaches for a higher fidelity approximation. The 3D effects of turbulence can be captured better, which is important for separated flows and vortex dynamics.

Demands for more detailed analysis of the dynamic behavior of offshore structures, lead engineers to take into account more than one physical aspect. Computational FSI is considered to be one of the most prominent fields of research, where more models are combined into the same framework to account for different physical aspects. These tools revolutionize design, analysis, and optimization of marine systems, improving safety and efficiency.

The thesis complying with the State–of–the–Art requirements proposes a complete methodology for incompressible free surface flows, where the motion of the structure is also considered as part of a FSI procedure. Starting from the incompressibility assumption, a method rooted in the compressible formulation is adopted and coupled with a two–phase model to accurately resolve the motion of the free surface. Within a RANS approach, limitations and enhancements to the turbulence modeling are also examined. Furthermore its applicability into the aforementioned problems in Ship & Marine Hydrodynamics is directly demonstrated.

1.2 Literature Review

Simulating free surface flows can be decomposed into two main components, a model to incorporate the motion of the free surface and a model to account for the incompressibility constraint in water (sound speed is assumed to be infinite). Here an attempt to outline the progress of these two components over the years is made. The survey begins from the numerical methods developed for free surface flows, it proceeds with the various incompressible formulation and in the last section, focuses on the work conducted on the application of the Artificial Compressibility (AC) framework in two–phase applications.

Free Surface Flows

Modeling free surface flows presents a unique set of challenges. Complexity arises from the dynamic nature of the free surface boundary, where the interface between two immiscible fluids interacts with the surrounding flowfield. In the next few paragraphs, the basic methods that have been developed to monitor the position of the free surface are described in brief.

In a finite volume framework, the free surface methods can be partitioned into two families, the surface tracking (or surface methods) and the surface capturing methods (or volume methods) [12, 13]. One of the methods that falls under the first category, is the surface fitting method [14, 15]. Boundary fitted grids are used to monitor the position of the free surface. This is a single phase approach, only the liquid phase is resolved and the free surface is an external boundary of the domain, and thus appropriate boundary conditions should be considered (the dynamic and kinematic boundary condition). At every timestep, the computational mesh is deformed to follow the motion of the free surface. Although, this surface fitting method manages to provide an accurate representation of the free surface, the need of mesh deformation, or even in some cases the re–initialization of the entire mesh, renders them as computationally expensive. Additionally, wave breaking can not be considered based on this method. Over–turning of the free surface would lead to negative volume cells.

Another method which belongs to the surface fitting approaches and has gained lot of attention is the Level Set Function [16]. This method is widely used, especially in cases where the surface tension is also taken into account. Contrary to the previous method, the computational mesh extends beyond the free surface and both liquid and gaseous phases are resolved. The level set method defines a distance function which measures the distance from the interface. Positive values typically denote distance from the free surface inside the liquid phase, while negative values are used in case of the gaseous phase. The motion of the interface is tracked by solving an advection equation. Geometric quantities such as normal or curvature of the free surface,

are easily obtained from the definition of the distance function. For this reason, the surface tension effect can be easily incorporated into this formulation. Despite its supreme characteristics, at some point of the simulation, due to numerical diffusion the distance function becomes distorted. In order to preserve its characteristics and maintain accuracy, re–initialization of the distance function is needed [17].

Finally, in the family of surface tracking methods, the front tracking method [18] should also be mentioned. This method explicitly follows the interface, however, in order to enhance numerical stability, it uses an auxiliary grid that provides a finite thickness to free surface and thus a smooth transition is made between the two fluids.

The second family of free surface models are the surface capturing methods. Compared to the previous methods, in this case the position of the free surface is not explicitly known. In order to calculate the exact geometric properties (position, normal vector, curvature) a secondary reconstruction step is required. One of the first methods introduced to account for the motion of an interface boundary, is the method of Marker and Cell (MaC) [19]. In this method, massless particles are placed in the region of the fluid, and subsequently move with the local velocity. The free surface is the boundary where cells with markers meet with empty cells. For this reason, the representation of the free surface is directly related to the number of markers used. Later [20], extended this method for multi–fluid calculations, where particles with mass are considered to account for the motion of the free surface. This version resembles to a Lagrangian approximation.

A more sophisticated approach that stems from the energy–based variational framework is the phase–field method [21]. This method is used widely in material science problems. The motion of the free surface is governed by an advection–diffusion equation. The interface is assumed to be of finite thickness and described by thermodynamically consistent conservation laws. The advantages of this method are that the smearing of the free surface can be artificially controlled, and, similarly to the level–set function, the phase–field function can be directly used to calculate geometric quantities on the free surface. As a result, this method can be used to incorporate surface tension effects. On the downsides of the method, the phase–field function lacks inherently of conserving the transported quantity and this is a major limitation for immiscible two–phase flows [22].

Perhaps the most well–known and broadly used method, especially in the field of ocean engineering, is the Volume of Fluid (VoF) method [23]. An indicator (volume) function is used to distinguish between the two fluids. If the volume is empty of liquid, the volume function is zero, otherwise it is equal to one. The volume function is evolved in time according to an advection equation. The free surface is a discontinuity in the field of the volume fraction. The free surface is commonly regarded to be an iso–surface (or iso–line in 2D) amongst the partially filled volumes and typically values of 0.5 are adopted. This method is relatively simple to implement and its built–in mass conservation property makes it an appealing choice. A critical issue of this method is the numerical diffusion that is introduced at the advection step. This leads to the smearing of the free surface over several cells, making difficult to locate its exact position.

Over the years, researchers have proposed various methods to mitigate the numerical diffusion and calculate exactly the numerical flux of the advection step, while at the same time guarantee that the function stays between its physical bounds (zero and unity). These methods can be divided into two categories; the algebraic and the geometric methods.

Starting from the algebraic methods, researchers tried either explicitly or implicitly to create numerical schemes for the compression of the free surface. In the first case, an artificial compression term is added to the advection equation of VoF to counteract the numerical diffusion and maintain a sharp interface [24]. The term is activated in regions of large gradient of volume function and its effect is regulated by an adhoc parameter. Furthermore, in case of the implicit methods, which can also be combined with the previous compression term, high

order resolution schemes are constructed to prevent the smearing of the free surface. These schemes typically combine a high–order interpolation scheme and a downwind scheme, which is responsible for the compression of the free surface. Well–known software use methods that lie on this category. For example, OpenFOAM uses the Multidimensional Universal Limiter with Explicit Solution (MULES) [25], ANSYS Fluent the Compressive Interface Capturing Scheme for Arbitrary Meshes (CISCAM) [26], and STAR–CCM+ the High–Resolution Interface Capturing Scheme (HRIC) [27]. The second category of methods, proposed for the advection of the volume fraction, uses an exact representation of the interface by following a geometric reconstruction. Afterwards, the reconstructed profile is advected with the local velocity field. Some notable examples are; the Piecewise Linear Interface Calculation (PLIC) [28] and the isoAdvector scheme [29]. A more comprehensive review of the geometric formulation of VoF can be found in [11].

Apart from these two broad categories for accounting the presence of the free surface, some hybrid methods have been formulated that try to match the best practices of each method. Some examples are; the couple level–set/VOF (CLSVOF) method [30] and phase–field/VOF [31].

Incompressible Flows

The core algorithm for solving free surface flows is the incompressible solver. The algorithm is responsible for calculating the vector velocity field $\vec{v}$ and the pressure field p. The incompressible equations have several features, that renders them as a demanding system to be solved. Several computational algorithms have been developed over the years that try to tackle its complications, provide accurate and cost effective numerical solutions. At this time, the various techniques have been well documented and reported in several text books (see for example [12, 32]). Here, the complications that arise from the incompressible formulations are outlined and an overview of the most widely spread technologies for solving incompressible equations on a computational grid is provided.

The mass and the momentum equations for incompressible, iso–thermal flows are expressed as

$$\nabla \cdot \vec{v} = 0 \tag{1.1a}$$

$$\frac{\partial \vec{v}}{\partial t} + \vec{v} \cdot \nabla \vec{v} = -\frac{\nabla p}{\rho} + \nu \nabla^2 \vec{v} + \vec{f}_B \tag{1.1b}$$

The density ρ is constant everywhere, thus the continuity Equation (1.1a) appears as a constraint for conservation of the fluid's volume. Equation (1.1b) expresses the rate of change of the velocity field relative to the non–linear advection term of the velocity field ($\vec{v} \cdot \nabla \vec{v}$), the pressure gradient (∇p), the diffusion caused by the shear stresses ($\nu \nabla \overline{\tau}$), as well as the various body forces ($\vec{f_b}$) that add–up to the field (e.g. gravity). The above elliptic–parabolic system of equations needs to be solved to acquire the pressure and the velocity vectors.

The first complication arises from the calculation of the pressure field. The previous system of equations lacks of a time–evolution equation for pressure. In compressible equations, the mass equation can be used to calculate the density field and then, by making use of the state equation, the pressure can be computed. However, in this case the mass equation appears as kinematic constraint, rather than a dynamic equation that can be used to advance the solution in time. An equation to acquire the pressure field that satisfies a divergent–free velocity field should be constructed. The second challenge is to account for the non–linearity of the advection term in the momentum Equation (1.1b). The unknown velocity field is advected by the same velocity. In a computational framework non–linearities are taken into account by formulating an iterative process. Successive prediction–correction steps are made until a converged solution is obtained. This linearization step, typically, depends on the implementation details of the pressure–velocity coupling.

Historically, two opposing classes of incompressible solvers have been developed; (a) the pressure projection (or pressure–correction) methods and (b) the Artificial Compressibility methods. Their main difference between the two is that the first creates a series of successive steps to acquire the solution, while the second creates a single–block (non–segregated) process. While several implementations examples of both methods can be found in literature, the first class of methods has clearly dominated over the years.

By choosing a process based on a pressure projection method, the first thing that should be addressed is the variable arrangement in the grid. A straight forward discretization of the system, where all variables (pressure and velocities) are stored in the same positions (co–located arrangement), leads to the decoupling of equations and gives rise to unphysical solutions. Adopting either a finite volume or a finite difference approximation, a simple linear discretization scheme would involve non–consecutive cells in the calculation of pressure gradient term, as well as in the discretized continuity equation. As a result, the discrete system of equation admits non–physical zigzag solutions, giving rise to the well–known checker–board problem.

The first method for enforcing the coupling of the equations and prevent unphysical solutions was made possible by staggering the grid points for the different unknowns, with respect to each other. The Grid Staggering technique, which is the most straightforward solution to the checkerboard problem, was introduced by Harlow and Weltch [19] and had become a standard practice until mid–80s. In this approach, the velocity field is stored at cell faces, while pressure is stored at cell centroids. In this arrangement, the discretization involves directly the variables at their known location, and thus no interpolation is needed. The theoretical convergence analysis is well–developed and no special features are needed to prevent oscillations in pressure and velocity fields. The staggered grid approach is the method of choice for orthogonal grids. However, its extension to unstructured grids is complicated and computationally demanding.

A co–location arrangement, where all variables are stored in the same point, is favored due to its easy implementation in unstructured grids. Complex flow phenomena and complex geometries are well fitted by using a set of control volumes that can be refined and coarsened arbitrarily with no restrictions. The deficiency of the straight–forward discretization in a co–located arrangement lies in the linear interpolation of the variables. In 1983, Rhie and Chow [33] proposed an interpolation scheme that involves a higher–order scheme with a larger grid stencil. It is widely used and is employed in many commercial CFD codes.

Once a proper variable arrangement on the grid has been decided, an algorithm to calculate the pressure and the velocity field should be constructed. Both problems of the system of equations associated with, the non–linearity of the velocity advected by itself and the pressure–velocity linkage, can be resolved by adopting an iterative process. The most widely used methods is the pressure–correction algorithms and its variants. These methods attempt the inter–equation coupling by perturbing the mass equation with pressure terms.

In order to derive an equation for pressure, Equations (1.1a) and (1.1b) can be combined, by taking the divergence of the momentum equation

$$\nabla \cdot \left[\frac{\partial \vec{v}}{\partial t} + \vec{v} \cdot \nabla \vec{v} + \frac{\nabla p}{\rho} - \nu \nabla^2 \vec{v} - \vec{f}_B \right] = 0 \tag{1.2}$$

Since $\nabla \cdot \vec{v} = 0$ holds at all times, $\nabla \cdot {}^{\partial \vec{v}}/_{\partial t} = 0$ and by neglecting body forces $\vec{f}_B$, the Poisson Equation (1.3) can be constructed and used as reference for pressure.

$$\nabla^2 p = -\rho \nabla \cdot \left[\vec{v} \cdot \nabla \vec{v} - \nu \nabla^2 \vec{v} \right] \tag{1.3}$$

The pressure–correction methods use a similar Poisson equation, however not for the primitive variables of the field, but as a mean to correct them. The field variables are decomposed in an initial and perturbed field. A guessed pressure field is used as a starting point, to solve the momentum equations. Afterwards, a pressure correction equation deduced from the continuity

equation is solved to obtain a correction for pressure, which is in turn used to update the velocity and pressure fields. The process continues until the perturbations of velocity and pressure converge to zero. The most well–known pressure–correction algorithm, developed primarily for steady flows, is the Semi–Implicit Method for Pressure–Linked Equations (SIMPLE) [34], while several variants have been introduced that try to improve some of its deficiencies, such as SIMPLER [35], SIMPLEC [36]. These types of methods have been widely used in many commercial software. An extension of the SIMPLE algorithm was reformed to account for unsteady flows, the PISO algorithm, which stands for Pressure Implicit with Splitting of Operators, of Issa [37].

Another approach for the incompressible equations are the projection methods [38]. These methods perform a decomposition of the velocity field into divergence–free and curl–free parts (Hodge/Helmholtz decomposition). The solution is performed into two steps. The first step is to compute the potential part of the decomposition process. The second step uses the pressure to project the velocity field of the previous step onto a solenoidal velocity field and get the updated solutions. These methods can be viewed as a generalization of the pressure–correction and staggered grid approach, ultimately formulating a Poisson equation for pressure [32].

Another family of methods introduced aiming to perform the inter–equation coupling are the Fractional Step methods [39]. This concept is more of a generic approach than a particular method. In this context, an operator splitting is performed and the different physical aspects are accounted for in the sub–steps. For example, using an explicit time formulation a velocity component u_i known at the time instance n can be advanced in time using the following symbolic formulation,

$$u_i^{n+1} = u_i^n + (C_i + D_i + P_i)\,\Delta t \tag{1.4}$$

The equation can be readily split into three components convection C_i, diffusion D_i and the pressure gradient P_i.

$$u_i^* = u_i^n + (C_i)\,\Delta t \tag{1.4a}$$
$$u_i^{**} = u_i^* + (D_i)\,\Delta t \tag{1.4b}$$
$$u_i^{n+1} = u_i^{**} + (P_i)\,\Delta t \tag{1.4c}$$

This general framework can incorporate various methods to account for each sub–step. For example for the gradient pressure, a similar Poisson equation as in (1.3) can be constructed.

In case of constant density flows, the Navier–Stokes equations can be replaced by the vorticity/streamfunction equations [40]. In two dimensions, the pressure and the velocity components can be eliminated from the equations, by the streamfunction and vorticity, which are scalar fields. This reduction in the number of the dependent variables are one major advantage of the method. In three–dimensional flows, however, the formulation leads to six variables compared to four dependent variables in the case of primitive variables Navier–Stokes [32]. The main perplexity of this method, that makes it unattractive compared to a pressure–velocity formulation is the implementation of boundary conditions at solid boundaries and symmetry planes. These boundaries are surfaces of constant streamfunction and the boundary conditions are unknown and should be calculated as part of the solution.

All the previous mentioned algorithms have some features in common. Firstly, all methods form a segregated (sequential) iterative process to perform the coupling of the individual equations. Although, this features may be appealing in some cases, because every step can be considered and improved separately, nevertheless it significantly complicates the final solution algorithm. The second feature, and perhaps the greatest downside of these methods is that at some point they construct a Poisson equation for the pressure or its perturbed component. Poisson solvers are algorithmically complicated and they add great computational cost especially in a multi–processing environment.

An alternative to this for coupling mass and momentum equations is the Artificial Compressibility method (AC) [41, 42]. The concept of AC is to transform the elliptic equations describing

incompressible flows into a coupled hyperbolic system. The whole idea is to mimic the numerical procedure followed in compressible flows, and adopt their appealing features such as its efficiency in massively parallel applications and the vast arsenal of hyperbolic solvers offered for the advection step.

The first step to perform the inter–equation coupling, is to assume a pseudo–relation between pressure and density, similar to the definition of the sound speed in compressible flows $\frac{\partial \rho}{\partial p} = \frac{1}{c^2}$. This relation does not have any physical meaning and it is artificially controlled by a free numerical parameter β. The following relation is defined

$$\left.\frac{\partial \rho}{\partial p}\right|_{\tau} = \frac{1}{\beta} \tag{1.5}$$

Since this relation does not hold once an admissible solution is found, it can only be defined during convergence. Thus, the relation has only meaning during pseudo–time–τ, the time variable used to measure the dimension that an iterative process follows until it reaches a convergent solution.

The second step is to perform the pseudo–time preconditioning of the governing equations (1.1a) and (1.1b). This step involves the augmentation of the equations with pseudo–time derivatives of the conservative variables (mass and momentum). These derivatives introduced to the Navier–Stokes equations modify the way the solution evolves towards convergence. This is a very popular approach and it is widely used to change the nature of the steady equations in compressible flows. Additionally, its use has been extended to unsteady flows by introducing the dual–time stepping approach. In case of steady flows, the pseudo–time derivatives are used to initiate an iterative process and once convergence is accomplished, these terms vanish and the original set of equations is retrieved. In time–true computations, time is discretized in a number of finite intermediate steps (timesteps). In each step, a pseudo–state problem is solved by performing the pseudo–time preconditioning. Again, convergence is accomplished once the pseudo–time derivatives of the unknown variables tend to zero and the iterative process proceeds to next timestep.

By considering the previous remarks, the incompressible Navier–Stokes equations augmented with pseudo–time derivatives of the conservative variables and using the AC definition of sound speed (Eq. (1.5)), the following system of equations is formed

$$\frac{1}{\beta}\frac{\partial p}{\partial \tau} + \nabla \cdot \vec{v} = 0 \tag{1.6a}$$

$$\frac{\partial \vec{v}}{\partial \tau} + \frac{\partial \vec{v}}{\partial t} + \vec{v} \cdot \nabla \vec{v} = -\frac{\nabla p}{\rho} + \nu \nabla^2 \vec{v} + \vec{f}_B \tag{1.6b}$$

The coupling is performed once a derivative to advance the solution in (pseudo–) time has been introduced. Checker–board effects are directly avoided thus no staggering of variables or other remedies are needed and the variables can be discretized directly. Furthermore, employing the AC method the elliptic equations are transformed into hyperbolic in pseudo–time. This is specifically important, because a great variety of Riemann solvers, initially developed for compressible flows, can be utilized to account for the non–linearities. The advection step can be viewed as a local Riemann problem, with discontinuous data on the two sides of the control volume boundary. In literature of the compressible solvers, a variety of Riemann solvers have been developed, HLLC [43], Osher [44] and Roe [45] to name a few, to compute the convective fluxes across the boundary of the control volumes.

The concept of the AC method comes with the expense of an arbitrary parameter (β) that needs to be specified. This parameter regulates the coupling of the equations. Large values leads to a loose coupling of the equations and small values to stiff numerical procedure. In [46] where a comparison for pressure–based and AC methods can be found, it is reported that the

AC parameter can affect the stability and the convergence of the solver and its choice requires some intuition on behalf of the user. On the present thesis, the effect of the AC parameter will be further discussed.

As already mentioned, the solution of the free surface flows is based on the incompressible assumption. A numerical algorithm of this type involves firstly, a method to solve the incompressible equations and secondly, a method to predict the motion of the free surface. Projection methods and especially the pressure–corrections variants are by far the most employed approaches in this area [47, 48], while fractional step methods have also emerged recently in literature [49]. These algorithms incorporate the free surface modeling as an additional step into this "shattered" iterative process. This segregation, in theory, sets on upper limit to the time marching step in order to prevent the time lagging of the equations. In the present thesis, a single–block system of equation that incorporates both the incompressible and free surface modeling is constructed and tested, using the AC method coupled with the VoF model for two–phase flows.

In this section, the two opposing families have been contrasted against each other and their upsides and downsides have been presented. As a last remark, it should be mentioned that, the two families have been combined into one algorithm, which exhibits the desirable characteristics of both. The combined method is titled as Artificial Compressibility Characteristic–Based Split (CBS–AC) [50] and has been also extended to account for free surface flows [51].

Artificial Compressibility

Artificial Compressibility (AC) method, at the early stages of its development was designed to account for one–phase incompressible flows. As already described, the AC method introduces pressure derivatives in the mass equation and as a result creates an equation to evolve the pressure field in (pseudo–)time. Initially the method was proposed by Chorin [41] for solving steady state incompressible viscous flows. Later the method extended for unsteady flows by Merkle, adopting either an explicit time stepping scheme [42] or a fully implicit scheme by introducing the dual–time stepping technique [52]. At the same period, Turkel [53] offered an alternative formulation for the AC method. In his work, pressure pseudo–time derivatives were added also, to the conservative form of the momentum equations to strengthen the coupling of the equations. He argued, additionally, that the AC parameter can have a local character, depending on the local velocity field. This concept was later generalized by Malan *et al.* [54], where they showed that the pressure contribution in the momentum equations can also scale locally. Apart from the fully incompressible version of the AC method, various authors formulated the AC method as a preconditioning method to accelerate convergence in weakly compressible flows [55] (flows in the low Mach regime). As it becomes clear, the AC method has gradually found its way in the assessment of incompressible (or weakly compressible) flows and nowadays has been a standard practice in many research applications, especially in aerodynamic flows (see for example in [56–58]). Additionally, due to the successful implementation of AC method, more recent studies have used it as basis for constructing higher order numerical methods [59, 60].

Due to the appealing characteristics of the AC formulation, researchers have managed to generalize its concept and apply it to multi–phase flows. In the last two decades the AC has become popular for solving cavitating flows. One of the most fundamental works in the field of the two–phase flows in general was performed by Kunz *et al.* [61]. In their work, a preconditioned AC formulation was proposed to accelerate convergence. Their method has been widely used since then [62]. Based on the preconditioner of Kunz and in the same spirit as Turkel [53] and Malan [54] for one–phase flows, Hejranfar [63] and Yue *et al.* [64] introduced pressure perturbations in the momentum equations and employed their method in cavitating flows. As in the case of single phase flows, works have been presented that use the AC formulation as a generalized preconditioning method for weakly compressible flows [65].

Apart from the work performed in cavitating flows, the AC has been used also in free surface

flows. Typically, free surface flows are regarded as a special case of two–phase flows since they are primarily driven by the gravitational field. In this direction, Kelecy and Pletcher [66] have extended the AC method for free surface flows in closed containers by creating a coupled system of equations involving the incompressible equations and the VoF method. In [67], the AC method is used to simulate falling water columns in containers by performing an operator splitting to integrate the VoF method. Bhat and Mandal [68] successfully implemented the AC method in simple free surface flows in two dimensions in case of sloshing and bubble splash. More recently, [69] have directly extended their work and conducted a comparative study by making use of various Riemann solvers. A thorough review of the use of the AC method in in two–phase flows can also be found in [70].

Despite the extended use of the AC method in two–phase flows, the literature for applications in the field of ocean engineering is rather limited. Some of the works in this research area are; firstly, Hino [71] demonstrated the use AC in flows around fully submerged hydrofoils and around the streamed line Series 60 (S60) ship hull. Some fundamental works have also been carried out for the propagation of steady water waves in [72, 73]. Perhaps one of the most complete works in this area was performed by D.S. Nichols [74]. In his work, he managed to extend the work presented from Kunz *et al.* [61] for cavitating flows and implemented it in simple steady problems around ship hulls.

1.3 Present Contributions

Although many studies have successfully exploited the advantages of the AC method in one–phase and two–phase flows, there is a lack of research in the field of Ship & Marine Hydrodynamics. The objective of this thesis is to explore the capabilities of the AC formulation coupled with the VoF method in marine applications. To this end, using as a starting point the preconditioned AC formulation of Kunz *et al.* [61], a coupled AC/VoF methodology in arbitrary polyhedral grids is developed using the finite volume method and validated in series of test cases for free surface flows. Challenges as generation, propagation and absorption of surface waves, turbulent flows around surface piercing structures and wave induced rigid body motions are directly addressed.

In addition to the hydrodynamic methodology, a standard 6 Degrees of Freedom (6–DoF) rigid body solver is developed and coupled with the flow solver to investigate FSI problems. The motion of the rigid body inside the computational grids is made possible by applying deformation algorithms. The coupling is performed within an iterative procedure until convergence of DoFs is accomplished, leading to the strong coupling of the two procedures.

In short, the thesis makes the following contributions in the assessment of hydrodynamics problems using CFD:

- A coupled formulation AC/VoF in arbitrary polyhedral volumes
- A framework for generation and absorption of regular (linear and non–linear) and irregular free surface waves
- A correction method for the hydrostatic pressure terms in polyhedral terms
- A strong coupled methodology for FSI problems

In order to prove the validity of the proposed numerical framework, a series of numerical experiments are conducted. An extensive Validation and Verification (V&V) procedure is performed. The validation is carried out by comparing numerical results with analytical, experimental and other available numerical data. The verification is performed by contacting separate sensitivity studies on the spatial and temporal resolution, for each computational experiment. Moreover, parametric studies are conducted to establish the influence of various numerical parameters, such as the AC parameter β, as well as of the parameters affecting wave generation and absorption.

The following sets of test cases are considered in this study:

1. Generation, propagation and absorption of two non–linear waves (one Cnoidal and one 3rd Stokes)
2. Interaction of a linear wave with variable bathymetry
3. Response of a moonpool type floater under wave excitation in 2D
4. Evaluation of a propeller's performance in open water tests
5. Resistance calculation, free trim and sinkage conditions, as well as response in head waves conditions with 2 DoFs for the KCS ship
6. Preliminary evaluation of a ship augmentation propulsion concept using a fully submerged hydrofoil. Test cases in calm water and in head waves conditions with 2 DoFs are conducted
7. Response of a semi–submersible floater to an initial displacement and under excitation from irregular waves

The present methodology was implemented as an extension to an unstructured cell–centered finite volume code *MaPFlow*. The solver is capable of solving the compressible URANS equations [75] and has further capabilities of predicting laminar to turbulent transition, as well as modeling turbulence using high fidelity models (DES and LES) [76]. MaPFlow is capable of running in a multi–processor environment. Each process solves a specific part (or block) of the computational domain and communication is made at the inter–block boundaries. The grid partitioning is performed by the *Metis* library [77], while the interprocess communication is achieved through the MPI protocol.

1.4 Structure of Thesis

The remainder of the thesis is structured as follows:

- In Chapter 2, the theoretical foundations of the work are set. The governing equations of free surface flows in moving and deforming grids are formulated. Additionally, the basic water wave theories, that are used to introduce regular and irregular waves in a computational wave tank are described and finally the equations of motion of a rigid body with 6 degrees of freedom are also presented.
- In Chapter 3, the discretization of the flow equation is given in detail. Spatial and time discretization, as well as, the linearization of the system of equations are included. Furthermore, the numerical framework for regular and irregular wave generation is also included.
- In Chapter 4, the basic verification of the numerical methodology is presented. Simplified flows in two dimensions are chosen to demonstrate the ability of the solver to propagate free surface waves, resolve dispersive phenomena and account for motions induced by the wave–structure interaction.
- In Chapter 5, the modeling of more complex geometry is considered with actual engineering interest. The results of the computational methodology are compared with experimental data in a series of computational test cases. Specifically, validation is carried out on; (a) a rotating propeller in open water tests, (b) resistance calculations for two different ship hulls (a container and ferry ship) in fixed and in free conditions, (c) seakeeping tests for the two hulls hulls in head waves conditions and lastly, (d) the response of a scaled Y–shaped floater in decay tests and under polychromatic wave excitation.
- In Chapter 6, the basic outcomes of the thesis are summarized and suggestions for possible extension of this work are given.

All computations were performed in the National HPC facility – ARIS. The computational time was granted by the Greek Research & Technology Network (GRNET) under a series of annual production projects (MaPFloat–pr014043_thin, DYNASEA–pr012019_thin, SHIPFLOW–pr010039_thin)

Chapter 2

Theoretical Background

The governing equations of fluid and rigid body motion are considered. The chapter emphasizes on the Artificial Compressibility formulation for free surface, turbulent flows. The motion and the deformation of the grid is also accounted for in the derivation of the flow equations. Furthermore, the basic analytical theories used for wave generation inside a computational wave tank are also presented.

2.1 Governing Equations of Two–Phase Flows

Artificial Compressibility

The Artificial Compressibility (AC) [41] permits the inter–equation coupling by introducing pressure derivatives in the mass equation. This is performed by assuming a pseudo–relation between density and pressure. The whole idea is rooted in the formulation of the compressible flows, where pressure and density are linked through the definition of the sound speed c, $\frac{\partial \rho}{\partial p} = \frac{1}{c^2}$. AC adopts a similar definition, it creates a linking of the equations by considering a pseudo–relation between pressure and density. The relation is controlled by a purely numerical parameter β strictly greater than zero. To this end, the following relation is introduced

$$\left.\frac{\partial \rho}{\partial p}\right|_{\tau} = \frac{1}{\beta} \tag{2.1}$$

Equation (2.1) holds only in the context of a numerical procedure, where iterations are performed until a convergent solution is obtained. The convergence rate can be quantified by a time variable, commonly referred to as pseudo–time, τ. Relation (2.1) is valid only during pseudo–time.

Returning to the governing equations of unsteady incompressible flows. Firstly, the incompressible form of the mass equation expresses the conservation of fluid volume, meaning that the divergence $(\nabla\cdot)$ of the 3–dimensional (3D) velocity vector $\vec{v} = (u, v, w)$ is equal to zero. Secondly, the change in the momentum in real time (t) is associated with the advection of momentum by the underlying velocity field $(\nabla \cdot (\rho \vec{v}\vec{v}))$, the pressure gradient (∇p), the change due to diffusion $\nabla \cdot \overline{\tau}$ and the body forces $(\vec{f}_B)$ that act on the flowfield. The governing equations are summarized below

$$\nabla \cdot \vec{v} = 0 \tag{2.2a}$$

$$\frac{\partial \rho_m \vec{v}}{\partial t} + \nabla \cdot (\rho_m \vec{v}\vec{v}) + \nabla p = \nabla \cdot \overline{\tau} + \vec{f}_B \tag{2.2b}$$

The AC method introduces secondary time derivatives that measure the convergence rate of the unknown variables within an iterative process. These pseudo–time (τ) derivatives tend to zero upon convergence and thus the original system of equations is retrieved. By augmenting the governing system of equations with pseudo–time derivatives of the conservative variables (mass and momentum) and introducing the AC definition (2.1), a single coupled system of equations is formed

$$\frac{1}{\beta}\frac{\partial p}{\partial \tau} + \quad \nabla \cdot \vec{v} = 0 \tag{2.3a}$$

$$\frac{\partial \rho_m \vec{v}}{\partial \tau} + \quad \frac{\partial \rho_m \vec{v}}{\partial t} + \nabla \cdot (\rho_m \vec{v}\vec{v}) + \nabla p = \nabla \cdot \overline{\tau} + \vec{f}_B \tag{2.3b}$$

The AC method has managed to create an equation for pressure and additionally, by introducing in the momentum equation pseudo–time derivative, a coupled system is formed during convergence. Once convergence is accomplished, pseudo–time derivatives vanish and the original system of equations is retrieved. The coupling is controlled by the numerical parameter β. Large values of β imply a loose coupling of the equations resulting in slow convergence characteristics, while for small β values the system is strongly coupled, which may lead to a stiff numerical scheme. It becomes clear that, parameter β can affect convergence and a familiarity with the details of the numerical implementation is required.

Volume of Fluid Method

In order to resolve the motion of the free surface, the Volume of Fluid (VoF) [23] approach is considered. The VoF method is widely used to describe the motion of two (or more) immiscible fluids, as is air and water in case of free surface flows. The method begins with the definition of the volume fraction α_l, which indicates the presence of either the one or the other fluid. In the present thesis, the usual convention is adopted, if α_l is equal to one the liquid phase (water) is identified, otherwise, for zero values, the gaseous phase (air) is indicated. The previous convention leads to the following density definition of the volume fraction

$$\alpha_l = \frac{\rho_m - \rho_a}{\rho_w - \rho_a} \tag{2.4}$$

where indices m, w and a, refer to the properties of the mixture, water and air.

The definition of the volume fraction can be generalized to account for multi–phase flows. Each phase i can be assigned with a corresponding volume fraction α_i, then at each point, the sum of the volume fractions should be equal to one, meaning that

$$\sum_{i=1} \alpha_i = 1 \tag{2.5}$$

The above equation for free surface flows, where only water and air are considered, is simplified in

$$\alpha_l + \alpha_g = 1 \tag{2.6}$$

where α_g is the volume fraction indicating the presence of gas phase (air).

VoF method dictates that the total derivative of the volume fraction is everywhere equal to zero

$$\frac{D\alpha_l}{Dt} = 0 \Rightarrow \frac{\partial \alpha_l}{\partial t} + \vec{v} \cdot \nabla \alpha_l = 0 \tag{2.7}$$

This implies that the free surface is an iso–surface of constant volume fraction that is materially conserved over time. Typically, the free surface is identified for $\alpha_l = 0.5$. The free surface is

regarded as discontinuity in the volume fraction field, or equivalently as a discontinuity in the density field, according to the definition of Equation (2.4).

Once the evolution of the volume fraction field has been defined based on the advection Equation (2.7), the properties of the mixture can be decided. The density ρ_m and viscosity μ_m are computed as

$$\begin{aligned} \rho_m &= \rho_a + \alpha_l \Delta\rho \\ \mu_m &= \mu_a + \alpha_l \Delta\mu \end{aligned} \tag{2.8}$$

where the difference between the properties of water and air are noted as $\Delta\rho = \rho_w - \rho_a$ and $\Delta\mu = \mu_w - \mu_a$. Again, indices w and a, indicate the properties of water and air, respectively.

Governing Equations of Free Surface Flows

Using the mass (2.3a), the momentum (2.3b) and the VoF (2.7) equations, the governing equations of free surface flows are formed. At this point, it is worth making a few comments on the mass conservation and the incompressibility constraint in case of density–variable flows.

In the same spirit as in [47, 74], starting from the general form of the continuity equation expressed separately for air (a) and water (w)

$$\begin{aligned} \frac{\partial \rho_a}{\partial t} + \nabla \cdot (\rho_a \vec{v}) = 0 \\ \frac{\partial \rho_w}{\partial t} + \nabla \cdot (\rho_w \vec{v}) = 0 \end{aligned} \tag{2.9}$$

multiplying the air density equation with α_g and similarly with α_l the water equation

$$\begin{aligned} \frac{\partial \alpha_g \rho_a}{\partial t} + \nabla \cdot (\alpha_g \rho_a \vec{v}) = 0 \\ \frac{\partial \alpha_l \rho_w}{\partial t} + \nabla \cdot (\alpha_l \rho_w \vec{v}) = 0 \end{aligned} \tag{2.10}$$

adding the previous equations together

$$\frac{\partial \left(\alpha_g \rho_a + \alpha_l \rho_w\right)}{\partial t} + \nabla \cdot \left(\left(\alpha_g \rho_a + \alpha_l \rho_w\right) \vec{v}\right) = 0 \tag{2.11}$$

and using the definitions (2.4) and (2.6), the general form of the continuity equation (2.12) is obtained. Thus as a first comment, it should be noted that the density ρ_m of the mixture is conserved.

$$\frac{\partial \rho_m}{\partial t} + \nabla \cdot (\rho_m \vec{v}) = 0 \tag{2.12}$$

A similar approach can be followed to show that the general form of the momentum equation (2.3b) also applies in multi–phase flows.

Moving on, to the incompressibility constraint applied in multi–phase incompressible flows. Recalling that $\rho_m = \alpha_l \rho_w + (1 - \alpha_l)\, \rho_a$ and by splitting the divergence product, the continuity equation of the mixture density (2.12) can be written as

$$\left(\rho_w \frac{\partial a_l}{\partial t} + \rho_w \vec{v} \cdot \nabla \alpha_l\right) - \left(\rho_a \frac{\partial a_l}{\partial t} + \rho_a \vec{v} \cdot \nabla \alpha_l\right) + \rho_m \nabla \cdot \vec{v} = 0 \tag{2.13}$$

and using the definition of the VoF function of Equation (2.7), the divergence free velocity field is retrieved

$$\rho_m \nabla \cdot \vec{v} = 0 \tag{2.14}$$

As a result, a divergence free velocity field is recovered using the multi–phase equations.

The last step to derive the governing equation for free surface flows is to perform the coupling of the VoF method with the AC formulation. The divergent free velocity field can be introduced into the VoF Equation (2.7) and produce its conservative form. Furthermore, as in the case of the momentum equations, the VoF equation is augmented with pseudo–time derivative. The last two remarks are shown below

$$\frac{\partial \alpha_l}{\partial \tau} + \frac{\partial \alpha_l}{\partial t} + \nabla \cdot (\vec{v}\alpha_l) = 0 \tag{2.15}$$

To sup up, the coupled AC and VoF method introduces a system of 5 equations, the incompressible constrain (2.3a), the conservation of momentum of the mixture (2.3b) and the conservative counterpart of the VoF (2.15). The 5 unknowns of the system are the pressure field p, the 3D velocity field $\vec{v}$ and the volume fraction α_l. All equations have been augmented with pseudo–time derivatives and a coupled system of equations is formed.

One of the appealing features of the AC method is that, the coupled system of equations is hyperbolic in *pseudo–time*. The same holds for the coupled AC/VoF formulation, since the eigenvalues of the system are real and distinct. The density discontinuity is marked as a contact discontinuity wave, where jumps of density are permitted but not of pressure or velocity. The arsenal of the Riemann solvers developed for the compressible equations can be exploited to advance the solution in (pseudo–) time.

One of the first attempt to use the AC/VoF approach to simulate the motion of the free surface was performed by Kelecy and Pletcher [66]. The resulted eigensystem of the flow equations was derived. A downside of the method is that the eigenvalues of the system scale with the local density value. In case of high density ratios, as in free surface flows, small values of wave propagation speed are computed and thus information propagates slowly. The next paragraph presents preconditioning method to remove the density dependency from the eigenvalues of the system and accelerate convergence.

Preconditioned Conservative Form

In order to remove the density dependency from the eigenvalues of the system, preconditioning is applied to the governing equations. The present work uses the preconditioner matrix proposed by Kunz *et al.* [61], initially for cavitating flows, and extended later by D.S. Nichols [74] for steady free surface flows. Before presenting the preconditioner matrix and the final form of the equations, it is useful to discuss some features of the governing equations and introduce also definitions that will help to understand the preconditioning effects.

Starting from the design features of the preconditioner matrix. Firstly, the system of equations should be casted in a form, where the primary unknowns (primitive) variables appear at the pseudo–time derivatives. Pressure and volume fraction are directly retrieved by the AC augmented continuity equation (2.3a) and the conservative form of the volume fraction (2.15). In order to formulate an equation for the velocity field, the pseudo–time terms of the momentum (2.3b) can be written as

$$\frac{\partial \left(\rho_m \vec{v}\right)}{\partial \tau} = \rho_m \frac{\partial \vec{v}}{\partial \tau} + \vec{v}\Delta\rho \frac{\partial a_l}{\partial \tau} \tag{2.16}$$

where in the previous equation the definition of the mixture quantities (Eq. (2.8)) were introduced. A similar equation can be derived for the unsteady derivatives.

Secondly, in the incompressibility constraint for multi–phase flows (2.14), the divergence free velocity scales with the mixture density ρ_m. Kunz *et al.* proposed the scaling of the pressure derivatives with this mixture density, obtaining the following form of the continuity equation

$$\frac{1}{\rho_m \beta}\frac{\partial p}{\partial \tau} + \nabla \cdot \vec{v} = 0 \tag{2.17}$$

Finally, for the derivation of the conservative form of the VoF equation, a divergence free velocity field is assumed. However, during convergence the divergence of the velocity is not

zero, since the pseudo–time derivative of pressure has not yet vanished. By introducing the preconditioned continuity equation (2.17) to the original advection form of the VoF definition (Eq. (2.7)), the following equation for the volume fraction is derived

$$\frac{\partial \alpha}{\partial \tau} + \frac{\alpha_l}{\rho_m \beta}\frac{\partial p}{\partial \tau} + \frac{\partial \alpha_l}{\partial t} + \nabla \cdot (\vec{v}\alpha_l) = 0 \tag{2.18}$$

Equations (2.16), (2.17) and (2.18) will be used to derive the preconditioned form of the governing equations.

Next, it is useful to define the vector of the primitive variables $\overrightarrow{Q}$ and the vector of conservative variables $\overrightarrow{U}$. Both vectors are given by Equation (2.19).

$$\overrightarrow{U} = \begin{bmatrix} 0 & \rho_m \vec{v} & \alpha_l \end{bmatrix}^T \quad \overrightarrow{Q} = \begin{bmatrix} p & \vec{v} & \alpha_l \end{bmatrix}^T \tag{2.19}$$

Furthermore, in Equation (2.20), the Jacobian transformation matrix, from conservative to primitive variables, $\overline{\Gamma}_e$ is defined

$$\overline{\Gamma}_e = \frac{\partial \overrightarrow{U}}{\partial \overrightarrow{Q}} = \begin{bmatrix} 0 & 0 & 0 \\ 0 & \rho_m \overline{I}_{3\times 3} & \vec{v}\Delta\rho \\ 0 & 0 & 1 \end{bmatrix} \tag{2.20}$$

In the previous equation, $\overline{I}_{3\times 3}$ denotes the 3 by 3 identity matrix.

Keeping the above considerations in mind, the governing preconditioned equations can be written in the following integral form for a control volume Ω.

$$\overline{\Gamma}\int_\Omega \frac{\partial \overrightarrow{Q}}{\partial \tau}\mathrm{d}\Omega + \int_\Omega \overline{\Gamma}_e \frac{\partial \overrightarrow{Q}}{\partial t}\mathrm{d}\Omega + \int_{\partial\Omega}\left(\overrightarrow{F}_c - \overrightarrow{F}_v\right)\mathrm{d}S = \int_\Omega \overrightarrow{S}_q \mathrm{d}\Omega \tag{2.21}$$

Breaking down Equation (2.21), the first term of the equation corresponds to the pseudo–time derivatives of the flow equations scaled by the preconditioner matrix $\overline{\Gamma}$ of Kunz. The matrix is given in Equation (2.22). The preconditioner matrix summarizes the design features discussed previously. The first row corresponds to the density preconditioned continuity equation (2.17), the next three rows to the primitive to conservative definition of (2.16), and the final row to the convection equation of VoF field perturbed by the pressure derivatives according to Equation (2.18).

$$\overline{\Gamma} = \begin{bmatrix} \frac{1}{\rho_m \beta} & 0 & 0 \\ 0 & \rho_m \overline{I}_{3\times 3} & \vec{v}\Delta\rho \\ \frac{\alpha_l}{\beta \rho_m} & 0 & 1 \end{bmatrix} \tag{2.22}$$

The second term corresponds to the unsteady term of the equations although. Although the system of equation is casted in primitive form, the conservative form of the equations is used to advance the solution in time. Finally, the spatial terms of the equations appear. The surface integral includes the convective (inviscid) $\vec{F}_c$ and viscous $\vec{F}_v$ fluxes, while the volume integral at the right hand side, includes any possible source terms $\vec{S}_q$ that add–up to the field. All previously mentioned vectors are defined below

$$\overrightarrow{F}_c = \begin{bmatrix} V_n \\ \rho_m u V_n + p n_x \\ \rho_m v V_n + p n_y \\ \rho_m w V_n + p n_z \\ \alpha_l V_n \end{bmatrix} \quad \vec{F}_v = \begin{bmatrix} 0 \\ \tau_{xx}n_x + \tau_{xy}n_y + \tau_{xz}n_z \\ \tau_{yx}n_x + \tau_{yy}n_y + \tau_{yz}n_z \\ \tau_{zx}n_x + \tau_{zy}n_y + \tau_{zz}n_z \\ 0 \end{bmatrix} \quad \overrightarrow{S}_q = \begin{bmatrix} 0 \\ 0 \\ 0 \\ -\rho g_z \\ 0 \end{bmatrix} \tag{2.23}$$

Regarding the notations used, V_n is the normal to the grid fluid velocity, meaning $V_n = \vec{v}\cdot\vec{n}$, with $\vec{n} = (n_x, n_y, n_z)$ being the unit normal of the boundary surface $\partial\Omega$ of the control volume. The viscous fluxes are given by the stress tensor described in (2.24), where μ_t is turbulent dynamic viscosity used for the turbulence modeling (see Sec. 2.4).

$$\tau_{ij} = (\mu_m + \mu_t)\left(\frac{\partial u_i}{\partial x_j} + \frac{\partial u_j}{\partial x_i}\right) \tag{2.24}$$

In case of free surface flows, vector $\vec{S}_q$ includes the gravitational acceleration. Neglecting for now any other possible sources and assuming that gravity acts on the negative z–axis $\vec{g} = (0, 0, -g_z)$, $\vec{S}_q$ has the form presented in Equation (2.23).

Lastly, it has to be noticed that Equation (2.21) can be reduced to a system of equations for one–phase flows by neglecting the VoF equation and setting $\rho = const.$ everywhere. In the present thesis, one–phase results are also presented, where the solid structure is fully–submerged and the influence of the free surface can be neglected.

Artificial Compressibility parameter β

The AC method relaxes the incompressibility constraint ($\nabla \cdot \vec{v} = 0$) by introducing acoustic waves with finite speed in order to distribute the pressure along the domain [60]. The speed of the waves is controlled by the AC parameter β. If large values are adopted, the waves will travel with greater speeds, which complies better with the incompressibility constraint. Accordingly, small values of β decrease the wave speeds and relax further the incompressibility constraint. In steady simulations the choice of β is less important, since the iterative process would eventually converge to a steady solution. Typically, β is set large enough to facilitate convergence. A more careful tuning of the AC parameter is required in time–true computations. In order to keep the computational cost low, the pseudo–steady state problem solved in every physical timestep, should converge within 10 to 50 iterations. β can significantly affect the convergence rate and cause the divergence of the numerical procedure or lead to un–physical solutions. For example, in [66, 69] it is reported that small values of β produced density oscillations near the free surface, while excessive values caused the divergence of the solver.

As a general guideline, β should be selected so that re–scaling of the eigenvalues results in acoustic wave speeds matching the convective velocities [63]. Thus, its value depends on the details of the numerical implementation. If no preconditioning is applied, then the acoustic wave speeds scale also with density, thus β should be set accordingly. For free surface flows, it is reported [59, 66, 68, 72] that, optimal values are found between 10^3 and 10^4 due to the high density ratio.

The precondition matrix utilized in the present thesis scales the continuity equation with the local density field and removes the density dependency from the acoustic wave speeds. Thus, the previous values are considered as exceedingly large. In similar applications with the ones discussed in the present thesis, β values that ensure accuracy are found between 0.1 and 15 [64, 74].

Furthermore, reports can be found in literature, where β value can vary locally according to the characteristics of the flows. In this direction, Turkel [53] proposed that β value should be selected such that it minimizes the ratio of the maximum to minimum eigenvalue. This is achieved by selecting $\beta = \max\left(K_o|\vec{v}|^2, \epsilon_o\right)$, where K_o equals 3 and ϵ_o a lower limit. In case of two phase flows, where the Kunz preconditioner is used different reports can be found that set K_o between 1 [54, 64] and 10 [61].

In the present work, the local varying approximation of the AC parameter β is used. As it will be later discussed, the lower threshold is set between 5 and 50 for regions of low velocity advection, while sufficient convergence properties were noted for K_o between 5 and 10.

2.2 Arbitrary Lagrangian–Eulerian Form

A control volume Ω is able to move in space with a velocity $\vec{v}_{vol}$. The Reynolds Transport Theorem can be used to account for the change of the control volume $\Omega(t)$ over time. The

temporal term of Equation (2.21) can be written as

$$\frac{\partial}{\partial t}\int_{\Omega(t)} \overrightarrow{U}\,\mathrm{d}\Omega = \int_{\Omega(t)} \frac{\partial \overrightarrow{U}}{\partial t}\mathrm{d}\Omega + \int_{\partial\Omega(t)} (\vec{v}_{vol}\cdot\vec{n})\,\overrightarrow{U}\,\mathrm{d}S \Rightarrow \tag{2.25}$$

The control volume during the pseudo–time does not change, thus the volume integral is not affected by the pseudo–time derivatives. Equation (2.21) can now be written as

$$\overline{\Gamma}\frac{\partial}{\partial \tau}\int_{\Omega(t)} \overrightarrow{Q}\,\mathrm{d}\Omega + \frac{\partial}{\partial t}\int_{\Omega(t)} \overrightarrow{U}\,\mathrm{d}\Omega + \int_{\partial\Omega(t)} \left(\overrightarrow{F}_{c,g} - \overrightarrow{F}_{v}\right)\mathrm{d}S = \int_{\Omega(t)} \overrightarrow{S}_{q}\mathrm{d}\Omega \tag{2.26}$$

$\overrightarrow{F}_{c,g}$ is the Arbitrary Lagrangian–Eulerian (ALE) flux given by Equation (2.27), ΔV is the difference between V_n and the volume velocity projected to $\vec{n}$, meaning $\Delta V = V_n - V_g$ and $V_g = \vec{v}_{vol}\cdot\vec{n}$.

$$\overrightarrow{F}_{c,g} = \begin{bmatrix} V_n \\ \rho_m u\Delta V + pn_x \\ \rho_m v\Delta V + pn_y \\ \rho_m w V + pn_z \\ \alpha_l \Delta V \end{bmatrix} \tag{2.27}$$

For a state vector $\vec{Q} = [0,1,1,1,1]^T$, Equation (2.26) reduces to the well–known Geometric Conservation Law (GCL) [78] and described in Equation (2.28). GCL states that the rate of change of a volume is equal to the area swept by its boundary $\partial\Omega$.

$$\frac{\partial}{\partial t}\int_{\Omega(t)} \mathrm{d}\Omega = \int_{\partial\Omega(t)} V_g \mathrm{d}S \tag{2.28}$$

The law is of great importance when deforming grids are utilized and conservation of volume should be enforced. In case of rigid motion of the control volume, Equation (2.28) is satisfied trivially.

2.3 Relative Frame of Reference

The previous formulation considered an earth–fixed coordinate system, where the observer is still and the fluid moves with a velocity $\vec{v}$. In some cases, it is convenient to change the reference coordinate system and express the flow equations in a frame moving with constant velocity relative to the fixed one.

Let $\vec{r}$ be a position vector in space with respect to the earth fixed coordinate system I, and R be a relative frame of reference that is able to move in space with linear velocity $\vec{v}_R$ and rotational velocity $\vec{\omega}$. The derivative of $\vec{r}$ in the inertial frame I can be expressed, with respect to the relative frame R as

$$\left.\frac{d\vec{r}}{dt}\right|_I = \left.\frac{d\vec{r}}{dt}\right|_R + \vec{\omega}\times\vec{r} \tag{2.29}$$

The above equation is an expression for the velocity in the inertial frame $\vec{v}_I$,

$$\vec{v}_I = \vec{v}_R + \vec{\omega}\times\vec{r} \tag{2.30}$$

Similarly, the acceleration of a point vector in the inertial frame of reference in case of constant rotational speed is given as

$$\left.\frac{d\vec{v}_I}{dt}\right|_I = \left.\frac{d\vec{v}_R}{dt}\right|_R + \cancelto{0}{\frac{d\omega}{dt}}\times\vec{r} + 2\vec{\omega}\times\vec{r} + \vec{\omega}\times\vec{\omega}\times\vec{r} \tag{2.31}$$

where ω is considered constant and the rotational terms $-2\left(\vec{\omega}\times\vec{u}_R\right)$ and $-\omega\times\left(\vec{\omega}\times\vec{r}\right)$ correspond to the Coriolis force and to the centrifugal force, respectively

As a result, the two–phase Navier Stokes equations without source terms can be expressed with respect to the relative system as

$$\begin{gathered}\nabla\cdot\vec{v}_R=0\\ \frac{\partial\vec{v}_R}{\partial t}+\nabla\cdot\left[\rho_m\vec{v}_R\vec{v}_R-p\overline{I}_{3\times3}+\overline{\tau}\right]=-2\rho_m\left(\vec{\omega}\times\vec{u}_R\right)-\rho_m\omega\times\left(\vec{\omega}\times\vec{r}\right)\\ \frac{\partial\alpha_l}{\partial t}+\nabla\cdot\left(\alpha_l\vec{v}_R\right)=0\end{gathered}\tag{2.32}$$

The equations of motion in the relative frame can be expressed in terms of the absolute inertial velocity since, $\vec{v}_R=\vec{v}_I-\vec{\omega}\times\vec{r}$.

$$\begin{gathered}\nabla\cdot\vec{v}_I=0\\ \frac{\partial\vec{v}_I}{\partial t}+\nabla\cdot\left[\rho\vec{v}_I\left(\vec{v}_I-\vec{\omega}\times\vec{r}\right)-p\overline{I}_{3\times3}+\overline{\overline{\tau}}\right]=-\rho\left(\vec{\omega}\times\vec{v}_I\right)\\ \frac{\partial\alpha_l}{\partial t}+\nabla\cdot\left(\partial\alpha_l\vec{v}_I\right)=0\end{gathered}\tag{2.33}$$

where the definition $\nabla\cdot\left(\vec{\omega}\times\vec{r}\right)=0$ has been used, assuming rigid body transformation. According to [79, 80] this leads to a more accurate representation of the fluxes for finite volume solvers.

By integrating over a control volume Ω, a similar expression with the ALE form of Equation (2.26) is produced

$$\overline{\Gamma}\int_\Omega\frac{\partial\overrightarrow{Q}}{\partial\tau}\mathrm{d}\Omega+\overline{\Gamma}_e\frac{\partial}{\partial t}\int_\Omega\overrightarrow{Q}\mathrm{d}\Omega+\int_{\partial\Omega}\left(\overrightarrow{F}_{c,rel}-\overrightarrow{F}_v\right)\mathrm{d}S=\int_\Omega\overrightarrow{S}_q\mathrm{d}\Omega\tag{2.34}$$

The inviscid flux $\overrightarrow{F}_{c,rel}$ in the relative frame is computed as the ALE flux of Equation (2.27), with the grid velocities being $V_g=\vec{\omega}\times\vec{r}$. Furthermore, in the previous equation a constant rotational speed is assumed. The source vector $\overrightarrow{S}_q$ incorporates the source term of Equation (2.33).

It is worth noticing that the momentum equations dictate that $\vec{\omega}\times\vec{v}_\infty=0$. This means that either the velocity vector $\vec{v}_\infty$ is parallel to the rotation axis or $\vec{v}_\infty$=0.

2.4 Turbulence Modeling

For turbulence modeling the Reynolds averaging process is followed. Taken as reference flow variable the velocity u_i in the i^{th} direction, a time averaging over a sufficient large period T is performed, meaning

$$\overline{u_i}=\frac{1}{T}\int_t^{t+T}u_i(t)\mathrm{d}t\tag{2.35}$$

The instantaneous value of the flow quantity u can now be written as a sum of a mean value, according to Equation (2.35), and a fluctuating part u', meaning

$$u_i=\overline{u_i}+u_i'\tag{2.36}$$

For the mean value and the fluctuating part, the following properties hold

$$\begin{gathered}\overline{\overline{u_i}}=\overline{u_i}\\ \overline{u_i'}=0,\quad\text{but}\quad\overline{u_i'u_j'}\neq0\end{gathered}\tag{2.37}$$

This is a standard procedure for incompressible constant density flows. However, in case of incompressible variable density flows, a slightly different approach is followed. In order to account for the density variation a density weighting is performed called Favre (or mass) averaging. This process leads to a significantly more complicated system of equations due to additional correlations that arise from the density fluctuations. For this reason it is advised to perform the Favre decomposition only for the velocity components. For the rest of the flow variables the standard Reynolds averaging is performed [81]. Specifically, performing a mass averaging for the velocity components, yields

$$\widetilde{u}_i = \frac{1}{\overline{\rho}} \frac{1}{T} \int_t^{t+T} \rho u_i dt \tag{2.38}$$

In the above equation, $\overline{\rho}$ denotes the Reynolds averaged density. The decomposition rules are the same as before

$$u_i = \widetilde{u}_i + u_i'' \tag{2.39}$$

while for the two parts, the mean and the fluctuating holds

$$\widetilde{\rho u}_i = \overline{\rho}\widetilde{u}_i \,, \;\; \widetilde{\rho u_i''} = 0, \quad \text{but} \;\; \widetilde{u_i'' u_j''} \neq 0 \tag{2.40}$$

Application of the Reynolds averaging to density and pressure variables, and of the Favre averaging to velocity components do not affect the mass or the VoF equations. However, additional terms arise in the momentum equations. Specifically, the momentum equations are written as

$$\frac{\partial \overline{\rho}\widetilde{u}}{\partial t} + \frac{\partial}{\partial x_j}\left(\overline{\rho}\widetilde{u}_j\widetilde{u}_i\right) = -\frac{\partial \overline{p}}{\partial x_i} + \frac{\partial}{\partial x_j}\left(\widetilde{\tau}_{ij} - \overline{\rho}\widetilde{u_i'' u_j''}\right) \tag{2.41}$$

The additional terms are identified as the Favre averaged Reynolds stress tensor

$$\widetilde{\tau_{ij}''} = -\overline{\rho}\widetilde{u_i'' u_j''} \tag{2.42}$$

Additional equations should be specified for the closure of the problem. To this end, eddy hypothesis has proven to be one of the standard approaches to compute the Reynolds stresses. This assumption, originally proposed by Boussinesq, states that the Reynolds stresses can be computed similarly to normal stresses, but with a variable viscosity, called turbulent viscosity, that needs to be specified from an appropriate turbulence model. The hypothesis states that

$$-\overline{\rho}\widetilde{u_i'' u_j''} = 2\mu_t S_{ij} - \frac{2}{3}\overline{\rho}k\delta_{ij} \tag{2.43}$$

where μ_t is the turbulent dynamic viscosity, S_{ij} the strain rate tensor $S_{ij} = \frac{1}{2}\left(\frac{\partial u_i}{\partial x_j} + \frac{\partial u_j}{\partial x_i}\right)$, k is the turbulent kinetic energy, and δ_{ij} is the Kronecker's delta. In the previous equations, the term $-(2/3)\overline{\rho}k\delta_{ij}$ has been added to obtain the right trace of the Reynolds–stress tensor and it is often neglected for stability.

2.4.1 Closure

For the turbulence closure the k–ω SST (Shear Stress Transport) [82] model is selected. The model computes the dynamic viscosity μ_t be solving two differential equations. The first equation computes the turbulent kinetic energy k, while the second, the turbulent dissipation rate ω.

$$\frac{\partial(\rho k)}{\partial t} + \nabla\cdot(\vec{v}\rho k) = \nabla\left[(\mu_m + \sigma_k\mu_t)\nabla k\right] + P_k - \beta^*\rho\omega k \tag{2.44a}$$

$$\begin{aligned}\frac{\partial(\rho\omega)}{\partial t} + \nabla\cdot(\vec{v}\rho\omega) = \nabla\left[(\mu_m + \sigma_\omega\mu_t)\nabla\omega\right] + \frac{\gamma}{\nu_t}P_k - \beta\rho\omega^2 + \\ + 2(1-F_1)\frac{\rho\sigma_{\omega 2}}{\omega}\nabla k\cdot(\nabla\omega)^T\end{aligned} \tag{2.44b}$$

In the previous equations P_k is the production term of the turbulent kinetic energy, and it is computed as

$$P_k = \tau_{ij} \frac{\partial u_i}{\partial x_j} \tag{2.45}$$

In order to enhance stability a limiter is applied to the production term of the turbulent kinetic energy. The k–ω SST model blends the original k–ω introduced by Wilcox, to account for the viscous effect close to the wall, with the k–ε model which has better characteristics for flows away from the solid boundaries. The blending is performed by two hyperbolic tangent functions, F_1 and F_2, given by Equation (2.46).

$$F_1 = \tanh\left\{\left\{\min\left[\max\left(\frac{\sqrt{k}}{\beta^* \omega y}, \frac{500v}{y^2\omega}\right), \frac{4\rho\sigma_{\omega 2} k}{CD_{k\omega} y^2}\right]\right\}^4\right\} \tag{2.46a}$$

$$F_2 = \tanh\left\{\left[\max\left(\frac{2\sqrt{k}}{\beta^* \omega y}, \frac{500v}{y^2\omega}\right)\right]^2\right\} \tag{2.46b}$$

where y is the distance of a field point from the nearest wall point and term $CD_{k\omega}$ is computed as

$$CD_{k\omega} = \max\left(2\frac{\rho\sigma_{\omega 2}}{\omega}\nabla k \cdot (\nabla\omega)^T, 10^{-10}\right) \tag{2.47}$$

The constants of the model are: $\beta^* = 0.09$, $\alpha_1 = 5/9$, $\beta_1 = 0.075$, $\sigma_{k1} = 0.85$, $\sigma_{\omega 1} = 0.5$, $\alpha_2 = 0.44$, $\beta_2 = 0.0828$, $\sigma_{k2} = 1.0$ and $\sigma_{\omega 2} = 0.856$. The subscript 1 denotes the constants of the outer region, while subscript 2 the k–ω, or inner, region of the field.

$$\phi = F_1\phi_1 + (1 - F_1)\phi_2 \tag{2.48}$$

Furthermore, the definitions of the magnitude of the strain rate and vorticity are given by

$$\begin{aligned} S &= \sqrt{S_{ij}S_{ij}}\,, \quad S_{ij} = \frac{1}{2}\left(\frac{\partial v_i}{\partial x_j} + \frac{\partial u_j}{\partial x_i}\right) \\ \Omega &= \sqrt{\Omega_{ij}\Omega_{ij}}\,, \quad \Omega_{ij} = \frac{1}{2}\left(\frac{\partial v_i}{\partial x_j} - \frac{\partial u_j}{\partial x_i}\right) \end{aligned} \tag{2.49}$$

Finally, once the values of k and ω have been computed, the turbulent viscosity is approximated as

$$\mu_t = \frac{\rho\alpha_1 k}{\max\left(\alpha_1\omega, \Omega F_2\right)} \tag{2.50}$$

2.4.2 Initial & Boundary Conditions

The initial and the boundary conditions of the farfield boundaries, according to the original SST model, are given as

$$\begin{aligned} \omega_{far} &= \frac{U_\infty}{L} \\ k_{far} &= \frac{10^{-3}U_\infty^2}{Re_L} \end{aligned} \tag{2.51}$$

The turbulence close to wall tends to zero, thus the wall boundary conditions for the k–ω model are

$$\begin{aligned} \omega_{wall} &= 10\frac{6\nu}{\beta\left(\Delta d_1\right)^2} \\ k_{wall} &= 0 \end{aligned} \tag{2.52}$$

2.4.3 Turbulence Overproduction in Surface Wave Flows

Application of RANS models in surface wave problems leads to an unrealistic growth of turbulent kinetic energy and eddy viscosity in the liquid phase close to the free surface, resulting in the premature decay of free surface waves. This is triggered by the shear layer forming near the free surface in case of propagating waves. Researchers have managed to resolve this issue by adding limiters to the turbulent kinetic energy or to the eddy viscosity calculations.

One of the most well–known solution to the turbulence overproduction is the buoyancy source term proposed by Devolder et al. [83, 84]. The source term is added on the right hand side of the turbulent kinetic energy equation and described by Equation (2.53). The purpose of the source term is to suppress turbulence in regions of large density gradient, e.g. close to the free surface. In Equation (2.53), $\vec{g}$ is the gravitational vector, $(0, 0, -g_z)$, ν_t the kinematic turbulence viscosity and σ_t is a constant equals to 0.85, used to regulate the amount of buoyancy modeled.

$$G_b = -\frac{\nu_t}{\sigma_t}\frac{\partial \rho}{\partial x_j} g_j \tag{2.53}$$

Although this modification has managed to restrain excessive turbulence production, it has not suppressed entirely its production, especially in long time simulations. A better established solution, that comes in addition to the buoyancy term, has been introduced by Larsen and Fuhrman [85]. They have demonstrated that there will be a non–zero production of turbulent kinetic energy in a potential flow region beneath surface waves. By performing a stability analysis they proposed a stabilization limiter in the calculation of μ_t. This limiter is activated in regions of nearly potential flow, which are identified as regions of very low rotation and high shear or equivalent $p_\Omega/p_o \leq \lambda_2$, where λ_2 is a small value, typically taken as 0.01.

$$\mu_t = \frac{\rho \alpha_1 k}{\max\left(\alpha_1 \omega, SF_2, \alpha_1 \lambda_2 \frac{\beta}{\beta^* \alpha}\frac{P_0}{P_\Omega}\omega\right)} \tag{2.54}$$

Compared to Equation (2.50), μ_t is limited in the outer region by the strain rather than vorticity magnitude. This approach has been successfully used to simulate turbulent surface waves up to breaking [86] using *MaPlow*. When the additional stress limiting is applied to turbulent flows with surface piercing objectives, a more precise tuning of the λ_2 parameter is required.

Another modification to resolve the overproduction of turbulence in regions of high shear stresses S and low vorticity magnitude, Ω has been proposed by Kato and Launder [87]. Their study of flows past square cylinders using the k–ϵ turbulence model has revealed excessive production of turbulence kinetic energy close to stagnation points. These regions are characterized by very high levels of shear, while the flow is nearly irrotational, which is similar to the remarks made by Larsen and Fuhrman for flows beneath surface waves. They recommended to replace the production limiter by

$$P_k = \mu_t S \Omega \tag{2.55}$$

Once again this modification will not have an effect on simple shear flows. As discussed in the next chapter, its application to surface wave flows manages to restrain the overproduction of μ_t close to the free surface.

It is worth noticing that all modifications presented here aim to change the behavior of turbulence model in specific regions only. The buoyancy term modifies production of the turbulent kinetic energy near the free surface, while the other two change turbulence calculations in regions away from solid boundaries where the flow rotation is insignificant. Thus the latter two are activated in the k–ϵ regions of the model.

2.5 Water Waves Theory

The previous sections focus on the formulation of the Navier–Stokes (NS) equations for turbulent free surface flows. The modeling of the free surface waves propagating over constant bathymetry can also be faced using analytical approaches by solving a boundary value problem. This solution may serve as the basis of a numerical wave making technique that can be used to introduce waves in a NS domain. Below, some analytical formulations of water waves propagating on constant bathymetry are described in brief.

The analytical description of water wave motion can be sufficiently made using two main assumptions. Firstly, the water can be considered purely incompressible and secondly, taking advantage that the viscous effects are concentrated in thin layers close to the free surface and the bottom, the assumption of irrotational inviscid flow can also be made [88, 89]. These simplifications enable the definition of a velocity potential and a stream function.

In general, the mathematical formulation of the problem is as follows; a two dimensional fixed inertial frame of reference is defined, with z–axis pointing upwards and its center located at the calm free surface. The domain is defined by the open boundaries at the left and right side, below by the bottom and by the free surface above. Using the assumption of irrotational and incompressible fluid a velocity potential is defined that satisfies the continuity equation. Let ϕ be the velocity potential, then

$$\nabla^2 \phi \left(x_I, z_I, t \right) = 0 \tag{2.56}$$

In the preceding equations, the index I denotes the spatial coordinates with respect to the fixed inertial frame of reference.

At every boundary of the domain, boundary conditions should be specified. For the bottom, the no penetration boundary condition holds. This states the normal component of the velocity on the boundary which is described by the normal vector $\vec{n}$ is zero, or

$$\vec{v} \cdot \vec{n} = 0 \tag{2.57}$$

where $\vec{v} = (u, v, w)$ is the velocity vector and n the normal vector that defines the seabed.

For the free surface, two boundary conditions are defined. Firstly, the kinematic boundary conditions which states that all particles that form the free surface in any time t will always remain on the free surface. More formally, the free surface can described by equation of the form $F \left(x_I, z_I, t \right) = 0$, in the earth fixed coordinate system. In a two dimensional context, the total derivative will be zero or

$$\frac{DF \left(x_I, z_I, t \right)}{Dt} = 0 \tag{2.58}$$

The second boundary condition arises from the requirement for a uniform pressure distribution across the free surface. This requirement can be expressed using the Bernoulli equation as,

$$-\frac{\partial \phi}{\partial t} + \frac{1}{2} \left(u^2 + w^2 \right) + \frac{p}{\rho} + gz = 0 \tag{2.59}$$

Boundary conditions should also be specified at the lateral boundaries. Assuming only wind generated waves, which can be considered as periodic in space and time, the length of the domain is chosen equal to one wavelength, thus the lateral boundaries can be set to periodic, meaning that for a wave with length λ and period T the following boundary conditions hold

$$\begin{aligned} \phi \left(x_I, t \right) &= \phi \left(x_I + \lambda, t \right) \\ \phi \left(x_I, t \right) &= \phi \left(x_I, t + T \right) \end{aligned} \tag{2.60}$$

Apart from the velocity potential, another useful approach for wind generated waves, which can be considered as steady in a reference frame that moves with the wave, is to use a stream

function formulation. Again considering a xz plane with the z–axis pointing upwards but this time the origin of the coordinate system is located at the bottom. A stream function can defined as

$$u = \frac{\partial \psi}{\partial z}, \;\; w = -\frac{\partial \psi}{\partial x} \tag{2.61}$$

and since the flow is considered as irrotational

$$\nabla^2 \psi = 0 \tag{2.62}$$

The boundary conditions that hold are, for the bottom the non–entry condition is expressed as

$$\psi\left(x, 0\right) = 0 \tag{2.63}$$

At the free surface, the kinematic boundary condition expressed is as

$$\psi\left(x, \eta\left(x\right)\right) = -Q \tag{2.64}$$

where $\eta(x)$ is the free surface elevation and Q is the volume rate of flow underneath the steady water. Additionally, the dynamic boundary condition implies

$$\frac{1}{2}\left[\left(\frac{\partial \psi}{\partial x}\right)^2 + \left(\frac{\partial \psi}{\partial z}\right)^2\right] + \eta = R \tag{2.65}$$

with R being the Bernoulli constant.

The following sections present briefly two well–known approximations for the solution of steady water waves, that will be used for wave generation in the framework of a numerical wave tank. The goal of this section is to present appropriate methodologies for the analytical description of water waves for any wave steepness. A wave can be uniquely described given the water depth d, the wave height H and either the wave length λ or the wave period T.

2.5.1 Linear Airy Wave Theory

The first approximation of water waves starts from the velocity potential formulation. In this framework, a linearization of the equations is performed assuming small amplitude waves compared to their wavelength, e.g. $(H/2)/\lambda << 1$, where H is the wave height and λ the wavelength, as well as small velocity perturbations thus the square of the velocity can be neglected.

A solution of the particular boundary value problem can be taken using the separation of variables method. Assuming a water wave that it is propagating towards the x–axis, in absence of current, then the velocity potential is given by

$$\phi\left(\vec{x}_I, t\right) = -\frac{H}{2}\frac{g}{\omega}\frac{\cosh k\left(d + z_I\right)}{\cosh kd}\sin\left(kx_I - \omega t\right) \tag{2.66}$$

In the preceding equation, k is the wave number, ω the wave frequency in rad/s, d the water depth, g the acceleration of gravity, t the time variable, z_I the vertical variable and x_I the horizontal variable in the inertial frame of reference.

The wave number k and the wave frequency ω are related with the linear dispersion relation

$$\omega^2 = gk\tanh kd \tag{2.67}$$

The free surface elevation for a linear progressive wave is given by

$$\eta = \frac{H}{2}\cos\left(kx_I - \omega t\right) \tag{2.68}$$

The velocities under the wave crest are defined as

$$\begin{aligned} u(\vec{x}_I, t) &= \frac{H}{2}\omega \frac{\cosh k\,(d + z_I)}{\sinh kd} \cos\left(kx_I - \omega t\right) \\ w(\vec{x}_I, t) &= \frac{H}{2}\omega \frac{\sinh k\,(d + z_I)}{\sinh kd} \sin\left(kx_I - \omega t\right) \end{aligned} \tag{2.69}$$

and the pressure field is described by,

$$p(\vec{x}_I, t) = \rho g \frac{H}{2} \frac{\cosh k\,(d + z_I)}{\cosh kd} \cos\left(kx_I - \omega t\right) \tag{2.70}$$

A water wave is uniquely defined given the wave height H, the water depth d, and either the wavelength λ or the wave period T. T and λ are connected by the dispersion relation, which can be used to retrieve the one or the other.

2.5.2 Stream–Function Theory

The water wave theory of Airy offered an analytical solution by considering only small amplitude and long crested waves. Further approaches have been proposed to account for the whole range of steady wave propagation [90]. Stokes wave theory has been introduced to describe water waves that are not very long compared to the water depth, while the complementary Cnoidal wave theory is used to describe long water waves. Rienecker and Fenton [91] proposed a unified numerical theory that can be used as a universal approximation for steadily propagating waves in horizontal bottom, and titled as Stream Function Theory.

The main idea behind the Stream Function theory is, by exploiting the symmetry around the crest, to approximate the stream function ψ, in $N + 1$ equispaced points from crest to though, with the following Fourier expansion

$$\psi\left(x, z\right) = B_o z + \sum_{j=1}^{N} B_j \frac{\sinh jk\eta_j}{\cosh jkD} \cos jkx \tag{2.71}$$

Stream function ψ needs to also satisfy the corresponding boundary conditions. For every point $x_j = j\lambda/2N$, with $j = 0, 1, \ldots, N$, the kinematic boundary condition (2.64) is expressed. Furthermore, another set of equations is retrieved from the dynamic boundary condition (2.65). In total, the boundary conditions introduce $2N + 2$ equations and involve $2N + 5$ unknowns, namely the Fourier coefficients B_j, the elevations η_j at the $N + 1$ points, the Bernoulli constant R, the flow rate Q and the wave number k. Additionally, the free surface points should satisfy the wave height H and the mean depth d. In order to close the system of equations additional equations should be defined.

As already mentioned, in order to define a wave, the wave height H, the water depth d and either the wave period T or the wave length λ have to be specified. Additional equations are derived from the properties of H, d, T and λ. Firstly, the elevation at the crest η_0 and at the trough η_N should respect the wave height definition H. Secondly, the mean elevation should satisfy the depth definition d. Furthermore, depending on the input data one more equation is derived either by the relation between the wave period T and frequency ω, if the wave length is defined, or for the wave length λ to wave number k relation, if the wave period is defined.

In case of non–linear waves the net flux across the domain is not zero and thus one additional unknown is introduced. The non–zero flux is expressed either by a Stokes drift c_S or through a constant velocity current known as Euler current c_E. Again, depending on the input data, a final equation is introduced that is based either on the one or the other definition. In total, a closed system of $2N + 6$ equations is formed for the $2N + 6$ unknowns. This system can be solved iteratively using the Newton's method. In the present thesis the numerical strategy, which is described in detail in [92], is followed.

2.5.3 Irregular Waves

Irregular waves in one direction are generated using a simple superposition of linear Airy waves of N wave components.

For a given water depth, each wave component i is defined by a wave amplitude A_i, a wave angular frequency ω_i, a corresponding wave number k_i, according to the dispersion relation (2.67) and wave phase ε_i.

The total elevation is computed by Equation (2.72), the velocity under the crest by Equation (2.73) and the pressure by Equation (2.74).

$$\eta(x,t) = \sum_{i=1}^{N} A_i \cos(k_i x - \omega_i t + \varepsilon_i) \tag{2.72}$$

$$\begin{aligned} u(x,z,t) &= \sum_{i=1}^{N} A_i \omega_i \frac{\cosh k_i (h+z)}{\sinh k_i h} \cos(k_i x - \omega_i t + \varepsilon_i) \\ w(x,z,t) &= \sum_{i=1}^{N} A_i \omega_i \frac{\sinh k_i (h+z)}{\sinh k_i h} \sin(k_i x - \omega_i t + \varepsilon_i) \end{aligned} \tag{2.73}$$

$$p(x,z,t) = \sum_{i=1}^{N} \rho g A_i \frac{\cosh k_i (h+z)}{\cosh k_i h} \cos(k_i x - \omega_i t) \tag{2.74}$$

In the case of a given wave spectrum, the amplitude of each wave is obtained by it into N bands of length $\Delta\omega$ and height S_i, which corresponds to the spectral density of the i–component. Then, the amplitude can be computed as

$$A_i = \sqrt{2 S_i(\omega)\, \Delta\omega} \tag{2.75}$$

2.6 Motion of Rigid Body

In the previous sections, the foundations of the fluid solver have been set. In this last section of the chapter, the motion of rigid body is studied under external excitation. During Fluid–Structure Interaction (FSI), the rigid body solver is responsible for calculating the three displacements and the three rotations of the body.

Rigid bodies are defined as structures that their deformation can be neglected compared to the amplitude of motion. Typically, two coordinate systems are used to define the motion of a body. One inertial system, fixed to the Earth and a second moving system, fixed to the center of mass of the body. A schematic illustration of the two systems is given in Figure 2.1a. The first system is an inertial system (non–accelerating) that is used to define the absolute position of the body, denoted as $OX_IY_IZ_I$ in the figure, while the relative system, $Cx_Ry_Rz_R$, follows the motion of the body and it is used to express the equations of motion.

The body has 6 degrees of freedom (DoFs) three translational and three rotational. The three translations are referred to as surge, sway and heave, while the three rotations as roll (or heel), pitch (or tilt) and yaw (or swing).

The position of the body can be defined by a position vector pointing at its center of mass and by its angular orientation. For the orientation of the body the modified Euler's angle convention is used. This means that, the rotations are performed in a specific order only. According to this convention, in order to find the orientation of a body (or equivalent the orientation of the relative reference frame) starting from the inertial, earth fixed, reference system, three successive rotations are performed, firstly about the z–axis (yaw) with angle ψ, then about y–axis (pitch) with angle θ and finally about x–axis (roll) with angle ϕ. An illustration of the pseudo–Euler

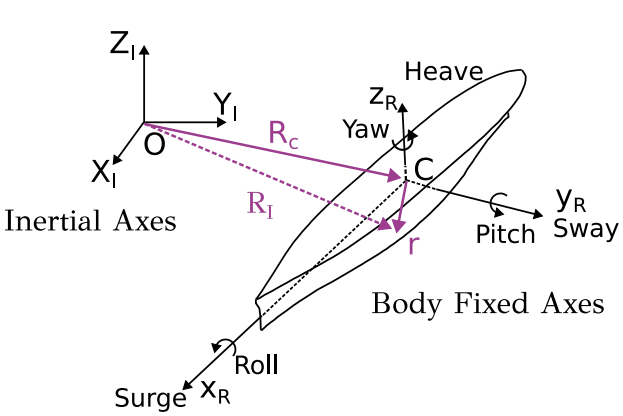

(a) Illustration of the inertial (global) coordinate system $OX_IY_IZ_I$ and the relative (body fixed) coordinate system $Cx_Ry_Rz_R$

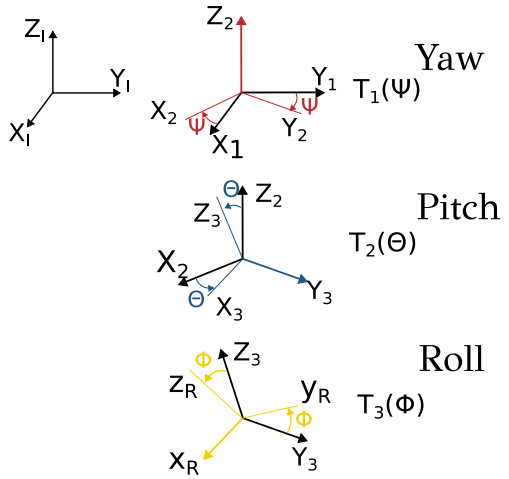

(b) Definition of the pseudo–Euler angles for the transformation from the inertial to the relative coordinate system

Figure 2.1: Schematic representation of the two coordinate system used to define the motion of a body (left) and the three successive rotations that used to obtain the orientation of the body (right)

angles convection is given in Figure 2.1b. It is can be easily proven that finite rotations can not be treated as vector quantities [93, 94].

Any point in space can be defined as

$$\overrightarrow{R}_I = \overrightarrow{R}_C + \overline{T}\,(\psi, \theta, \phi)\,\overrightarrow{r} \tag{2.76}$$

where $\overrightarrow{R}_I$ is the position of the point with respect to the global coordinate system, $\overrightarrow{R}_C$ the position of the body fixed coordinate system, $\overrightarrow{r}$ the position of the point with respect to the body fixed coordinate system and $\overline{T}$ the transformation matrix from the inertial to the relative system. The matrix is product of the rotation matrices, according to the pseudo–Euler angles convention $\overline{T} = \overline{T}\,(\psi)\,\overline{T}\,(\theta)\,\overline{T}\,(\phi)$. The transformation matrix is computed by

$$\overline{T} = \overline{T}\,(\psi)\,\overline{T}\,(\theta)\,\overline{T}\,(\phi) = \begin{bmatrix} \cos\psi\sin\theta & \cos\psi\sin\theta\sin\phi \\ & -\sin\psi\cos\phi \\ \sin\psi\cos\theta & \sin\psi\sin\theta\sin\phi \\ & +\cos\psi\cos\phi \\ -\sin\theta & \cos\theta\sin\phi \end{bmatrix} \begin{bmatrix} \cos\psi\sin\theta\cos\phi \\ +\sin\psi\sin\phi \\ \sin\psi\sin\theta\cos\phi \\ -\cos\psi\sin\phi \\ \cos\theta\cos\phi \end{bmatrix} \tag{2.77}$$

Based on the definition of Equation (2.76), which describes the coordinate transformation from the inertial to the relative frame of reference, it can be proven that [95], the rate of change of any arbitrary vector (or table) can be given by the following operator equation

$$\left.\frac{d\cdot}{dt}\right|_I = \left.\frac{d\cdot}{dt}\right|_R + \overrightarrow{\omega} \times \cdot \tag{2.78}$$

Indexes I and R denote derivative with respect to the inertial (global) and to the relative (body fixed) coordinate system, respectively, while $\vec{\omega}$ is the rotation vector of the body which passes through the center of mass.

The equations of motion can be derived using Newton's second law. For a rigid body with mass m, that experiences external forces $\overrightarrow{F}$ (e.g., hydrodynamic, gravity, etc.), its motion relative to the inertial (earth fixed) reference frame is described by

$$\overrightarrow{F} = m\left.\frac{d\overrightarrow{u}}{dt}\right|_I \tag{2.79}$$

It is more convenient [93, 94] to express the equations of motion with respect to the body fixed coordinate system. By making use of operator (2.78), Newton's second law in the relative frame of reference is expressed as

$$\overrightarrow{F} = m\left(\left.\frac{d\overrightarrow{u}}{dt}\right|_R + \overrightarrow{\omega}\times\overrightarrow{u}\right) \tag{2.80}$$

The above equation is a non–linear equation due to the cross product term result from the coordinate system transformation. Regarding the notation used, the forces on the local coordinate system are noted as $\vec{F}$, with components (X, Y, Z), the local velocity (absolute velocity with respect to the moving reference frame) as $\overrightarrow{u}$, with components (u, v, w) and $\overrightarrow{\omega}$ the angular velocity of the body in the body fixed coordinate system, with components (p, q, r).

The component–wise form of the equation for the linear acceleration of the body is

$$\begin{aligned} X &= m\left(\dot{u} + wq - vr\right) \\ Y &= m\left(\dot{v} + ur - wp\right) \\ Z &= m\left(\dot{w} + vp - uq\right) \end{aligned} \tag{2.81}$$

A second set of equations, which described the angular motion of the body, can be derived from the "moment–angular momentum relationship". If $\overrightarrow{G} = (M, N, K)$ is the moment vector about the center of gravity and $\vec{h}$ the angular momentum vector, then the moment equation of motion for the rigid body is

$$\overrightarrow{G} = \left.\frac{d\vec{h}}{dt}\right|_I \tag{2.82}$$

As in the case of linear accelerations, the moment equation can be written with respect to the body fixed coordinate system, as seen below

$$\overrightarrow{G} = \left.\frac{d\vec{h}}{dt}\right|_R + \vec{\omega}\times\vec{h} \tag{2.83}$$

The angular momentum vector is given as the product of the inertia matrix $\overline{I}$ and the angular velocity $\vec{\omega}$

$$\vec{h} = \overline{I}\vec{\omega} = \begin{bmatrix} I_{xx} & -I_{xy} & -I_{xz} \\ -I_{yz} & I_{yy} & -I_{yz} \\ -I_{zx} & -I_{zy} & I_{zz} \end{bmatrix}\vec{\omega} \tag{2.84}$$

By assuming that the rigid body consists of a swarm of particles with infinitesimal masses δm_i, then the elements of inertia matrix $\overline{I}$ are computed as $I_{ij} = \sum_i x_i y_i \delta m_i$

The component form of the moment equation with respect to the body's center of mass has the following form

$$\begin{aligned} K &= I_{xx} + \dot{p} + I_{xy}(\dot{q} - pr) + I_{xz}(\dot{r} + pq) + I_{yz}\left(q^2 - r^2\right) + \left(I_{zz} - I_{yy}\right)qr \\ M &= I_{yy} + \dot{q} + I_{yz}(\dot{r} - pq) + I_{yx}(\dot{p} + pr) + I_{zx}\left(r^2 - p^2\right) + \left(I_{xx} - I_{zz}\right)rp \\ N &= I_{zz} + \dot{r} + I_{zx}(\dot{p} - qr) + I_{zy}(\dot{q} + rp) + I_{xy}\left(p^2 - q^2\right) + \left(I_{yy} - I_{xx}\right)pq \end{aligned} \tag{2.85}$$

Equations (2.80) and (2.83), or equivalently the component forms of Equations (2.81) and (2.85), constitute a set of non–linear differential equations. They express the motion of a rigid body with respect to its center of mass. Noteworthy, a similar but more complicated system can be derived by expressing equations with respect to any arbitrary point [94]. Integration of the system leads to the calculation of generalized position vector $\vec{x} = (x, y, z, \theta, \phi, \psi)$, which contains the unknown displacements and rotations.

For the solution of the non–linear system a δ–formulation is considered. Iterations are performed between the flow solver and the rigid body solver until convergence of perturbations is

achieved. As described in detail in Appendix A, δ–formulation leads to the following second order, ordinary differential equation

$$\overline{M}\delta\ddot{\vec{x}} + \overline{C}\delta\dot{\vec{x}} + \overline{K}\delta\vec{x} = \delta\overrightarrow{Q} \tag{2.86}$$

where perturbations $\delta\cdot$ are with respect to the previous iteration of the flow–rigid body iterative process, $\overline{M}, \overline{C}, \overline{K}$ are the mass, damping and stiffness matrices, $\overrightarrow{Q}$ the external forces, while dots represent derivation with respect to time.

Time integration is performed using the Newmark–β method [96] with coefficient values $\beta = 0.25$ and $\gamma = 0.5$. Details about time integration are given in Appendix B.

Chapter 3

Numerical Framework

This chapter presents the discretization process of the flow equations for turbulent free surface flows. Details on geometric calculations, gradient and flux evaluations are given. The linearization process of the flow equation and the solution of the linear system of equations are also described. Furthermore, it provides the implementation details of the Fluid–Structure Interaction (FSI) algorithm, that couples the flow with the rigid body solver. Lastly, mesh deformation techniques used to communicate the motion of the rigid body to the flow solver are also presented.

3.1 Definition of a Control Volume

Space is discretized using a set of unstructured computational cells. The center of each control volume is defined at the geometric center of the computational cell. In Figure 3.1, an example of a polyhedral control volume is given, where in every computational face an outwards normal vector is defined.

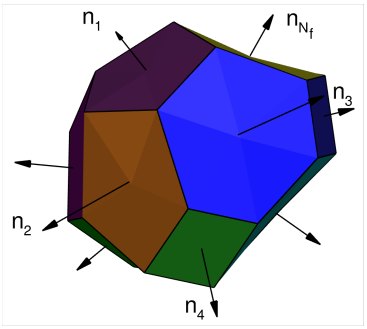

Figure 3.1: Illustration of a polyhedral control volume with N_f number of faces and definition of the $\vec{n}_i$ outwards pointing normal vectors

Prior to the discretization of the equations, the geometric quantities of the cells are computed. Starting from the calculations performed in every cell face, which in general forms a polygonal area, a standard practice is to triangulate the face. For every triangle, the area and the geometric center are calculated. Then, the area of the polygonal face becomes the sum of the triangle subareas, while the center is calculated as the geometric mean value of the triangles centers [97].

The center of every computational cell is defined as the geometric mean value of its vertices, meaning

$$\vec{x}_{ci} = \frac{1}{N_v} \sum_{j=1}^{N_v} \vec{x}_{vj} \tag{3.1}$$

where $\vec{x}_{ci}$ is the center of the i^{th} computational cell, N_v the total number of vertices that define the control volume, located at the $\vec{x}_{vj}$ positions.

For the calculation of volume the Green–Gauss theorem is used. By defining a function $\vec{F} = (0, 0, z)$ and since $\nabla \cdot F = 1$, the total volume of a computational cell can be computed as

$$\Omega_i = \sum_{f=1}^{N_f} z_f n_{zf} S_f \tag{3.2}$$

where, Ω_i is the volume of the i^{th} cell, z_f is the z–coordinate of the f face's midpoint and n_{zf} the z–component of the face's normal.

An alternative to the volume calculation is the approximation of the control volume as sum of pyramids with their apex being the center of the cell and its base (polyhedral in the general case) being a face of the cell [97, 98]. The volume of each pyramid can be easily computed. Both approximations were considered, however no major difference have been found between them.

Noticeable most of the computational cells are not water tight. In most cases the vertices of a face do not lie on the same plane. This implies that for the faces of a control volume the following condition arises

$$\sum_{f}^{N_f} \vec{n}_f S_f \neq 0 \tag{3.3}$$

This is the case for the majority of the computational meshes containing faces with more than 3 vertices, but it is more pronounced in meshes with arbitrary polyhedral volumes. As later discussed in Section 3.3.3, a correction can be applied to Equation (3.2) in order to account for the non–planar vertices of the mesh, and for this is preferred over the pyramids approximation. The non–water tight control volumes is a major source of accuracy degradation in 3D simulations. This is especially pronounced in free surface flows, where second order accuracy is required to preserve the hydrostatic equilibrium.

3.2 Finite Volume Method

The governing equations are discretized using the finite volume method. The method considers a spatial average of the flow quantities in every control volume. The averaged flow solution is stored at the center of the computational cell suggesting as cell–centered approximation. For a cell i with volume Ω_i the flow variables are approximated as

$$\overrightarrow{\overline{Q}}_i = \frac{1}{\Omega_i} \int_{\Omega_i} \overrightarrow{Q}(\vec{x}; t) \mathrm{d}\Omega \tag{3.4}$$

Returning to Equation (2.26) and applying the finite volume method, then the flow in the i^{th} computational cell is governed by the following equation

$$\overline{\Gamma}\Omega_i \frac{\partial \overrightarrow{\overline{Q}}_i}{\partial \tau} + \frac{\partial}{\partial t}\left(\overrightarrow{\overline{U}}_i \Omega_i\right) = -\overrightarrow{R}_s\left(\overrightarrow{\overline{Q}}_i\right) \tag{3.5}$$

where at the right–hand side of the equation, the term $\overrightarrow{R_s}\left(\overrightarrow{\overline{Q}}_i\right)$ is the spatial residual of the equations which includes, the surface integrals of the viscous and inviscid fluxes and the volume integral of the sources terms, i.e.

$$\overrightarrow{R}_s\left(\overrightarrow{\overline{Q}}_i\right) = \int_{\partial\Omega_i} \left(\overrightarrow{F}_{c,g} - \overrightarrow{F}_v\right) \mathrm{d}S - \int_{\Omega_i} \overrightarrow{S}_q \mathrm{d}\Omega \tag{3.6}$$

At the left–hand side of the Equation (3.5) the unsteady part appears, which includes both the flow quantities and the cell volume, since it can change over time. A linearization is applied to Jacobian matrix $\overline{\Gamma}_e$

$$\overline{\Gamma}\Omega_i \frac{\partial \overrightarrow{\overline{Q}}_i}{\partial \tau} + \overline{\Gamma}_e \frac{\partial}{\partial t}\left(\overrightarrow{\overline{Q}}_i \Omega_i\right) = -\overrightarrow{\overline{R}}_s\left(\overrightarrow{\overline{Q}}_i\right) \tag{3.7}$$

The bar above the flow quantities $\overrightarrow{\overline{Q}}$ denote the spatial averaging according to finite volume method. In order to simplify the notation, the symbol will be suppressed in the following sections and it is assumed that the $\overrightarrow{Q}$ denotes the mean spatial value.

The unsteady governing equations are given in a single vector form by equations Equation (3.7). The discretization process can be split into two parts, (a) the discretization of the spatial terms, and (b) the temporal discretization. Both are described in the following sections, Section 3.3 and Section 3.4.

3.3 Spatial Discretization

Starting the discretization process from the spatial residual of Equation (3.7), the surface terms are approximated as a sum over the faces of the computational cell and the source terms are considered constant inside the computational cell.

For a control volume Ω_i with N_f number of edges on each side the spatial residual is approximated as

$$\overrightarrow{\overline{R}}_s\left(\overrightarrow{\overline{Q}}_i\right) \simeq \sum_{f=1}^{N_{f,i}} \left(\overrightarrow{\overline{F}}_{c,g} - \overrightarrow{\overline{F}}_v\right)_f \Delta S_f - \Omega_i \overrightarrow{\overline{S}}_{q,i} \tag{3.8}$$

Equation (3.8) includes the evaluation of the inviscid $\overrightarrow{\overline{F}}_{c,g}$ and the viscous $\overrightarrow{\overline{F}}_v$ fluxes across a computational face f. The next paragraphs focus on the approximation of these two terms.

3.3.1 Evaluation of Inviscid Fluxes

In the artificial compressibility method, the system of equations becomes hyperbolic in pseudo–time. The inviscid fluxes are approximated by solving a Riemann problem at each computational face. A normal vector is defined in each face, which points from the left (L) to the right (R) state. A Riemann problem is defined by the extrapolated L and R states. The initial value problem with initial discontinuous data L and R is solved using the approximate Riemann solver of Roe [45]. In order to remove the density dependency from the eigenvalue, the Kunz preconditioner [61] is used to scale the eigenvalues.

Let $\overline{A}_c$ be the convective jacobian matrix, $\overline{\Gamma}$ the preconditioner matrix and $\overline{\Gamma}^{-1}$ its inverse, then the preconditioned jacobian matrix $\tilde{A}_c$ is introduces through

$$\overline{A}_c = \overline{\Gamma}\overline{\Gamma}^{-1}\overline{A}_c = \overline{\Gamma}\tilde{A}_c \tag{3.9}$$

and its analytical form

$$\tilde{A}_c = \begin{bmatrix} 0 & n_x & n_y & n_z & 0 \\ n_x & \rho_m\left(n_x u + \Delta V\right) & \rho_m n_y u & \rho_m n_z u & u\Delta V \Delta\rho \\ n_y & \rho_m n_x v & \rho_m\left(n_y v + \Delta V\right) & \rho_m n_z v & v\Delta V \Delta\rho \\ n_z & \rho_m n_x w & \rho_m n_y w & \rho_m\left(n_z w + \Delta V\right) & w\Delta V \Delta\rho \\ 0 & \alpha_l n_x & \alpha_l n_y & \alpha_l n_z & \Delta V \end{bmatrix} \tag{3.10}$$

The inviscid fluxes across face f can the be computed as,

$$\overrightarrow{\overline{F}}_{cg,f} = \frac{1}{2}\left(\overrightarrow{\overline{F}}_{c,g}\left(\overrightarrow{\overline{Q}}_R\right) + \overrightarrow{\overline{F}}_{c,g}\left(\overrightarrow{\overline{Q}}_L\right)\right) - \frac{1}{2}\overline{\Gamma}\left|\overline{\tilde{A}_{RL}}\right|\left(\overrightarrow{\overline{Q}}_R - \overrightarrow{\overline{Q}}_L\right) \tag{3.11}$$

where $\overline{|\tilde{A}_{RL}|}$ is the Roe averaged–precoditioned jacobian between the left $(\cdot_L)$ and right $(\cdot_R)$ states.

The diagonalization of the jacobian matrix implies

$$\left|\tilde{A}\right| = \tilde{R}^{-1}\left|\tilde{\Lambda}\right|\tilde{R} \tag{3.12}$$

In Equation (3.12), matrix $\tilde{R}$ contains the right eigenvectors of the jacobian matrix arranged in row wise order, $\tilde{R}^{-1}$ is the matrix of the left eigenvectors arranged in column wise order and $\tilde{\Lambda}$ is a diagonal matrix containing the absolute values of the system eigenvalues, i.e. $\tilde{\Lambda} = \text{diag}\{|\lambda_1|, |\lambda_2|, \ldots, |\lambda_5|\}$ and defined as

$$\begin{aligned} \lambda_{1,2,5} &= V_n - V_g \\ \lambda_3 &= V_n - c - \frac{V_g}{2} \\ \lambda_4 &= V_n + c - \frac{V_g}{2} \end{aligned} \tag{3.13}$$

In the previous, V_n is the flow velocity projected on the face normal, V_g the grid velocity projected on the face normal, while c is the "artificial speed of sound" which does not depend on the local density field and it is computed as

$$c = \sqrt{\beta + \left(V_n - \frac{V_g}{2}\right)^2} \tag{3.14}$$

The eigensystem is evaluated on the basis of the Roe averaged flow variables, which are defined as

$$\begin{aligned} \chi &= \sqrt{\frac{\rho_R}{\rho_L}} \\ \tilde{\rho} &= \chi\rho_L \\ \tilde{u}^i &= \frac{u_L^i + \chi u_R^i}{1+\chi}, \quad i = 1,2,3 \end{aligned} \tag{3.15}$$

The complete eigenstructure of the hyperbolic problem is detailed in Appendix C.

Equations (3.11) and (3.15) introduce the value of the flow variables at the unknown left and right states. The variables on each side of the computational face are approximated through flowfield reconstruction procedure, which is described next.

Reconstruction of Flow Variables

The present section summarizes the strategies used for the reconstruction of the primitive flow variables. Firstly, for the velocity field, a piece–wise linear reconstruction (PLR) scheme is used that extrapolates the cell center values of the neighboring cells i, j on the faces providing the left L and the right states R. In Figure 3.2 two neighboring cells i, j, with common boundary f, are illustrated. The two cells have volumes Ω_i and Ω_j, respectively. The face orientation f is defined based on the normal vector $\vec{n}$. It is necessary to extrapolate the known values at the cell centers to the states L and R. The velocities $\vec{v}_L$ and $\vec{v}_R$ can be approximated using a second order Taylor expansion as

$$\begin{aligned} \vec{v}_L &= \vec{v}_i + \nabla\vec{v}_i \cdot \vec{r}_i \\ \vec{v}_R &= \vec{v}_j + \nabla\vec{v}_j \cdot \vec{r}_j \end{aligned} \tag{3.16}$$

In the Taylor expansion $\vec{v}_i, \vec{v}_j$ are the known velocities at the cell centers i, j, r_i, r_j the vectors from the cell centers to the face midpoint p and the gradients $\nabla\vec{v}_i, \nabla\vec{v}_j$ are evaluated at cell centers.

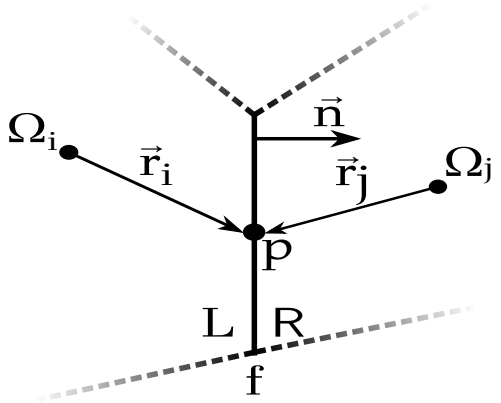

Figure 3.2: Reconstruction of variables on face f

The velocity field is continuous in incompressible one–phase flows, as well as, in two–phase flows since surface tension is neglected. For this reason, no limiter is applied to the PLR approximation.

Perplexities arise in the reconstruction of the volume fraction field. Due to the density discontinuity across the free surface, standard discretization schemes used for convection of scalar fields can not be used. For example a first upwind scheme will lead to extreme smearing of the surface over several computational cells, while a second–order central scheme would introduce un–physical oscillations in the volume fraction field. Various methods have been proposed to prevent this smearing and lead to a more accurate representation of the discontinuity, without compromising numerical stability.

Two main families of variable reconstruction that can handle discontinuous fields have been introduced. Both families use similar definitions to derive numerical schemes that preserve accuracy and do not produce oscillations near the discontinuity. Their key concept is to introduce a small amount of numerical diffusion, in specific regions, to preserve the solution within the physical bounds (bounded solution) and switch to a higher approximation elsewhere. The first family titled *Total Variation Diminishing* (TVD) states that, for any physical admissible solution, its total variation should not increase in time [99]. The total variation of a discrete 1D solution ϕ is defined by

$$TV\left(\phi^n\right) = \sum_i \left|\phi_{i+1} - \phi_i\right| \tag{3.17}$$

A numerical scheme is said to be TVD in time, if, for every time level n

$$TV\left(\phi^n\right) \leq TV\left(\phi^{n+1}\right) \tag{3.18}$$

TVD approach uses high–order interpolation schemes and supplements them with a flux limiter to comply with the TVD criterion. Limiters are applied to the high–order terms of the interpolation scheme. A switch is made to a first order upwind scheme in order to produce bounded solutions. Within the context of the present research, as high–order interpolation schemes the second order PLR and the third order MUSCL [100] have been considered. In order to comply with the TVD condition, the SUPERBEE limiter has been employed which has proved to have excellent resolution properties for contact discontinuities [99]. However, in all cases considered here the TVD approach has been found to be extremely diffusive, a remark that has been also reported elsewhere [101].

The second family of interpolation schemes, that have been devised to minimize diffusion and produce bounded solutions has been introduced by Leonard [102, 103]. It is based on the Normalized Variable Approach (NVA). In order to obtain a reconstructed quantity on face, ϕ_f, the following normalization is defined

$$\tilde{\phi} = \frac{\phi_f - \phi_D}{\phi_U - \phi_D} \tag{3.19}$$

where U, C and D denote the center, the downwind and the upwind cells, according to the flow direction. Reconstruction schemes can be formulated for the quantity $\tilde{\phi}_f$, based on $\tilde{\phi}_C$.

Using the normalization (3.19) for the two neighboring cells holds $\tilde{\phi}_D = 0$ and $\tilde{\phi}_U = 1$. In order for a solution to be bounded, it should remain between the limits defined by $\tilde{\phi}_D, \tilde{\phi}_U$. This condition is identified as the Convention Boundedness Criterion (CBC) [104].

$$0 \leq \tilde{\phi}_C \leq 1 \tag{3.20}$$

The boundedness criterion for convection differencing schemes of Equation (3.20) can be illustrated using the Normalized Variable Diagram (NVD) of Figure (3.3). An admissible solution should be bounded from below by the upwind cell value $\tilde{\phi}_C$ and from above by unity.

Equation (3.21) shows typical differencing schemes expressed based on the NVA, which are also plotted on the NVD of Figure 3.3.

$$\begin{array}{lll}
\text{Upwind (UD):} & \phi_f = \phi_C & \Rightarrow \tilde{\phi}_f = \tilde{\phi}_C \\
\text{Central (CD):} & \phi_f = \frac{1}{2}\left(\phi_C + \phi_D\right) & \Rightarrow \tilde{\phi}_f = \frac{1}{2}\left(1 + \tilde{\phi}_C\right) \\
\text{Linear Upwind (LUD):} & \phi_f = \frac{3}{2}\phi_C - \frac{1}{2}\phi_U & \Rightarrow \tilde{\phi}_f = \frac{3}{2}\tilde{\phi}_C \\
\text{QUICK:} & \phi_f = \frac{3}{8}\phi_D + \frac{3}{4}\phi_C - \frac{1}{8}\phi_U & \Rightarrow \tilde{\phi}_f = \frac{3}{8} + \frac{3}{4}\tilde{\phi}_C \\
\text{Downwind (CD):} & \phi_f = \phi_D & \Rightarrow \tilde{\phi}_f = 1
\end{array} \tag{3.21}$$

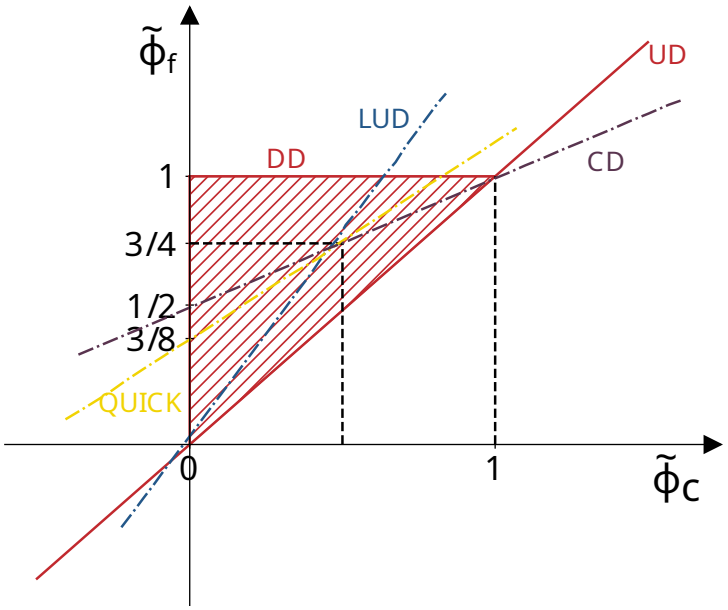

Figure 3.3: Normalized Variable Diagram (NVD). The CBC criterion states that in order preserve boundedness the reconstructed value should lie in the shaded area or in the line $\tilde{\phi}_f = \tilde{\phi}_C$ (Upwind Differencing–UD scheme). Figure shows also various interpolation schemes

The idea of constructing compressive schemes based on NVD is to adopt a blending between downwind differencing scheme and a high–order upwind scheme. The downwind branch of the scheme is used to compress the smearing of the discontinuous profile, while the upwind scheme to preserve monotonicity. The switch between the two is based on the angle θ formed between the flow and the grid line of the face, ranging from 0 to 90 degrees. For an interface aligned with the face ($\theta = 0$), a higher–order downwind scheme (HDS) is selected, while in cases the

flow is perpendicular to the face ($\theta = 90$) a high–resolution schemes (HRS) is used. Numerical schemes based on NVA can be written in the following compact form,

$$\tilde{\phi}_f = \gamma(\theta)\,\tilde{\phi}_f^{HDS} + [1 - \gamma(\theta)]\,\tilde{\phi}_f^{HRS} \tag{3.22}$$

In the previous, $\tilde{\phi}_f^{HRS}$ is the normalized face variable as obtained by a high–resolution scheme and $\tilde{\phi}_f^{HDS}$ the result from a downwind approximation. The blending is performed by the switching function $\gamma(\theta)$.

The blending function in most recent works depends also in the local Courant number (CFL) as defined by the advection velocity inside a computational cell i (see Eq. (3.23)). Usually, for values less than 0.3, a blending between high order downwind and upwind schemes are used, for values between 0.3 and 0.7, the blending reduces to first order accurate schemes, while for values greater than 0.7 a first order upwind scheme is used to enhance stability.

$$CFL_i = \frac{\Delta t}{\Omega_i}\vec{F}_{c,g} = \frac{\Delta t}{\Omega_i}\max\left(\sum_f \Delta V_f \Delta S_f, 0\right) \tag{3.23}$$

In the previous paragraphs, an outline for methods on constructing shock–capturing schemes has been given. The interested reader can be referred to [98] for more details about constructing schemes based on the NVD approach.

In the present thesis, various schemes has been implemented and tested. Among them it was found that STACS [105], HRIC [106] and BRICS [107] produce results with adequate accuracy in free surface applications, with the latter scheme producing the most satisfying results. In all cases presented here, the BRICS scheme is utilized, unless otherwise stated.

Lastly for the calculation of the inviscid fluxes, a reconstruction process should be followed for the pressure field. Pressure can be decomposed into two components, the dynamic part p_D and the hydrostatic part $p_H = \rho g(z - z_{ref})$, with ρ denoting density, g the gravity acceleration acting on the negative z–axis and z_{ref} a hydrostatic reference height.

Before presenting the details of the reconstruction scheme employed, it is useful to make two comments on the features of the pressure field in two–phase flows. Starting the analysis by making a comment on hyperbolic conservation laws with source terms. The momentum equation is a conservation law, where the gravity source term acts on the right hand side. A Riemann solver is used to calculate the flux across the interface. Riemann solvers do not inherently account for the presence of external forces [69, 72, 108–112], they translate any pressure jump across an interface, as fluid velocity even in a hydrostatic configuration. An exact representation of the fluxes at the cell's interface is required to cancel the source terms out, so the net flux is zero.

To elaborate further, the 1D conservation law of Equation (3.24) is taken as an example

$$\frac{\partial q}{\partial t} + \frac{\partial f(q)}{\partial x} = S_q \tag{3.24}$$

where S_q is a constant source term. Expanding into its semi–discrete form the following form is obtained

$$\frac{\Delta q_i}{\Delta t} + \frac{1}{\Delta x_i}\left(f_{i+1/2} - f_{i-1/2}\right) = S_{q,i}\Delta x_i \tag{3.25}$$

Similar to the hydrostatic equilibrium case, the value q varies linear in space, as illustrated in Figure 3.4, and should be balanced by S_q. If the cell center values q_i are used for the evaluation of fluxes $f_{i\pm1/2}$, implying a first order approximation, an imbalance between $S_{q,i}$ and the cell center values will be created. In order to prevent un–physical solutions, an exact second order reconstruction scheme should be employed to balance the external forcing $S_{q,i}$.

Returning to the momentum equations, it is important to maintain a second order accuracy, at least for the hydrostatic part p_H of the pressure field. This can be achieved by a adopting

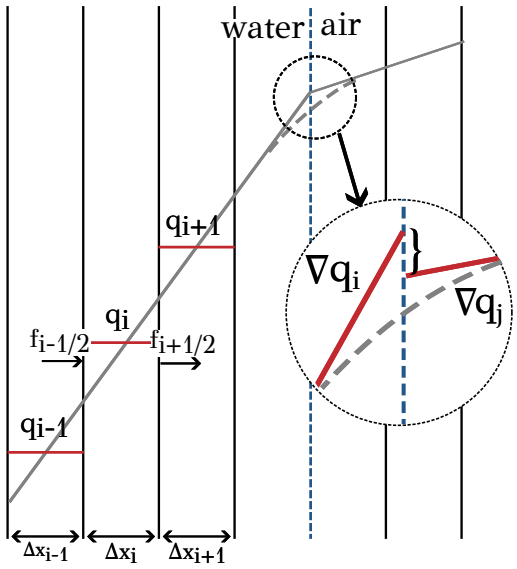

Figure 3.4: Linear varying hydrostatic pressure field. The figure depicts the cell center averaged values q_i, the linear varying pressure term (gray line) and discontinuity of gradient at the air/water interface. Furthermore, the dotted line in the detailed view shows the field after numerical diffusion is introduced

second order PLR interpolation scheme, similar to one used for the velocity field (Eq. (3.16)),

$$\begin{aligned} p_L &= p_i + \nabla p \cdot \vec{r}_i \\ p_R &= p_j + \nabla p \cdot \vec{r}_j \end{aligned} \tag{3.26}$$

where ∇p has to be computed with a second order accuracy. As it will be made clear later, calculation of ∇p with a second order accuracy is not trivial on unstructured grids. Various corrections should be applied to effectively balance the hydrostatic source terms.

The second point raised here, is with respect to the hydrostatic variation of pressure in two phase flows. At the free surface, although the pressure field is continuous and no jump appears, $[p] = 0$, this is not the case for its gradient. The different densities of the two fluids leads to a jump in the hydrostatic part $[\nabla p_H] \neq 0$. In the discretized field the free surface is perceived as an abrupt, yet smooth, variation of the density field and so is the hydrostatic component of pressure. This is illustrated in the detailed view of Figure (3.4). The pressure gradient varies smoothly, as indicated by the dashed line. Even if a second order reconstruction scheme is adopted (red lines in the detailed view), the numerical diffusion introduced at the free surface will result in a hydrostatic pressure jump across the interface.

A solution to this problem was given by Queutey and Visonneau [47]. They noted that, although, the pressure gradient is not continuous at the interface, its density weighted counterpart is. This means that, at the free surface, the following conditions apply,

$$\begin{aligned} [p] &= 0 \\ [\nabla p] \neq 0 \ \text{ but } \ \left[\frac{\nabla p}{\rho}\right] &= 0 \end{aligned} \tag{3.27}$$

They formulate a second order accurate reconstruction, based on a density averaging. The pressure gradient can be computed as,

$$p_f = \frac{h^R \rho^R p_i + h^L \rho^L p_j}{h^L \rho^L + h^R \rho^R} \tag{3.28}$$

where superscripts R, L denote extrapolated, left and right, quantities of the face and $h^{L/R}$ the projected distances to the face, $h^L = \vec{r}_i \cdot \vec{n}$ and $h^R = \vec{r}_j \cdot \vec{n}$, as defined in Figure 3.2. In the

present implementation, their approach is followed near the free surface, that is in regions of $\nabla\alpha_l \neq 0$.

Gradient Evaluation

For the flowfield reconstruction, the gradient at each computational should be computed. Two different approximations are adopted. The first, uses the Green–Gauss theorem, where the gradient of the primitive variables at the i^{th} computational cell can be computed as

$$\nabla\overrightarrow{Q}_i \approx \frac{1}{\Omega_i}\int_{\partial\Omega_i}\overrightarrow{Q}_{ij}\cdot\vec{n}\mathrm{d}S \ \ , j \in N_{f,i} \tag{3.29}$$

The term $\vec{Q}_{ij}$ denotes an approximation of the flow quantities at the face f. In some cases a simple averaging is chosen, which can deteriorate the order of accuracy, but can enhance the stability of the solver. Various corrections can be applied which can account for non–uniform meshes or skewness of the mesh [101]. For flows with gravity, it is important to maintain hydrostatic equilibrium, thus in MaPFlow, a simple averaging between the states of the two adjacent cells is chosen, supplemented with a hydrostatic correction, i.e.

$$\overrightarrow{Q}_{ij} = \frac{1}{2}\left(\overrightarrow{Q}'_i + \overrightarrow{Q}'_j\right) \tag{3.30}$$

where

$$\begin{aligned}\overrightarrow{Q}'_i &= \overrightarrow{Q}'_i + \rho_i\vec{g}\cdot\vec{r}_i\\ \overrightarrow{Q}'_j &= \overrightarrow{Q}'_j + \rho_j\vec{g}\cdot\vec{r}_j\end{aligned} \tag{3.31}$$

and $\vec{r}_i$ denotes the vector from the i cell center to the midpoint of the face p, as illustrated in Figure 3.2.

A second, more accurate approximation of the gradients, can be performed using the Least Square Method [98]. If $\nabla\vec{Q}_i$ is the unknown gradient at the control volume i, $\vec{Q}_j$ is the vector of the flow quantities of a neighbor i and $\vec{r}_{ij}$ is vector from the center of the control volume i to the center of the control volume j, then the vector $\vec{Q}_j$ can be approximated, with second order accuracy, as

$$\overrightarrow{Q}'_j = \overrightarrow{Q}_i + \left(\nabla\overrightarrow{Q}\right)_i\cdot\vec{r}_{ij} \tag{3.32}$$

The method of the Least Squares computes the gradient based on the following optimization problem,

$$\begin{aligned}\Delta_i &= \sum_{j=1}^{Neis(i)}\left\{w_j\left[\overrightarrow{Q}_j - \left(\overrightarrow{Q}_i + \left(\nabla\overrightarrow{Q}\right)_i\cdot\vec{r}_{ij}\right)\right]^2\right\} \ \ \Rightarrow\\ \Delta_i &= \sum_{j=1}^{Neis(i)}\left\{w_j\left[\Delta\overrightarrow{Q}_{ij} - \left(\Delta x_j\frac{\partial\overrightarrow{Q}_i}{\partial x} + \Delta y_j\frac{\partial\overrightarrow{Q}_i}{\partial y} + \Delta z_j\frac{\partial\overrightarrow{Q}_i}{\partial z}\right)\right]^2\right\}\end{aligned} \tag{3.33}$$

The minimum of the quantity Δ_i is sought

$$\frac{\partial\Delta_i}{\partial\left(\frac{\partial\overrightarrow{Q}_i}{\partial x}\right)} = \frac{\partial\Delta_i}{\partial\left(\frac{\partial\overrightarrow{Q}_i}{\partial y}\right)} = \frac{\partial\Delta_i}{\partial\left(\frac{\partial\overrightarrow{Q}_i}{\partial z}\right)} = 0 \tag{3.34}$$

The matrix form of the above optimization problem yields

$$\begin{bmatrix} w_j\Delta x_j\Delta x_j & w_j\Delta x_j\Delta y_j & w_j\Delta x_j\Delta z_j\\ w_j\Delta y_j\Delta x_j & w_j\Delta y_j\Delta y_j & w_j\Delta y_j\Delta z_j\\ w_j\Delta z_j\Delta x_j & w_j\Delta z_j\Delta y_j & w_j\Delta z_j\Delta z_j\end{bmatrix}\begin{bmatrix}\frac{\partial\overrightarrow{Q}_i}{\partial x}\\ \frac{\partial\overrightarrow{Q}_i}{\partial y}\\ \frac{\partial\overrightarrow{Q}_i}{\partial z}\end{bmatrix} = \begin{bmatrix} w_j\Delta x_j\Delta\overrightarrow{Q}_{ij}\\ w_j\Delta y_j\Delta\overrightarrow{Q}_{ij}\\ w_j\Delta z_j\Delta\overrightarrow{Q}_{ij}\end{bmatrix} \tag{3.35}$$

The weighting factor w_j is computed as

$$w_j = \frac{1}{\left|\vec{r}_j - \vec{r}_i\right|^2} \tag{3.36}$$

The above method is second order accurate thus it can reconstruct the hydrostatic field exactly without any corrections. Least square method is the method of choice for two dimensional simulations, however in 3D simulations the Green–Gauss approximation is preferred for stability reasons.

3.3.2 Evaluation of Viscous Fluxes

For the calculation of the viscous fluxes, (see Eq. (2.23)) the values and the gradients of the flow variables should be approximated on the face f. Firstly, for the flow variables on the face, a simple averaging between the neighboring cells i, j

$$\overrightarrow{Q}_{ij} = \frac{1}{2}\left(\overrightarrow{Q}_i + \overrightarrow{Q}_j\right) \tag{3.37}$$

is used.

Moreover, gradients are computed using the mean value of the known gradients at the cell center, sumpplemented with a directional derivative to account for the skewness of the mesh, according to

$$\nabla\overrightarrow{Q}_{ij} = \overline{\nabla\overrightarrow{Q}_{ij}} + \left[\overline{\nabla\overrightarrow{Q}_{ij}} \cdot \vec{t}_{ij} - \left(\frac{\partial\overrightarrow{Q}}{\partial l}\right)_{ij}\right] \cdot \vec{t}_{ij} \tag{3.38}$$

In the above, $\vec{t}_{ij}$ is the unit vector pointing from cell center i to cell center j and the mean gradient is computed as

$$\overline{\nabla\overrightarrow{Q}_{ij}} = \frac{1}{2}\left(\nabla\overrightarrow{Q}_i + \nabla\overrightarrow{Q}_j\right) \tag{3.39}$$

The gradient across the line that passes through the cell centers i,j is computed by a finite difference method.

$$\left(\frac{\partial\overrightarrow{Q}}{\partial l}\right)_{ij} \approx \frac{\overrightarrow{Q}_j - \overrightarrow{Q}_i}{l_{ij}} \tag{3.40}$$

3.3.3 Flux Correction for Non–Planar Vertices

Modern CFD applications have increased demands in terms of the perplexities of the studied geometries and flow processes. Complex geometries and field discontinuities are some of the typical features that CFD solvers need to tackle. These difficulties render the meshing step significantly more complex and time consuming. In some cases by adopting classical meshing algorithms, such as structured–like hexahedral or even unstructured tetrahedral meshing strategies, can lead to a cumbersome process and probably will fail to meet the requirements of the studied application.

Polyhedral or trim meshing have emerged as a solution for simpler and faster grid generation. Polyhedral meshing has the advantages of anisotropic refinement and smoother mesh coarsening. The meshing strategy is usually simple and automated, thus reducing the pre–processing time significantly. Unfortunately, this algorithmic abstraction of grid generation may lead to low cell quality that flow solvers should take into account. One common downside of polyhedral meshing is that the face of the generated cells have vertices that do not lie on the same plane. Although this is the case even in cells with one or more quadrilateral faces (such as pentas or hexas), in case of the polyhedral cells with polygonal faces this is further pronounced. This

could lead to a loss of accuracy and error amplification. Figure 3.5 shows two examples of polyhedral cells, as generated by commercial meshing softwares. The polyhedral cell of Figure 3.5a has been created to resolve the curvature near a solid boundary, while the cell of Figure 3.5b is encountered typically in regions away from solid boundaries and is used for smoother grid coarsening. It is evident that a single plane per face can not be used to define a closed volume.

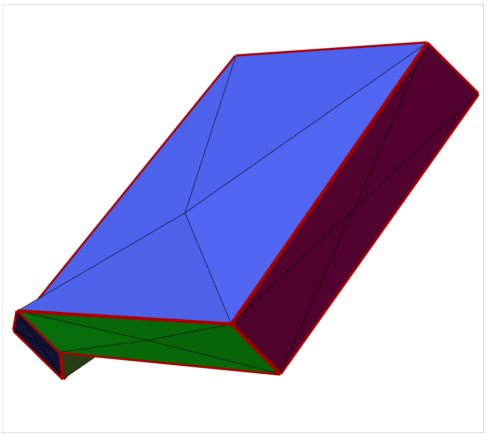

(a) Polyhedral cells used for resolving wall boundaries

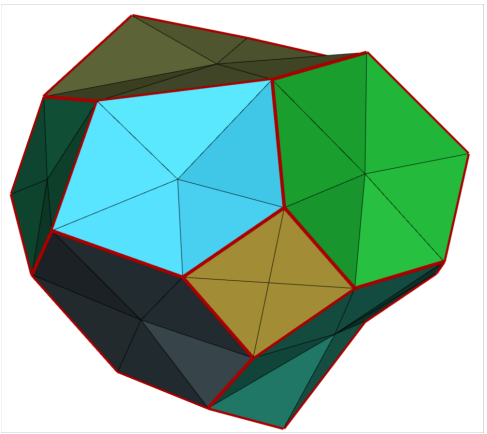

(b) Polyhedral cell used for efficient grid coarsening. Typically encountered away from solid boundaries

Figure 3.5: Examples of polyhedral cells used in modern CFD applications. Each colors depicts a different cell face, the triangles are defined based on the the face's geometric center and a face edge

Standard CFD second order finite volume solvers, as the one discussed in the present dissertation, use an one–point quadrature method for the flux evaluation of Equation (3.8). The existence of non–planar vertices deteriorate the accuracy of the solver. A remedy is to split the polygonal face into a set of triangles and use a multi–point quadrature integration method, in the expanse of increased computational cost. A more cost effective solution has been proposed by [113]. In this approach, given a polyhedral volume Ω_i with its boundary described by a set of polygonal faces $\partial\Omega_{i,f}$, then the equivalent flux vector $\overrightarrow{F}$ across a face f can be approximated by a second order Taylor expansion around the geometric midpoint p of the face.

$$\int_{\partial\Omega_{i,f}} \overrightarrow{F} \cdot \vec{n} \mathrm{d}S_f = \int_{\partial\Omega_{i,f}} \left[\overrightarrow{F}_p + \nabla \overrightarrow{F} \big|_p (\vec{x} - \vec{x}_p) \right] \cdot \vec{n} \mathrm{d}S_f \tag{3.41}$$

The zero term of the expansion can be approximated with a linear reconstructed flux of Equation (3.8). The second term defines the correction in case of non–planar vertices. The evaluation of the correction flux is performed by tessellating the polygonal face into a set of triangle $T_{i,f}$ as illustrated in Figure 3.5. The flux across face f can be computed as

$$\int_{\partial\Omega_{i,f}} \overrightarrow{F} \cdot \vec{n} \mathrm{d}S_f = \overrightarrow{F}_p \cdot \vec{n}_f S_f + \sum_{T \in T_{i,f}} \int_T \left[\nabla \overrightarrow{F} \big|_p (\vec{x} - \vec{x}_p) \right] \cdot \vec{n} \mathrm{d}S_T \tag{3.42}$$

Now, since three points define uniquely a plane, the evaluation of fluxes is performed in a closed volume, thus a single point evaluation per triangle will lead to a second order accurate solution in space. Equation (3.42) is approximated as

$$\int_{\partial\Omega_{i,f}} \overrightarrow{F} \cdot \vec{n} \mathrm{d}S_f = \overrightarrow{F}_p \cdot \vec{n}_f S_f + \sum_{T \in T_{i,f}} \left[\nabla \overrightarrow{F} \big|_p (\vec{x}_T - \vec{x}_p) \right] \vec{n}_T \Delta S_T \tag{3.43}$$

In the above $\vec{x}_T$ is the midpoint of the triangle T which is part of face f, and $\vec{n}_T$ its normal vector.

To complete the evaluation of the flux, the flux gradient on the face is needed. The gradient can be computed based on simple averaging between the adjacent cells. These gradients are not known and must be computed. In the original reference ([113]) a chain rule is proposed to calculate the gradients from the variable gradients, which are already known.

It is clear that this approach is more efficient than a multi–point integration and can be easily incorporated in any standard second order finite volume method without changing the basic computational strategy.

As already discussed, in case of hyperbolic conservation laws with source terms it is important to maintain accuracy in order to imbalance the external forces. If linear varying hydrostatic term is present in the flowfield, the flux reconstruction should be at least second order. Any loss of accuracy will be translated to acceleration of the flow at the hydrostatic equilibrium. Second order accuracy can be achieved, by applying the aforementioned procedure at least for the hydrostatic part of the equations.

In absence of velocity field ($\vec{v} = 0$) and any other source of pressure disturbance, thus the dynamic pressure is equal to zero ($p_D = 0$), the hydrostatic equilibrium yields

$$\int_{\partial\Omega} p_h \vec{n} \mathrm{d}S = \int_{\Omega} \rho \overrightarrow{g} \mathrm{d}V \tag{3.44}$$

where $\vec{g}$ is the gravity acceleration pointing towards the negative z–axis, p_h is the hydrostatic pressure relative to a reference vector $\vec{x}_0 = (0, 0, z_0)$ and it is expressed as $p_h = \rho\vec{g} \cdot (\vec{x} - \vec{x}_0)$.

In the same spirit as in Equation (3.43), the integral over a polygonal face f can be approximated within second order accuracy, using a second order expression for the point value $p_{h,p}$ and a sum over the set of triangles $T_{i,f}$ that define face f.

$$\int_{\partial\Omega_{i,f}} p_h \vec{n} \mathrm{d}S = p_{h,p} \vec{n}_f S_f + \sum_{T \in T_{i,f}} \int_T \left[\nabla p_h \big|_p (\vec{x} - \vec{x}_p) \right] \cdot \vec{n} \mathrm{d}S_T \tag{3.45}$$

The gradient of the hydrostatic pressure is,

$$\nabla p_{h,f} = \begin{bmatrix} 0 \\ 0 \\ -\rho_f g_z \end{bmatrix} \tag{3.46}$$

The surface integral of Equation (3.45) over the set of triangles can be exactly computed for linear functions as,

$$\int_T \left[\nabla p_h (\vec{x} - \vec{x}_p) \right] \vec{n}_T \mathrm{d}S_T = -\frac{1}{2} (\vec{r}_1 \times \vec{r}_2) \sum_{n=1}^{3} \frac{1}{3} \rho_f g_z (z_n - z_p) \tag{3.47}$$

where $\vec{r}_1, \vec{r}_2$ are the side vectors that define triangle T.

Furthermore, the imbalance due to non–planar vertices should be accounted for in every step of the computational algorithm, where the Green–Gauss theorem is used. For example, a similar correction flux is applied to the volume calculation (Eq. (3.2)) and to the gradient evaluation, if formula (3.29) is used.

A Simple Numerical Example

To illustrate the importance of the above correction flux a simple numerical experiment is conducted. The hydrostatic equilibrium test case is considered, for one–phase flow (without free surface). Inside an empty box of base 1, pressure is initialized as $p = p_H = \rho g z$, the velocity is set to zero ($\vec{v} = 0$) and farfield boundary conditions are applied to all box's sides. The domain is discretized by arbitrary polyhedral elements. An overview of the computational mesh and the initial pressure disturbance can be seen in Figure 3.6.

The numerical experiment is performed twice, once *without* considering any correction flux and once *with* the correction flux of Equation (3.47). In Figure 3.7, the distribution of the dynamic pressure p_D is plotted, for both cases, after 500 iterations. The results on the left correspond to the un–corrected case, while results on the right to the case with correction.

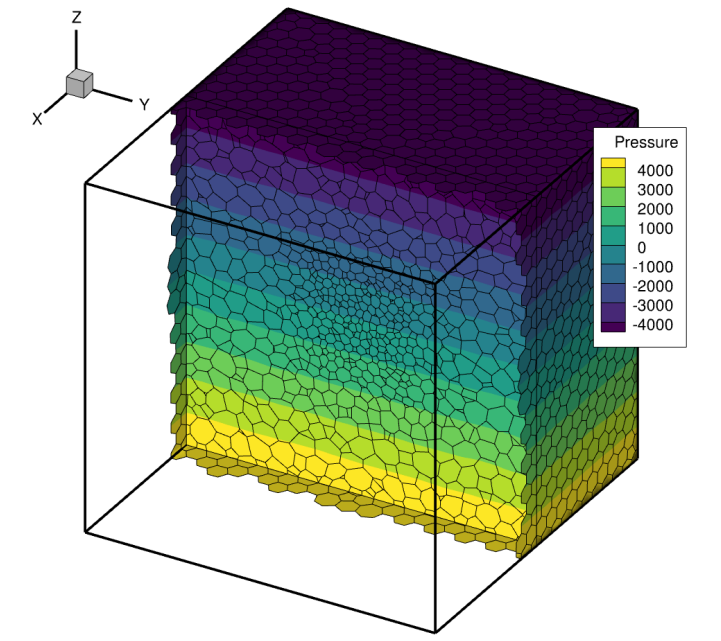

Figure 3.6: One–phase hydrostatic equilibrium. Simulation in an empty rectangular box of length 1. The figure shows the initialization of pressure ($=\rho g z$) inside the box. Mesh consists of approximately 12,000 polyhedral elements. The density of the fluid is $\rho = 1000 kg/m^3$ and the acceleration of gravity is set to $g = 9.81 m/s$

In the case of no correction is applied, Figure 3.7a, a pressure imbalance appears in the field and it is more pronounced in larger cells. This numerical noise is produced by the non–planar vertices of the cell. In the second case, Figure 3.7b, the dynamic pressure is close to machine precision, as it should be in case of hydrostatic equilibrium.

As already mentioned, out of plane vertices may appear even in simple grid configurations. For example, similar results can be obtained using hexahedral meshing. Thus correction of the numerical flux is necessary, regardless of the meshing strategy.

3.4 Temporal Discretization

For every time true computational step a pseudo-steady problem is solved. Let $\overrightarrow{Q}^*$ denote the flow variables that are used to solve the pseudo–steady time problem, which until convergence they do not satisfy the original unsteady problem. At every pseudo–time step iteration k, for a computational cell i a problem of the form

$$\overline{\Gamma}\Omega_i \frac{\partial \overrightarrow{Q}_i^*}{\partial \tau} + \overrightarrow{R}_u \left(\overrightarrow{Q}_i^* \right) = 0 \tag{3.48}$$

is solved, where $\overrightarrow{R}_u$ is the unsteady residual, defined as the sum of the spatial residual and the time–derivatives, i.e.

$$\overrightarrow{R}_u \left(Q_i^* \right) = \overrightarrow{R}_s \left(\overrightarrow{Q}_i^* \right) + \overline{\Gamma}_e \frac{\partial \left(\Omega_i \overrightarrow{Q}_i^* \right)}{\partial t} \tag{3.49}$$

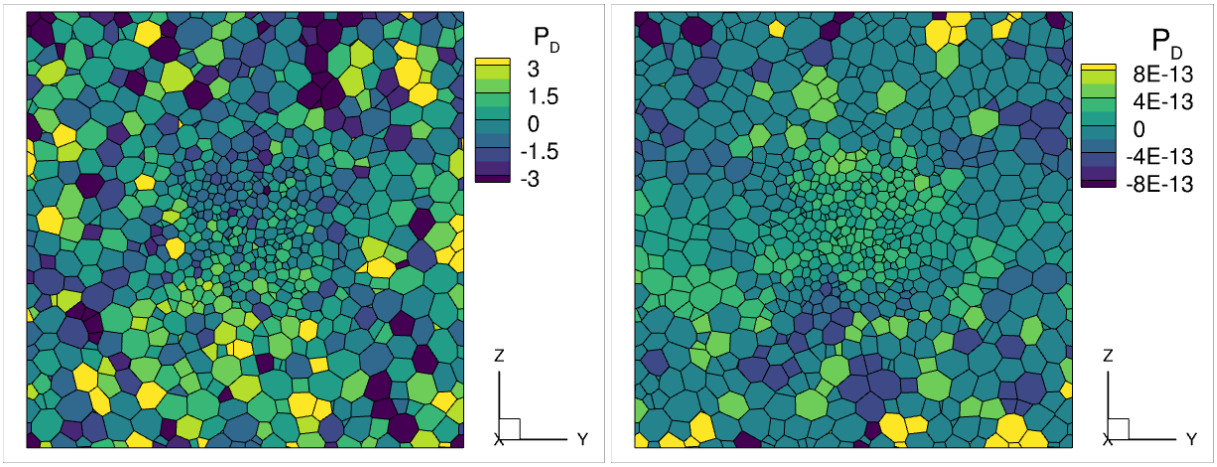

(a) $N_{iter} = 500$, without hydrostatic correction flux. Contour range [-3:3]

(b) $N_{iter} = 500$, with hydrostatic correction flux. Contour range $[-8 \cdot 10^{-13} : 8 \cdot 10^{-13}]$

Figure 3.7: Hydrostatic equilibrium in one phase flows. Dynamic pressure distribution in an empty box with polyhedral elements. Error introduced due to the non–planar vertices. Figures shows the dynamic pressure distribution, at the plane $x = 0$, without (left) and with (right) correction flux

The convergent solution of the problem is obtained when $\overrightarrow{R}_u \to 0$ and thus $\overrightarrow{Q}^* \to \overrightarrow{Q}^{n+1}$ (n is the time marching iterator). In case of steady flow problems the unsteady residual is equal to the spatial, since the unsteady term is omitted. In this case, the pseudo–time marching begins with $k = 0$ and the convergent steady solution of the problem is obtained once the pseudo–time derivatives tend to zero.

A fully implicit scheme is used for the discretization of the unsteady terms. Let $n+1$ be the unknown time level, with the flow quantities being known for the time levels $n, n-1, n-2, \ldots$, writing the time derivative as a series expansion of successive levels backward in time [114], the following backwards difference formula (BDF) is obtained

$$\frac{\partial\left(\Omega_i \overrightarrow{Q}_i\right)}{\partial t} = \frac{1}{\Delta t}\left[\varphi_{n+1}\left(\Omega_i \overrightarrow{Q}_i\right)^{n+1} + \varphi_n\left(\Omega_i \overrightarrow{Q}_i\right)^{n} + \varphi_{n-1}\left(\Omega_i \overrightarrow{Q}_i\right)^{n-1} + \varphi_{n-2}\left(\Omega_i \overrightarrow{Q}_i\right)^{n-2} + \ldots\right] \tag{3.50}$$

By rearranging the terms of the above equation, the discretized unsteady term can be written as

$$\frac{\partial\left(\overrightarrow{Q}_i \Omega_i\right)}{\partial t} = \frac{1}{\Delta t}\left[\overrightarrow{Q}^n\left(\varphi_{n+1}\Omega_i^{n+1} + \varphi_n\Omega_i^n + \varphi_{n-1}\Omega_i^{n-1} + \varphi_{n-2}\Omega_i^{n-2} + \ldots\right) + \varphi^{n+1}\left(\overrightarrow{Q}^{n+1} - \overrightarrow{Q}^n\right)\Omega_i^{n+1} + \varphi^{n-1}\left(\overrightarrow{Q}^{n-1} - \overrightarrow{Q}^n\right)\Omega_i^{n-1} + \varphi^{n-2}\left(\overrightarrow{Q}^{n-2} - \overrightarrow{Q}^n\right)\Omega_i^{n-2} + \ldots\right] \tag{3.51}$$

In order to enforce volume conservation, the GCL is imposed on the time discretization process. Using the same sequence of the BDF scheme and assuming constant value fluxes at each face of the cell i, Equation (2.28) can be discretized as

$$\frac{1}{\Delta t}\left[\left(\varphi_{n+1}\Omega_i^{n+1} + \varphi_n\Omega_i^n + \varphi_{n-1}\Omega_i^{n-1} + \varphi_{n-2}\Omega_i^{n-2}\right) + \ldots\right] = \sum_f^{N_{f,i}} V_{g,f}\Delta S_f = R_{gcl}^{n+1} \tag{3.52}$$

Now, the unsteady term can be written as

$$\frac{\partial\left(\overrightarrow{Q}_i\Omega_i\right)}{\partial t} = R_{gcl}^{n+1}\overrightarrow{Q}_i^n + \frac{1}{\Delta t}\left[\varphi_{n+1}\left(\overrightarrow{Q}_i^{n+1}-\overrightarrow{Q}_i^n\right)\Omega^{n+1} + \varphi_{n-1}\left(\overrightarrow{Q}_i^{n-1}-\overrightarrow{Q}_i^n\right)\Omega^{n-1} + \varphi_{n-2}\left(\overrightarrow{Q}_i^{n-2}-\overrightarrow{Q}_i^n\right)\Omega^{n-2} + \ldots\right] \tag{3.53}$$

Finally, the pseudo–steady term of equation (3.48) is discretized using first order Euler scheme

$$\Omega_i\frac{\partial\overrightarrow{Q}_i^*}{\partial\tau} = \Omega_i^{n+1}\frac{\overrightarrow{Q}_i^{*,k+1}-\overrightarrow{Q}_i^{*,k}}{\Delta\tau} = \Omega_i^{n+1}\frac{\Delta\overrightarrow{Q}_i^{*,k}}{\Delta\tau} \tag{3.54}$$

The above discrete equations describe the problem that governs a particular computational cell i. By using this formulation for every computational cell a closed non–linear algebraic system of $\mathcal{N}$ vector equations and $\mathcal{N}$ unknown vectors is formed. A linearization process is required for the system solution, as described in the next section, Section 3.6.

Local Time Stepping

In order to facilitate convergence the local time stepping technique is used. At each computational cell the pseudo–timestep is determined by

$$\Delta\tau_i = CFL_\tau\frac{\Omega_i}{\hat{\Lambda}_{c,i}} \tag{3.55}$$

The convective spectral radii $\hat{\Lambda}_c$ is the sum over the faces of the cell

$$\hat{\Lambda}_{c,i} = \sum_f^{N_f}\left(\left|\vec{v}_{ij}\cdot\vec{n}_f - \frac{V_g}{2}\right| + c_{ij}\right)\Delta S_f \tag{3.56}$$

Subscript ij denotes the evaluation of the quantities at face f with simple averaging between the neighboring cells i and j.

The CFL_τ number is a numerical parameter that depends on the specific simulation. It regulates the convergence rate and typically gets values way greater than 1. Usually, a linear ramping is performed during the first few iterations. Especially in boundary valued problems (e.g., the flow around a hydrofoil), a small CFL_τ value is preferred for the few first iterations when the flow is shaped. Once the flow starts to form around the body, large values of CFL_τ number are adopted for quicker convergence to the solution. In case of initial valued problems, medium values of CFL_τ number are usually adopted during the whole simulation, since a fast convergence rate is needed in every time–true step.

3.5 Boundary Conditions of the Flow Equations

In order to close the system of the discretized flow equations, an appropriate set of boundary conditions is specified. The boundary conditions are used for the calculation of the numerical flux imposed at the boundary faces of the domain. In the present work, four types of boundary conditions are defined; (a) wall boundary conditions, (b) farfield boundary conditions (c) symmetry boundary conditions and (d) periodic boundary conditions. In *MaPFlow*, the conditions for the farfield, symmetry and periodic boundaries are specified using ghost cells. The boundaries of the computational mesh are extended for one computational cell outwards of the domain. The values of the primitive variables at the ghost cells are specified depending on the type of the boundary conditions.

Below the four computational types are described in detail.

Wall Boundary Conditions

A wall boundary can either be fixed (e.g. seabed) or moving with body velocity $\vec{U}_B$ (e.g. a rotating propeller). Solid boundaries can be considered either as a slip boundaries, where the non–entry boundary condition is applied or as no–slip boundaries. For example, in free surface flows, the viscosity effects at the sea bottom are usually neglected and the slip boundary condition is considered. However, when ship resistance calculations are performed or the response of a platform is studied, viscosity cannot be neglected and the no–slip boundary condition is applied.

A slip boundary is typically considered in inviscid flows or in cases, where viscosity effects close to the wall can be neglected. In these cases, the vertical to the wall velocity is set to zero using

$$\left(\vec{v}\big|_w - \vec{U}_B\right) \cdot \vec{n} = 0 \tag{3.57}$$

If viscosity effects are also considered close to the wall, the no–slip boundary condition implies that the fluid particles move with the velocity of the body

$$\vec{v}\big|_w = \vec{U}_B \tag{3.58}$$

The pressure on the wall boundary should satisfy the linear variation of pressure due to the hydrostatic term. The pressure $p\big|_w$ in the wall boundary is computed as

$$p\big|_w = p_c + \nabla p \cdot \Delta\vec{x}_w \tag{3.59}$$

where p_c is the pressure at the center of the boundary cell, $\nabla p = [0, 0, -\rho g_z]$ and $\Delta\vec{x}_w$ the distance from the boundary.

For the volume fraction, a zero–Neumann boundary condition is applied with first order approximation

$$\alpha_l\big|_w = \alpha_{l,c} \tag{3.60}$$

At this point it is worth making a note on the case where the free–surface meets with moving no–slip boundaries. In this case, a triple discontinuity is created among air, water and the solid boundary. The no–slip boundary does not allow for the convection of the volume fraction on the surface of the body. This can significantly affect the convergence of the solver. A remedy that can be used in steady simulations, for example in ship resistance calculations, is to sweep the volume fraction, within a user–defined region normal to the wall. This could be activated at the early stages of the solution, until an estimation of the wave elevation on the solid boundary is obtained, and then switched–off for the rest of the simulation. Recommended values for the sweep region is approximately 10^{-4} for a body unit length [74].

Farfield Boundary Conditions

Farfield boundary conditions are imposed at the end of the computational domain, where the flow can be considered as undisturbed and matches approximately the states at infinite. Due to the hyperbolic nature of the equations, the information is propagated inwards (inlet) or outwards (outlet) of the domain depending on the local sign of the eigenvalues.

A first approximation is to treat farfield boundaries as an interior cell. A local Riemann solver can be solved between the numerical values of the interior boundary cells and the physical boundary conditions specified at infinite using the Riemann solver of Roe.

A more accurate approximation can be made by solving the characteristic equations of the hyperbolic problem on the direction normal to the boundary [57, 115]. The 1D–Euler equations are solved locally by neglecting any source terms of the field. This can be achieved by making a simplification regarding the hydrostatic term. The hydrostatic pressure can be removed locally from the field and subsequently added once the characteristic problem has been solved.

Moving on to the definition of the characteristic problem, let x_n be the normal direction to boundary, the 1D unsteady Euler Equations can be written as

$$\overline{\Gamma}\frac{\partial \vec{Q}}{\partial \tau} + \tilde{A}_o \frac{\partial \vec{Q}}{\partial x_n} = 0 \tag{3.61}$$

where $\tilde{A}_o$ is the preconditioned jacobian matrix which can be considered as locally constant.

The decoupling of the equations can be performed by utilizing the diagonal form of the jacobian matrix, $\tilde{\Lambda}_o = \tilde{R}_o^{-1}\tilde{A}_o\tilde{R}_o$, and thus the Euler equations can be written as

$$\frac{\partial w_i}{\partial \tau} + \lambda_i \frac{\partial w_i}{\partial x_n} = 0, \;\; i = 1, \ldots, m \tag{3.62}$$

where w_i are the characteristics variables defined as $\partial \vec{W} = R_o^{-1}\partial \vec{Q}$

Integrating the 5 scalar differential of Equation (3.62) the values of the characteristics variables at infinite can be computed. The primitive variables are obtained by solving a five by five linear equation system based on the definition of the characteristic variables. Finally, the flux imposed at the boundary is computed as $\overrightarrow{F} = \overrightarrow{F}\left(\overrightarrow{Q}\right)$. A more detailed description of the characteristic boundary condition can be found in Appendix D of the present thesis.

Symmetry Boundary Conditions

Symmetry boundary conditions are useful for reducing the total computational cost. The symmetry over plane can be exploited to reduce the size of the domain. These type of boundary conditions impose a zero flux over the symmetry plane. The boundary condition resembles to the boundary conditions applied in case of inviscid wall, with an extra requirement about the velocity gradient which is set to zero as well. For the velocities the boundary conditions applied are

$$\begin{aligned} \vec{v} \cdot \vec{n} &= 0 \\ \nabla \vec{v} \cdot \vec{n} &= 0 \end{aligned} \tag{3.63}$$

For the pressure and the volume fraction zero–Neumann boundary conditions are applied, with a first order approximation. That is

$$\begin{aligned} p_{sym} &= p_c \\ \alpha_{l,sym} &= \alpha_{l,c} \end{aligned} \tag{3.64}$$

The indices sym and c indicate the values at the symmetry plane and the values at the boundary cell, respectively.

Once, the boundary values are computed, they are stored at the ghost–cells of the extended grid and the fluxes are calculated as in any interior face.

Periodic Boundary Conditions

Periodicity can be either lateral or rotational. For example, the propagation of water waves inside a numerical tank can be dealt using lateral periodic boundary conditions. Similarly, rotational periodicity is applied in case of a propeller rotating in a uniform flow where only blade is simulated inside an angular domain. Either way, the periodic boundary conditions can be defined using a rotation matrix $\overline{R}_A$. In the case of lateral periodicity, $\overline{R}_A$ is equal to the identity matrix $\overline{I}_{3\times3}$ and in case of rotational periodicity, $\overline{R}_A$ is the rotation matrix defined by by the periodicity angle around its corresponding axis. The boundary conditions applied, in case of periodic boundaries are

$$\begin{aligned} p_A &= p_B \\ \vec{v}_A &= \overline{R}_A \vec{v}_B \\ \alpha_{l,A} &= \alpha_{l,B} \end{aligned} \tag{3.65}$$

where the indices A and B denote the two periodic planes.

Similarly to the symmetry boundary conditions, the primitive values resulted from the periodic boundary conditions are stored in the ghost–cells of the extended grid and the convective and the viscous fluxes are computed according to Equations (3.11) and (3.38).

3.6 Linearization & Matrix Assembly

The fully implicit discretization process results to a set of non–linear equations, since the spatial terms are expressed in terms of the unknown flow quantities $\overrightarrow{Q}_i^*$. The solution process linearizes the system of equations assuming small variations during pseudo–time. The unsteady residual can be written as a Taylor expansion in the time level $k+1$ as

$$\overrightarrow{\mathbf{R}}_u^{*,k+1} \approx \overrightarrow{\mathbf{R}}_u^{*,k} + \left(\frac{\partial \overrightarrow{\mathbf{R}}_u^{*,k}}{\partial \overrightarrow{\mathbf{Q}}^{*,k}} \right) \Delta \overrightarrow{\mathbf{Q}}^{*,k} \tag{3.66}$$

where, in the above, $\overrightarrow{\mathbf{R}}_u^{*,k+1}$ is a vector that assembles the unsteady residuals of all computational cells, $\overrightarrow{\mathbf{R}}_u = \left[\overrightarrow{R}_{u,1}, \overrightarrow{R}_{u,2}, \ldots, \overrightarrow{R}_{u,\mathcal{N}} \right]^T$. Similarly, the assembly of the unknown vector quantities is defined as $\overrightarrow{\mathbf{Q}} = \left[\overrightarrow{Q}_1, \overrightarrow{Q}_2, \cdots, \overrightarrow{Q}_{\mathcal{N}} \right]^T$. The jacobian matrix has dimensions of $\mathcal{N} \times \mathcal{N}$. For syntax simplicity, the following equations are expressed for the i^{th} cell. Making use of Equation (3.51), the unsteady residual is written as

$$\overrightarrow{R}_{u,i}^{*,k+1} = \overrightarrow{R}_{u,i}^{*,k} + \left(\frac{\varphi_{n+1}}{\Delta t} \left(\Omega^{n+1} \overline{\Gamma}_e^{*,k} \right)_i + \frac{\partial \overrightarrow{R}_i^{*,k}}{\partial \overrightarrow{\mathbf{Q}}^{*,k}} \right) \Delta \overrightarrow{\mathbf{Q}}^{*,k} \tag{3.67}$$

Furthermore, by using the definition of the unsteady residual (3.49)

$$\begin{aligned} \overrightarrow{R}_{u,i}^{*,k+1} = \overrightarrow{R}_i^{*,k} + R_{gcl}^{n+1} \overrightarrow{Q}_i^n + \\ \frac{1}{\Delta t} \left[\varphi_{n+1} \left(\overrightarrow{Q}_i^{*,k} - \overrightarrow{Q}_i^n \right) \Omega_i^{n+1} + \varphi_{n-1} \left(\overrightarrow{Q}_i^{n-1} - \overrightarrow{Q}_i^n \right) \Omega_i^{n-1} + \varphi_{n-2} \left(\overrightarrow{Q}_i^{n-2} - \overrightarrow{Q}_i^n \right) \Omega_i^{n-2} + \ldots \right] \\ + \left(\frac{\varphi_{n+1}}{\Delta t} \left(\Omega^{n+1} \overline{\Gamma}_e^{*,k} \right)_i + \frac{\partial \overrightarrow{R}_i^{*,k}}{\partial \overrightarrow{\mathbf{Q}}^{*,k}} \right) \Delta \overrightarrow{\mathbf{Q}}^{*,k} \end{aligned} \tag{3.68}$$

Finally, by replacing the resulting Taylor expansion to the pseudo–steady Eq. (3.48), the final form of the discretized problem is obtained, for the computational cell i,

$$\underbrace{\left[\frac{1}{\Delta \tau_i} \left(\overline{\Gamma}^{*,k} \Omega^{n+1} \right)_i + \frac{\varphi_{n+1}}{\Delta t} \left(\overline{\Gamma}_e^{*,k} \Omega^{n+1} \right)_i + \frac{\partial \overrightarrow{R}_i^{*,k}}{\partial \overrightarrow{\mathbf{Q}}^{*,k}} \right]}_{Implicit\ Operator} \Delta \overrightarrow{\mathbf{Q}}_i^{*,k} = -\overrightarrow{R}_i^{*,k} - \overrightarrow{S}_{dual,i}^{*,k} \tag{3.69}$$

where the vector $\overrightarrow{S}_{dual}^{*,k}$ is a source resulted from the temporal discretization process and contains the values from the previous real timesteps. The terms inside the brackets constitute the Implicit Operator of the numerical problem.

Construction of the Jacobian

The implicit operator of the Equation (3.69) requires the evaluation of the jacobian matrix $\partial\vec{R}/\partial\vec{Q}$, which expresses the change in the spatial residual to a variation of the flow quantities. According to Equation (3.8), the spatial residual consists of the inviscid fluxes, the viscous fluxes and the source terms. The expressions for the first matrices is given in the following paragraphs. The jacobian of the source terms varies depending of the problem and the source terms considered.

Inviscid Part:

The inviscid fluxes are evaluated on every face f of cell i, according to Equation (3.11). The contribution of the inviscid fluxes in the jacobian for every left cell is

$$\frac{\partial \overrightarrow{F}_{cg,f}}{\partial \overrightarrow{Q}_R} = \frac{1}{2}\left[A_{cg}\left(\overrightarrow{Q}_R\right) + \overline{\Gamma\left|\widetilde{A}_{RL}\right|}\right] \tag{3.70}$$

while for every right cell

$$\frac{\partial \overrightarrow{F}_{c,j}}{\partial \overrightarrow{Q}_L} = \frac{1}{2}\left[A_{cg}\left(\overrightarrow{Q}_L\right) - \overline{\Gamma\left|\widetilde{A}_{RL}\right|}\right] \tag{3.71}$$

Viscous Part:

For the viscous contribution, by neglecting the averaged quantities in the directional derivatives, a unique expression for each face f, for both left and right cells, is obtained

$$\frac{\partial \overrightarrow{F}_{v,f}}{\partial \overrightarrow{Q}_i} = A_v \tag{3.72}$$

where the viscous jacobian is computed by

$$A_v = \begin{bmatrix} 0 & 0 & 0 & 0 & 0 \\ 0 & \dfrac{\lambda_v}{d_{ij}} & 0 & 0 & 0 \\ 0 & 0 & \dfrac{\lambda_v}{d_{ij}} & 0 & 0 \\ 0 & 0 & 0 & \dfrac{\lambda_v}{d_{ij}} & 0 \\ 0 & 0 & 0 & 0 & 0 \end{bmatrix} \tag{3.73}$$

with distance d_{ij} and viscous spectral radii defined as

$$d_{ij} = \sqrt{(\vec{x}_i - \vec{x_j})^2}, \quad \lambda_v = 2\frac{\mu_\lambda + \mu_t}{\rho} \tag{3.74}$$

System Solution

Expressing Equation (3.69) for each computational cell a linear system of vector equations is formed, with dimensions $\mathcal{N} \times \mathcal{N}$, which can be written simply as

$$\mathbf{A}\vec{\mathbf{x}} = \vec{\mathbf{b}} \tag{3.75}$$

Matrix $\mathbf{A}$ is a sparse matrix, thus only the elements needed for the solution of the system are stored. The system is solved using a Gauss–Seidel iterative method, supplemented with a Reverse Cuthill–Mckee reordering scheme [116].

Alternative methods have been also explored for the solution of the linear system of equations. *MaPFlow* incorporates the PETSc library [117], which offers a large variety of iterative solvers for sparse and dense linear systems. In steady state problems, it was found that other methods

offered by the PETSc library were able to accelerate convergence and larger values of $\Delta\tau$ and β were permitted. However for unsteady simulations, the built–in implementation of the Gauss–Seidel is preferred. This implementation had proven to be more effective computationally–wise, in a multi–processing environment.

3.7 Discretization of the Turbulence Model

For the discretization of the turbulence equations a similar approach is followed as in the case of the main variables. A spatial residual similar to Equation (3.8) is formulated. The convective fluxes are discretized using a first order upwind scheme

$$\rho V_n = \max\left(\rho V_{nL}, 0\right) + \min\left(\rho V_{nR}, 0\right) \tag{3.76}$$

in which the left (L) and right (R) states are computed based on the cell center values of the adjacent cells.

The diffusion terms on a face is calculated as an arithmetic mean of the values at the center of the adjacent cells. The viscous gradients are computed similarly to the gradients of flow variables, according to Equation (3.39).

For the calculation of the closest distance to the wall y, which appears in the blending function (2.44), the kD–tree algorithm of [118] is used.

For the temporal discretization, a backwards difference scheme is used analogous to Equation (3.50) and again the dual time stepping technique is employed. A $2N \times 2N$ system of equations is formed, with N being the total number of cells in the mesh. For a more detailed description of the discretization process of the k–Ω SST model in MaPFlow, the reader can be referred to [75].

3.8 Numerical Wave Generation & Absorption

Two main challenges that a free surface numerical method should face is the generation of desired wave profiles and the effective damping of outgoing waves close to the boundary. Starting from the wave generation inside a computational tank, given specific characteristics of a wave (such as wave height, wave period and water depth), an appropriate wake making procedure should be adopted to create the corresponding wave profile. The wave making process should be precise since any induced generated disturbances could spread throughout the computational domain.

In literature, the wave generation methods are divided into two wide categories. On the one hand, there are the physical wave makers, where waves are generated similar to a wave flume by employing deforming meshes. On the other hand, there are the numerical methods, where the physical variables are manipulated in a specific part of the domain to generate the corresponding wave profile.

Physical wave makers, mimic the flap or piston motion of solid boundary, just like the case of real wave maker, a solid boundary moves according to a specified law [88]. In a computational context, this can be achieved using either deforming or overset meshes. Although this process seems more natural and more consistent to the laboratory tests, it is rather computational expensive for practical implementations.

Usually, a numerical approach is preferred. Various methods have been proposed [119] on how a wave can be introduced in a numerical wave tank. A first approach to generate progressive waves is by adopting an internal wave making method. In this context, source terms are added either in the mass [120, 121] or momentum equations [122]. The source terms are specified only in the rectangular region beneath the mean water level. The generated waves are propagated in all directions. This is an efficient method that is able to generate linear and non–linear waves. However, since the generated waves are propagating in all directions, an extended domain is

needed and all boundaries should be equipped with damping zones. All these come to increase the computational cost.

Another more simplistic approach is to impose the wave characteristics directly through the boundary conditions. According to a wave theory, the free surface position (VoF function) and the velocities under the crest are specified as Dirichlet boundary conditions [48]. This method has the advantage of the simple implementation and reduces mesh size, since no additional zones should specified for the wave generation.

Perhaps, one of the most widely used approach for the generation of free surface waves is the relaxation zone method. This process can either be explicit [123] or implicit [124]. In both cases, a zone is specified near the boundary, where the wave field is specified according to an analytical solution. In the explicit case, the wave solution is specified exactly inside the zone and an exponential blending function is used for the smooth transition between the boundary and the CFD solution. The implicit relaxation zones use source terms to drive the solution inside the specified zone to the desired wave solution. Again, a similar exponential function is used minimize the effect of the computational solution away from the boundary. Both variants are very efficient for wave generation. Although a larger domain is needed compared to the previous approximation, this approach is more robust and guarantees the effective generation of waves, regardless their characteristics. Regarding the differences between the two, on the one hand explicit relaxation zones enforce the desired solution directly inside the specified zone. On the other hand, the implicit counterpart drives the flowfield to the desired wave profile as part of the computational solution. Thus the latter case, is considered to be more natural for a numerical solver. In this work, the implicit relaxation zones are used for the wave generation.

In a specified part of the computational domain near the boundary, which typically extends for a few wavelengths, the numerical solution is forced to follow a wave solution provided by a wave theory. This is achieved by introducing source terms in the momentum equations. The source terms, aim to drive the numerical velocity field to the one given by the wave theory. The general form of the source terms is presenting in Equation (3.77). The source term of Equation (3.78) is a function of the non–dimensional space variable x_r, which depends on the starting position x_s of the specified zone and the end point of the zone x_e. The wave generation is performed by imposing the velocity $\vec{v}_{tar}$ as given by an appropriate wave theory.

$$\vec{S}_{nwt} = C_{nwt}\rho_m \left(\vec{v}_{tar} - \vec{v}\right) \tag{3.77}$$

The effect of the source terms is regulated through the C_{nwt} function, its form is given in Equation (3.78), while in Figure 3.8 its form is plotted for different values of α and n. The maximum value of the function is regulated through parameter α, while its spatial distribution through n parameter.

$$C_{nwt} = \alpha \frac{\exp\left(x_r^n\right) - 1}{\exp\left(1\right) - 1}\,, \quad x_r = \frac{x_s - x}{x_s - x_e} \tag{3.78}$$

The function is zero away from the boundaries of the computational domain, scales exponentially inside the specified zone and it reaches its maximum value α at the boundary. The source term (3.78), should be dominant enough to drive the solution to the desired one, while at the same time to be able to maintain the convergence properties of the method. Large values of C_{nwt} may lead to numerical instabilities, while small values of α may not be able to drive properly the solution. Typical values for the exponent n is between 2 and 5 and usually α is not greater than 200. In the section of the two–dimensional results, it will be shown that there is an acceptable range of values for the coefficient C_{nwt} where no numerical instabilities appear. Furthermore, guidelines about the values of the exponential functions are given also in [125].

Apart from the wave generation, in a numerical wave tank an appropriate strategy should be adopted to absorb any reflections before reaching the boundary. The boundary conditions applied in the inlet and outlet boundary, assume a uniform field and thus any physical disturbance

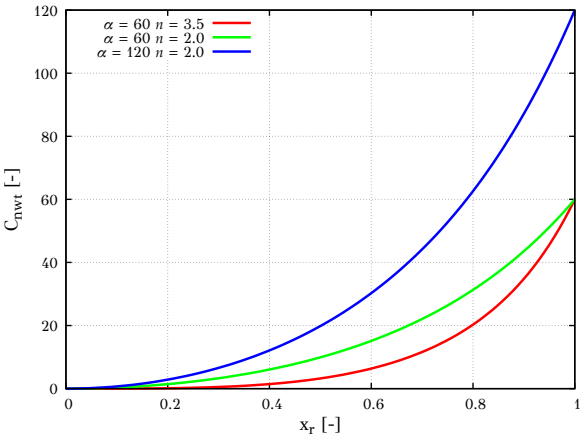

Figure 3.8: The effect of the values α and n in function C_{nwt}.

created inside the domain is not easily radiated outside of the domain. Mesh coarsening can help reduce the amplitude of the fluctuations, nevertheless, for the decay of free surface waves a extensive domain would be needed. In most cases, the boundaries are supplied with sponge layers or absorption zones, where the farfield conditions are imposed [124, 126]. The farfield boundary values can be similarly imposed using the implicit relaxation zones as in the case of wave generation. In this case, the target of the source term is to minimize the vertical velocity components. In a two–dimensional context, where the wave propagation is along the x–axis, the velocity vector $\vec{v}_{tar}$ takes the following form $\vec{v}_{damp} = (u, v_{inf})$, where u is the x–component of the velocity inside the computational domain and v_{inf} the y–component of the freestream velocity. The damping is applied only to the vertical component of the velocity field. If velocity u was also set to the farfield values, there would not be any mass flow exiting the domain. The latter case would resemble the presence of a vertical wall at the boundary.

3.9 Coupling Algorithm for Fluid–Structure Interaction problems

Fluid Structure Interaction (FSI) problems combine two different physical aspects. In the framework presented here, on the one hand, flow phenomena are examined by solving the Navier–Stokes equations. On the other hand, the response of the rigid structure under the flow excitation, is considered using force and moment balance laws. The theoretical and computational aspects of both problems has been extensively presented up to this point. In the next paragraphs the coupling process of the two is described.

The FSI process can be split into two main stages. Firstly, there is the flow solver which is responsible for computing the hydrodynamic excitation field (forces and moments) and secondly the rigid body dynamics (RBD) solver, which computes the new position of the body. Those two are combined into an iterative procedure, performed in every computational step until an appropriate convergence criterion is met. The new position of the body is communicated to the flow solver by applying a mesh deformation algorithm.

The iterative procedure, followed in each real timestep, can be broken into the following steps

1. Given a flow solution, the forces and the moments that act on body are computed
2. The 6 DoF problem is solved by the RBD solver. The new position and orientation of the body is computed
3. A mesh deformation algorithm is employed to account for the body motion
4. The new flow characteristics are computed by the flow solver

5. Check if convergence criterion is met, if not return to Step 1

The hydrodynamic forces computed in Step 1 of the FSI algorithm, are computed as

$$\overrightarrow{F}_B = \int_{\partial B} p\vec{n}\mathrm{d}S + \int_{\partial B} \mu_m \left(\nabla\vec{v} + \nabla\vec{v}^T\right)\cdot\vec{n}\mathrm{d}S \tag{3.79}$$

while the moments that act on the body with respect to its center of gravity are computed as

$$\overrightarrow{M}_B = \int_{\partial B} p\vec{n}\times\vec{r}\mathrm{d}S + \int_{\partial B} \mu_m \left(\nabla\vec{v} + \nabla\vec{v}^T\right)\cdot\vec{n}\times\vec{r}\mathrm{d}S \tag{3.80}$$

In the preceding equations, p is the pressure of the fluid, μ_m the viscosity of the mixture, $\vec{v}$ the velocity of the fluid, $\vec{n}$ the unit normal vector on the surface of the rigid body, $\vec{r}$ the position vector with its origin being the center of gravity of the body and ∂B the body boundary.

The above algorithm is terminated once a convergence criterion is met. Typically, the maximum difference between the previous and new values of the 6 DoFs are is compared against a user–defined threshold, meaning that if $\vec{x}$ is the vector containing the thee translation and the three rotation of the body, then the convergence criterion specified is

$$\max\left(|x_i^{l+1} - x_i^l|\right) \leq eps \quad i = 1,\ldots,6 \tag{3.81}$$

where l is the index of the FSI iteration. Typical values of eps are below 10^{-6}.

The previous iterative process imply a strong coupling between the two solver. This means, that at the end of the process, the characteristics of the flow match the final position of the body up to a convergence criterion.

Furthermore, in order to provide a better understanding of the FSI algorithm a logical chart of the process is given in Figure 3.9, which describes every step of strong coupling of the solvers.

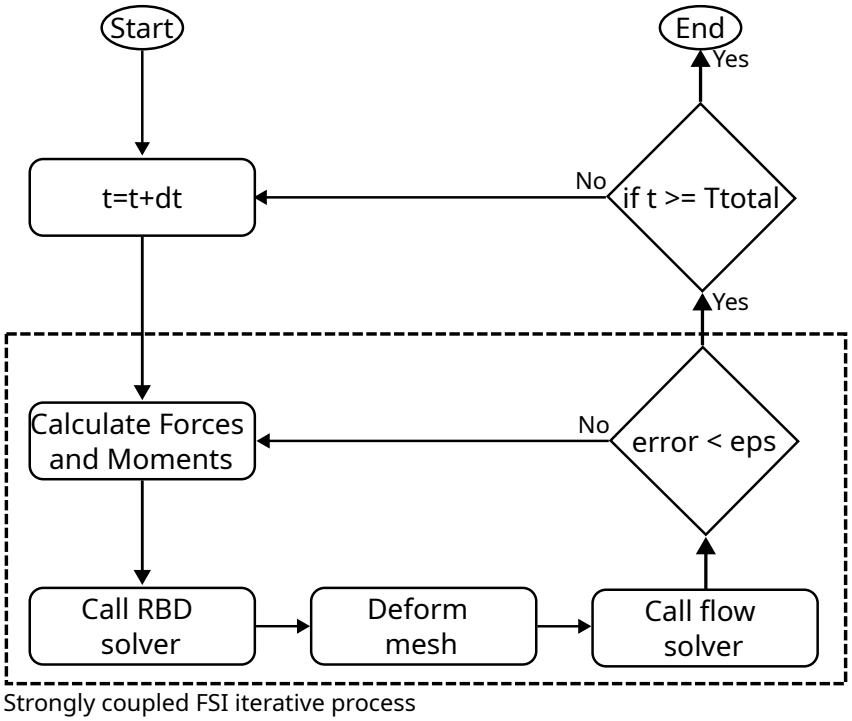

Figure 3.9: Flow chart of the Fluid–Structure Interaction algorithm. For each real time step, internal iterations between the dynamics and the flow solver are performed to ensure a strong coupling between the two

3.10 Deforming Grids

The motion of the rigid body inside the computational domain is communicated to the flow solver by moving the mesh nodes on the solid boundary. In the present thesis, the deforming mesh approach is used in order to the motion of the rigid body.

Generally, various methods have been proposed in literature that try to offer the advantages of an efficient grid deformation along with high quality characteristics of the final mesh. However, none of the methods presented so far have optimal characteristics that can be applied universally in all cases. In [127] an overview of the most well–known methods is presented and the pros and cons of each method are summarized.

In the present work, two methods have been chosen with complementary characteristics. The first is a simple method that applies an exponential damping to decay the deformation away from solid boundaries, while the second treats deformation as an interpolation problem with radial basis functions. The first is a simple and fast method, easily implemented, but it is able to account for simple and relative smooth geometries. The second method is more general, it is able to produce good quality meshes even in large deformation, regardless the shape of the geometry, but it is more complicated and major difficulties arise in cases of large meshes (more than 1 million cells).

The next two paragraphs describe briefly the deforming methods used in the Fluid–Structure Interaction problems that will later be discussed.

3.10.1 Exponential Damping

The first method used has been originally proposed by Zhao *et al.* [128]. An internal node, based on its distance from its closest wall node, experiences a displacement $d\vec{r}\,(node)$ according to an exponential damping function $f\,(node)$. If $d\vec{r}\,(node_{wall})$ is the displacement of wall node, then the displacement of every internal node is computed based on the following expression,

$$d\vec{r}\,(node) = f\,(node)\, d\vec{r}\,(node_{wall}) \tag{3.82}$$

where the damping function $f(x)$ is defined as,

$$f\,(x) = \frac{ly^2\,(x)}{lx^2\,(x) + ly^2\,(x))} \tag{3.83}$$

and the exponential functions $lx\,(x)$ and $ly\,(x)$ are given by

$$\begin{aligned} lx\,(x) &= \frac{1 - \exp\left(-d(x)/d_{max}\right)}{(e-1)/e} \\ ly\,(x) &= \frac{1 - \exp\left(1 - d(x)/d_{max}\right)}{(e-1)/e} \end{aligned} \tag{3.84}$$

$d\,(x)$ is the distance of the node to the nearest solid node and d_{max} is a maximum distance outside of which mesh nodes are not affected by the deformation.

3.10.2 Radial Basis Functions

The second deformation method is based on the Radial Basis Function (RBF) approach [129]. This method defines around every wall node an area of influence in which the motion of the internal mesh nodes is dictated according to a weighting factor. This approach regards the mesh deformation as an interpolation problem. The deformation algorithm has been further extended by Rendall and Allen [130] and their work will be presented here briefly. The displacement s of an in internal mesh node is described by an interpolation function that uses a sum of basis

functions ϕ, supplemented with a polynomial function $p(x)$ to recover the rotation of the mesh. The basis function are defined on every wall node s_i.

The interpolation function is given by,

$$s(\vec{x}) = \sum_{i=1}^{N} \alpha_i \phi\left(||\vec{x} - \vec{x}_{s_i}||\right) + p(\vec{x}) \tag{3.85}$$

where $s(\vec{x})$ is the interpolation function of an internal node $\vec{x}$, α_i the interpolation weights, ϕ the RBF function which depends on the normed distance between the internal node $\vec{x}$ and the wall nodes $\vec{x}_{s_i}$. Typically, Wendland functions C^0 and C^2 [131] are used as basis functions for the interpolation process. A first order polynomial $p(x)$ [132] is selected of the following form

$$\begin{aligned} p^x(\vec{x}) &= \gamma_o^x + \gamma_x^x x + \gamma_y^x y + \gamma_z^x z \\ p^y(\vec{x}) &= \gamma_o^y + \gamma_x^y x + \gamma_y^y y + \gamma_z^y z \\ p^z(\vec{x}) &= \gamma_o^z + \gamma_x^z x + \gamma_y^z y + \gamma_z^z z \end{aligned} \tag{3.86}$$

Equation (3.85) should hold exactly for the displacement of the wall nodes. Thus, the first condition that the interpolation scheme should satisfy is

$$s(\vec{x}_{s_i}) = \vec{X}_{s_i} \tag{3.87}$$

Secondly, when the polynomial term that accounts for the rotation is used a complementary condition is introduced

$$\sum_{i=1}^{N} \alpha_i q(x) = 0 \tag{3.88}$$

where $q(x)$ is a polynomial with degree lesser or equal to $p(x)$.

The previous two requirements can be combined into a single linear system of equations, one in each direction, that can be solved to acquire the weights α_i of the basis functions and the coefficients $\gamma_i^{x/y/z}$ of the polynomial. As a result, the following expressions are obtained

$$\begin{aligned} \vec{X}_s &= \overline{C}_{ss}\vec{\alpha}_x \\ \vec{Y}_s &= \overline{C}_{ss}\vec{\alpha}_y \\ \vec{Z}_s &= \overline{C}_{ss}\vec{\alpha}_z \end{aligned} \tag{3.89}$$

where vectors $\vec{X}_s$ and $\vec{\alpha}_x$, and similarly in the y and z, can be written as

$$\vec{X}_{s_i} = \begin{bmatrix} 0 \\ 0 \\ 0 \\ 0 \\ \vec{x}_{s_i} \end{bmatrix}, \quad \vec{x}_{s_i} = \begin{bmatrix} x_{s_1} \\ x_{s_2} \\ \vdots \\ x_{s_N} \end{bmatrix}, \quad \vec{\alpha}_x = \begin{bmatrix} \gamma_0^x \\ \gamma_x^x \\ \gamma_y^x \\ \gamma_z^z \\ \alpha_{s_1}^x \\ \alpha_{s_2} \\ \vdots \\ \alpha_{s_N} \end{bmatrix} \tag{3.90}$$

and the matrix $\overline{C}_{ss}$ is block matrix defined as

$$\overline{C}_{ss} = \left[\begin{array}{cccc|cccc} 0 & 0 & 0 & 0 & 1 & 1 & \cdots & 1 \\ 0 & 0 & 0 & 0 & x_{s_1} & x_{s_2} & \cdots & x_{s_N} \\ 0 & 0 & 0 & 0 & y_{s_1} & y_{s_2} & \cdots & y_{s_N} \\ 0 & 0 & 0 & 0 & z_{s_1} & z_{s_2} & \cdots & z_{s_N} \\ \hline 1 & x_{s_1} & y_{s_1} & z_{s_1} & \phi_{s_1 s_1} & \phi_{s_1 s_2} & \cdots & \phi_{s_1 s_N} \\ 1 & x_{s_2} & y_{s_2} & z_{s_2} & \phi_{s_2 s_1} & \phi_{s_2 s_2} & \cdots & \phi_{s_2 s_N} \\ \vdots & \vdots & \vdots & \vdots & \vdots & \vdots & \ddots & \vdots \\ 1 & x_{s_N} & y_{s_N} & z_{s_N} & \phi_{s_N s_1} & \phi_{s_N s_2} & \cdots & \phi_{s_N s_N} \end{array}\right] = \left[\begin{array}{c|c} 0 & \overline{P} \\ \hline \overline{P}^T & \overline{M} \end{array}\right] \tag{3.91}$$

with $\phi_{s_i s_j} = \phi\left(||\vec{x}_{s_i} - \vec{x}_{s_j}||\right)$ being the basis function defined in wall node s_j and evaluated in wall node s_i. The sub–matrices $\overline{P}$ and $\overline{P}^T$ of $\overline{C}_{ss}$ constitute the polynomial part of the interpolation and matrix M makes up for the RBF part.

For the calculation of the displacement of the internal nodes, the vector equations (3.89) should be solved for vectors $\vec{\alpha}_{x/y/z}$. Rather than computing the inverse matrix $\overline{C}_{ss}^{-1}$, a more efficient method can be followed [130] that takes advantage of the block form of $\overline{C}_{ss}$.

Returning to Equation (3.85). The matrix form for the displacement calculations of the internal points is

$$\begin{aligned} \vec{x}_a &= \overline{A}_{as}\vec{\alpha}_x \\ \vec{y}_a &= \overline{A}_{as}\vec{\alpha}_y \\ \vec{z}_a &= \overline{A}_{as}\vec{\alpha}_z \end{aligned} \tag{3.92}$$

in which $\vec{x}_a, \vec{y}_a, \vec{z}_a$ are the new position of the internal nodes, vectors $\vec{\alpha}_{x/y/z}$ include the weights of the RBF interpolation and the polynomial coefficients (see Eq. (3.90)), and matrix $\overline{A}_{as}$ is given by

$$\overline{A}_{as} = \begin{bmatrix} 1 & x_{\alpha_1} & y_{\alpha_1} & z_{\alpha_1} & \phi_{\alpha_1 s_1} & \phi_{\alpha_1 s_2} & \cdots & \phi_{\alpha_1 s_N} \\ 1 & x_{\alpha_2} & y_{\alpha_2} & z_{\alpha_2} & \phi_{\alpha_2 s_1} & \phi_{\alpha_2 s_2} & \cdots & \phi_{\alpha_2 s_N} \\ \vdots & \vdots & \vdots & \vdots & \vdots & \vdots & \ddots & \vdots \\ 1 & x_{\alpha_N} & y_{\alpha_N} & z_{\alpha_N} & \phi_{\alpha_N s_1} & \phi_{\alpha_N s_2} & \cdots & \phi_{\alpha_N s_N} \end{bmatrix} \tag{3.93}$$

Matrices $\overline{A}_{as}$ and $\overline{C}_{ss}$ can be combined by using Equation (3.90) into the following relation, for the x–direction

$$\vec{x}_a = \overline{A}_{as}\vec{a}_x \Rightarrow \vec{x}_a = \overline{A}_{as}\overline{C}_{ss}^{-1}\vec{X}_s \Rightarrow \vec{x}_a = \overline{H}\vec{X}_s \tag{3.94}$$

and similarly in the y– and z–direction. Thus the displacement of each internal node is given by

$$\begin{bmatrix} \vec{x}_\alpha \\ \vec{y}_\alpha \\ \vec{z}_\alpha \end{bmatrix} = \begin{bmatrix} \overline{H} & 0 & 0 \\ 0 & \overline{H} & 0 \\ 0 & 0 & \overline{H} \end{bmatrix} \begin{bmatrix} \vec{X}_s \\ \vec{Y}_s \\ \vec{Z}_s \end{bmatrix} \tag{3.95}$$

In order to calculate matrix $\overline{H}$, the inverse of matrix $\overline{C}_{ss}$ should be found. By taking advantage of its block form and splitting vectors $\vec{\alpha}_{x/y/z}$ in the polynomial part (labeled as *poly*) and in the RBF part, Equation (3.90) can be solved as

$$\begin{aligned} \vec{\alpha}_x^{poly} &= \overline{M}_P\overline{PM}^{-1}\vec{X}_s \\ \vec{\alpha}_x^{RBF} &= \left(\overline{M}^{-1} - \overline{M}^{-1}\overline{P}^T\overline{M}_P\overline{PM}^{-1}\right)\vec{X}_s \end{aligned} \tag{3.96}$$

where $\overline{M}_p$ is the Schur complement of $\overline{M}$, $\overline{M}_P = \left(\overline{PM}^{-1}\overline{P}_T\right)^{-1}$. Using the previous definitions matrix $\overline{H}$ can now be calculated as,

$$\overline{H} = \overline{A}_{as}\begin{bmatrix} \overline{M}_P\overline{PM}^{-1} \\ \overline{M}^{-1} - \overline{M}^{-1}\overline{P}^T\overline{M}_P\overline{PM}^{-1} \end{bmatrix} = \overline{A}_{as}\overline{C}_{ss}^{-1} \tag{3.97}$$

The previous process can be split into two steps. Firstly, the "solution" step is preceded, in which the computations of matrix $\overline{M}^{-1}$ and of the interpolation weights α_i take place, according to Equation (3.96). Afterwards, the "update" step follows, in which the displacement of the internal nodes is calculated by performing the matrix multiplication of Equation (3.95).

In a multi–processing environment each rank creates its own unique $\overline{H}$ matrix. This matrix has dimension of $M \times N$, where M is the number of points per rank and N the total nodes on the surface of the rigid body across all ranks. It is evident, that depending on the size of the computational grid, it may not be feasible to store the entire matrix in runtime. A workaround

for this is: each process stores $\overline{H}$ matrix in binary files and at each "compute" step accesses the file to perform the deformation of the mesh. However, even this approach is limited to relative small grids (no less than 1 million volume cells and only few thousand surface nodes). For larger grids, a surface reduction algorithm should be employed in order to reduce the dimension of the interpolation process. In the present thesis, a greedy algorithm based on the *unit function* approach, as described in [133], is adopted.

This page intentionally left blank

Chapter 4

Applications in Two–Dimensional Flows

This chapter presents a variety of two–phase flow results ranging from simple wave propagation to more complicated wave structure interaction problems. By taking advantage of the simplifications arising from the 2–dimensional (2D) approximation in terms of mesh, CPU time and flowfield characteristics, a series of parametric studies are conducted. Focus is given on the effect of the artificial compressibility factor β, wave generation and absorption and turbulence modeling in case of free surface flows. Recommendations and guidelines regarding their selection are provided.

The chapter is structured as follows; firstly, the propagation of two non–linear free surface waves in constant bathymetry is considered. Details about wave generation and absorption are discussed. Secondly, the interaction of free surface waves with a variable bathymetry is presented. The results are compared against available experimental data. Finally in the last test case, the interaction of free surface waves with a barge type floater is studied. The floater has a distinctive opening in the middle, typically called moonpool. The free surface inside this opening is able to oscillate under the wave excitation and regulate the motion of the floater. The excitation of the floater is considered for a range of wave frequencies. Furthermore in the present, section discussion is made upon the turbulence overproduction, caused by the shear stresses developed near the free surface.

4.1 Free Surface Waves in Constant Bathymetry

The validation of the numerical methodology begins by considering the propagation of two non–linear regular waves. For the classification of water wave theories, Le Méhauté [134] proposed the diagram presented here in Figure 4.1. The x–axis of the diagram represents the swallowness of the water, while the y–axis the non–linearity of the wave. The swallowness is expressed as the water depth d over the product between gravity g and wave period T squared, and the non–linearity as the wave height H over the same product.

For the test cases considered here, two water waves are chosen. The first is a swallow water wave that is classified as Cnoidal type wave and it is noted with a red dot in Figure 4.1, while the second case considers a 3^{rd} order Stokes wave and it is depicted with a yellow dot in the same figure.

4.1.1 Cnoidal Wave

As a starting point, the propagation of a Cnoidal wave at constant bathymetry is considered. The wave period is equal to $T = 5s$, the wave height is $H = 0.05m$, while the depth of the numerical wave tank is $d = 0.5$m. Using the Stream Function theory of Fenton [92],

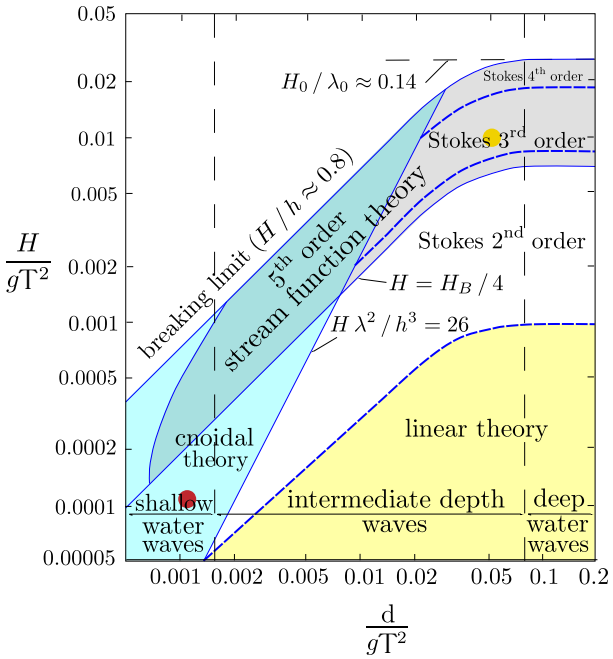

Figure 4.1: Le Mehaute diagram for the classification of water wave theories. The dots correspond to the waves studied in this section. The red dot corresponds to the Cnoidal type wave, while the yellow to the 3rd order Stokes wave. H is the wave height, g the gravity acceleration, TT the wave period and d the water depth

the wavelength is calculated as $\lambda = 11.08m$. In order to evaluate the influence of the various numerical parameters, the discussion is primarily focused on the free surface elevation inside the wave tank, as well as the elevation at various wave gauges. A schematic representation of the wave tank and the position of the wave gauges (or probes) is given in Figure 4.2.

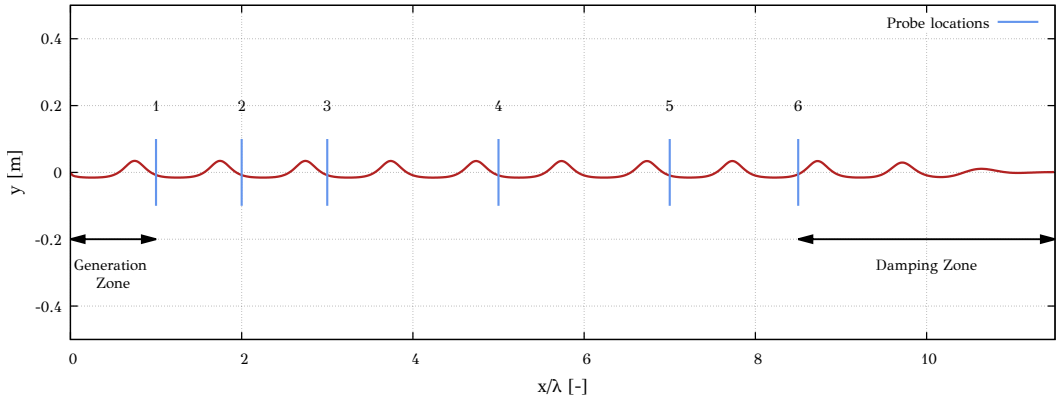

Figure 4.2: Schematic representation of the numerical setup used for wave propagation in constant bathymetry. The waves are generated at the left of the domain and damped at the right. Six probes are used to measure the wave elevation at different location inside the numerical wave tank

Wave Generation and Absorption

The influence of the generation parameters α, n, as defined in Equation (4.1) (see also Sec. 3.8) is investigated by conducting a parametric study. In Table 4.1 six test cases are defined. The same grid configuration is used in all cases. In the direction of the wave propagation, the mesh is uniform almost everywhere with 150 cells per wavelength, except for the damping

zone where the mesh coarsens based on a geometric rule. In the vertical direction, 20 cells per wave height are employed. Regarding the timestep discretization, a constant timestep is chosen corresponding to 800 timesteps per wave period ($dt = 0.0625$ s).

$$C_{nwt} = \alpha \frac{\exp\left(x_r^n\right) - 1}{\exp\left(1\right) - 1}\,, \quad x_r = \frac{x_s - x}{x_s - x_e} \tag{4.1}$$

Table 4.1: Parametric study of the influence of the source term values a and n in case of wave generation. Table presents the definition of the case studies

# Case	Forcing α	Exponent n
1	60	3.5
2	120	3.5
3	300	3.5
4	60	2
5	60	5
6	600	2

The surface elevation for all cases inside the generation zone is shown in Figure 4.3a and is compared with the analytical solution provided by the Stream Function Theory. It can be seen that the waveform is distorted for large values of α. Furthermore, it is noted that near the farfield boundary the numerical solution deviates from the analytical one. This is attributed to the approximation made at the boundary conditions. In case of a wave generation boundary, if the geometric center of the ghost cell is below the current free surface position, its state is defined based on the Stream Function solution, regardless if it is partially or totally filled with water. This approximation seems to cause a discrepancy near the boundary, which however is not propagated away, as it can be seen in the Figure 4.3. In all cases, the solution converges to the desired wave profile as depicted in Figure 4.3b, where the free surface elevation is plotted against time and is compared with the corresponding analytical form.

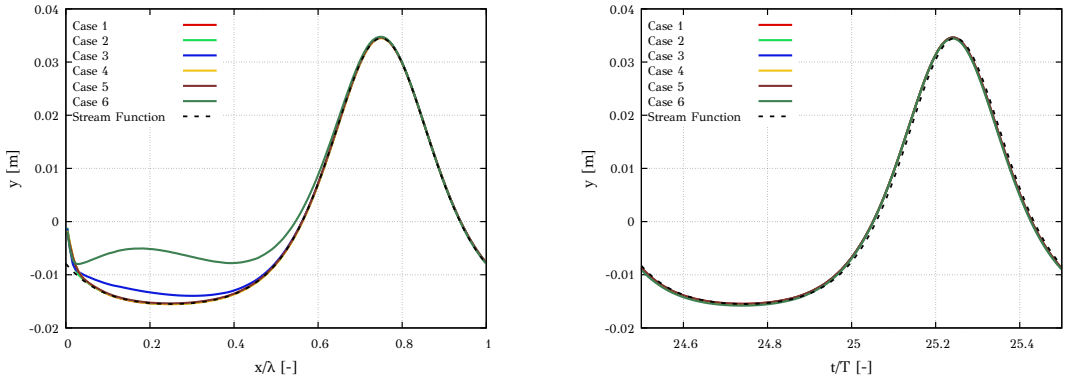

(a) Wave elevation inside the generation zone after 25 wave periods

(b) Wave elevation at a station at the end of the generation zone

Figure 4.3: Influence of parameters α and n in the generation of a wave. Wave characteristics: $T = 5$ s, $H = 0.05$ m, $d = 0.5$ m, $\lambda = 11.08$ m.

The Fast Fourier Transformation (FFT) can be exploited for more detailed comparison. Tables 4.2 and 4.3 present the error of the amplitude of the first four harmonics and the error of the phase angle in degrees between the analytical and numerical solution. Overall, the error of the amplitude at the dominant frequency is below 0.5% in all cases, while for large values of α, an amplification in higher frequencies is evident. The exponent n does not seem to have a significant influence on the results. In order to enhance the stability of the solver, the source term should not be exceedingly large. For this reason, large values of exponent n and small values of the parameter α are desired. On these grounds, an accurate representation of the wave

profile, while keeping the influence of the source terms small, is obtained by choosing $\alpha = 60$ and $n = 3.5$.

Table 4.2: Parametric study of the influence of the source term values a and n in case of wave generation. Table presents the relative error of the amplitude of the first four harmonics compared to the analytical solution

# Case	Harmonics			
	1st	**2nd**	**3rd**	**4th**
1	0.40	0.45	0.88	0.87
2	0.40	0.42	0.77	0.91
3	0.37	0.39	0.63	1.08
4	0.44	0.38	0.69	1.29
5	0.40	0.49	1.10	0.87
6	0.42	0.37	0.31	1.72

Table 4.3: Parametric study of the influence of the source term values a and n in case of wave generation. Table presents the relative error of the phase angle of the first four harmonics compared to the analytical solution

# Case	Harmonics			
	1st	**2nd**	**3rd**	**4th**
1	0.12	0.06	0.78	1.60
2	0.20	0.09	0.58	1.41
3	0.30	0.27	0.33	1.15
4	0.31	0.33	0.21	1.04
5	0.03	0.32	1.11	1.90
6	0.42	0.71	0.32	0.35

Following the wave generation test case, the damping performance of the solver is evaluated. A parametric study is conducted by varying the values of the parameters α, n and the length of the damping zone L_D. The case studies are defined in Table 4.4. The star in the last two cases indicates that a coarser mesh is used in the damping zone. In Figure 4.4a, the surface elevation inside the damping zone is shown for the six test cases, while in Figure 4.4b the free surface elevation during a wave period at the beginning of the damping zone is presented. As illustrated in Figure 4.4c, the elevation of the free surface near the outlet boundary is completely damped in Case 4, contrary to Cases 1 and 3. It is also worth noticing that for the same parameters α, n (Cases 2 and 5) the grid coarsening does not affect the damping of the wave. However, all cases produce the same wave profile at the beginning of the damping zone.

Table 4.4: Parametric study of the influence of the source term values a and n in case of wave damping and the length L_D of the damping zone. Table presents the definition of the case studies

# Case	**Forcing α**	**Exponent n**	**Damping Length $[L_D]$**
1	60	3.5	3
2	120	3.5	3
3	120	3.5	1.5
4	120	3.5	6
5	120	3.5	3 *
6	250	3.5	3 *

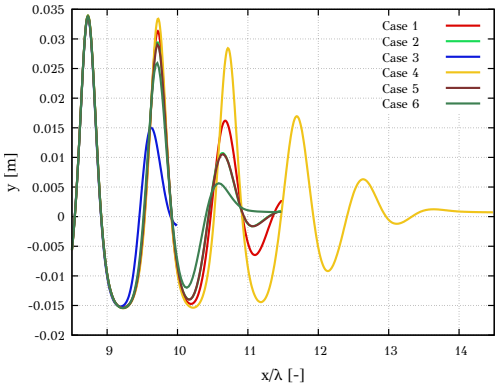

(a) Wave elevation inside the damping zone after 25 wave periods

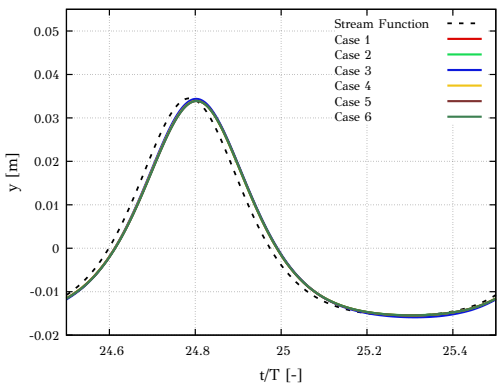

(b) Wave elevation at a station before the damping zone

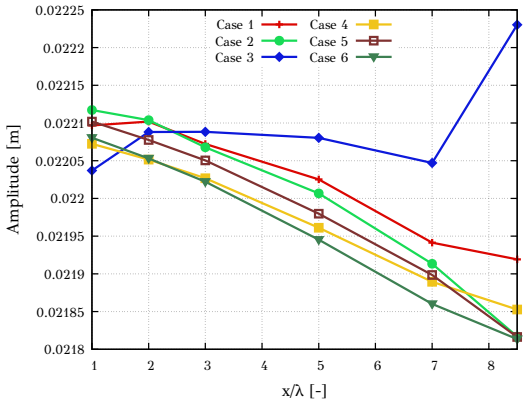

(c) Amplitude of the 1st harmonic of the wave at various grid locations

Figure 4.4: Influence of parameters α, n and of the damping length L_D in the generation of a wave. Wave characteristics: $T = 5$ s, $H = 0.05$ m, $d = 0.5$ m, $\lambda = 11.08$ m.

Furthermore, in order to examine in detail the effect of the damping zone in the wave flume, the amplitude of the 1st harmonic of the free surface elevation is plotted in Figure 4.4c at various stations across the computational domain. As expected, in all cases the amplitude decays due to numerical diffusion. However, in Case 3 an oscillatory behavior of the harmonics amplitudes is noticed. This is caused by reflections at the boundary of the domain. Also, in Case 1 the amplitude of the 1st harmonic is not monotonically decreasing in space. This can be attributed to reflections at the farfield boundary. In all other cases, the differences are regarded negligible. A damping zone extending six wavelengths is excessive for practical implementations while large values of α may cause numerical instabilities. For all these reasons mentioned above, for the rest of the work $\alpha = 120$ and $n = 3.5$ are chosen (Case 2) for wave generation.

In conclusion, the majority of the results showed that the generation and damping technique can produce accurate results. The differences noted for different values of α and n can be considered small. In case of wave generation, the numerical procedure was able to provide acceptable results in all cases. However, for large values of α (>300) numerical instabilities were noticed. Regarding wave damping, the method can absorb the outgoing waves, provided that the length of the zones is sufficient. Finally, the damping sensitivity study indicates that the damping performance is more sensitive to the chosen value of α. For this reason, a larger value of α, compared to wave generation, is chosen.

Grid and Timestep Independence

Once α and n have been decided, the next step is to perform a grid and a timestep sensitivity study. The grid parametrization is based on the number of cells per wavelength (λ/dx) and the number of cells per wave height near the free surface (H/dy_{FS}). Predictions from four grids are compared in Figure 4.5 with respect to free surface elevation in Figure 4.5a and the elevation at a specific station during a wave period in Figure 4.5b.

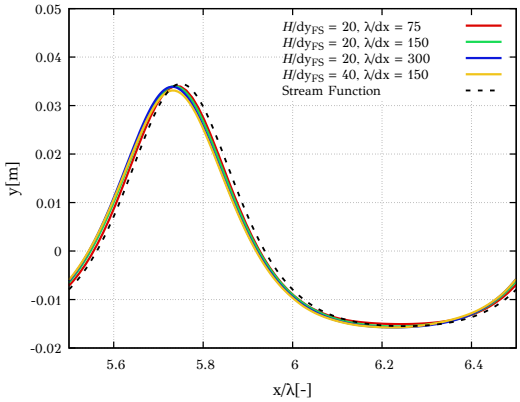

(a) Grid Independence Study: Wave elevation 5 wave lengths after the wave generation zone

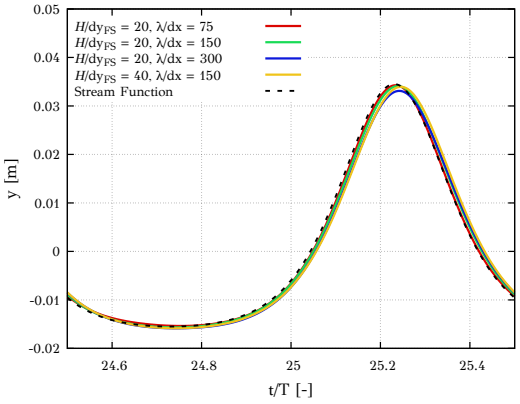

(b) Grid Independence Study: Wave elevation at a station 5 wave lengths after the wave generation zone. The snapshot is after 25 wave periods.

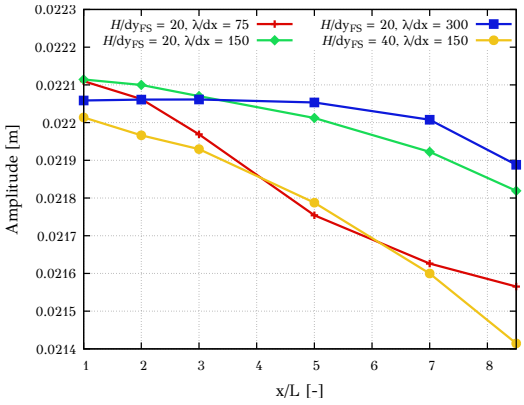

(c) Grid Independence Study: Amplitude of the 1st harmonic of the wave at various grid locations

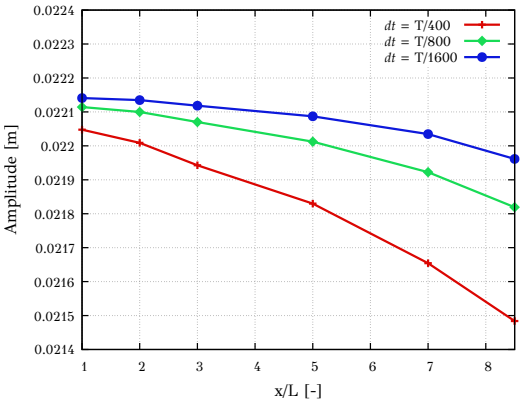

(d) Timestep Independence Study: Amplitude of the 1st harmonic of the wave at various grid locations

Figure 4.5: Grid and Timestep independence studies. Wave characteristics: $T = 5$ s, $H = 0.05$ m, $d = 0.5$, $\lambda = 11.08$ m.

In Figure 4.5c, the amplitude of the first harmonic of the propagating wave is depicted. The Figure shows that in case of the fine grid (blue line) the amplitude of the wave elevation remains almost constant across the domain. The coarse grid (red line) produces significant numerical diffusion and the amplitude of the waves is decreasing. The yellow line corresponds to a mesh with highly skewed cells near the free surface. It should be noticed that although the green line corresponds to a coarser grid, the numerical diffusion introduced is smaller. Due to very thin cells near the free surface, the CFL number is large and consequently the numerical diffusion introduced by the temporal discretization is significant [101]. The computational mesh with 150 cells per wavelength and 20 cells in the wave height (green line) exhibits similar characteristics with the finer grid (blue line) and consequently, it is kept for the rest of the simulations.

In Figure 4.5d, the amplitude of the first harmonic of the Cnoidal wave can be found. Three different timesteps are considered, based on the wave period. Predictions for 400, 800 and 1600 timesteps per period are shown. It is evident that, even when 400 timesteps per period

are chosen the relative error after 8 wavelengths is ≈ 2.5%. Predictions with 800 and 1600 timesteps per wave period are in very close agreement and thus the former timestep is selected.

Influence of the Artificial Compressibility β Parameter

The next case studies the impact of the artificial compressibility parameter β on wave propagation. In general, β regulates the coupling between pressure and density during convergence, i.e., β regulates the pseudo-sound speed (c). On the one hand, small values of β lead to small values of c thus the system is strongly coupled, on the other hand large values of β lead to a loose coupling of the equations. Because parameter β affects the convergence of the method, it is imperative to quantify how the choice of β affects the predictions.

Several recommendations for choosing β can be found in the literature, as was already covered in Section (2.1). For example, in one–phase incompressible flows, Turkel [53] proposed that β should scale with the square of the local velocity, and hence β varies across the domain. Special care should be taken near stagnation points where its value should be safeguarded. In case of wave propagation, the velocities under the crest are small and so β should not depend on the local characteristics of the flow. Nevertheless, the flows considered in his work did not involve gravity. Kunz et al. [61] applied the AC method in cavitation problems and suggested values of β ranging from 5 to $15 \cdot \vec{v}_\infty^2$. In order to understand the effect of β on the predictions, a parametric study is conducted using five different constant values of $\beta = 1$, 10, 50, 100 and 1000.

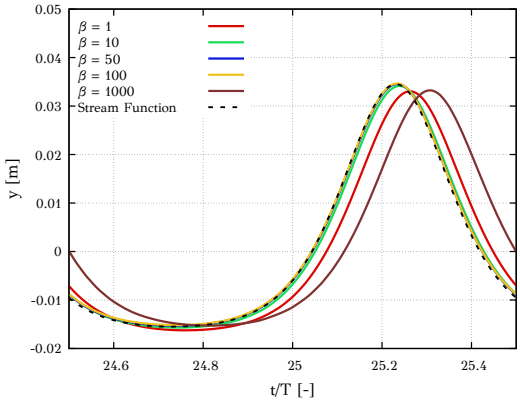

(a) Wave elevation 5 wave lengths after the wave generation zone. The snapshot is after 25 wave periods.

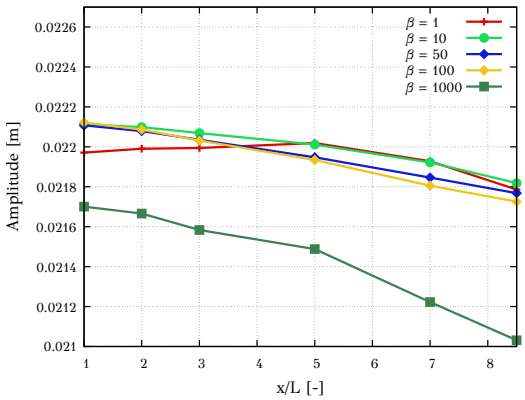

(b) Amplitude of the 1st harmonic of the wave at various grid locations

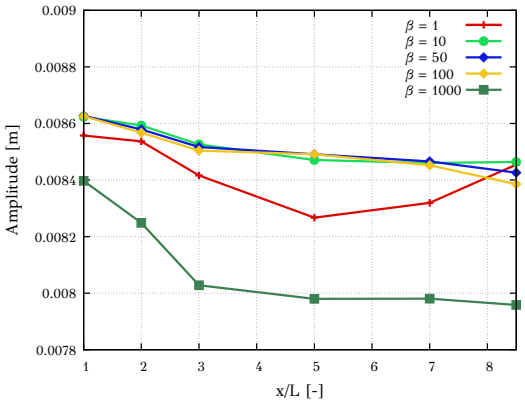

(c) Amplitude of the 2nd harmonic of the wave at various grid locations

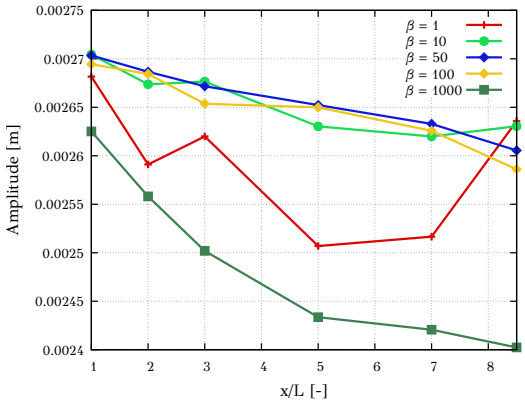

(d) Amplitude of the 3rd harmonic of the wave at various grid locations.

Figure 4.6: Influence of the AC parameter β: Wave characteristics: $T = 5$ s, $H = 0.05$ m, $d = 0.5$ m, $\lambda = 11.08$ m.

The numerical setup is based on the previous parametric studies. Specifically, the grid is uniform almost everywhere with 150 cells per wavelength and 20 cells in the wave height. The

timestep corresponds to 800 steps per wave period. For the wave generation, the numerical parameters are set to $\alpha_G = 60$ and $n_G = 3.5$, with length of the generation zone $L_G = \lambda$. The corresponding values for the wave damping are, $\alpha_D = 120$, $n_D = 3.5$ and $L_D = 3\lambda$.

The results are summarized in Figure 4.6a. Figure 4.6b shows the free surface elevation 5 wavelengths downstream of the generation zone. It is evident that, the predictions yield large differences for the two extreme values of β ($\beta = 1$ and $\beta = 1000$). However, for values ranging from 10 to 100 the predictions yield negligible differences. This is also exhibited in Figure 4.6b, where the amplitude of the first harmonic for the various β values is shown. For values $\beta = 1$ and $\beta = 1000$, elongation of the wavelength is observed. This is an artifact that implies undesired compressibility effects.

To further investigate the effect of β on the solution, the 2nd and 3rd harmonics are provided in Figure 4.6. It is apparent that, within the range $\beta = 10$ and $\beta = 100$ the solution is insensitive to the chosen value for both the 2nd (Figure 4.6c) and 3rd (Figure 4.6d) harmonic. Nonetheless, for $\beta = 1$ the differences are larger but still within an acceptable limit. For $\beta = 1000$ the solution is clearly affected.

From the preceding analysis it is evident that, for the present formulation, predictions are insensitive of value of β within an acceptable range. With these considerations and taking into account the guidelines of the literature, the value $\beta = 10$ is suggested for the AC parameter and used as reference for the rest of test cases.

The results of the preceding parametric studies are summarized in Table 4.5. Apart from the already discussed parameters the table presents the value of the CFL number used in pseudo–time (τ). The CFL number scales linearly from 1 to 50 in 50 iterations and in all cases is the same.

Table 4.5: Results of the parametric studies for the Cnoidal type wave in constant bathymetry. Index G denotes generation parameter, while D damping parameter

Approx.	Mesh	dt	β	CFL_τ	L_G	α_G	n_G	L_D	α_D	n_D
Inviscid	112973	T/800	10	50	λ	3.5	60	3λ	3.5	120

As a last remark, two figures are given for the comparison of the numerical solution with the analytical one. Firstly, the free surface elevation at the entire numerical wave tank is presented in Figure 4.7 and compared against the expected free surface elevation. In the figure, the generation zone of one wavelength is noted in blue color and the damping zone of the three wavelengths in gray color. The comparison between the two is fair, numerical results follow the theoretical approximation. Minor differences in the wave height are noted at the two last wavelengths. As it has already been discussed, CFD approximation introduces inherently numerical diffusion, especially near the free surface, where the density discontinuity is present. This leads to deviations between the numerical and the analytical solution, and they are depicted in Figure 4.7 as minor changes in the wave height and length. Furthermore, in Figure 4.8 the pressure field below the free surface and the corresponding velocity vectors are plotted for the exact solution (Fig. 4.8b) and for the numerical solution (Fig. 4.8a) 5 wavelengths downstream of the generation zone. No major differences are noted between the two. The numerical solution is well compared against the exact solution. The numerical diffusion can also be seen here as a smearing of the pressure field near the seabed and of the velocity field at the crest of the wave.

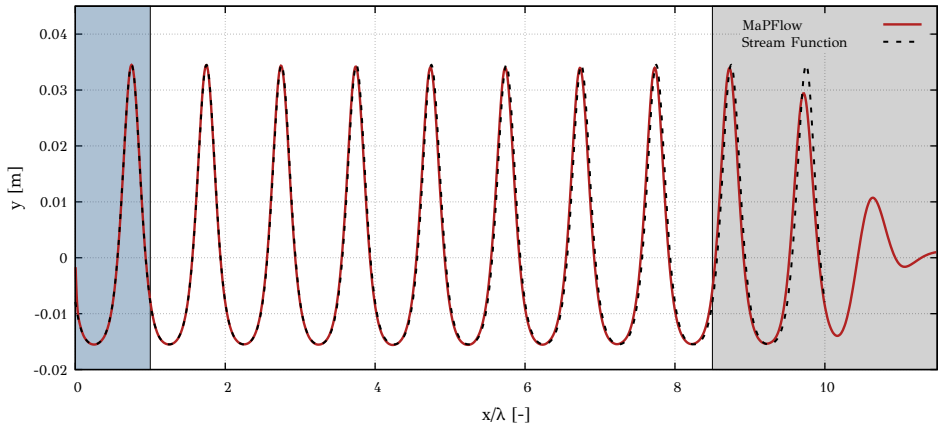

Figure 4.7: Free surface elevation for a Cnoidal type wave. Comparison between theoretical and numerical results. Wave characteristics: $T = 5s$, $H = 0.05m$, $d = 0.5m$, $\lambda = 1.57m$.

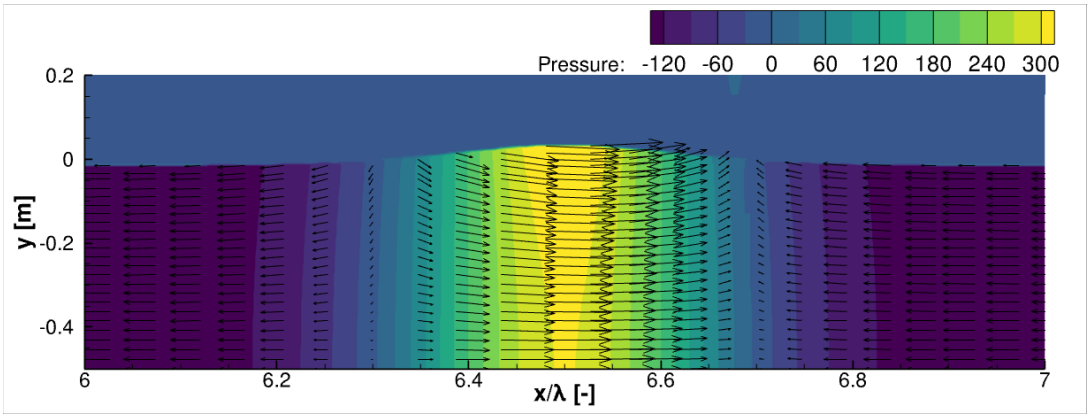

(a) Analytical solution

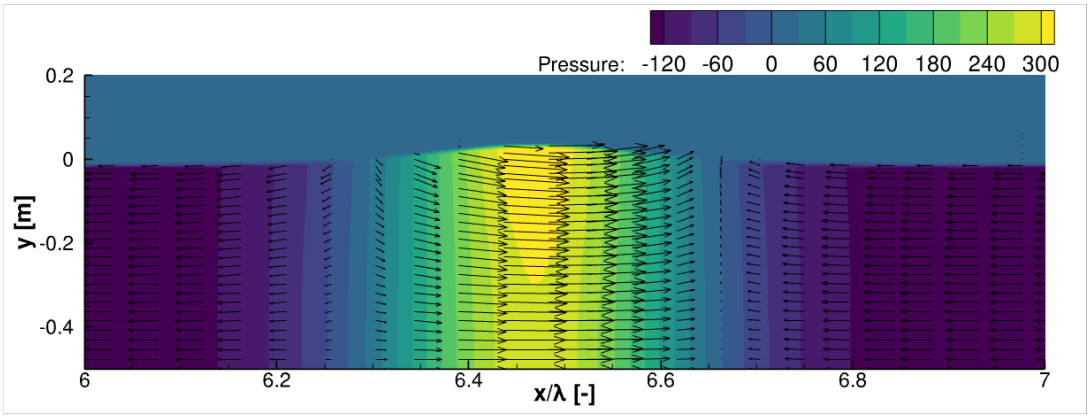

(b) CFD solution

Figure 4.8: Pressure contours and velocity vectors over one wave length for a Cnoidal type wave. Above results based on the analytical solution, while below the CFD solution is presented 5 wavelengths after the generation zone

4.1.2 3rd Order Stokes Wave

The second test case in constant bathymetry considers a wave with stepper crest compared to the previous case. Specifically, based on Figure 4.1, a wave is chosen that lies in the region of 3^{rd} order Stokes theory. The characteristics of the wave are: the wave height is H=0.1m, the wave period is T=1s and the tank has depth d=0.5m. The resulted wave length as computed from the Stream Function theory is $\lambda = 1.57m$. For the numerical setup, the outcomes of the previous parametric studies are used. The grid near the free surface is discretized using 20 cells in the wave height and 150 in the wave length. The timestep is chosen as $dt = 0.00125s$, which corresponds to 800 timesteps per wave period. For the wave generation, a zone extended for one wavelength ($L_G = \lambda$) was used and the coefficients of the exponential function (Eq. (4.1)) are set to $\alpha_G = 60$ and $n_G = 3.5$. Similarly, for the wave absorption, a source zone of three wavelengths ($L_D = 3\lambda$) is used and the coefficients are set to $\alpha_D = 120$ and $n_D = 3.5$ The artificial compressibility parameter equals 10 everywhere. Finally, it is worth noticing that due to the increased wave height, the flow separation of the air behind the crest is significant and should be considered in the numerical setup. Even though this separation is not expected to affect wave propagation, a viscous approximation is followed to enhance numerical stability. In Table 4.6 the numerical parameters used in this test case are summarized.

Table 4.6: Numerical parameters used for the 3rd Order wave in constant bathymetry. Index G denotes generation parameter, while D damping parameter

Approx.	Mesh	dt	β	CFL_τ	L_G	α_G	n_G	L_D	α_D	n_D
Viscous	112973	T/800	10	50	λ	3.5	60	3λ	3.5	120

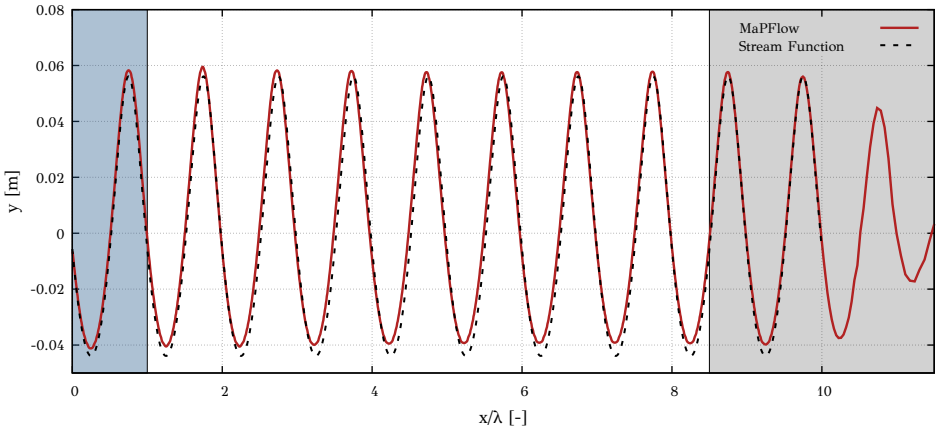

Figure 4.9: Free surface elevation for a 3rd order Stokes wave. Comparison between theoretical and numerical results. Wave characteristics: $T = 1s$, $H = 0.1m$, $d = 0.5m$, $\lambda = 1.57m$.

Figure 4.9 compares the wave elevation, as computed from the Stream Function theory and the numerical solution. The comparison is made after 25s of simulation (or 25 wave periods). As a first remark, the numerical results follows adequately well the theoretical result. However, the numerical solution seem to predict a different mean elevation, which leads to an upwards shift of the entire wave profile. As it will be made clear below, this is caused by the increase of the total water mass in the domain. One main difference of non–linear waves compared to linear is that, the fluid particles under the crest experience a net drift velocity in the direction of the waves, commonly referred to as *Stokes Drift*. This leads to a net mass flux entering the domain at every wave period. For the specific wave, the Stokes drift velocity is computed as $c_s = 0.0155m/s$. This can be clearly seen in Figure 4.10a. The total mass that enters the

domain is constantly increasing, while the mass that exits the domain is zero for the first 10s of the simulation. Once the wave reaches the outlet boundary, the total mass leaving the domain is the same as in the inlet boundary. This time window of 10s, where no mass outflow occurs, leads to an increase of the total water mass. The water mass increased from 9980kg, at the beginning of the simulation, to an average of 10038kg ($\pm 12kg$) after 25s. This corresponds to a mean water elevation of 2.9mm, as is the difference between the curves in Figure 4.9.

The previous statement is also supported by Figure 4.10b, where the mass flow rates at the inlet and outlet boundaries are plotted. The outflow flux is zero for the first 10s of the simulation and once the first wave crest reaches the boundary, an outflow mass flux is noted. In Figure 4.10b, besides the mass flow rates, the mean mass flux values at the inlet and outlet boundary, as well as, the theoretical mass flux due to Stokes drift are also noted. It can be seen that, the mean values as computed at the inflow and the outflow boundaries coincide and are close to the theoretical (due to Stoked drift) flux.

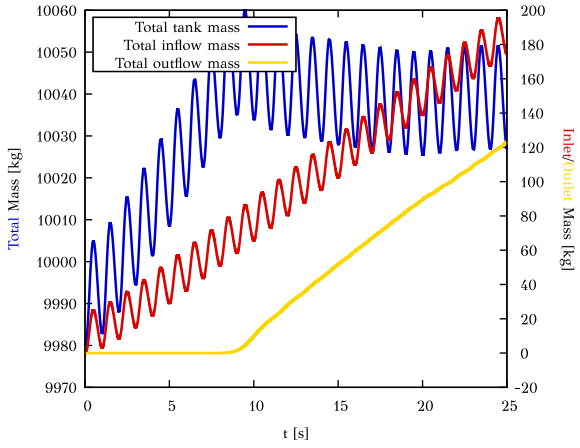

(a) Total water mass inside the wave tank (left axis) and total mass flow the passes thought the inlet and outlet boundary (right axis)

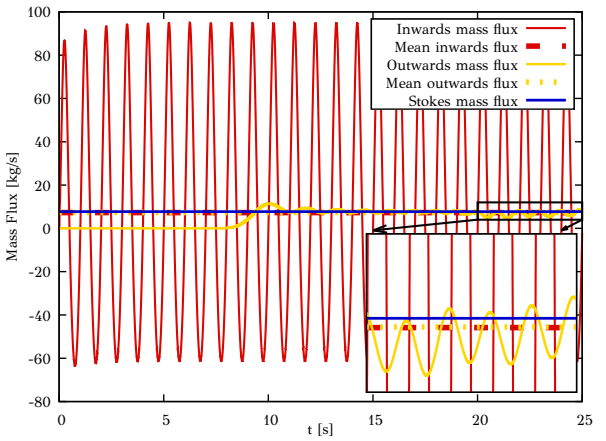

(b) Mass flow rates and mean values of the mass flux that passes through the inlet and outlet boundary. Additionally the mean flow rate as computed by Stokes drift value is presented (blue line). The detailed view corresponds to the last 5 seconds of the simulation

Figure 4.10: Increase of total water mass inside the numerical wave tank due to Stokes drift. The left figures presents total mass values, while the right figure presents mass flow rates. A constant mass flux enters the inlet boundary due to Stokes drift, however the flux at the outlet boundary is zero until the first wave reaches the boundary (after approx. 10s)

The increase of water mass is strictly related to the wave generation process. The source terms at the wave generation zone are based on analytical solution of a periodic boundary value problem. The periodicity imposed at the lateral boundaries implies, that the mass flux entering the domain is the same as the one leaving the domain. However, this is not the case for the wave propagation using wave generation and absorption zones. The solution is not periodic and the source terms at the left boundary introduce mass in the domain, while at the right boundary the outgoing flux is zero. One remedy to this problem would be to introduce a space (over water depth) and time (over wave period) averaged velocity at the outlet boundary. However, this remedy would be case specific and would only apply in case of wave propagation over constant bathymetry. If a different case was studied where the direction of propagation can not be easily determined, for example if the domain contains a structure that interacts with waves, this remedy can not be easily implemented.

This increase primarily affects non–linear waves with significant Stokes drift. As it was seen in case of the Cnoidal wave, the Stokes drift is not significant and of course this is the case for linear waves in which the Stokes drift is zero. In practical implementations and in all results

presented here, linear or low order (up to 2nd order Stokes waves) are considered. Thus, the increase of the total water mass is insignificant and does not affect the results.

4.2 Wave Interaction with Variable Bathymetry

Once the ability of the numerical method to effectively propagate waves in constant bathymetry has been determined, next the interaction of a wave with a trapezoidal bathymetry is considered. This is a standard benchmark to evaluate the solver ability to accurately simulate dispersive phenomena. The original experiment was setup and conducted by Beji and Battjes [135], where seven wave gauges were placed along the wave tank. Later, Dingemans [136] repeated the same experiment using four more probes and this will be used here as referece. The location of the eleven wave probes are depicted in Figure 4.11. The generated wave profile has height $h = 2.0$cm and period $T = 2.02$s.

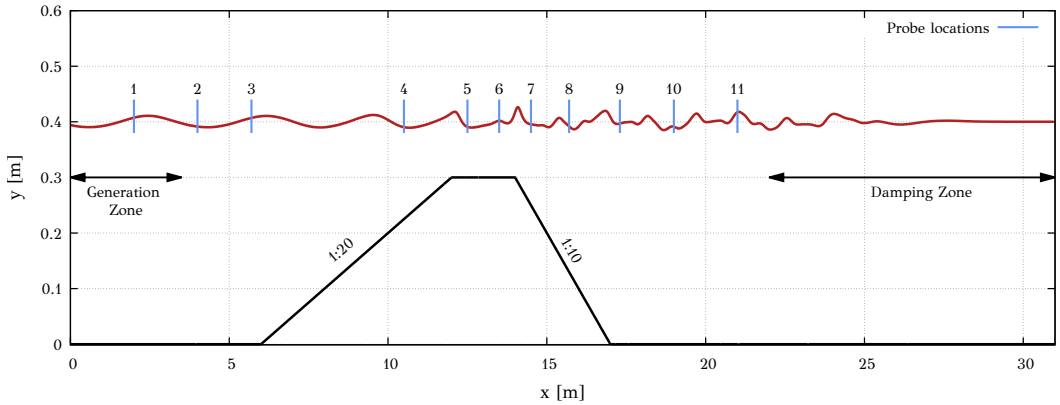

Figure 4.11: Schematic representation of the numerical setup for interaction of regular waves with variable bathymetry. The waves are generated at the left of the domain and damped at the right. Eleven probes are used to measure the wave elevation at different location in the numerical wave tank and used for comparison with experimental data

Figure 4.11 also illustrates the numerical setup. The length of the numerical wave tank is 31m. The damping zone is 9m and the wave generation zone extends for 3.5m. The coefficients of the generation and damping zones are chosen according to the preceding investigation. Following the guidelines from the previous analysis, a timestep and grid sensitivity study was conducted. The timestep resolution was based on the incident wave period, and the parametric study included the values $dt = T_{inc}/400, T_{inc}/800$ and $T_{inc}/1600$. The spatial mesh should have sufficient resolution to account for the higher harmonics created by the interaction with the bathymetry.

For the grid generation a structured–like technique was adopted. Three grids were generated labeled here as *Coarse*, *Medium* and *Fine*. In the x–direction, the grid in all cases is uniform with resolutions $dx = 2, 1$ and 0.5cm, for the three grids respectively. In the y–direction, a refinement zone is dfeined near the free surface to capture wave elevation. The vertical step was set to $dy = 2$mm for the *Coarse* grid and to 1.5mm for the other two. The parameters for the three grids led to mesh sizes of 90, 180 and 320 thousand cells, respectively. The results of the two studies are presented in Figure 4.12, where free surface elevation at the last probe is plotted for 2.5 seconds. Convergence of results is noted for the two finest discretizations in each case. Thus, the solution can be considered as independent from parameters associated with time and space, if either of them is selected. As basis for the comparison with experimental data the finest mesh is selected with timestep resolution $dt = 2.5 \cdot 10^{-3}$ ($=T_{inc}/800$). The numerical parameters used in this study are also summarized in Table 4.7.

It needs to be noticed, that the viscosity effects can be neglected because the boundary layer thickness is relative small compared to depth and thus it is not expected to affect wave elevation. For this reason, a viscous–free approximation is adopted to reduce the computational cost. Regarding the other numerical parameters, the artificial compressibility factor β is equal to 10. The pseudo–CFL_τ number is equal to 50 and at each time true iteration 10 dual steps are executed for the convergence of the pseudo-steady state problem. At the bottom, no slip boundary condition is applied.

Table 4.7: Numerical parameters used wave interaction with variable bathymetry. Index G denotes generation parameter, while D damping parameter

Approx.	Mesh	dt	β	CFL_τ	L_G	α_G	n_G	L_D	α_D	n_D
Inviscid	319565	$T_{inc}/800$	10	50	λ	3.5	60	3λ	3.5	120

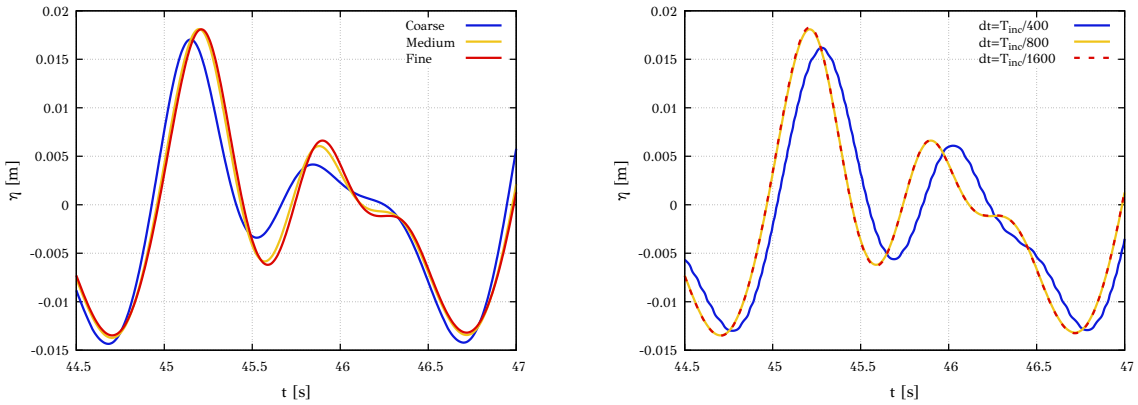

(a) Grid independence study **(b)** Timestep independence study

Figure 4.12: Grid and timestep independence study. Free surface elevation at probe 11 ($x = 21.0m$)

The predicted free surface elevation in the entire domain is presented in Figure 4.11 (continuous red line). Due to shoaling, the wavelength is compressed and energy is transferred to higher harmonics. The deepening after the bar releases energy from higher harmonics and an irregular wave profile is created. The signals recorded at the wave probes are compared against the experimental data in Figure 4.13 at eleven stations. At the first probe (Fig. 4.13a), the two signal appear to have a small difference in amplitude. However, as the comparison at the other probes suggests, it does not affect the overall comparison. At probe 7 (Fig. 4.13g) a small phase shift is observed between the simulation and the measurements. Nevertheless, the comparison of free surface displacement is very good at all stations even when higher harmonics are excited after the shoaling (Figures 4.13f-4.13k).

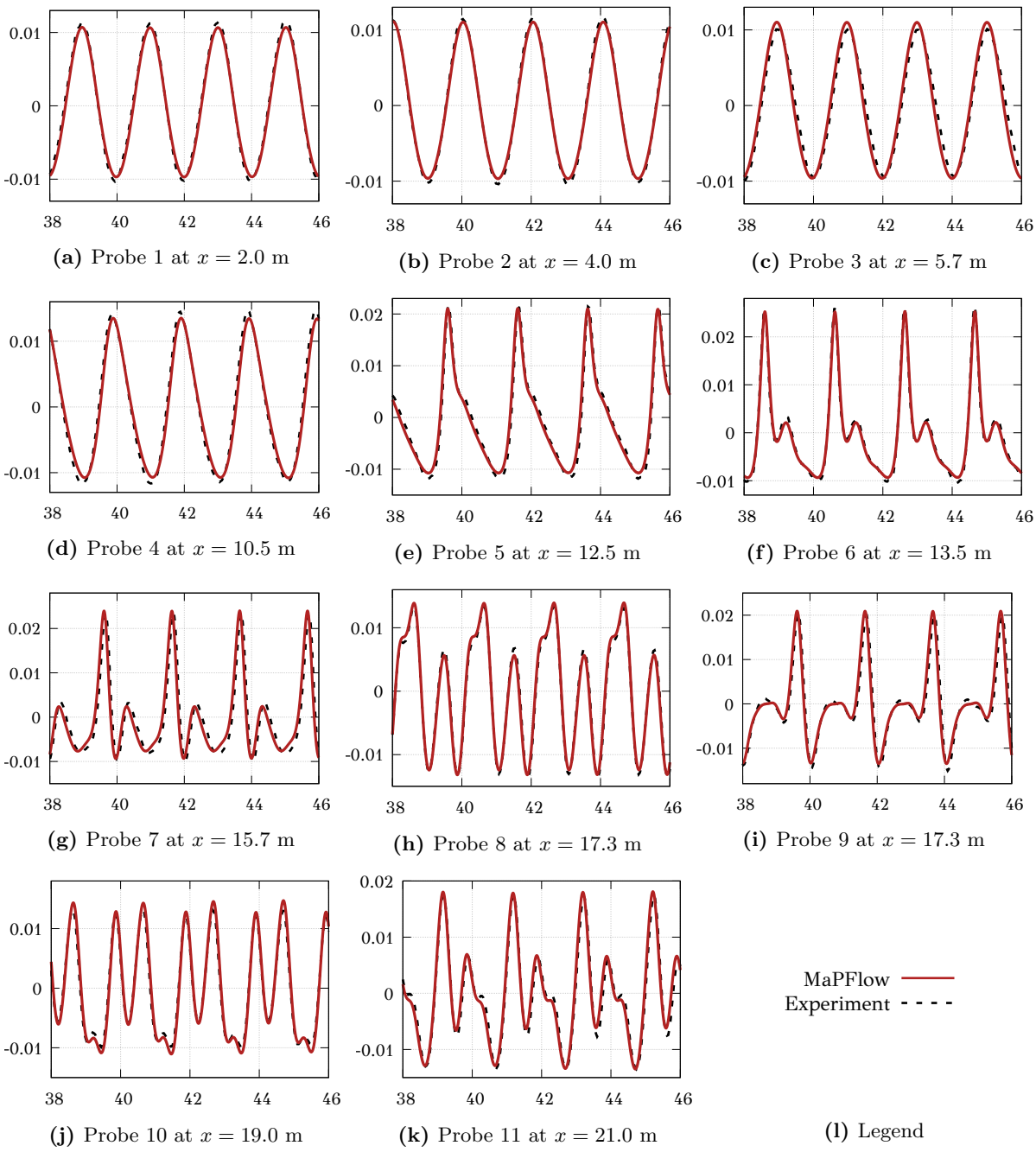

(a) Probe 1 at $x = 2.0$ m **(b)** Probe 2 at $x = 4.0$ m **(c)** Probe 3 at $x = 5.7$ m

(d) Probe 4 at $x = 10.5$ m **(e)** Probe 5 at $x = 12.5$ m **(f)** Probe 6 at $x = 13.5$ m

(g) Probe 7 at $x = 15.7$ m **(h)** Probe 8 at $x = 17.3$ m **(i)** Probe 9 at $x = 17.3$ m

(j) Probe 10 at $x = 19.0$ m **(k)** Probe 11 at $x = 21.0$ m **(l)** Legend

Figure 4.13: Interaction of regular waves with variable bathymetery. Free surface elevations at the wave probes. Comparison of numerical results and experimental data

4.3 Moonpool–Type Floater

In this final section, a wave structure interaction problem is examined aiming to validate the FSI algorithm presented in Section 3.9. To this end, the response of a moonpool–type floater in incident waves is investigated and compared with available experimental data taken from [137]. Under wave excitation, the floater is displaced and the free surface inside the moonpool is subjected to a vertical motion, commonly called piston motion, while additional sloshing modes may appear. The piston motion inside the moonpool reduces the motion of the structure induced by the incident waves. This problem poses additional challenges since the motion of the floater is induced by the underlying flowfield. It is noted that in this case, viscous effects are significant. The flow separation on the sharp edges directly affects the free surface elevation inside the moonpool.

In the experiments conducted by [137] two barges of rectangular cross section of 20cm were mounted together to form a moonpool of 10cm. The draft of the model is 0.097m. The breadth of the barges was 14mm smaller than the width of the experimental wave tank and thus 3D effects are limited. Following the notation of the experiments, the test case is defined on the y–z plane. The mass of the floater is $m = 22.885$kg, its radius of gyration around the x–axis is $r_{xx} = 0.18$m and its center of gravity (CoG) is 0.091m above the bottom of the hull. In a two-dimensional context, a body has three degrees of freedom, namely the sway motion (motion along the y–axis, η_2), the heave motion (motion along the z–axis, η_3) and the roll motion (motion around the x–axis, η_4).

The setup of the experiment is depicted in Figure 4.14. The structure is mounted with horizontal mooring lines to prevent it from drifting. At the end of these lines springs were connected to allow the structure to move. Pre–tension was applied to the springs. The pre–tension was much larger than the tension due to the motion of the structure, thus the restoring effect of the mooring system was always active. A coupling between sway and roll motion is assumed since the center of gravity of the model and the mounting point of the mooring lines were not at the same height. Considering the above mentioned remarks, the rigid body motion is described by equations (4.2).

$$\begin{aligned} m\ddot{\eta_2} &= \int_{\partial S} -pn_y \mathrm{d}S + \int_{\partial S} (\bar{\tau}\vec{n}) \cdot \vec{n}_y \mathrm{d}S - K_{22}\eta_2 - K_{24}\eta_4 \\ m\ddot{\eta_3} &= \int_{\partial S} -pn_z \mathrm{d}S + \int_{\partial S} (\bar{\tau}\vec{n}) \cdot \vec{n}_z \mathrm{d}S \\ I\ddot{\eta_4} &= \int_{\partial S} -p\vec{n} \times \vec{r} \mathrm{d}S + \int_{\partial S} (\bar{\tau}\vec{n} \times r)\, \mathrm{d}S - K_{42}\eta_2 - K_{44}\eta_4 \end{aligned} \tag{4.2}$$

In the above equations m is the mass of the structure, $\overline{I}$ is the moment of inertia about its center of gravity, $\vec{n}$ is the normal unit vector defined on the boundary S of the body, n_y, n_z the components of $\vec{n}$, p is the fluid pressure and $\bar{\tau}$ is the viscous stress tensor. In addition, K_{22} and K_{44} are the spring constants for the heave and roll motion, respectively. The spring constants K_{24} and K_{42} are of the same magnitude and couple the heave and roll motions. They result from the level arm created between the axis of the restoring forces and the center of gravity. A more detailed report for the experimental setup and the physical modeling of the rigid body motion can be found in [138]. The experiment considered three types of waves based on the wave height to wavelength ratio for several wave periods. In the present study, only results for waves with ratio $H/\lambda = 1/30$ for wave periods between the range $[0.6 : 1.2]$ s are presented.

The flow is considered fully turbulent in all cases. The numerical setup is based on a previous study and can be found in [139]. Grid and timestep sensitivity studies were conducted and used as reference here. The grid and the timestep is the same in all cases. In the stream–wise direction, the grid is almost uniform with size of $dy = 0.008$m, while in the transverse direction close to the free surface, the grid size is $dz = 0.001$m. On the damping zone region, the mesh

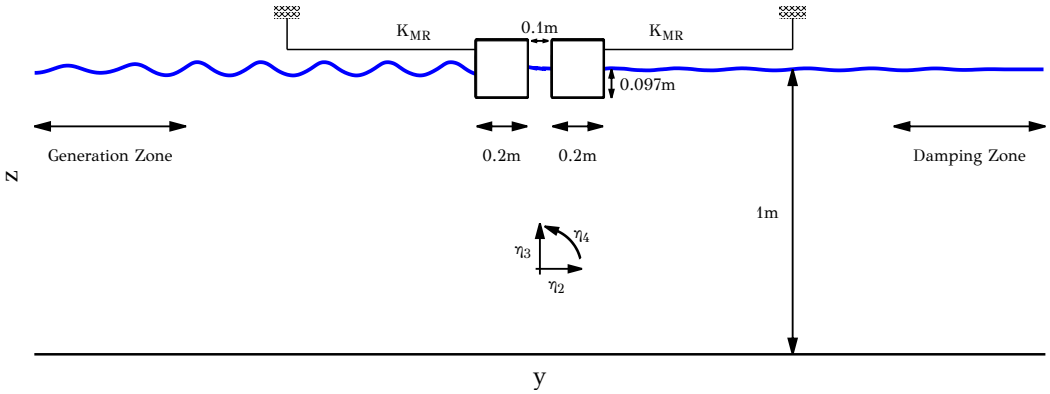

Figure 4.14: Schematic representation of the numerical setup for the moonpool-type floater test case.

coarsens with a geometric rule to effectively damp the outgoing waves. The grid around the structure has an O–grid topology which is dense to account for the vortex formation near the sharp edges. The total size of the mesh is $3 \cdot 10^5$ cells. The selected timestep is equal to 0.001s.

Overproduction of turbulence kinetic energy (TKE) at the free surface regime is a well–known shortcoming of RANS approximation, as already mentioned in Section 2.4. Various modifications have been proposed to mitigate the turbulence overproduction near the free surface. One of the most widely used models has been proposed by Devolder [83] and described here in Section 2.4. A buoyancy turbulence limiter is added in the turbulent kinetic energy equation that is activated near the free surface. Although, the proposed limiter restrains the excessive overproduction of turbulence, as it will be demonstrated here, turbulence viscosity is still high far from the solid boundaries. In the case examined here, waves impinge on a floater in absence of current in 2D. The turbulence generated near the free surface is not able to move beneath the floater and advect to the downstream boundary. As a result, turbulence builds up gradually upstream of the floater. This leads to increased levels of dissipation inside the flowfield, which eventually decreases the amplitude of the floater motion especially in long time simulations. Turbulence is built up away from the wall boundary where the k–ϵ branch of SST model is activated. Kato and Launder [87] faced a similar problem when they tried to predict the flow over stationary cylinders. The very high levels of shear near the stagnation point produced excessive levels of turbulent kinetic energy, k, similarly to the case discussed here. They proposed to calculate turbulence viscosity (μ_t) not only based on the shear strain S, but to the vorticity magnitude Ω as well. By adopting this definition in conjunction with the Devolder limiter, in the k–ω SST formulation, turbulence overproduction has been decisively suppressed. In Figure 4.15 two snapshots of the turbulence field is presented with (Fig. 4.15a) and without (Fig. 4.15b) the Kato–Launder limiter. In both cases, the Devolder limiter is also employed. On the one hand, it is clear that predictions which include only the modification of Devolder fail to suppress the artificial overproduction of TKE. On the other hand, using also the Kato–Launder limiter the levels of turbulent viscosity are considerably restrained.

The excessive production of TKE directly affects the motion of the floater. In Figure 4.16, the signal of the roll motion is illustrated. The amplitude of the roll motion is considerably reduced for long time simulations when only the turbulent buoyancy term is used. The results are improved when the turbulence production limiter is used and as it is depicted the amplitude remains constant.

The previous agrees with the work of Larsen and Fuhrman [85] where they also suggest that the Devolder modification is not enough to suppress the artificial overproduction of TKE. In [85], they employ another approach, where the turbulence viscosity is suppressed by identifying nearly potential flow regions. Nonetheless, in this case study, this distinction is not trivial. By

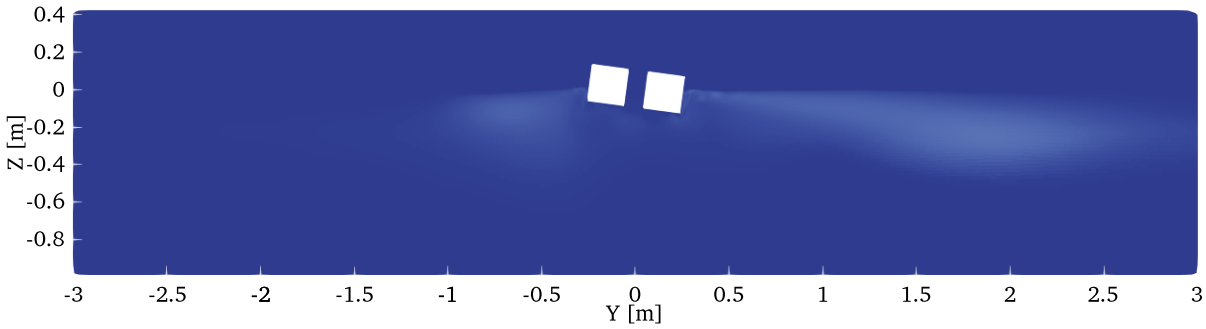

(a) With the Kato-Launder production limiter

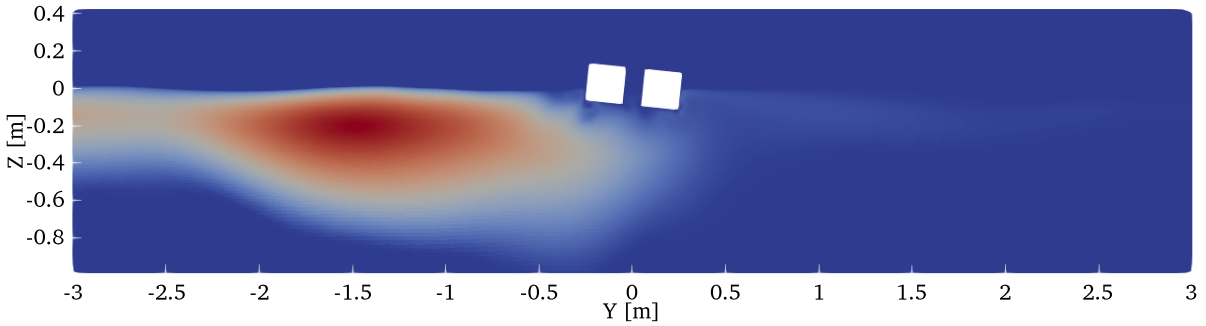

(b) Without the Kato-Launder production limiter

(c) Contour Palette

Figure 4.15: Snapshot of the turbulent viscosity (μ_t) for the moonpool type floater after 10^3 iterations with (upper) and without (middle) the Kato-Launder production limiter [87]. Test case characteristics $T = 0.95s$ and $H/L = 1/30$. In both cases the Devolder [83] production limiter is applied.

employing the Kato limiter the overproduction of TKE was successively suppressed without making any case–specific modifications. In Table 4.8 an overview of the numerical parameters used in this study is presented. Mesh, timestep characteristics and also the turbulence approximation are noted.

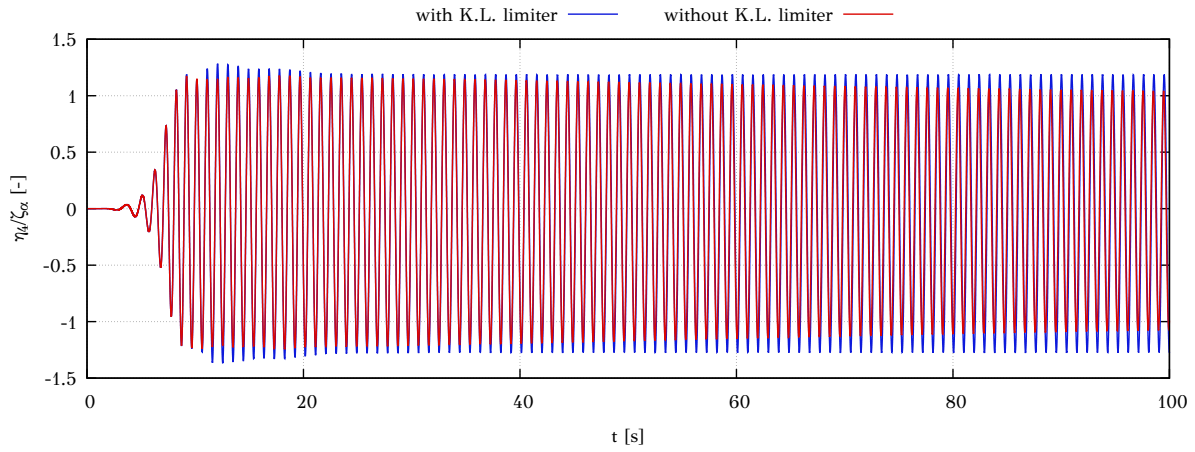

Figure 4.16: Time signal of the roll motion with and without the Kato-Launder production limiter [87]. Test case characteristics $T = 0.95s$ and $H/L = 1/30$. The figure illustrates a constant reduction of the amplitude of the roll motion due to turbulence overproduction, when no production limiter is used. In both cases the Devolder [83] is applied.

Table 4.8: Numerical parameters used for the wave excitation of a moonpool–type floater

Approx.	Turb. Limiters	# DoFs	Mesh	dt [s]	β	CFL_τ
Fully Turb.	Devolder Kato–Launder	3	294435	0.001	10	50

Next the results of the systematic evaluation are presented. In Figure 4.17, the results are compared with the experimental data. In Figures 4.17a to 4.17c, the Response Amplitude Operators (RAOs) of the motions are presented, while Figure 4.17d presents the amplitude of the space averaged free surface elevation inside the moonpool. Regarding the sway motion, the amplitudes scale linearly with respect to the wave period and the results coincide with the experimental ones. The heave amplitudes appear to have a resonant behavior for wave periods between $T = 0.65$s and $T = 0.8$s. This behavior is depicted in the amplitudes of the free surface as well. Small discrepancies are observed near this resonant region. Furthermore, as noted in Figure 4.17c, the numerical results are similar with the experimental in case of the roll motion for wave period below $T = 1$s. However, for wave periods above $T = 1$s larger amplitudes of roll motion are are predicted by the numerical solver. This could be caused by the assumption of two–dimensional flow. Drag forces may appear in the experimental setup in the thin layer created at the side of the structure, between the floater and the wave tank. Additionally, another source of deviations between the experimental and the numerical results is the roughness of the structure. The surface of the floater, in the simulations, is considered smooth, which does not reflect the experimental case.

In Figure 4.18, vorticity near the edges of the structure is depicted where the flow separation at the corners of the structure is evident. The flow separation at the lower entrance of the moonpool regulates the resonant behavior of the piston mode which is apparent for wave periods between $T = 0.75$s and $T = 0.85$s. Finally, the pressure field upstream of the structure is presented in Figure 4.19. The figure illustrates the pressure distribution on the incident wave, the free surface elevation inside the moonpool, as well as the pressure drop due to vortex formation near the sharp edges of the structure.

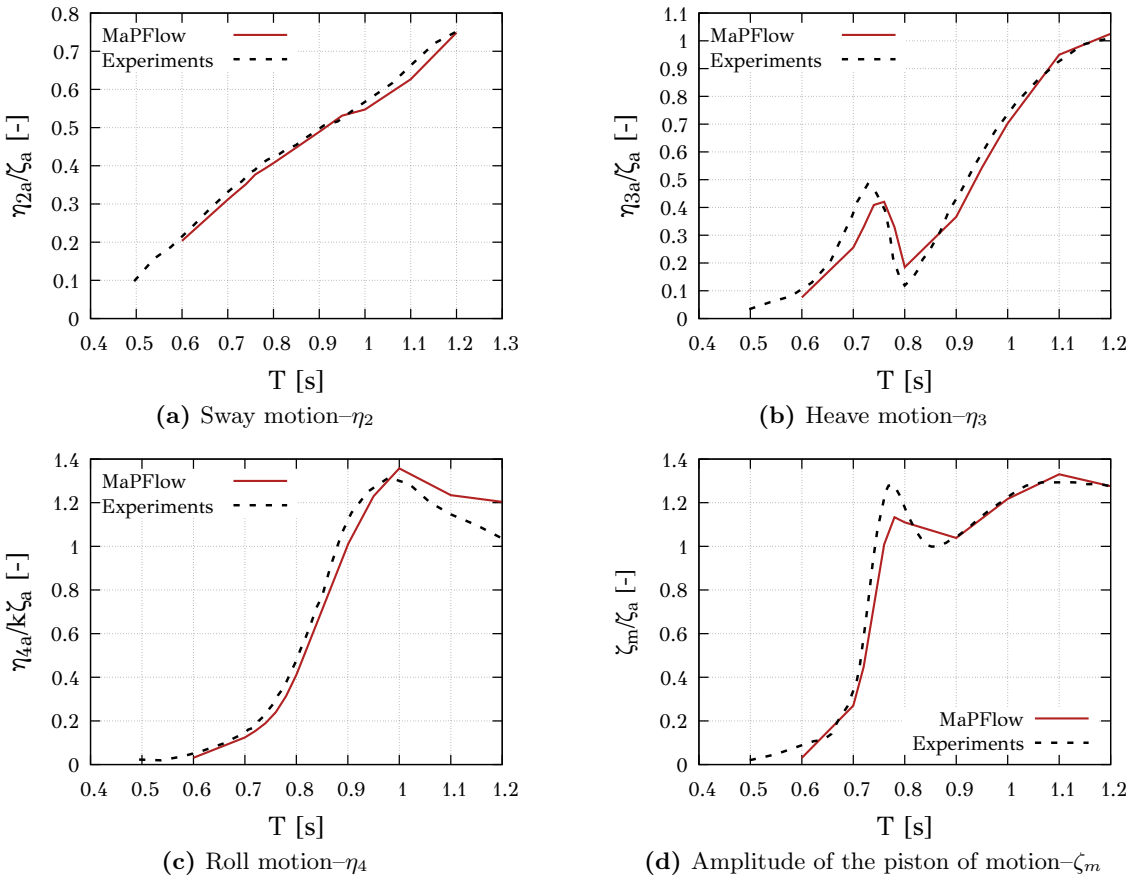

(a) Sway motion–η_2 **(b)** Heave motion–η_3

(c) Roll motion–η_4 **(d)** Amplitude of the piston of motion–ζ_m

Figure 4.17: Comparison of experimental and numerical results for the moonpool–type floater test case. Response Amplitude Operators (RAOs) of the three motions and the space averaged free surface elevation inside the moonpool for wave steepness $H/\lambda = 1/30$. ζ_a is the amplitude of the incoming wave and k the wave number

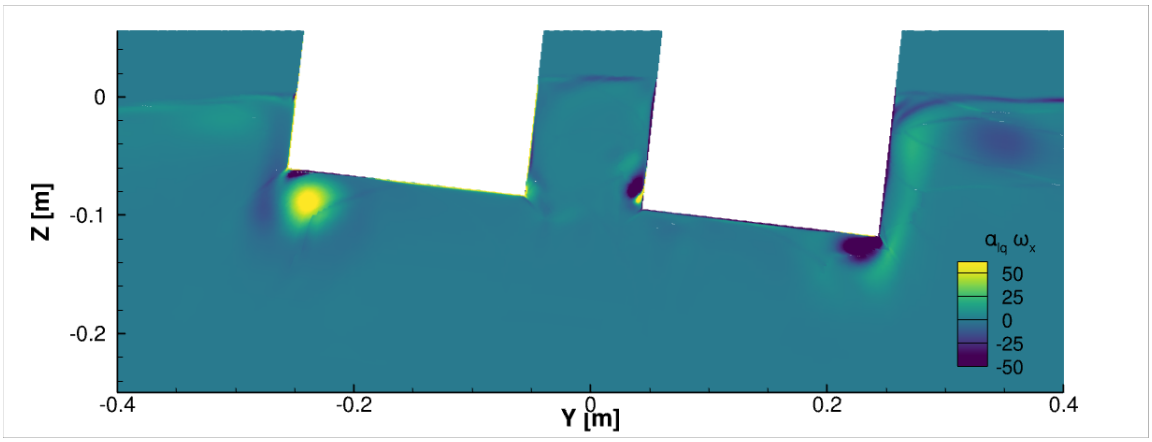

Figure 4.18: Vorticity contours multiplied by the volume fraction near the moonpool–type structure. The wave steepness is $H/\lambda = 1/30$ and the period is $T = 0.95$s.

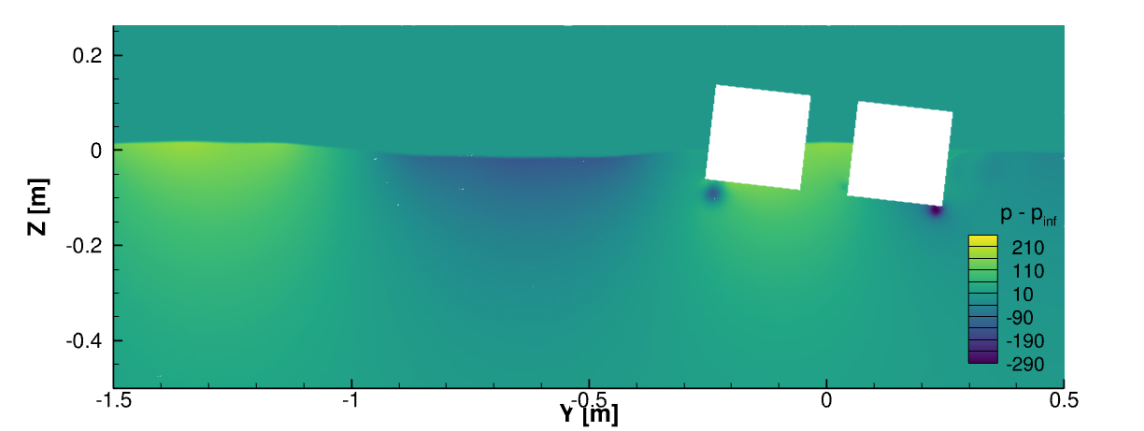

Figure 4.19: Pressure contours upstream of the moonpool–type structure. The wave steepness is $H/\lambda = 1/30$ and the period is $T = 0.95$s.

Chapter 5

Applications in Three–Dimensional Flows

The present chapter focuses on the performance of the hydrodynamic solver in 3–dimensional cases. The case studies that follow cover every feature of the numerical solver, including wave generation and absorption, fixed and moving solid boundaries, the presence of only water (one-phase) or both air and water (two-phase), among other things. The criteria for selecting the case studies are; literature recommendations for validating numerical solvers, availability and quality of experimental results, and modern engineering concepts for improving the design of offshore structures. In every case study, the numerical setup, mesh and timestep independence studies are given prior to numerical results.

The results start from an example of one–phase flow simulation, followed by three test cases where both the liquid and the gaseous phases are present. Specifically, the first case considers the performance of a model scaled propeller in open water tests. Numerical results are compared against experimental data provided by the Laboratory of Ship & Marine Engineering (LMSH). In the second case the hydrodynamic response of the Kriso Container Ship (KCS) is assessed in calm water conditions and in head waves with two degrees of freedom. Moreover, results by restraining completely the motion of the (fixed conditions) are also presenting. In the latter case, additional flowfield characteristics are available from experimental data. The third section presents a preliminary study of a ship retrofitting concept. Starting from the bare hull of a model ferry ship, its performance is evaluated in calm water conditions and in head waves. Afterwards, the performance of the vessel equipped with a static hydrofoil submerged in front of its bow is examined. The findings of this study are set side by side with the ones taken from the tow tank experiments conducted in LMSH. This study was part of the EU funded project SEATECH (https://seatech2020.eu/, accessed on 25 July 2023) and the results have also been published in [140]. The final case is a part of an international comparative study for the numerical evaluation of hydrodynamic response of floating offshore wind turbines. This work is part of the 1st Comparative Study for Floating Offshore Wind Turbines [141]. The study follows an experimental campaign [142] that examines the response of a model wind turbine floater in initial displacement and under excitation of two focused wave trains.

5.1 Evaluation of Propeller in Open Water Tests

Assessing propeller efficiency is a demanding task since it is operating in the wake of the ship. Before evaluating the performance of the propeller in this turbulent wake, it is common to execute open water tests and assess its performance in uniform flow. The propeller and its hub are mounted on a carriage moving with constant speed. Due to the submergence depth of the propeller, its interaction with the free surface is considered negligible. For this reason, the one–phase version of the numerical solver is utilized.

The simulations use as reference experiments conducted in the tow tank of LMSH [143]. The experiments consider the performance of a handcrafted 4–blade Wageningen B–Series propeller. The propeller is a model scale of 0.16m diameter, with pitch diameter ratio, P/D, 0.88 and expanded blade area ratio equal to 0.628. In the experimental setup, the submergence depth is 40cm, which is enough to eliminate cavitation effects.

The results are compared in terms of thrust coefficient K_T, torque coefficient K_Q and efficiency η, as given in Equation (5.1). In this equation, T is the thrust produced by the propeller, Q is the applied torque, D is the propeller diameter, n is the rotation speed in rps and V_A is the carriage velocity in m/s.

$$\begin{aligned} K_T = \frac{T}{\rho n^2 D^4}\ ,\ \ K_Q = \frac{Q}{\rho n^2 D^5} \\ J = \frac{V_A}{nD}\ ,\ \ \eta = \frac{J}{2\pi}\frac{K_T}{K_Q} \end{aligned} \tag{5.1}$$

The experiments were conducted for a series of advancing ratios J. The different advancing ratios can be achieved by either altering the rotation speed of the propeller or changing the carriage advancing velocity. In order to evaluate the consistency of the results, two series of experiments were carried out. Firstly, the propeller speed and the carriage velocity were appropriately selected to match a constant Reynolds number defined at a cross section at the 75% of the propeller radius, according to relation (5.2). The second test series regarded a constant carriage velocity V_A and altered the rotation speed of the propeller to match the advancing ratio. In the latter case, the Reynolds number varied between $2 \cdot 10^5$ and $6 \cdot 10^5$. The test conditions are summarized in Table 5.1. It is noted that for small values of J, the velocity of the carriage was altered instead of the rotation speed in order to avoid overloading the dynamometer.

$$Re_{0.75} = \frac{C_{075R}\sqrt{V_A^2 + (\pi n 0.75 D)^2}}{\nu_w} \tag{5.2}$$

In Equation (5.2), C_{075R} is the chord length at the 75% of the propeller span and is equal to 0.062m. Also, ν_w is the kinematic viscosity of water.

Table 5.1: Carrier velocity (V_A) and propeller rotation speed (n) for the two series of experiments

Re_{075} const			V_A const		
V_A [m/s]	n [rps]	J	V_A [m/s]	n [rps]	J
0.304	18.78	0.1	0.4	24.9	0.1
0.604	18.8	0.201	0.8	24.93	0.2
0.901	18.8	0.3	1.209	29.94	0.25
1.2	18.78	0.40	1.51	31.27	0.3
1.501	18.86	0.50	1.504	23.54	0.4
1.803	18.85	0.60	1.505	18.82	0.5
1.9	18.28	0.65	1.503	17.07	0.55
2.048	18.29	0.7	1.502	15.62	0.6
2.301	18.01	0.80	1.502	14.43	0.65
2.603	18.08	0.9	1.502	13.44	0.7
2.698	17.73	0.95	1.501	12.49	0.75
			1.501	11.76	0.8
			1.5	10.45	0.9
			1.501	9.88	0.96

5.1.1 Numerical Setup

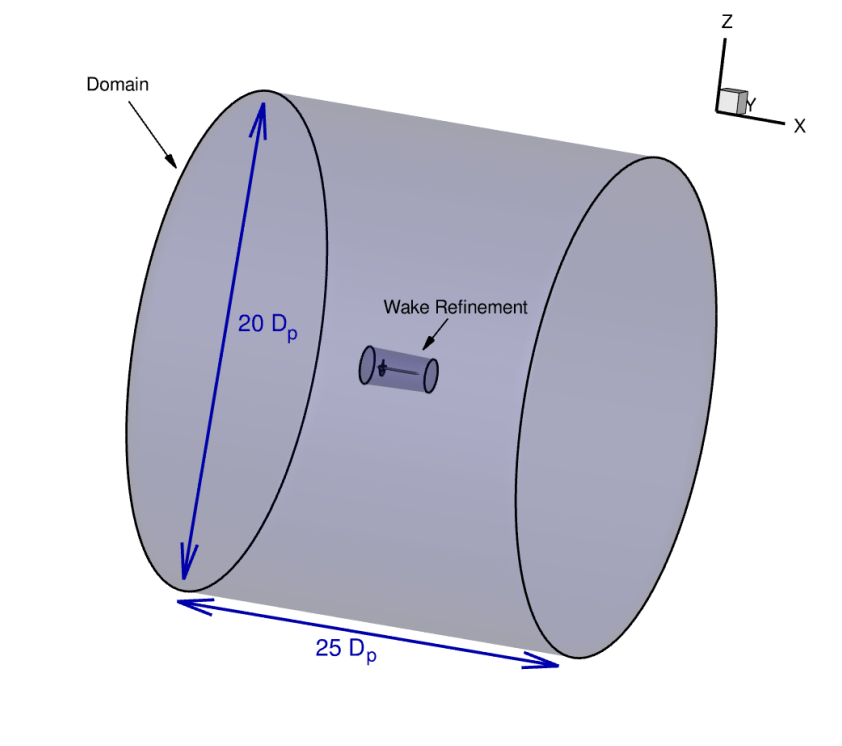

Figure 5.1: Computational domain used for the open water tests

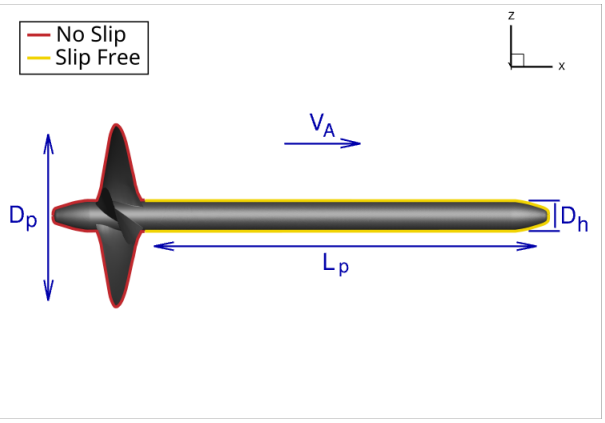

(a) Propeller and hub characteristics used in the CFD calculations. V_A is the inflow velocity

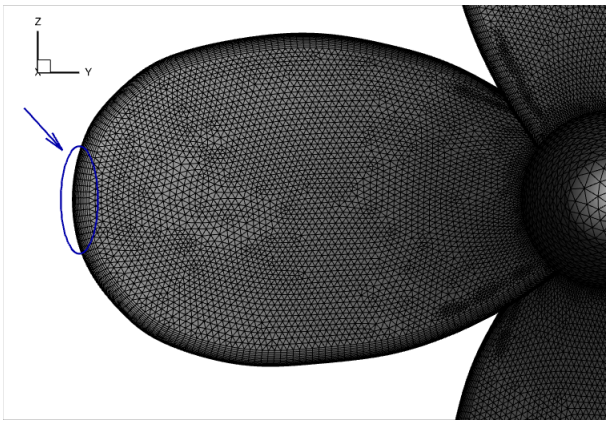

(b) Detailed view of the propeller's mesh near the sharp tip

Figure 5.2: Numerical setup for open water test of the handcrafted Wageningen B–Series propeller

The CFD simulations are performed in a cylindrical domain of 25 propeller diameters in length and radius of 10 propeller diameters, as illustrated in Figure 5.1. The flow is solved in the rotating frame of reference using absolute velocity representation, as described in Section 2.3. The flow is uniform and parallel to the x–axis. Due to the Reynolds number, the flow is considered fully turbulent and the standard k–ω SST model of Menter is utilized. The propeller geometry used is depicted in Figure 5.2a. The geometry has been extended for two propeller diameters downstream to emulate the hub used in the experimental setup. The boundary condition of the extended hub was set to slip–free to avoid the development of the boundary layer, while for the propeller blades and the hub upstream, no–slip boundary conditions were defined (see Figure 5.2a).

For the domain discretization, a mesh sensitivity study was conducted. Three different computational meshes were studied, created by the unstructured mesher ANSA developed by BETA CAE systems [144]. In order to control the mesh size close to the propeller a cylindrical refinement zone of 2 propeller diameters in diameter and 3.5 in length (0.5 upstream and 3 downstream of the propeller) was created. Furthermore, to capture the generated tip vortex (see Figure 5.2b) special care has been taken near the sharp tip of the propeller. Lastly, in all meshes mesh layers were generated normal to the wall boundaries to accurately resolve the boundary layer. In all examined meshes 25 layers were generated with growth ratio 1.2 and the first wall node was places $0.01mm$ away from the wall.

The first mesh, denoted as *Coarse*, had a total size of 2.68 million cells and the surface mesh was consisted of 63.3 thousand elements. The second, *Medium* mesh, had 4.3 million cells and 131.8 thousand elements on the solid surface. The third *Fine* mesh had the same surface mesh as the *Medium* mesh, but the mesh at the wake of the propeller was further refined. *Fine* mesh had a total size of 7.8 million cells. As an example of the mesh discretization, in Figure 5.2 the surface mesh of the *Medium* mesh on the blades is depicted in a detailed view. On the 4 blades 90 thousand cells are created while the propeller and hub consist of 42 thousand surface cells.

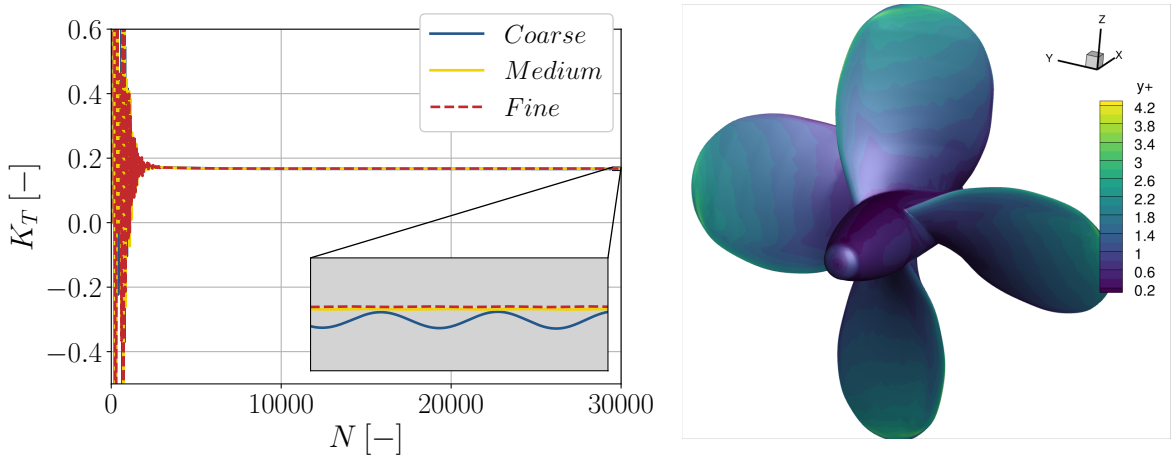

(a) Grid sensitivity study. The detailed view focuses on the last 500 iterations

(b) y^+ values on the propeller

Figure 5.3: Mesh sensitivity study and y^+ values for advancing ratio $J = 0.6$

The sensitivity study was conducted for a constant Reynolds number equal to 360,000 for 4 different advance ratios (J). The results are presented in Table 5.2 us percentage deviations with respect to the *Fine* mesh. In all cases, the differences are relatively small. However, as it is seen in Figure 5.3a, in case of *Coarse* mesh, the thrust coefficient is not constant and oscillates around a mean value. This is attributed to the coarse mesh discretization near the tip of the blade. On the contrary, the other two meshes produce similar results with adequate convergence characteristics; thus the coarser of the two (*Medium* mesh) is chosen for the rest of simulations. As a last remark for the mesh setup, the y^+ values on the surface of the propeller are presented in Figure 5.3b. The mean y^+ value is below 2 and large values are noted near the tip of the propeller as expected.

The majority of the simulations examine the steady state problem. However, in case of advancing ratios smaller than 0.3 ($J < 0.3$) an unsteady approximation is adopted, due to flow separation occurring at the propeller tip. For the unsteady simulations the timestep is adjusted at 1500 timesteps per propeller revolution. For the convergence of the pseudo–steady problem, the β factor has been set to 750 due to the rotation speed, and the pseudo–time CFL is equal to 10 increasing linearly from 1 to 1000 steps. An overview of the numerical setup is presented in Table 5.3.

Table 5.2: Mesh sensitivity study for evaluation of a propeller in open water tests. Relative errors compared to *Fine* mesh

	Coarse		*Medium*	
J	$\delta K_t[\%]$	$\delta K_q[\%]$	$\delta K_t[\%]$	$\delta K_q[\%]$
0.5	0.496	0.189	0.182	0.143
0.6	0.730	0.248	0.162	0.111
0.7	0.985	0.225	0.052	0.011
0.8	1.496	0.434	0.187	0.059

Table 5.3: Numerical parameters used for the evaluation of the propeller in open water tests

Approx.	Mesh	dt	β	CFL_τ
Fully Turb.	4273611	if $J > 0.3$: Steady else: $T/1500$	750	10

5.1.2 Systematic Evaluation of the Propeller

In Figure 5.4, the results from the experimental (EFD) and the computational (CFD) approximations are compared. The two figures correspond to the constant Reynolds number as defined at 75% of the blade ($Re_{075} = 3.6 \cdot 10^5$) and to the constant carriage speed test cases. Additionally to the previous results, the characteristics of the Wageningen B–series provided by [145] in form of a polynomial are plotted in dotted lines and denoted as *Wageningen*. The polynomial is independent from the Reynolds number in case of $Re < 2 \cdot 10^6$, thus the same curve is plotted in both figures.

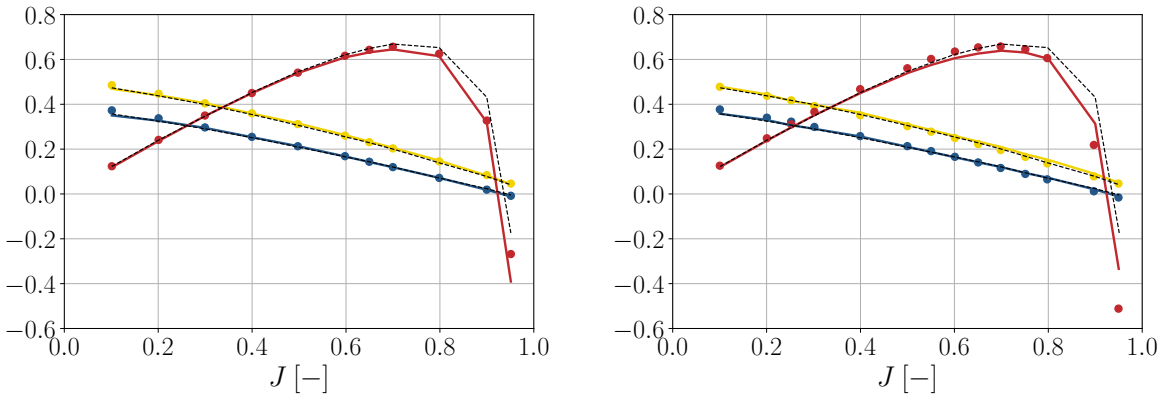

(a) Constant Reynolds number ($Re = 3.6\,10^5$)

(b) Constant carriage velocity ($V_A = 1.5m/s$)

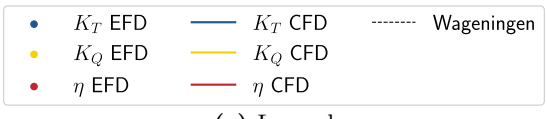

(c) Legend

Figure 5.4: Comparison between experimental (EFD), computational (CFD) results and theoretical values provided for the Wageningen propeller (dotted line)

Both procedures presented here produce similar results for a wide range of advancing ratios and compare well to the curves given by the literature. More precisely, all data seem to be in agreement for advancing ratios up to 0.6, especially for the constant Reynolds case. CFD results

start to deviate from experiments and polynomial at larger advancing ratios, particularly in case of constant carriage speed. The simulations seem to under–predict the thrust of the propeller, which is further pronounced in the efficiency coefficient – η plot. Larger differences are noted among all datasets for advancing ratios greater than 0.9. However in this range, the thrust of the propeller tends to zero and all approximations introduce uncertainties. Regarding the two series of test cases, similar results are obtained and the comparison between the datasets is fair. Nevertheless, more consistent results seem to be obtained from the constant Reynolds number series where all approximations seem to converge in the same values.

The differences between the experimental and computational results are given also in a percentage form, relative to the experimental data, in Table 5.4. The differences between the two sets are less than 1% and 8% for the constant Reynolds number and the constant carriage speed case, respectively, in regions of interest ($0.1 < J < 0.8$).

Table 5.4: Differences between EFD and CFD results in evaluation of the propeller in open water tests

Re_{075} const			V_A const		
J	δK_t [%]	δK_q [%]	J	δK_t [%]	δK_q [%]
0.1	6.07	3.37	0.1	5.06	0.25
0.2	3.21	1.57	0.2	3.04	1.43
0.30	0.67	0.16	0.25	4.73	0.42
0.40	0.56	0.25	0.3	2.61	1.51
0.50	0.23	1.04	0.4	0.69	3.33
0.60	0.62	0.91	0.5	1.34	2.69
0.65	0.76	1.09	0.55	1.93	2.59
0.70	0.57	1.29	0.6	1.02	3.83
0.80	0.19	2.14	0.65	0.59	4.91
0.90	5.13	2.82	0.7	3.34	6.71
0.95	38.83	4.85	0.75	5.19	7.47
			0.8	10.57	11.49
			0.9	61.46	13.06
			0.95	29.4	8.29

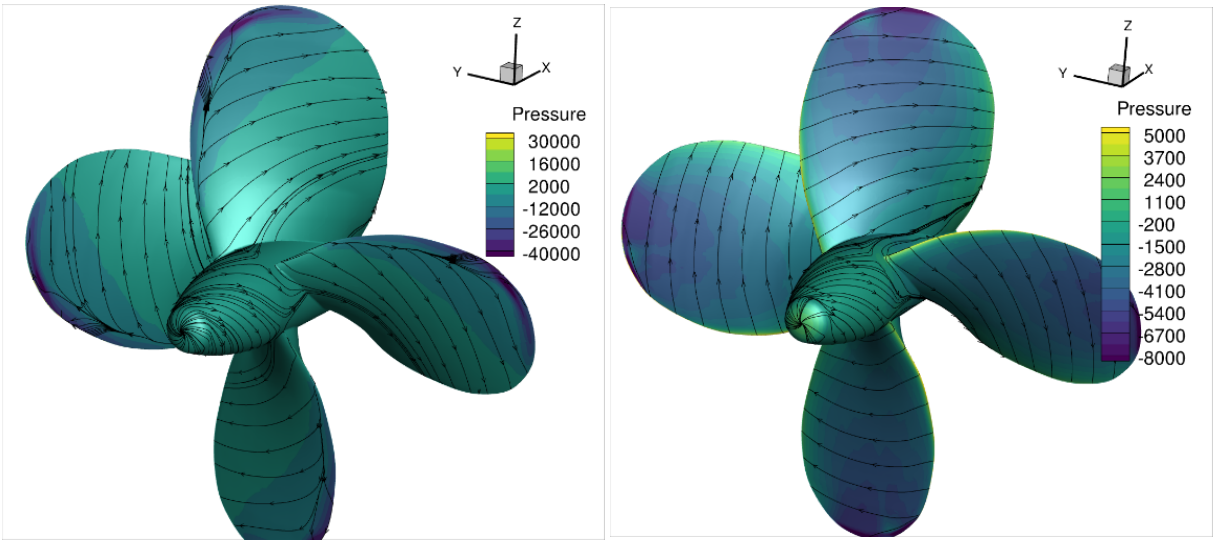

(a) J=0.1 **(b)** J=0.6

Figure 5.5: Pressure contour and stream–traces on the surface of the propeller for two advancing ratios

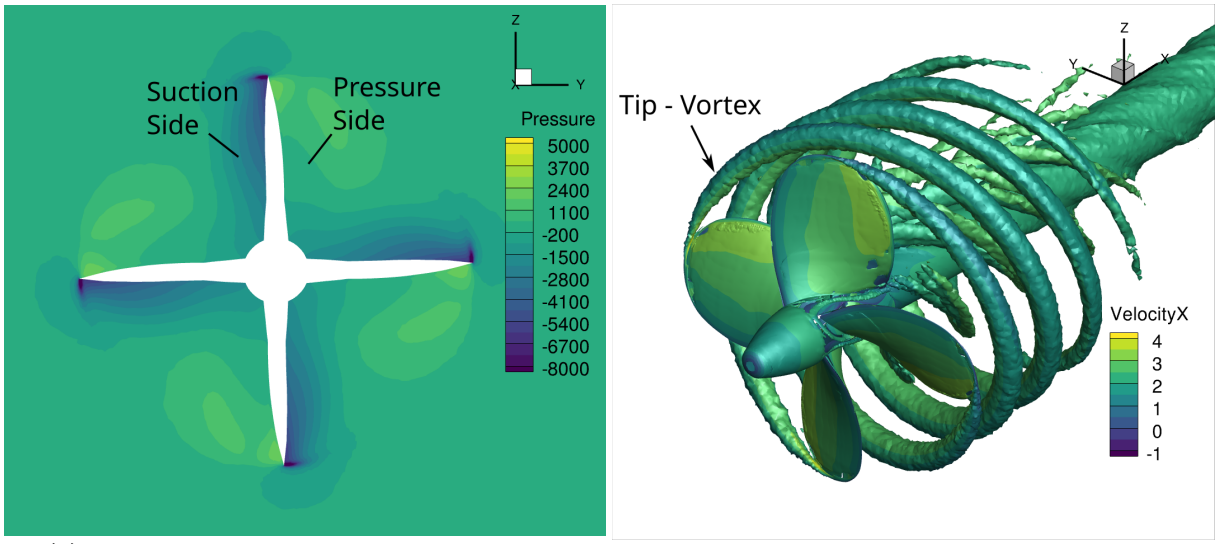

(a) Slice of the pressure field at $x = 0$. Pressure difference on the propeller's blades for advance ratio J=0.6

(b) Iso–surface of the Q-criterion (Q=1000) colored by the longitudinal velocity component for advance ratio J=0.6

Figure 5.6: Flow Visualization for two different advancing ratios, in case of Reynolds Number $3.6 \cdot 10^6$

In order to gain a better insight of the flow around the propeller and the influence of the advancing ratio J, two surface plots are presented, in Figure 5.5, for $J = 0.1$ and $J = 0.6$. For the larger advancing ratio, the streamtraces are aligned with the geometry and the pressure is larger at the leading edge of the propeller indicating a small effective angle of attack. On the contrary, at small advance ratios, the effective angle of attack is larger and consequently the stagnation point is moving upstream towards the trailing edge as the radius increases. Moreover, for $J = 0.1$, the streamtraces on the propeller and the pressure values near the tip of the propeller indicate flow a separation region.

Last but not least, Figure 5.6 presents visualization of the flow around the propeller. Figure 5.6a illustrates the pressure around the propeller and Figure 5.6b the tip and the hub vortices around the propeller. For the identification of the vortex structures the Q–criterion [146] is used. In this example, an iso–surface of Q=1000 is plotted, colored by the horizontal velocity component for J=0.6. The tip and the hub vortex can be identified in the plot. Due to flow separation at the hub of the propeller, the generated vorticity interacts with the root of the propeller and the generated vortex tubes are advected downstream.

5.2 KRISO Container Ship

Having completed the testing of the solver in one–phase flows, in the present section and forth, the evaluation of its performance in two–phase flows is examined. The next test case regards the hydrodynamic behavior of the KRISO Container Ship (KCS) in calm water conditions and in head waves. KCS is a concept container ship with a bulbous bow used as benchmark for displacement hulls. The analysis considers both the ship in fixed conditions (not able to move), as well as with two degrees of freedom in heave and pitch directions. A series of experiments have been conducted from the Korean Research Institute for Ships and Ocean Engineering (KRISO) to obtain resistance, amplitude of motions, free surface elevations and mean flow characteristics. This plethora of experimental results made it as one of the most popular test cases for validating numerical tools (see for example [147],[148]). The KCS hull has also been used as reference for a series of computational workshops, such as in Gothenburg 2010 [149], in Tokyo 2015 [150] and others. The characteristics of the full scale ship are summarized in Table 5.5.

Table 5.5: Main particulars of KCS in full scale

Length between perpendiculars	L_{pp} (m)	230.0
Maximum beam of waterline	B (m)	32.2
Draft	T (m)	10.8
Displacement	Δ (m^3)	52030
Wetted area w/o rudder	S_W (m^2)	9424
Wetted Surface area of rudder	S_R (m^2)	115
Block Coefficient	C_B	0.6505
Propeller center, long. location (from FP)	x/L_{pp}	0.9825
Propeller center, vert. location (below WL)	-z/L_{pp}	0.02913
LCB (%Lpp), fwd+		-1.48
Vertical Center of Gravity (from keel)	KG (m)	7.28
Metacentric Height	GM (m)	0.60
Moment of Inertia	K_{xx}/B	0.40
Moment of Inertia	K_{yy}/L_{pp}, K_{zz}/L_{pp}	0.25
Service Speed	U_s (knots)	24.0
	Fn	0.26

The present section follows the setup of three different experiments, attempting to compare the numerical results against a variety of data provided in literature. The section is divided as follows; firstly, the numerical setup is described, afterwards the resistance of KCS in calm water conditions is considered with two degrees of freedom, namely, the vertical displacement in the z axis –heave– and the rotation around the transverse y axis –pitch–. The numerical results are compared with experimental data taken from [151]. The available data from experiments are the resistance of the hull, as well as, the trim and sinkage of the ship, for 6 Froude numbers between 0.108 and 0.28. Furthermore, the free surface elevations in four longitudinal wave cuts are compared in the nominal Froude number (Fn=0.26). Afterwards, in order to compare free surface elevations and flow patterns, KCS is again examined in calm water conditions with zero degrees of freedom (fixed conditions) and the results are compared with experiments reported in [152]. Finally, KCS is assessed in head waves conditions. The Response Amplitude Operators (RAOs) and time series are compared with experimental data available from [150].

5.2.1 Numerical Setup

Prior to the systematic evaluation of the solver against experimental data, a parametric study to select the appropriate numerical setup is conducted. As benchmark test case, KCS in calm water conditions at the nominal Froude number is considered, based on the setup of [151]. The ship is able to move in heave and pitch directions. The scale ratio of the model is $\lambda = 31.6$ and the rudder of the ship is in place. According to Table 5.5, the nominal Froude number of the ship is $Fn = 0.26$, which results in $U_s = 2.196m/s$ for the model scale.

The computational domain is illustrated in Figure 5.7. Due to symmetry and in order to save computational resources, only the half of the ship is consider. The hull is positioned on the x–axis, the free surface at $z = 0$, the front perpendicular of the ship is positioned at $x = 0$ and the after perpendicular at $x = 7.2786m$. A rectangular numerical wave tank is selected for the simulations. Its dimensions are: in the longitudinal direction $x \in [-20, 25]$, in the transverse direction $y \in [0, 25]$ and in the vertical $z \in [-25, 10]$. In Figure 5.7, the dimensions of the computational domain in terms of L_{pp} are also given. As already mentioned, KCS is evaluated in calm water conditions and in head waves. The same computational domain is used in both cases. However, different boundary conditions and forcing zones are applied at the farfield boundaries of the domain. In case of calm water conditions all boundaries are set to farfield, except for the symmetry plane which is set to symmetry. The boundary conditions on the ship

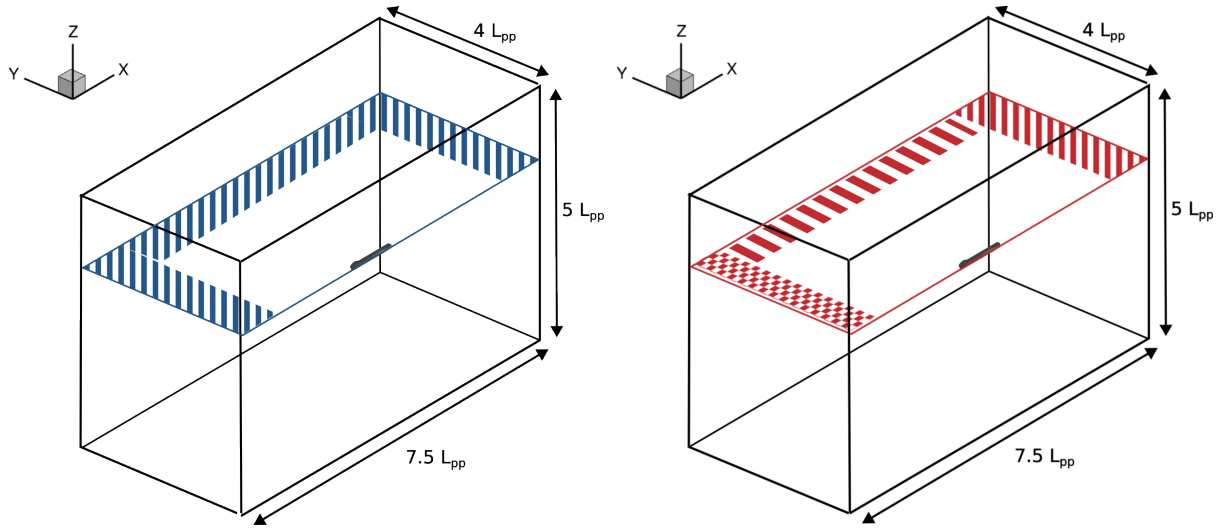

(a) Calm water conditions **(b)** Head waves conditions

Figure 5.7: Computational domain with implicit forcing zones for KCS evaluation, in calm water and in head waves conditions. Stripped areas denote wave absorption zones, while checkerboard areas wave generation zones

hull are set to no–slip, while on the deck the viscous effects are neglected and slip–free boundary conditions are applied. All farfield boundaries are equipped with wave damping zones of one ship length (L_{PP}) to ensure zero reflections from domain boundaries (see Figure 5.7a). The damping zones aim to minimize the vertical velocity component according to Equation (3.78) ($w_{tar} = 0$). In case of head waves, apart from the symmetry plane, the lateral plane on the starboard side is also set to symmetry and the rest of the boundaries are set to farfield as in the previous case. Regarding wave generation, upstream of the hull, a forcing zone of one wave length is defined, while downstream of the ship the wave absorption zone of the previous case is retained (see Figure 5.7b). Furthermore, a damping zone is defined at the lateral boundary of one ship length wide as well. However its purpose is to minimize the reflections from symmetry plane due to waves radiating by the ship. For this purpose the vertical to the boundary velocity component is minimized by setting $v_{tar} = 0$ to the source terms of Equation (3.78).

The flow is solved in the relative frame of reference with respect to the absolute velocity. As already described in Section 2.3, this means that the velocity of the surrounding fluid is zero, and the apparent grid velocity is $V_g = U_s$. In order to avoid strong transient effects, starting from rest, a tangential hyperbolic function is used to increase the speed of the ship within 500 timesteps. In the wall boundary conditions the VoF value is swept for a distance of $1mm$ normal to the wall. For the turbulence closure, the k–ω SST of Menter is used supplemented with the Devolder production limiter that mitigates the turbulence over–production near the free surface.

The Hexpress polyherdal trim mesher [153] was used for the generation of the computational mesh. Trim meshers are unstructured meshers that use an initial uniform rectangular mesh as base mesh and then cells are consecutively divided in half until the user–defined requirements are met. Typically, mesh refinement is imposed close to the solid boundaries and also in special defined areas (refinement zones) that are meant to capture various flow patterns, such as vortex streets or field discontinuities. Each cell can be divided either isotropically in all directions creating nodes that may not be shared by the neighboring cell (hanging nodes) or anisotropically in selected directions. The last feature renders them as ideal for test cases with strong discontinuities, as in the case of a numerical wave tank where also air is taken into account. The refinement zones used in the presented case studies are depicted in Figure 5.8. The refinement zones can be divided into two groups. The ones in Figure 5.8a aims at resolving

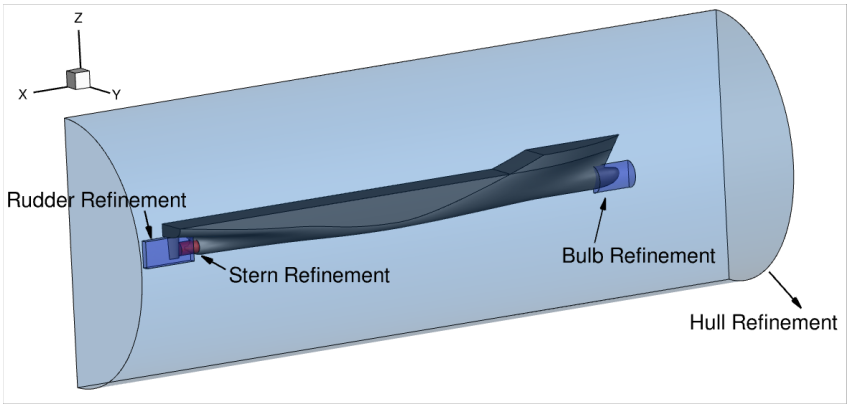

(a) Refinement boxes used to resolve the hull and its characteristics

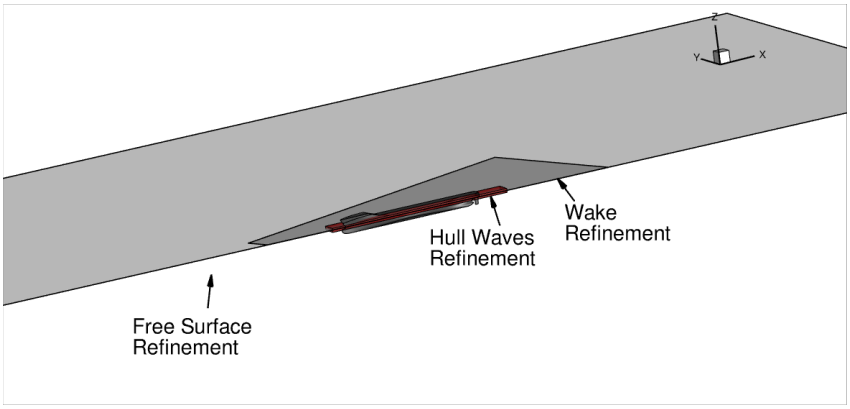

(b) Refinement boxes used to capture the free surface

Figure 5.8: Refinement boxes defined in the trim mesher to accurate resolve the geometry of the KCS and the created flow patterns

details of the geometry such as the bulbous bow, the stern and the rudder, while that in Figure 5.8b aims at accounting for the deformation of the free surface. One box is used to capture the wave elevation on the hull, the two crests formed on the bow and the stern of the ship and two troughs at the forward and aft shoulder. The second group is used to refine mesh in the vertically direction to capture the free surface elevation. A box is created in the vicinity of the free surface and another one to account for the Kelvin wake of the ship extended downstream over one ship length.

For the mesh parameters in the region of the wake, the ship advancing speed and the dispersion relation for deep water waves are used as reference. Assuming that $\omega^2 = kg$ holds, an estimation of the wave length in the ship's wake can be made as, $\lambda = 2\pi U_s^2/g$, with g being the gravity acceleration. Particularly, regarding the details of the three meshes, the *Coarse* grid consists of 1.48 million cells. The surface of the hull is discretized using 20 thousand elements. In order to capture the resulting wave system, a uniform refinement in the x and y direction is applied which corresponds to 50 grid cells per wavelength and in the z direction the grid step size is $12mm$ or 10 cells over the largest elevation based on the experimental data. The *Medium* consists of 3.93 million cells and the surface mesh has 41 thousand cells. The wake refinement has 100 cells per wave length and 20 cells over the wave height. Finally, the *Fine* consists of 8.9 million cells and the mesh on the hull surface is discretized using 46 thousand cells. The wake refinements consist of 200 cells along the wave length and 20 cells along the wave height. In order to, account for the wall friction, in all cases, cell layers are inserted at the viscous boundaries (ship hull). The first cell is placed 0.01mm normal to the wall which corresponds to y^+ values close to 1. Furthermore, 25 layers are inserted with growth rate 1.2 to effectively resolve the turbulent boundary layer. For the time discretization, a reference time length is defined based on the length of the ship between perpendiculars and the nominal service

speed, $T_{ref} = L_{pp}/U_s$. Three step sizes are selected which correspond to 250, 500 and 1000 per reference time scale, T_{ref}.

Table 5.6: Results of the mesh sensitivity study and comparison with respect to the finest mesh. The timestep size is dt=$T_{ref}/500$. Froude number $Fn = 0.26$

	$C_T \times 10^3$	C_T [%]	$\sigma \times 10^2$ [m]	σ [%]	τ[^{o}]	τ [%]
Coarse	3.887	4.55	-1.360	0.90	-0.180	2.35
Medium	3.725	0.2	-1.371	0.13	-0.177	0.39
Fine	3.717	-	-1.372	-	-0.176	

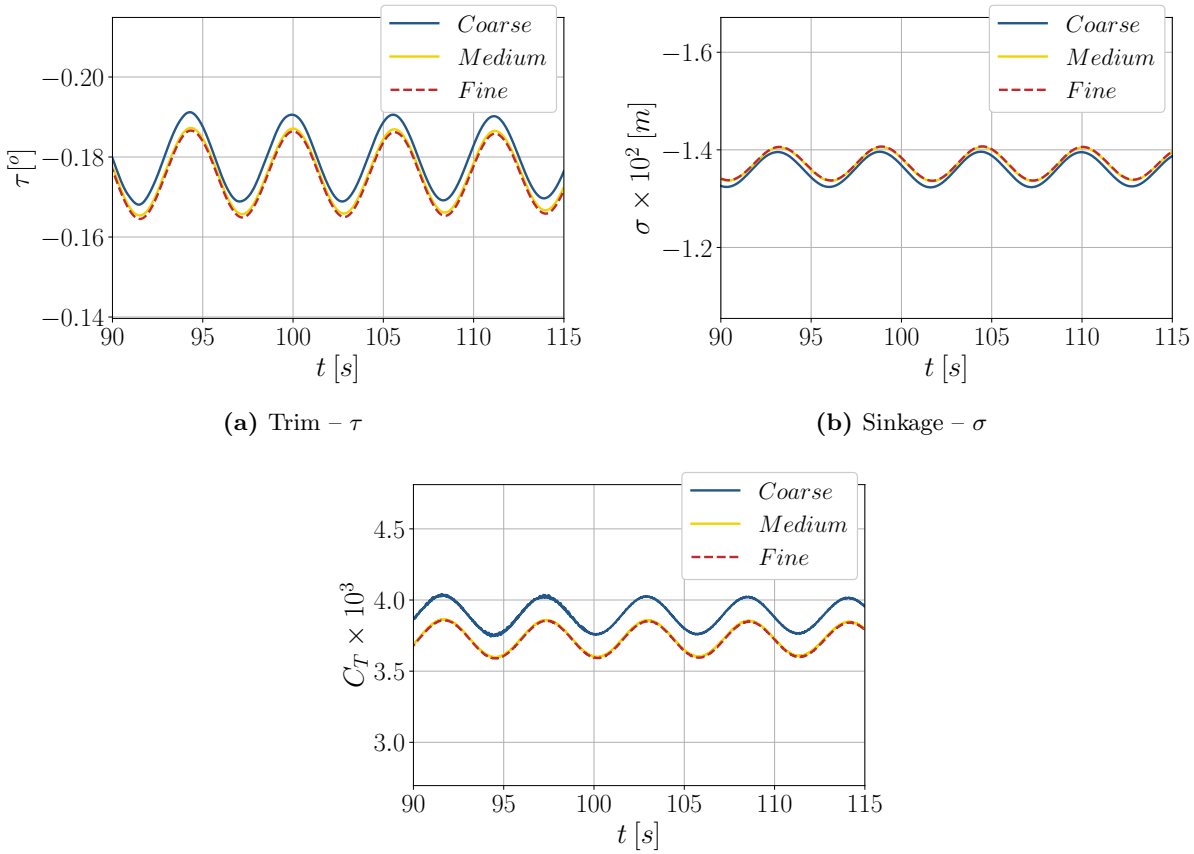

(a) Trim – τ

(b) Sinkage – σ

(c) Resistance Coefficient – C_T

Figure 5.9: Mesh sensitivity study for KCS in free running conditions in case of the *Medium* mesh. Froude Number $Fn = 0.26$. Convergence history of **(a)** trim, **(b)** sinkage and **(c)** resistance coefficient

The mesh sensitivity study precedes. In order to ensure small CFL values in all grids, the finest timestep is adopted for the study. The comparison is made upon the resistance coefficient – C_T, trim angle – τ and sinkage – σ. The results are presented in tabulated form in Table 5.6. Regarding the sign convention, the upward motion is defined as positive sinkage and a bow up rotation indicates positive trim angle. A convergence is noted for the *Medium* and *Fine* grids, with the maximum deviation being smaller than 0.4%.

Furthermore, in Figure 5.9, the three time series of the mesh sensitivity study are depicted. In all cases, the convergence histories have similar characteristics and the time signals for the *Medium* and *Fine* mesh do not present any major differences. For this reason, the *Medium* mesh is chosen for the rest of the simulations in calm water conditions.

Similarly, the timestep sensitivity study is conducted and the results are presented in Table 5.7. The differences between the three timesteps are minor and convergence is noted for a timestep size smaller than 500 steps per T_{ref}. This is further illustrated in Figure 5.10 where the time series of the three corresponding values are depicted. It can be pointed out that, the results for the two smaller timesteps practically coincide. At this point, it should be noted that in all signals an oscillatory behavior is noticed. As will be further discussed in Section 5.2.4, this is probably attributed to the wall treatment, which causes the slow convergence of the solver. The amplitude of the motion in all cases is smaller than 5% of the mean value.

Table 5.7: Results of the timestep sensitivity for the *Medium* mesh and comparison with respect to the smallest timestep. Froude number $Fn = 0.26$

	$C_T \times 10^3$	C_T [%]	$\sigma \times 10^2$ $[m]$	σ [%]	$\tau[^o]$	τ [%]
$T_{ref}/250$	3.714	0.28	-1.371	0.04	-0.176	0.61
$T_{ref}/500$	3.731	0.16	-1.37	0.02	-0.177	0.25
$T_{ref}/1000$	3.725	-	-1.371	-	-0.177	

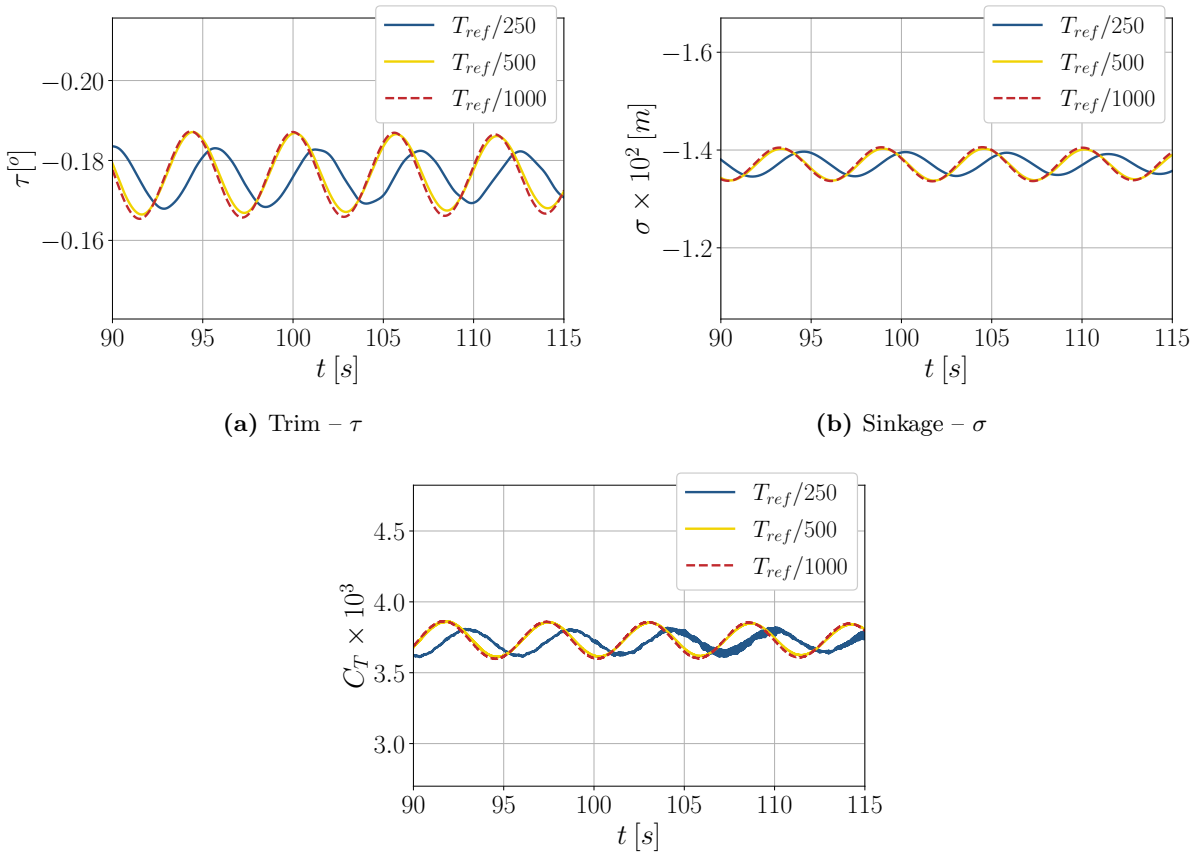

(a) Trim – τ

(b) Sinkage – σ

(c) Resistance Coefficient – C_T

Figure 5.10: Timestep sensitivity study for KCS in free running conditions for the *Medium* mesh. Froude Number $Fn = 0.26$. Convergence history of **(a)** trim , **(b)** sinkage and **(c)** resistance coefficient

An overview of the numerical parameters used in the simulations are detailed in Table 5.8.

The free surface elevation in the wake of the ship is presented for each grid, in Figure 5.11. All axes are non–dimensionalized with respect to the ship length between perpendiculars (L_{pp}). The free surface elevation is obtained as an iso–surface of the VoF field for $\alpha_l = 0.5$. A smearing of the wave pattern is noted in case of the *Coarse* grid. Nonetheless, minor differences are noted

Table 5.8: Numerical parameters used for the evaluation of KCS in calm water conditions with free trim and sinkage

Approx.	Turb. Limiter	# DoFs	Mesh	dt	β_i	CFL_τ
Fully Turb.	Devolder prod.	2	4379782	$T_{ref}/500$	$\max(10, 10\|U\|^2)$	10

between the *Medium* and the *Fine* grid.

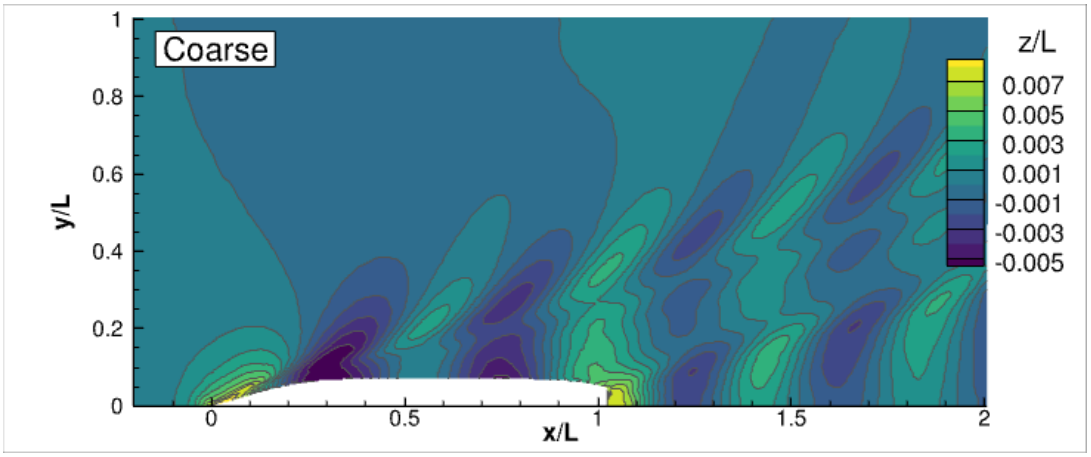

(a) *Coarse* mesh

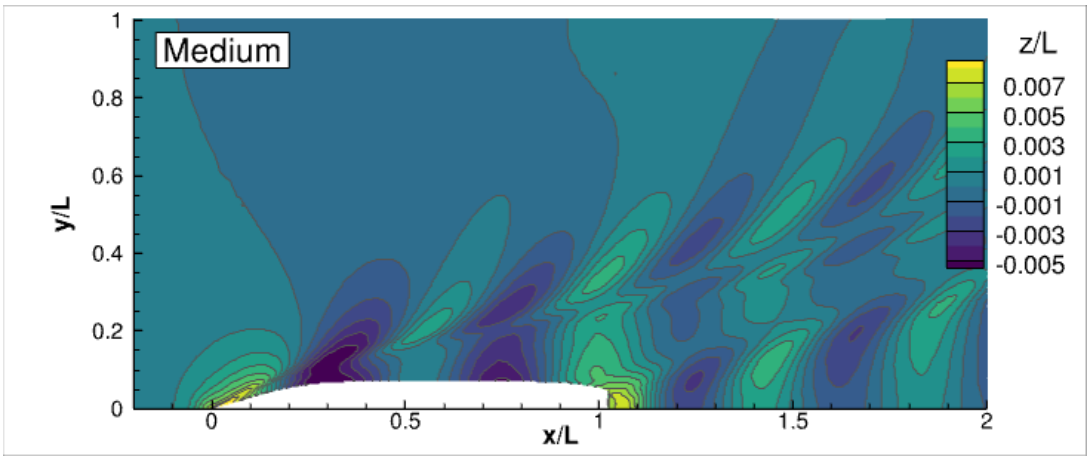

(b) *Medium* mesh

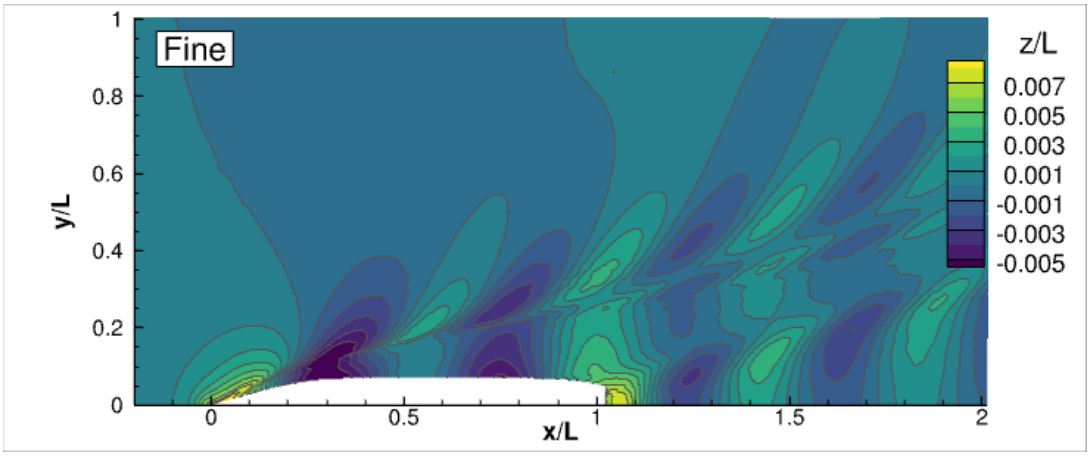

(c) *Fine* mesh

Figure 5.11: Mesh sensitivity study for KCS in free running conditions. Free surface elevation for the three meshes. Froude number $Fn = 0.26$

5.2.2 Fixed Conditions

Prior to present the systematic evaluation of the hull in heave and pitch free conditions, the hull in static condition, with zero degrees of freedom is considered. This test case focuses, primarily, on the flow formation around KCS. Various flow data such as wave elevation and velocity profiles are compared against experiments conducted in [152]. The ship is in the same scale as previously, $\lambda = 31.6$, however, in the present example the rudder is not installed. The same mesh parameters are used as before and mesh of 3.8 million cells is constructed. The mesh size is reduced compared to the previous study due to the absence of the rudder. Additionally, the timestep is $T_{ref}/500$ based on the previous analysis.

Comparing the computations with the experiments, firstly, the resistance coefficient measured is $3.56 \cdot 10^{-3}$, while simulations predict $3.43 \cdot 10^{-3}$ which is a deviation of 3.8%. Moreover the free surface elevation around the hull is provided by the experiments. In Figure 5.12, the comparison between the numerical (top) and the experimental (bottom) results is made. The comparison is fair and no major differences are noted between the two. The CFD simulations are able to produce adequate results and reproduce the wave system generated from the hull even for one ship length downstream.

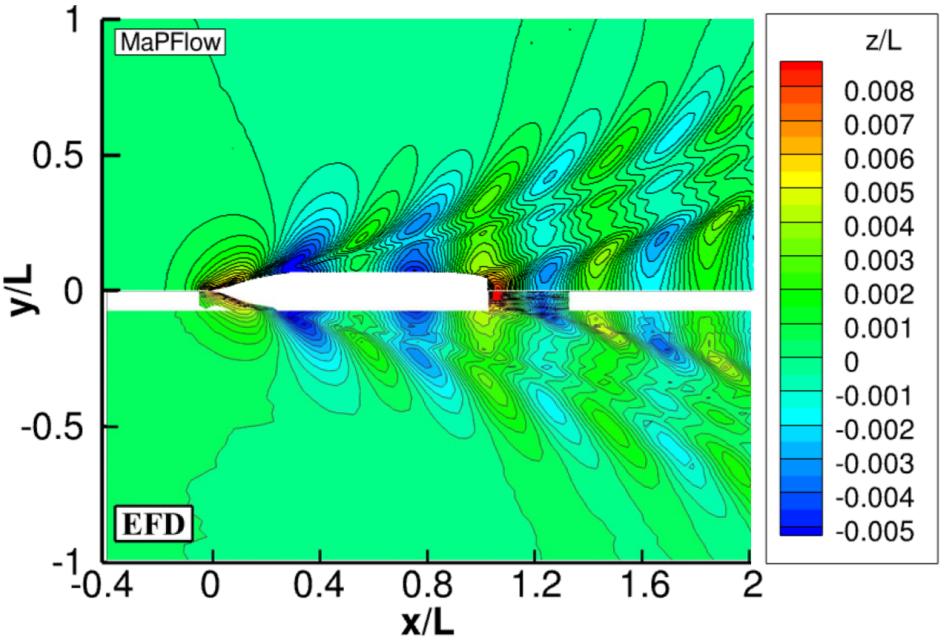

Figure 5.12: KCS in static conditions. Free surface elevation. Comparison between experimental and numerical results. Picture for experiment taken from [148].

Apart from the free surface elevation around the hull, during the experiments the free surface elevation on the surface of the hull was measured. In Figure 5.13 the elevation is plotted as obtained by the experiments and the simulations. A steep wave crest is produced at the bow of the ship, which the CFD is abl to reproduce but an offset lesser than 0.03% of the L_{pp} towards the bow is noted. Additionally, the crest of the stern wave is slightly overestimated by the CFD results. The wave troughs formatting at the front and aft shoulder of the ship are identical in the CFD and experimental results.

Finally, for the fixed conditions the local mean velocity fields are compared at the propeller plane, $x/L_{pp} = 0.9825$. In Figure 5.14a contours of the relative axial velocity, divided by U_s, are plotted, while Figure 5.14b presents the cross flow vectors and streamlines. Due to the propeller hub at the ship's stern, a weak vortex is formed which directly affects the propeller, this is indicated as velocity deficit in the axial component and it can also be seen in the cross flow vectors in form of swirl. Additionally, in Figure 5.14a the boundary layer thickness can

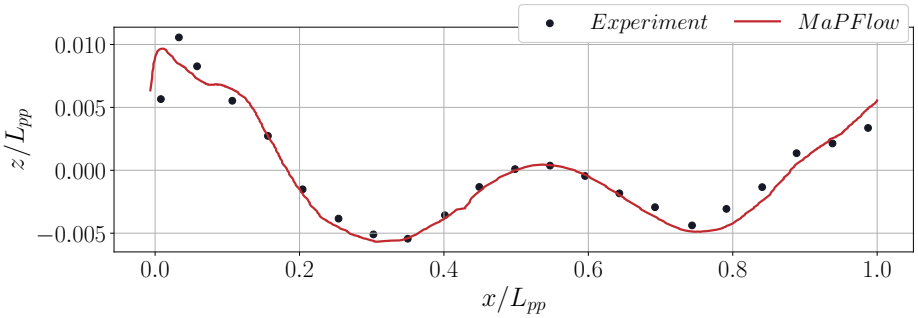

Figure 5.13: KCS in static conditions. Free surface elevation on the hull. Comparison between experimental and numerical results

be evaluated by the distribution of the axial velocity component. The numerical results are compared well against the experiments for both axial velocity and cross flow. A difference is noted at the effect of the stern bulb between the two. The CFD results under–predict the velocity deficit and the size of the vortex, which is attributed to numerical diffusion. Nevertheless, the comparison is considered fair.

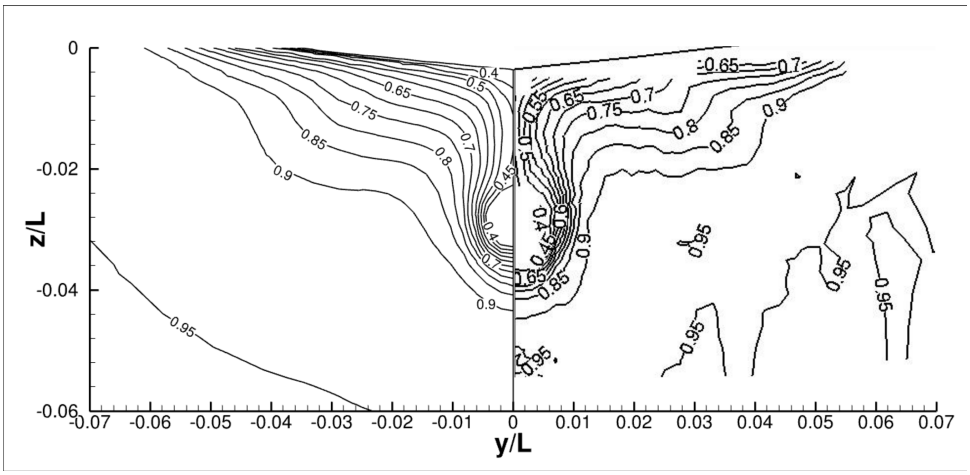

(a) Contour of the relative axial velocity divided by service speed U_s

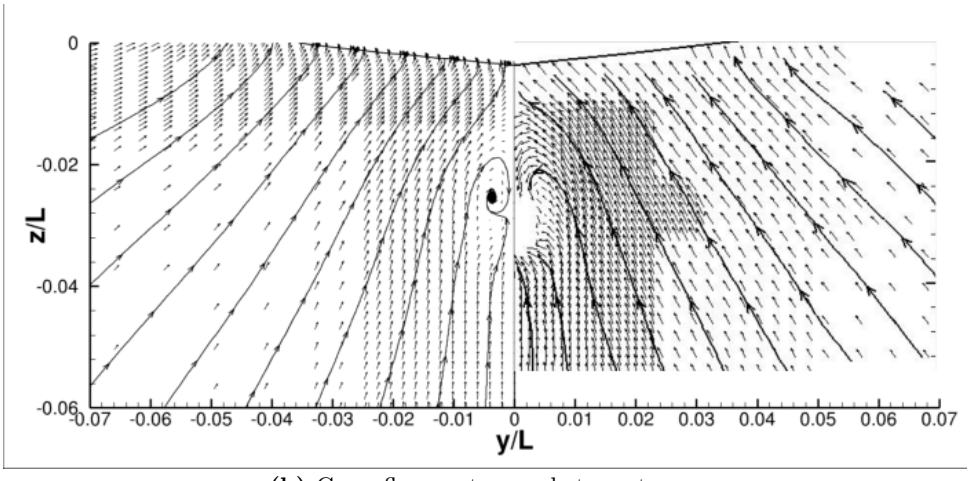

(b) Cross flow vectors and streamtraces

Figure 5.14: KCS in static conditions. Flow visualization comparison between numerical (left panels) and computational (right panels) results. At the top, figure contour lines of the axial velocity are presented, while at the bottom cross flow vectors along with streamlines. Pictures for the experimental date taken from [154]

5.2.3 Dynamic Trim & Sinkage

Since the numerical parameters of the problem, grid and timestep, have been selected and comparisons are made upon the static hull, the next step concerns the systematic evaluation of the hydrodynamic behavior of KCS in various Froude numbers with two degrees of freedom. Following the experiments reported in [151] and can be also found in [150], the hydrodynamic behavior of KCS in model scale is examined in calm water conditions. The ship is free to move in heave and pitch directions. In Figure 5.15, the computational results are presented for 6 different Froude numbers, between 0.108 and 0.28. The results regard resistance, trim angle and heave displacement. As previously mentioned for the sign convention, a positive trim angle moves the bow of the ship upwards and positive sinkage moves the center of mass upwards.

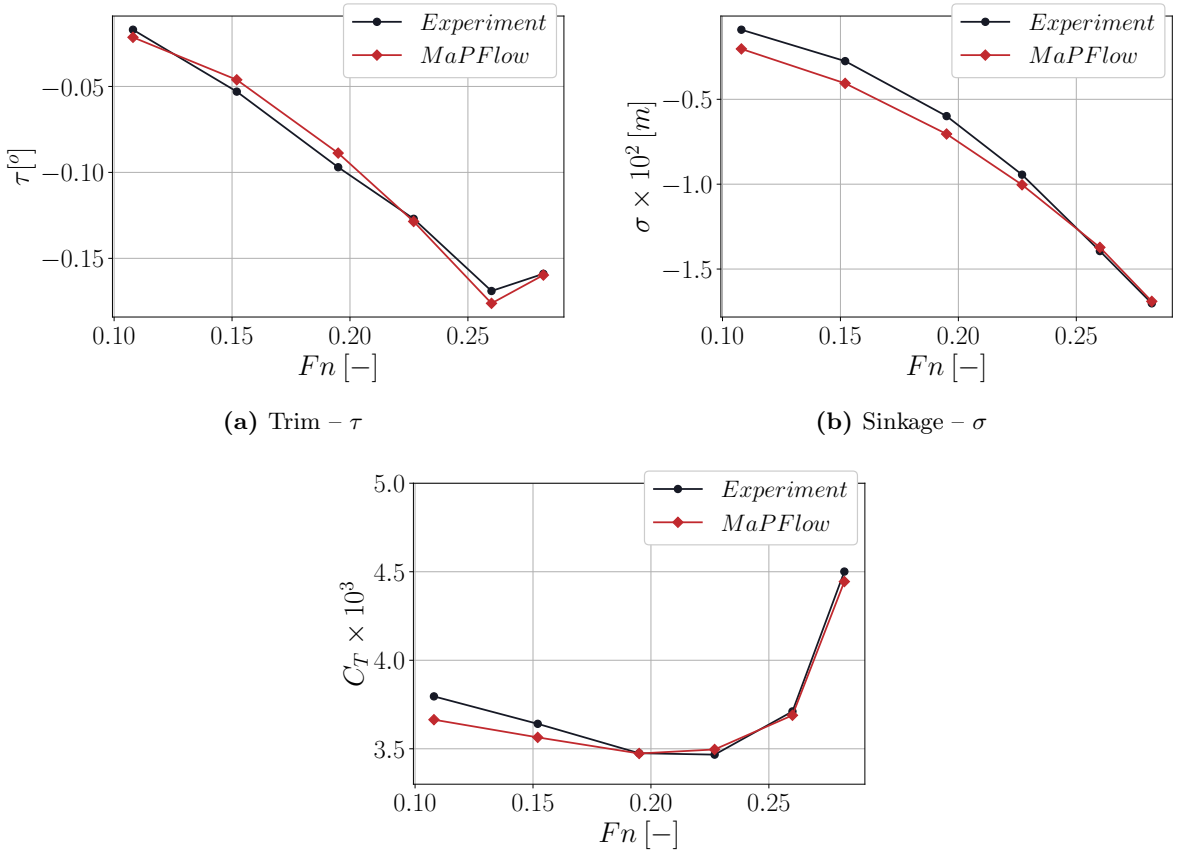

(a) Trim – τ

(b) Sinkage – σ

(c) Resistance coefficient – C_T

Figure 5.15: KCS in free running conditions. Comparison between experimental and numerical results

Overall, the computational results follows the trend of the experimental data. Specifically, the trim angle is always negative and increases in amplitude with increasing Froude number. This means, that the bow is moving down as the Froude number increases, except for the largest value $Fn = 0.28$, where a sudden decrease in amplitude is noted. The sinkage of the ship is decreasing with Froude number. Finally, the resistance of the ship becomes minimum for Froude numbers between 0.195 and 0.227, where also a sudden increase is noted for the largest Froude number. In general, the computational results present the same behavior as the experimental one and quantitative agreement is noted between the two. The trim angles predicted by the computational solver are very close to the experimental with the largest deviation being 0.008^o in trim at $Fn = 0.195$, $1.3mm$ in sinkage at $Fn = 0.152$ and 3.5% in resistance in case of $Fn = 0.108$. Moreover, as discussed in Appendix E, predictions obtained with *MaPFlow* agree

well with other numerical results.

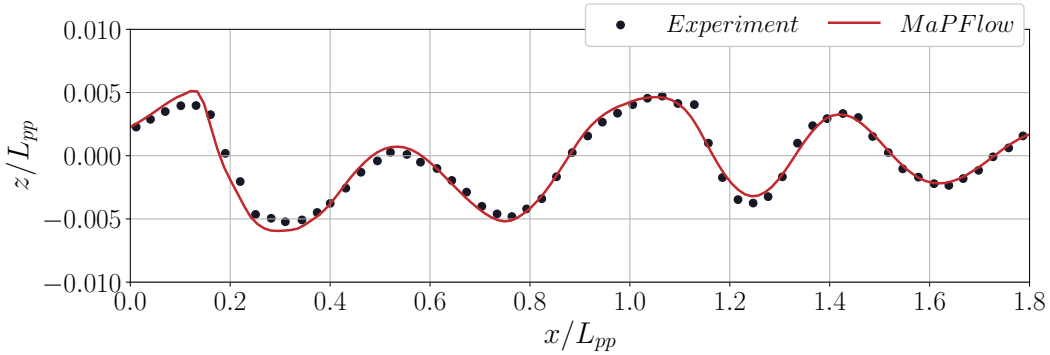

(a) $y/L_{pp} = 0.0741$

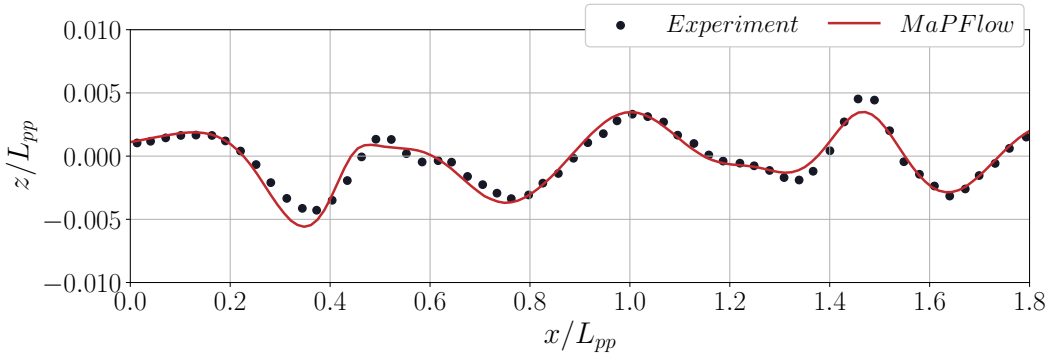

(b) $y/L_{pp} = 0.1509$

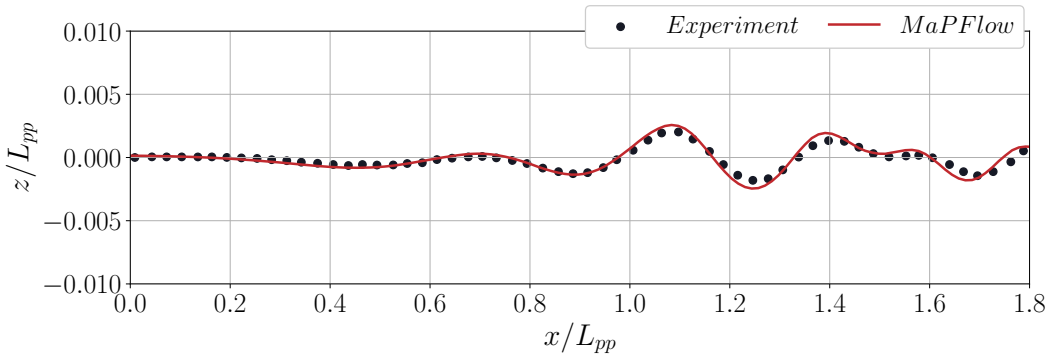

(c) $y/L_{pp} = 0.4224$

Figure 5.16: KCS in free running conditions. Comparison between experimental and numerical results. Longitudinal wave cuts in three different positions

Furthermore, in order to compare the wave elevation around the hull, three longitudinal wave cuts are compared in Fig. 5.16. The numerical results are able to follow the experimental adequately even away from the hull where the surface elevation is relative small (Fig. 5.16c).

5.2.4 Evaluation in Regular Head Waves

Up to this point, the numerical methodology has been assessed in calm water conditions. The next step is the assessment of the methodology, when the structure is excited under the presence of incident waves. The following test case regards the response of the KCS hull in regular head waves with two degrees of freedom. The ship, as in the previous case, is able to move in the pitch–θ and heave–z directions. The simulations follow experiments conducted at the FORCE technology center of Denmark [155] and also presented in the proceedings of the Tokyo 2015 CFD Workshop [150]. At this section, comparison is made against experimental results, while complementary comparison with numerical results submitted in the Tokyo CFD workshop is made in Appendix E.

The experimental model has length $6.070m$, which corresponds to scale ratio $r = 36.51$. The service speed, for this scale, is $2.0m/s$ and the rudder of the ship is installed. The experiments have considered 5 different wave lengths based on the ship's length (L_{pp}). Specifically, the characteristics of the head waves are $\lambda/L_{pp} = 0.65, 0.85, 1.15, 1.37, 1.95$, and in all cases the wave height is defined as $H/\lambda = 1/60$.

For the numerical setup, a single mesh is used for all simulations. The computational mesh near the structure is the same as in the previous cases, but scaled to match the FORCE experiments Furthermore, for the effective propagation of the surface waves, additional refinement zones are defined, which stretch from the inlet boundary until the wave absorption zone. The discretization in the x–direction corresponds to 60 cells per wavelength for the shorter wave and to 170 for the longer. In the z–direction, the mesh ranges from 6 to 17 cells per wave height for the 5 cases considered. The total mesh size is 5.38 million. The timestep is defined in all cases as 750 steps per wave period. The flow is solved in the relative frame of reference. The boundary conditions are the same as before, except from the starboard lateral boundary which is set to symmetry. For the forcing zones defined, as already described in Section 5.2.1, at the inlet boundary a wave generation zone is defined, at the outlet boundary an absorption zone is defined to damp the vertical velocity component ($w_{tar} = 0$), while an additional absorption zone is defined at the starboard lateral boundary avoid and reflection from the symmetry plane by setting v_{tar} . A schematic representation of the computational domain is given in Figure 5.7b. As in the previous cases, in order to avoid strong transient effects, the velocity of the vessel is increased gradually within 2000 based on a hyperbolic tangent function. Once, the vessel has reached its nominal speed, then the wave generation begins. The Stream Function theory of Fenton [92] is used for the wave generation. Finally, apart from the wave excitation test cases, the ship is evaluated in calm water conditions as well to obtain the added resistance of ship. The simulation is performed with the same mesh but neglects the refinements for the wave propagation, while the timestep is set to $dt = T_{ref}/500$ according to the previous sensitivity study.

Figures 5.17 to 5.21 compare the time historiesbetween FORCE experiments and numerical results for the 5 cases, for a ten period time window. Each figure presents the wave elevation ζ over the wave amplitude A, the resistance coefficient C_T and the response of hull in the degrees of freedom, heave–z/A and pitch–θ/kA, where k is the wavenumber. The experiments have reported structural resonance of the rigid mount close to the heave and pitch resonance condition [150]. This is clear in all C_T time histories and especially for λ/L equal to 0.85 and 1.15.

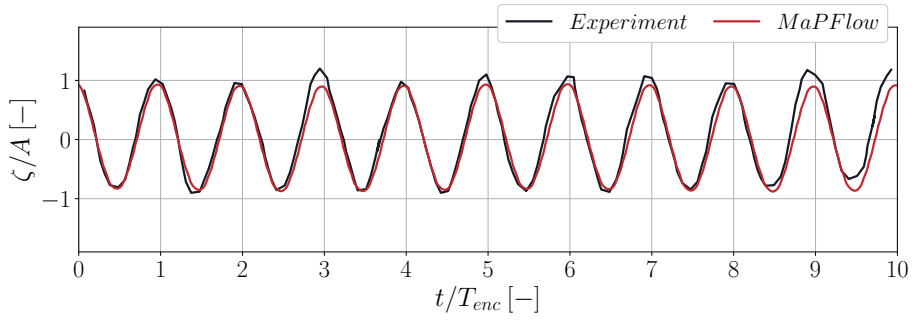

(a) Free Surface Elevation

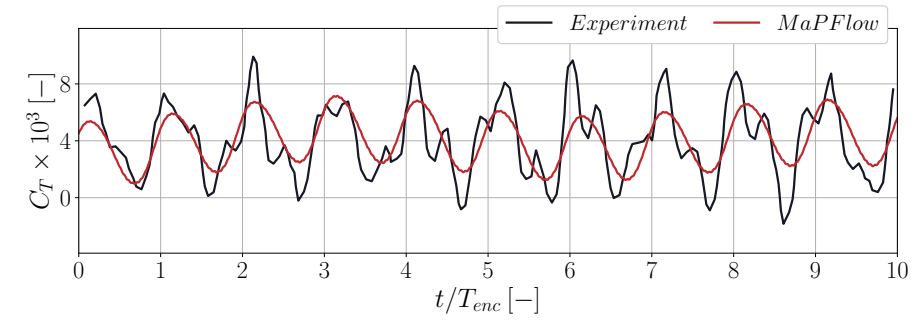

(b) Resistance Coefficient

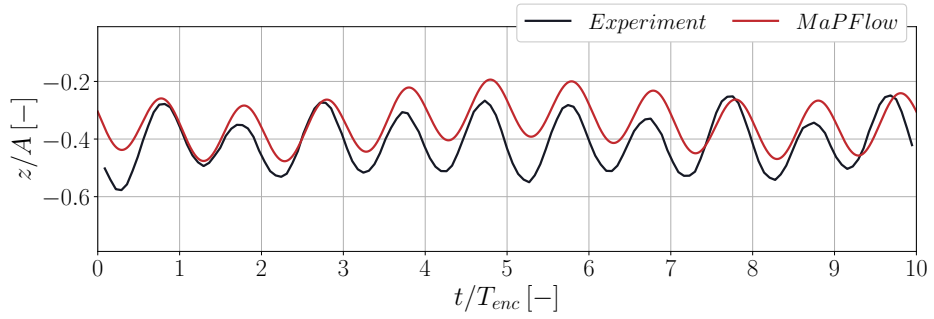

(c) Heave motion

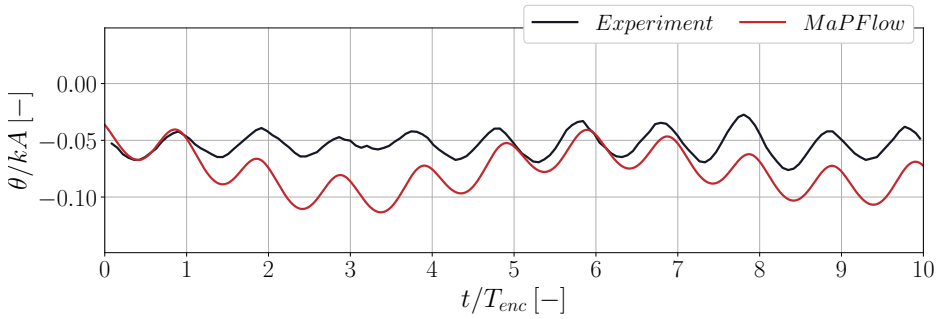

(d) Pitch motion

Figure 5.17: KCS in head waves conditions with $\lambda/L = 0.65$. Comparison between experimental and numerical results in a ten–period segment for wave elevation–ζ, resistance coefficient–C_T, heave–z and pitch–θ motion. Wave elevation and pitch motion are given with respect to the wave amplitude A, while pitch motion with respect to the wave amplitude A and the wave number k

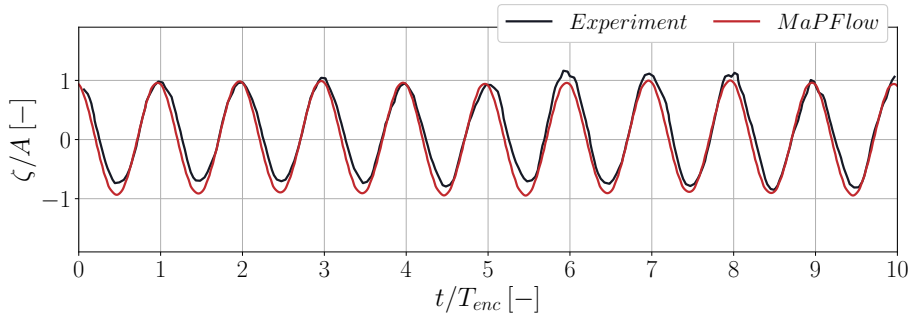

(a) Free Surface Elevation

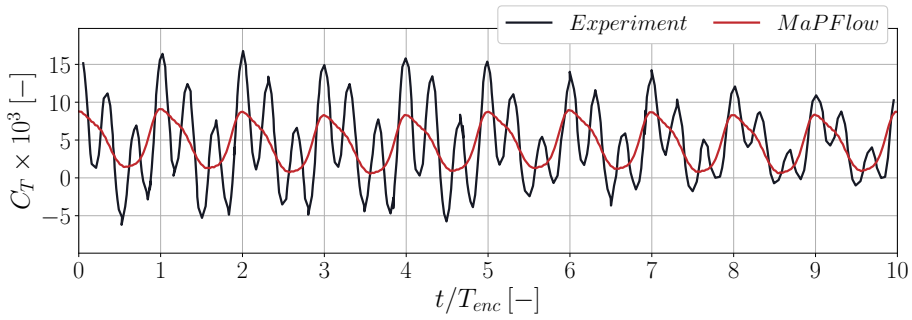

(b) Resistance Coefficient

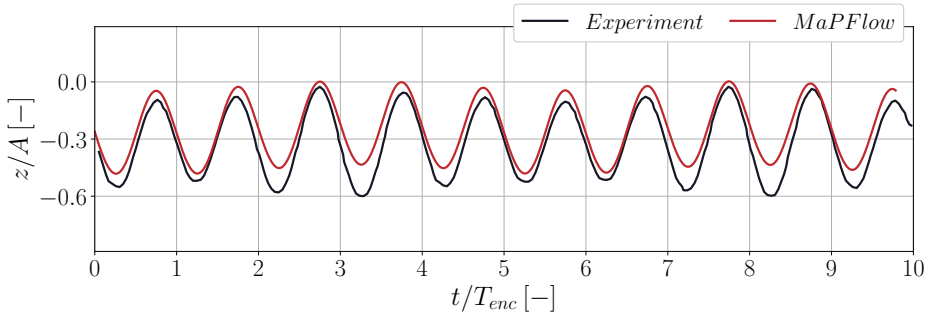

(c) Heave motion

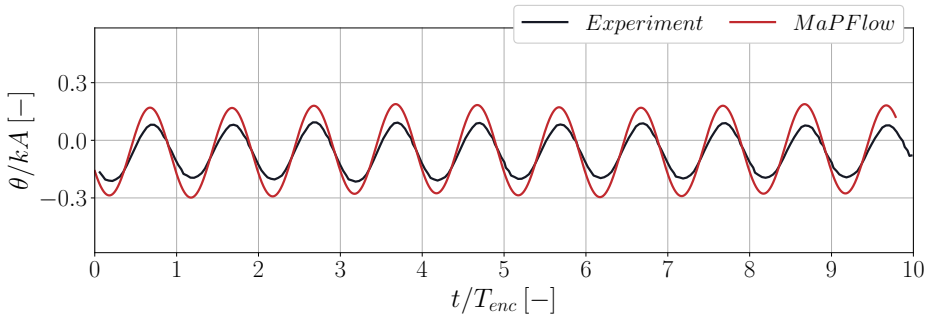

(d) Pitch motion

Figure 5.18: KCS in head waves conditions with $\lambda/L = 0.85$. Comparison between experimental and numerical results in a ten–period segment for wave elevation–ζ, resistance coefficient–C_T, heave–z and pitch–θ motion. Wave elevation and pitch motion are given with respect to the wave amplitude A, while pitch motion with respect to the wave amplitude A and the wave number k

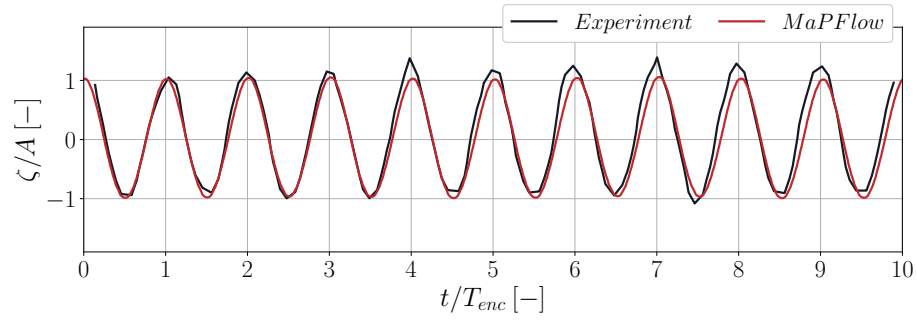

(a) Free Surface Elevation

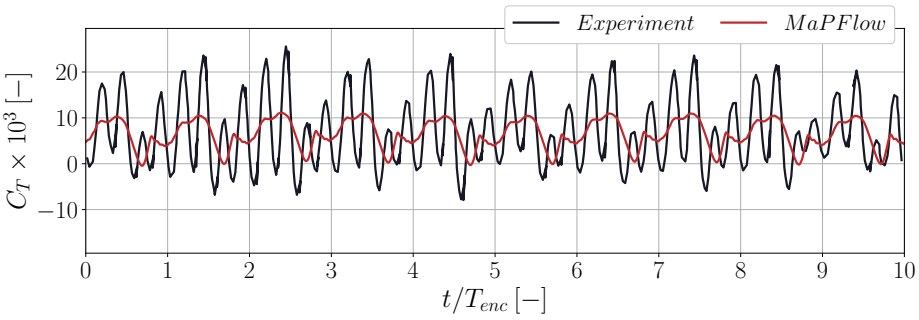

(b) Resistance Coefficient

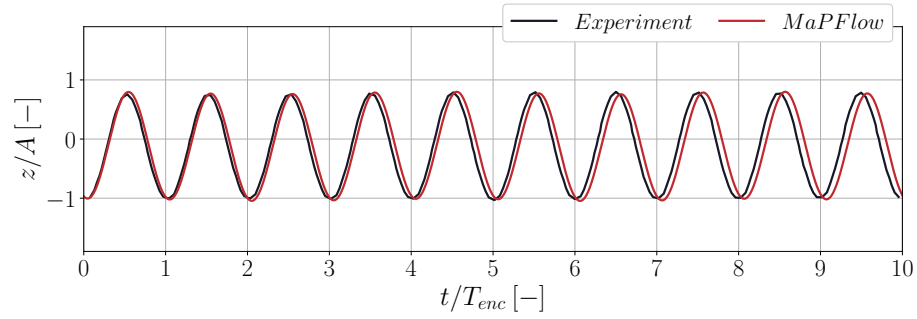

(c) Heave motion

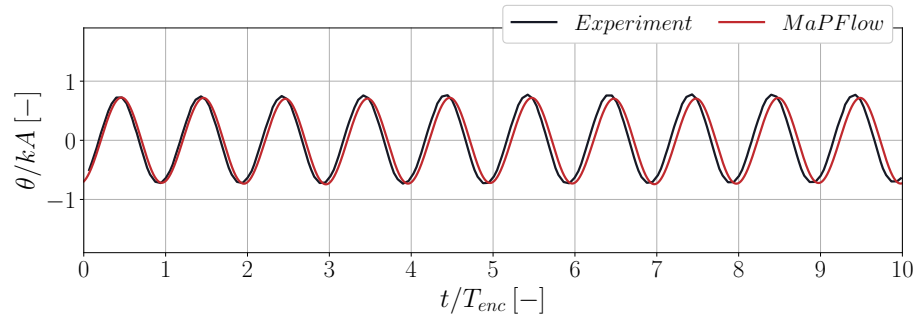

(d) Pitch motion

Figure 5.19: KCS in head waves conditions with $\lambda/L = 1.15$. Comparison between experimental and numerical results in a ten–period segment for wave elevation–ζ, resistance coefficient–C_T, heave–z and pitch–θ motion. Wave elevation and pitch motion are given with respect to the wave amplitude A, while pitch motion with respect to the wave amplitude A and the wave number k

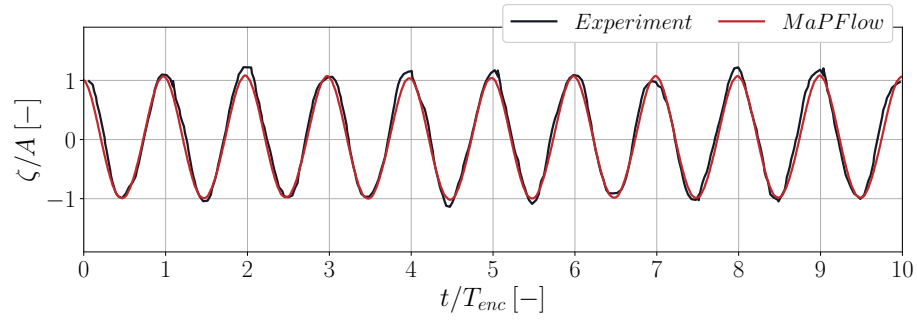

(a) Free Surface Elevation

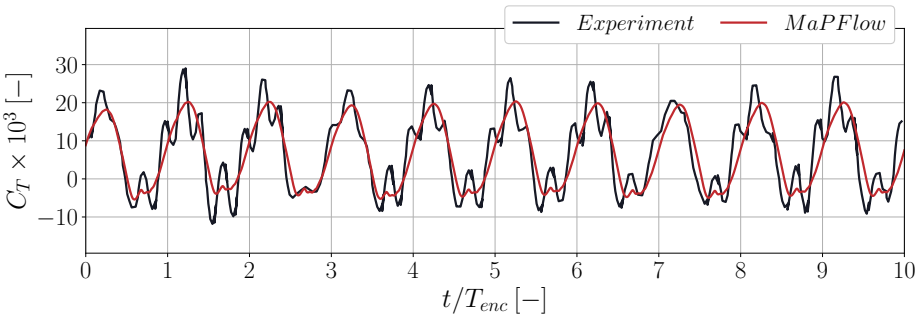

(b) Resistance Coefficient

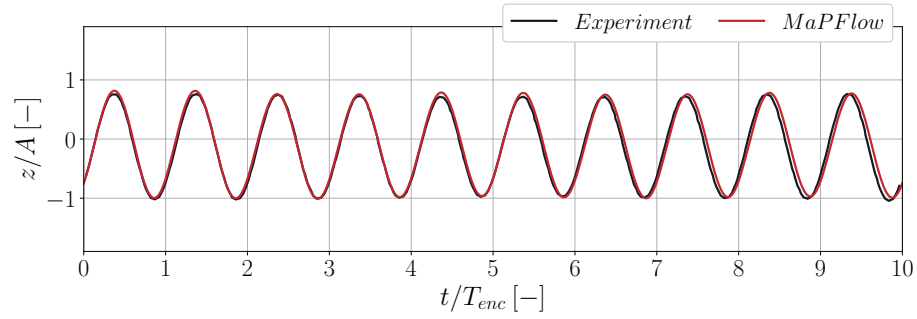

(c) Heave motion

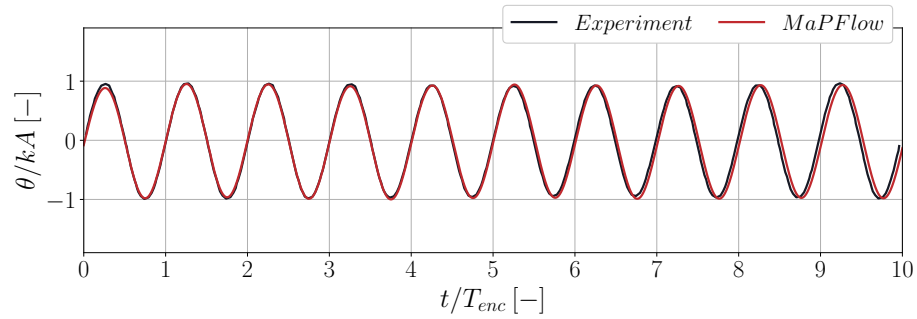

(d) Pitch motion

Figure 5.20: KCS in head waves conditions with $\lambda/L = 1.37$. Comparison between experimental and numerical results in a ten–period segment for wave elevation–ζ, resistance coefficient–C_T, heave–z and pitch–θ motion. Wave elevation and pitch motion are given with respect to the wave amplitude A, while pitch motion with respect to the wave amplitude A and the wave number k

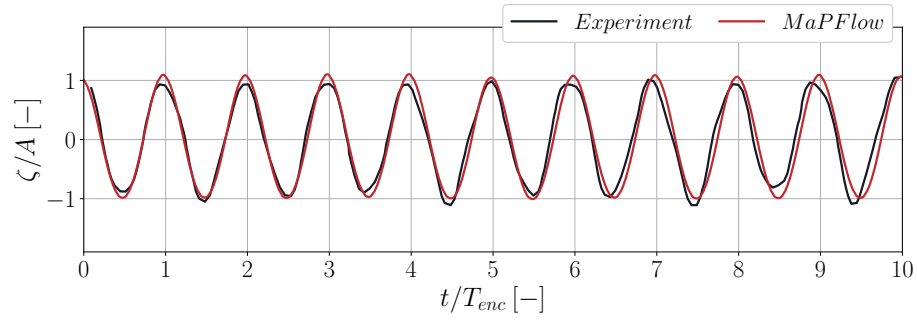

(a) Free Surface Elevation

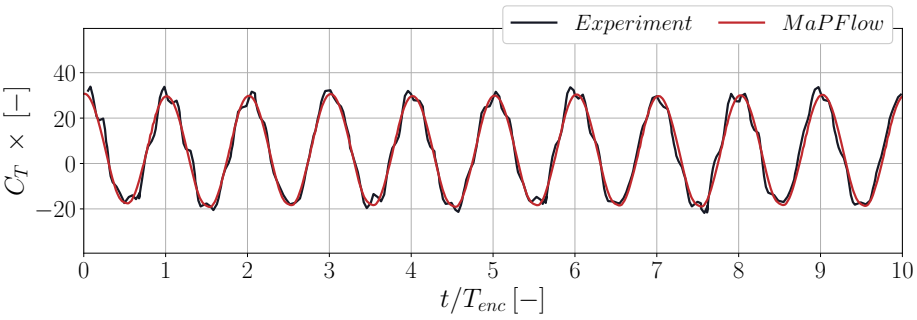

(b) Resistance Coefficient

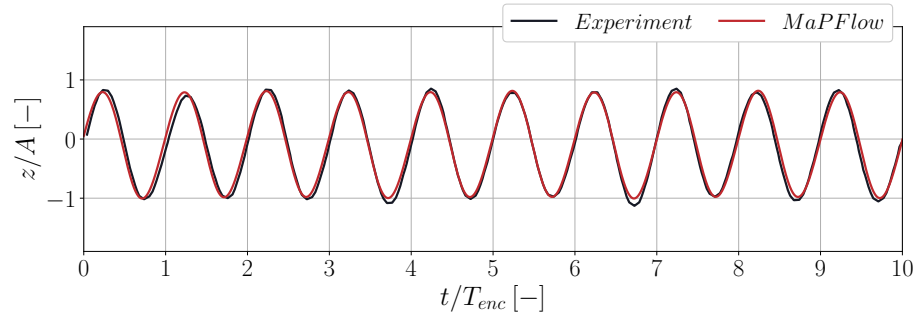

(c) Heave motion

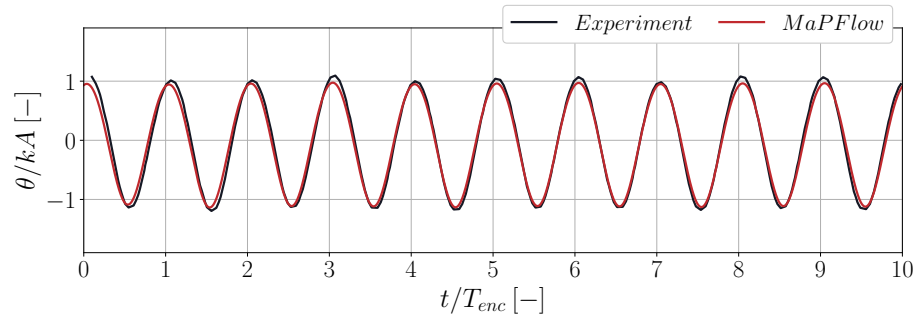

(d) Pitch motion

Figure 5.21: KCS in head waves conditions with $\lambda/L = 1.95$. Comparison between experimental and numerical results in a ten–period segment for wave elevation–ζ, resistance coefficient–C_T, heave–z and pitch–θ motion. Wave elevation and pitch motion are given with respect to the wave amplitude A, while pitch motion with respect to the wave amplitude A and the wave number k

The comparison is fair for all wavelengths, and especially for λ/L greater than 0.85 where the two datasets are in very close agreement. Deviations from the experiments are noted for $\lambda/L = 0.65$ and 0.85. Firstly, the simulations predict a larger amplitude in pitch for $\lambda/L = 0.85$ than the experiments. This difference is also present in other numerical approximations presented in Appendix E. Secondly, in both cases, the numerical results present a second slower frequency, which is more pronounced in the pitch and heave responses (Figs. 5.17c, 5.17d). This frequency is due to oscillations in trim and sinkage, present in the calm water conditions as well. In Figure 5.22a, the convergence history of the free trim case, in calm water conditions, is compared against the pitch convergence history for $\lambda/L = 0.65$. Both cases present similar characteristics and converge to the same mean trim value. Since, at these wavelengths the wave excitation is relatively small, the oscillation around the mean trim value is comparable to the response amplitudes and this is apparent in the time histories of pitch. This is also the case in all frequencies, however in case of larger excitation is less pronounced. This is further illustrated in Figure 5.22b, where a Fourier analysis is performed for all wave excitation cases and for the calm water conditions. An amplification is clearly seen, in low frequencies which is present in all cases.

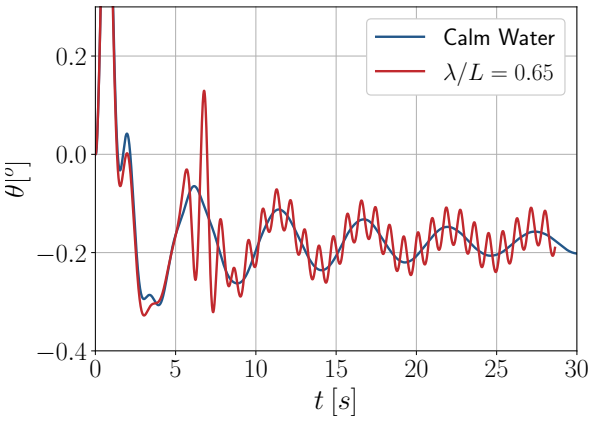

(a) Convergence history of pitch (θ) for the calm water and head waves ($\lambda/L = 0.65$) conditions

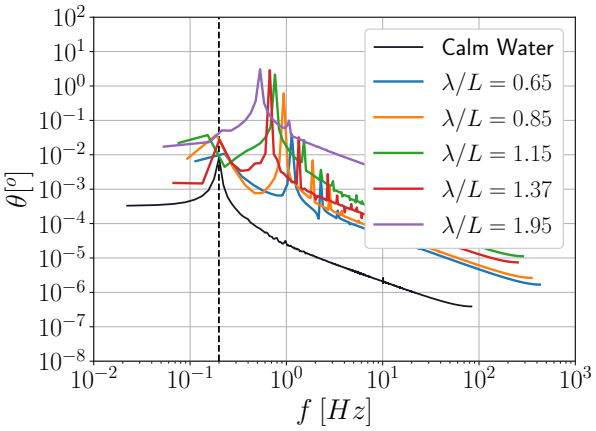

(b) Fourier analysis of the pitch convergence signals for the calm water and all examined head wave conditions

Figure 5.22: Convergence characteristics in calm water conditions of the pitch signal. The time history for calm water and for head waves are given on the left figure, while the right figure presents a Fourier analysis for all examined cases. A secondary frequency is present in all simulations related to convergence to mean values

Apart from the time histories the experimental data provide the added resistance coefficient– σ_{AR} and the 0th, 1st and 2nd harmonic amplitudes for the ζ/A, C_T, z/A and θ/kA. Figure 5.23 illustrates the comparison of the two sets. The added resistance, σ_{AR} is computed according to Equation (5.3), where $\bar{R}$ is the mean resistance in waves, R_{calm} the corresponding resistance in calm water conditions for Fn=0.26, A is the wave amplitude and B is the ship's beam.

$$\sigma_{AR} = \frac{\bar{R} - R_{calm}}{\rho g A^2 B^2 / L} \tag{5.3}$$

CFD and experiments produce similar results in all cases, especially, for the mean values and the first harmonics amplitudes. Minor deviations can be seen in the secondary harmonics. It is worth noticing that CFD computes the resistance coefficient of the ship as 3.708×10^{-3} against the 3.860×10^{-3} value given by the experiments. This deviation, of approximately 4%, is pronounced in the added resistance figure (Fig. 5.23a), especially for the short wavelengths.

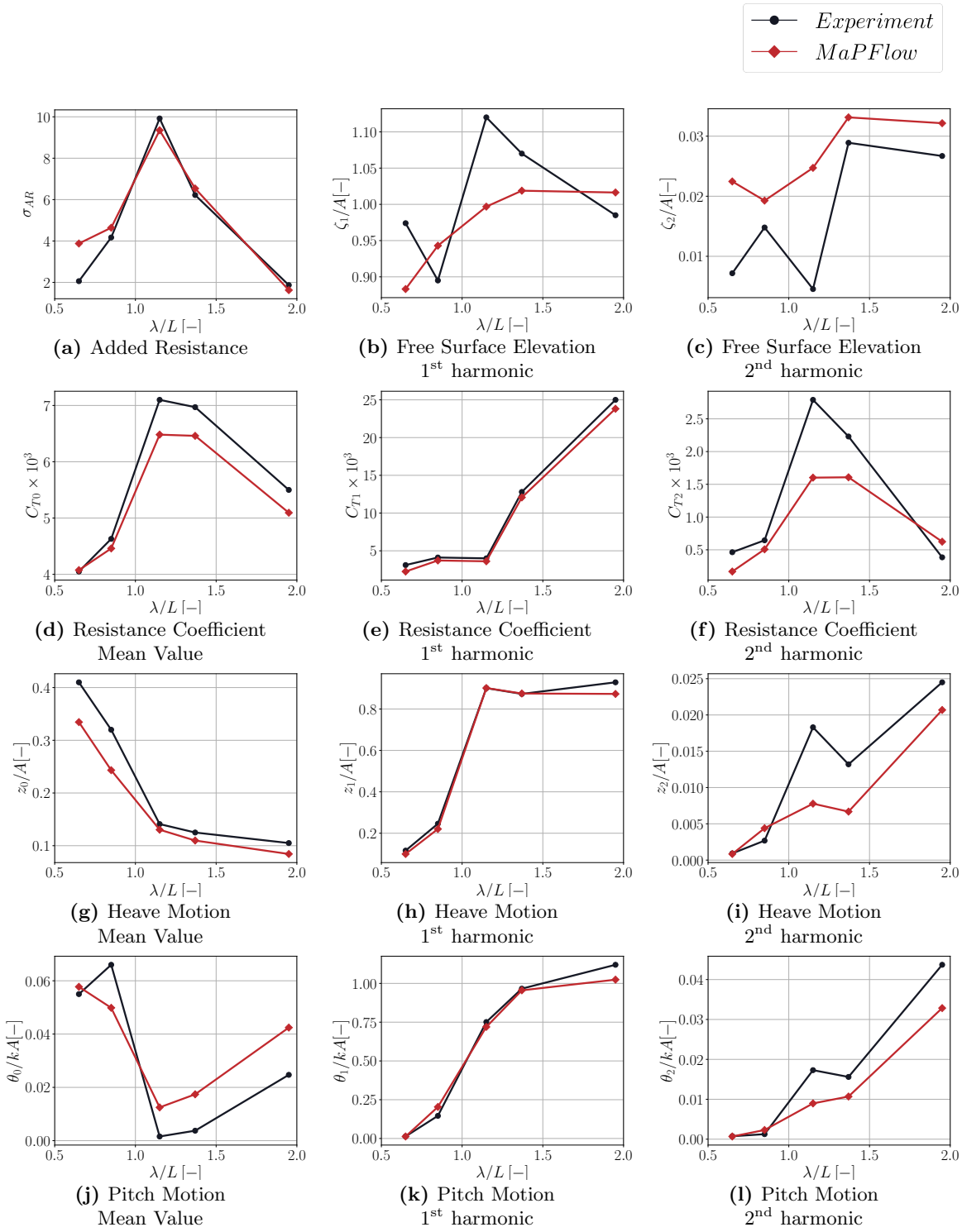

(a) Added Resistance **(b)** Free Surface Elevation 1st harmonic **(c)** Free Surface Elevation 2nd harmonic

(d) Resistance Coefficient Mean Value **(e)** Resistance Coefficient 1st harmonic **(f)** Resistance Coefficient 2nd harmonic

(g) Heave Motion Mean Value **(h)** Heave Motion 1st harmonic **(i)** Heave Motion 2nd harmonic

(j) Pitch Motion Mean Value **(k)** Pitch Motion 1st harmonic **(l)** Pitch Motion 2nd harmonic

Figure 5.23: Response Amplitude Operators (RAOs) of KCS in head waves conditions at $Fn = 0.26$. Comparison between experimental and numerical results, in terms of added resistance σ_{AR}, free surface elevation–ζ, resistance coefficient–C_T, heave–z and pitch–θ motion. The comparison is made upon the mean value (indexed with 0) and the amplitudes of the 1st and 2nd harmonics (indexed with 1 and 2 respectively). Free surface elevation ζ and heave displacement z are presented normalized the wave amplitude A, and pitch θ with respect to the wave amplitude A and the wave number k

5.3 Ship Bow Dynamics

Traditional screw–like propellers driven by an internal combustion engine is the most common form of marine propulsion. Internal combustion engines are responsible for the emission of the greenhouse gases (GHG). The maritime transportation industry was responsible for the 2.89% of the total anthropogenic emission in 2018 [156], or using an expression in equivalent carbon dioxide units (CO_{2e}), for 1,076 million tones annually. The Initial GHG Strategy [157] of International Maritime Organization (IMO) has been adopted which aims to reduce GHG emissions from international shipping. This strategy includes milestones as reduction of GHG emissions by at least 50% by 2050 compared to 2008 and further reduction by the end of the century. Ship retrofitting is an important aspect of the shipping industry efforts to reduce its environmental impact and comply with the IMO's initial. Retrofitting a ship's hull can involve a range of modifications that improve its efficiency, reduce its carbon footprint, and extend its lifespan. By retrofitting existing ships with more efficient technologies and alternative fuels, the industry can reduce its emissions while also improving its operational efficiency.

To this end, Seatech H2020 EU funded project, titled as "Next generation short-sea ship dual–fuel engine and propulsion retrofit technologies" (`https://seatech2020.eu/`, accessed on 28 July 2023), studied the development of two symbiotic ship engine and propulsion innovations. This project proposes the use of a wing arranged in front of the bow in order to augment ship propulsion in moderate and higher sea states by capturing the energy wave. The idea stems of the field of biomemetics, in which inspiration is drawn from nature to create mechanisms than can used to solve complex human problems. Sea animals propel themselves by creating an oscillatory motion with their bodies. This rhythmic motion allows to either propel themselves or harvest kinetic energy from incoming flow to enhance their forward motion [158], [159]. Mimicry of this motion has led to the investigation of either passively or actively set wings that can be used either as energy harvesting or as means of propulsion. This motion can be imitated by a flap and a pitch motion with an appropriate phase difference. Seatech H2020's project takes this simple concept and applies to a vessel. Ships undergo an oscillatory vertical motion due to waves, this can be exploited for thrust production by installing a wing in front of the ship bow, supplemented with a pitch control mechanism. Results have shown [160–162] that the dynamic wing can be used to generate additional thrust and enable the engine to operate in part–loads conditions without compromising the vessel's speed and thus improving its emission profile. Apart from the generated thrust, the dynamic wing can be used to improve the dynamic stability of the vessel in case of head waves.

This section aims to enrich the current findings and study the use of a static foil arranged at the ship bow and investigate its effect in presence of waves. Static foils can be used to reduce the ship motion and eventually the added resistance of the ship in presence of waves. Moreover, before examining the ship under the excitation of waves, a preliminary study of the behavior of the vessel in calm water condition with and without the foil is presented as well as the use of the wing for trim control. Numerical simulations are compared with available experimental data. The experiments were conducted in the Towing Tank of LSMH at NTUA [143]; see also [163]. More precisely, this chapter is divided into 5 subsections. Firstly, the numerical setup of the investigation is presented. Secondly, the base hull is considered in two different draughts, in six Froude numbers between 0.043 and 0.28 and compared with experimental data. In this case the vessel is able to rotate around the transverse, y–axis (pitch) and move vertically in the z–axis (heave). The second subsection, focuses on the effect of the wing and its supporting structure in calm water conditions. In addition, a quantification of the impact of the experimental setup is presented. Afterwards, the use of a static wing for trim control is investigated. Lastly, the effect of a static wing arranged at the bow is assessed in head waves and numerical results are compared against experimental data.

The vessel is a ferry ship model of length $L = 3.3m$, while the foil planform is orthogonal

and the foil section is a NACA0012. The body plan of the ferry is presented in 5.24 and its particulars are given in Table 5.9 along with the geometrical characteristics of the foil.

Table 5.9: Main Particulars of the ferry ship model and submerged wing

Length between perpendiculars	L_{pp} (m)	3.3
Maximum beam of waterline	B (m)	0.43
Draft	T_1 (m)	0.135
	T_2 (m)	0.125
Block Coefficient	C_B	0.45
LCB (%Lpp), fwd+		-2.4
Vertical Center of Gravity (from keel)	KG/T	0.2
Moment of Inertia	K_{xx}/B	0.25
Moment of Inertia	K_{yy}/L_{pp}	0.20
Service Speed	U_s (m/s)	1.42
	Fn	0.26
Foil span	s (m)	0.50
Aspect Ratio	AR	4
Foil location (from FP)	x_{wing} (m)	0.5
Foil submergence	d/T	1.6

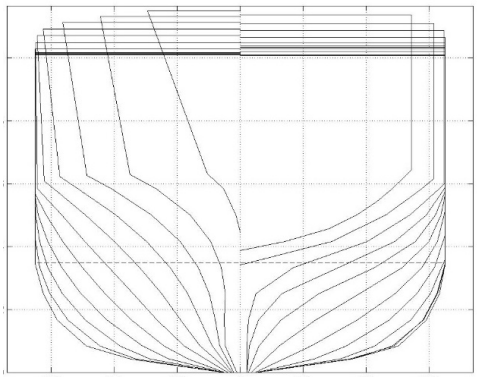

Figure 5.24: Ferry Body Plan

5.3.1 Numerical Setup

For the numerical simulations a single wave tank is used. Its basic dimensions are illustrated in Figure 5.25a. In order to save computational resources only the half model is simulated by applying symmetry conditions. The origin of the coordinate system is positioned at the section where the front perpendicular meets the plane that defines the bottom of the hull. The x–axis points towards the aft of the ship, the z–axis upwards and the y–axis towards the starboard side in order to form a right handed coordinate system. Based on this definition, a positive trim angles results to bow up rotations and positive sinkage to an upwards motion of the ship center of mass.

In Figure 5.25b, the implicit source zones applied near the boundaries of the domain are depicted. In case of calm water conditions, all zones serve as damping zones aiming at reducing the amplitude of the vertical velocity component. In this case, all boundary conditions are set to farfield. However, in case of head waves, Z3 is used for generating waves, Z2 for damping the transverse velocity component, while Z3 damps the vertical component of the velocity as before. The boundary conditions are the same as in the calm water case, with the exception of

the lateral boundary which is set to symmetry. For the wall boundaries, viscous effects are only considered on the hull of the ship and neglected on the deck. No–slip boundary conditions are applied on the hull, while slip–free conditions are considered on the deck. Similarly to the case of KCS, in order to avoid strong transient effects on the body, the model is accelerated using a hyperbolic tangent function, this time for 1000 timesteps, which is found to provide better numerical convergence characteristics. As in the case of the KCS, presented in the previous chapter, to model turbulence, the k–ω SST model is used along with the Devolder production limiter.

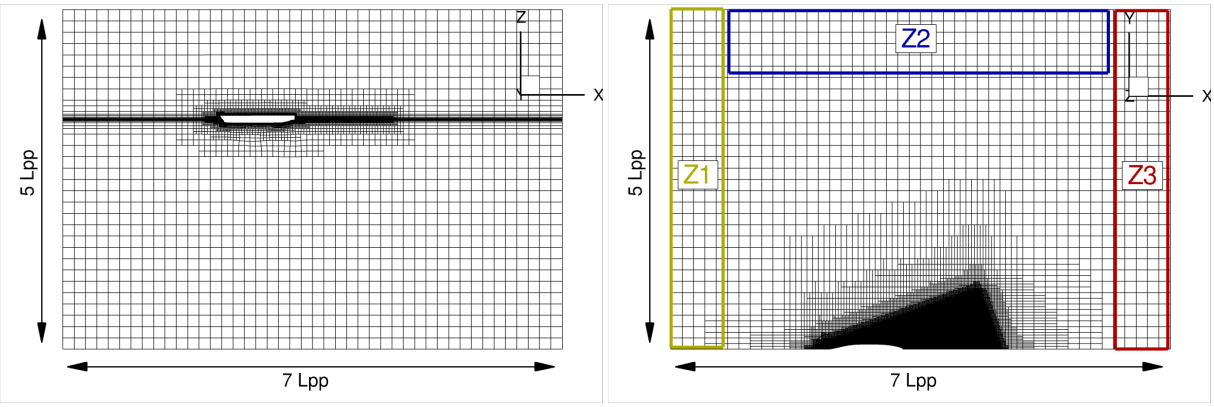

(a) Grid side view **(b)** Grid slice view

Figure 5.25: Overview of the computational domain. The forcing zones (Z1, Z2, Z3) are noted on the right figure

Three different grids are generated consisted of 902 thousand (*Coarse* mesh), 2.46 million (*Medium* mesh) and 6.11 million (*Fine* mesh) cells. The parameters used for the grid refinement are the number of cells on the body (surface mesh), the number of cells over the height of the hull generated waves and the number of cells per wavelength. The same timestep is adopted in all simulations and it is small enough to keep the mean CFL value below 1 in the finest mesh (approximately 0.60). Table 5.10 provides the results of the sensitivity studies. Convergence of the results is noted between *Medium* and *Fine* mesh, since the differences are less than 1% for the resistance and sinkage, and 3.5% for the trim angle, thus the *Medium* mesh is chosen in the sequel. Furthermore, in order to choose the right timestep for the computations, a similar parametric study was conducted. The three different timesteps were chosen based on $T_{ref} = L_{pp}/U_s$, where L_{pp} is the ship length and U_s the nominal advance speed. The results can be found in Table 5.11. Since the problem converges to a steady solution, all cases produce similar results. For the rest, the intermediate timestep is used.

Table 5.10: Mesh sensitivity studies for the ferry ship model

	R [kp]	δR [%]	τ [deg]	$\delta\tau$ [%]	σ [cm]	$\delta\sigma$ [%]
Coarse	0.682	3.12	0.0922	5.63	-0.392	1.5
Medium	0.687	2.41	0.0954	2.35	-0.388	0.5
Fine	0.704	–	0.0977	–	-0.386	–

Table 5.11: Time sensitivity studies for the ferry ship model

	R [kp]	τ [deg]	σ [cm]
$T_{ref}/250$	0.686	0.0958	-0.387
$T_{ref}/500$	0.686	0.0959	-0.387
$T_{ref}/2500$	0.687	0.0954	-0.388

In order to provide a better illustration of the convergence studies, in Figure 5.26, the results of the grid and timestep independence are shown in terms of vessel resistance. Again, consistency of results is noted between *Medium* and *Fine* mesh and between the two smaller timesteps. The numerical setup used for the evaluation of the ferry ship is summarized in Table 5.12.

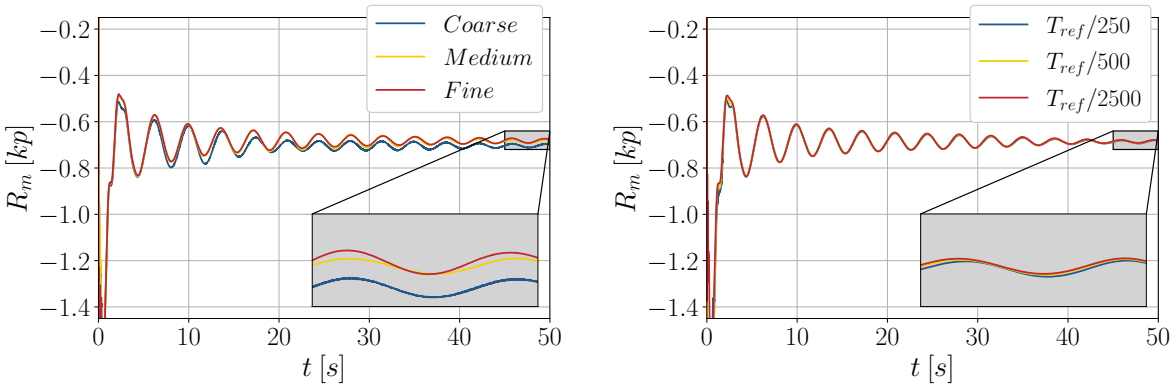

(a) Mesh Sensitivity Study **(b)** Time Sensitivity Study

Figure 5.26: Convergence studies of the time and mesh discretization

Table 5.12: Numerical parameters used for the study of the ferry ship hull

Approx.	Limiters	# DoFs	Mesh	dt	β_i	CFL_τ
Fully Turb.	Devolder prod.	2	2218013	$T_{ref}/500$	$\max(10, 10\|U\|^2)$	20

Figure 5.27 presents the density field on the hull of the ship. Apart from a steep wave crest formed on the bow, no apparent elevation is noted in the rest of the hull and no major deformation is noted. It is noteworthy that the density field changes smoothly between water and air on the surface of the hull and no areas of density diffusion are observed. The no–slip boundary condition which is imposed on the model, can lead to a singular behavior of the free surface on the wall. As described in the Boundary Conditions Section 3.5, in case of the solid boundaries to facilitate convergence the values of α_l are swept close to the hull. As the free surface deforms due to the model motion, the no–slip boundary condition does not allow convection of the volume fraction on the wall. A triple phase contact line is created among the hull, water and air. In steady simulations (e.g. hull resistance) this line reaches at a equilibrium once the wave on the hull has converged. This transient behavior may significantly affect convergence of the simulation. For this reason, it is preferred to performing a sweeping of α_l values normal to the hull.

Furthermore, Figure 5.27 also includes a contour of the y^+ values on the hull. The first grid node is placed 0.01mm away from the solid boundary, which leads to $y+ < 1$ almost everywhere over the hull and thus the turbulent boundary layer is fully resolved.

5.3.2 Dynamic Trim & Sinkage of the Bare Hull

Having decided the numerical configuration of the simulations, the results obtained from the systematic evaluation of the hull with and without the foil are presented. Firstly, the dynamic behavior of the bare hull is considered. Figure 5.28 presents the comparison of the numerical predictions against the measurements for the two draughts. It is evident, that the computational results are close to the experimental data especially for the heavier condition (T=0.135m). For the lighter condition, larger deviations are evident.

Regarding the comparison of the trim and sinkage characteristics of the vessel, Figure 5.28a illustrates the predicted trim values against the measured ones, for the two draughts. As

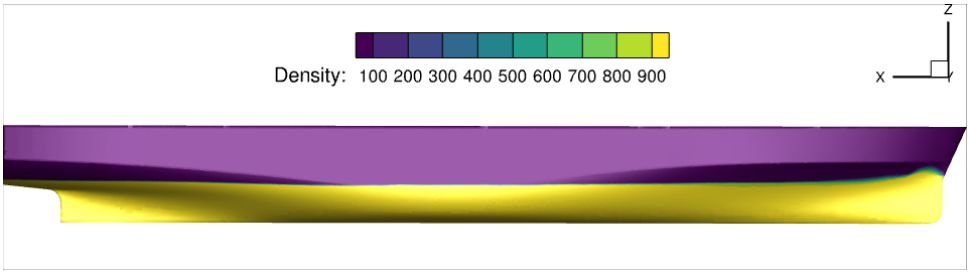

(a) Free surface elevation

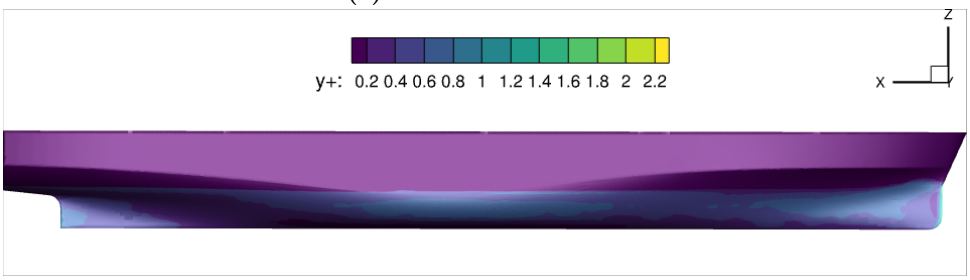

(b) y^+ values

Figure 5.27: Free surface deformation on the ship hull in case of calm water conditions. Draught $T = 0.135m$ and $Fn = 0.25$

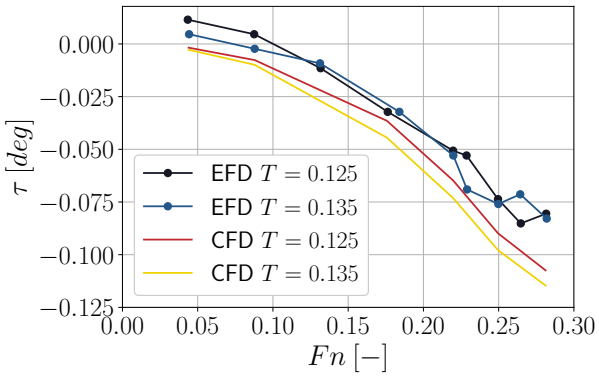

(a) Trim angle

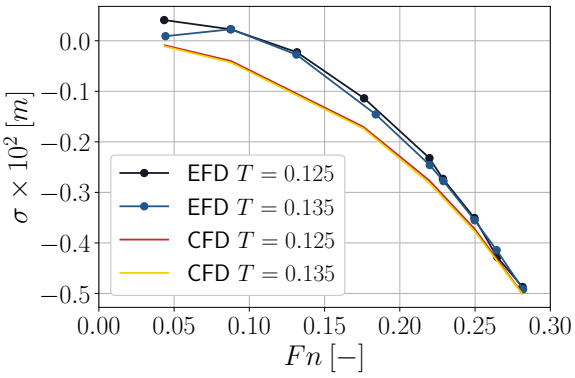

(b) Sinkage

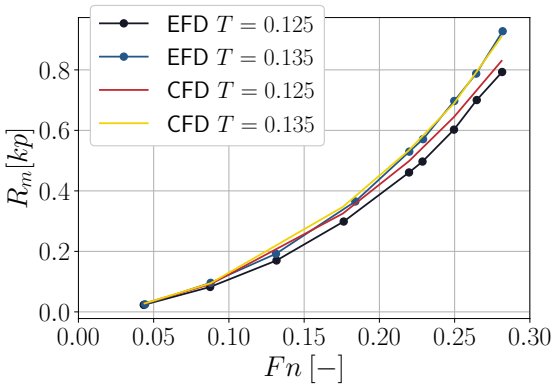

(c) Resistance

Figure 5.28: Comparison of the CFD data and experimental predicted for the two draughts for the ship's resistance and the two degrees of freedom

already mentioned based on the defined coordinate system, negative trim values denote bow down rotation. Although deviations are noted between the two approximations, the differences

can be considered as minor, in all cases, since they remain less than 0.05 degrees. It is noted however, that the oscillations of the trim data at the higher Froude numbers evident in the measurements, are not reproduced by the numerical results. In Figure 5.28b the comparison of the sinkage between the experiments and the simulations can be seen. The differences between the computational and the experimental data are more pronounced in the low Froude number regime up to $Fn = 0.15$. In this range, simulations predict larger displacements compared to measurements. As the Froude number increases the comparison becomes better. Summarizing the results, experiments and CFD simulations produce similar results, although some deviations are noted for the lighter draft.

5.3.3 Resistance of the Full Configuration

The present subsection focuses on the effect of the static wing arranged in front of the bow. Experiments conducted in LMSH of NTUA are taken as reference. The whole experimental setup (vessel–wing configuration) is presented in Figure 5.29. Apart from the dynamic wing, in from of the bow an instrument used to measure the local angle of attack (AoA), typically called vane, is present as well as the vertical struts (or skegs) that support the foil. The size of vane is comparable with the wing, thus it is expected to affect the overall results. Thus, in order to quantify the effect of each component, measurements and numerical simulations are employed, and regarding the measurements, additional experiments were conducted excluding the vane.

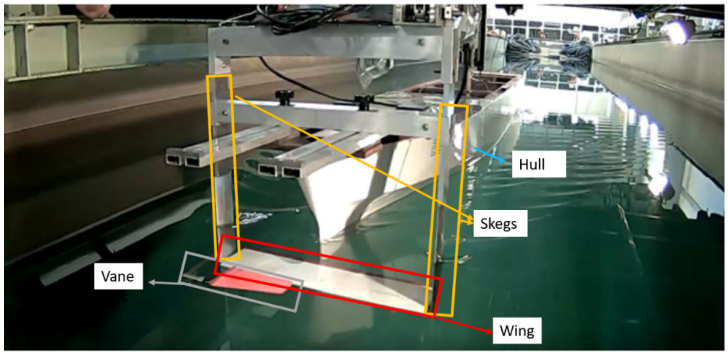

Figure 5.29: Experimental configuration of the dynamic wing arranged at the bow of the ferry ship model tested in the tank of LMSH–NTUA, Photo credit: [143]

In the CFD analysis the vane was omitted and the wing was considered, also fixed at zero inclination, AoA=0°. The hull, the supporting skegs and the wing are modeled. An overview of the mesh used is presented in Figure 5.30. The computational mesh for the hull is the same as in the previous section while on the skegs and the wing a surface of 15000 cells was generated. Additionally, in the free surface region the mesh was refined near the skeg to capture the skeg–generated wave system, as well as refinement boxes were added around the configuration to resolve the effects of the wake.

The experimental results with and without the presence of the vane for both draughts are presented in Figures 5.31a and 5.31b. The CFD simulations considered for three velocities namely $U = 1m/s$, $1.3m/s$ and $1.42m/s$, which correspond to Froude number 0.176, 0,22 and 0.25. More specifically, the comparison for the heavy draught is presented in Figure 5.31a, while the lighter draft is shown in Figure 5.31b.

Firstly, from both figures it becomes clear that the wing and the supporting structure configuration adds extra resistance to the vessel, which increases with the Froude number. Furthermore, it is noted that the vane amounts approximately 15% of the total resistance. This is attributed to its large size as previously discussed. However, in the full–scale vessel, the vane will remain the same (it does not scale with the rest of the geometry). The numerical predictions and the measurements, as shown in Figure 5.31a and Figure 5.31b, for the two drafts, respectively, are

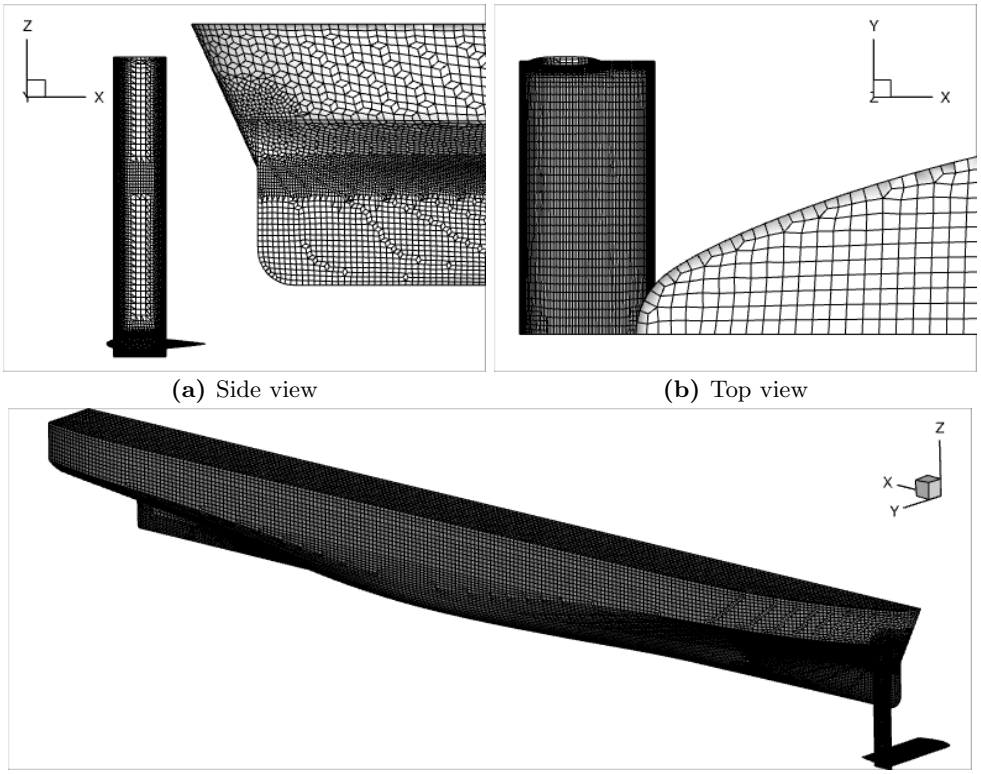

(a) Side view **(b)** Top view

(c) 3D view

Figure 5.30: Computational mesh on the hull with the skegs–wing configuration

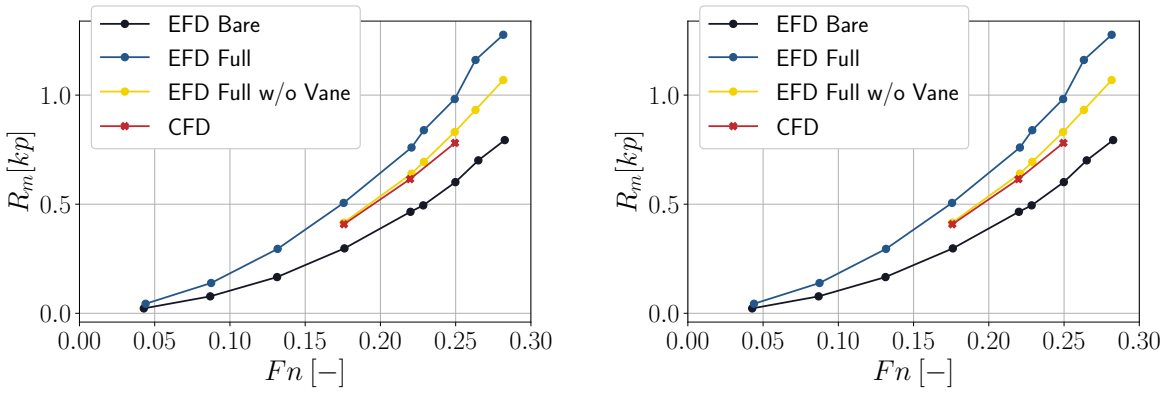

(a) Light Condition $T = 0.125m$ **(b)** Heavy Condition $T = 0.135m$

Figure 5.31: Resistance comparison for the various configurations, for the two different draughts

in very good agreement, without the vane. This reinforces the experimental observation that the presence of the vane significantly increases in the model's resistance.

Furthermore, using the CFD solution the contribution of each individual component (hull, skegs and wing) can be retrieved. The contribution of each component of the configuration in the total resistance can be found in the two following tables for the two draughts.

It is evident that the resistance of the skegs and the foil, increase significantly the resistance of the model. The resistance, of the supporting skegs is about 9.5% of the total value, while the wing at inclination AoA=0° constitutes around 12% of the total resistance.

Table 5.13: Contribution of the several components of the full configuration on the model's resistance. Three different Froude numbers are examined for draught T=0.135m

Froude	Total [kp]	Hull [kp]	Skegs [kp]	Wing [kp]
0.25	0.829	0.66	0.077	0.092
0.22	0.653	0.52	0.061	0.072
0.176	0.431	0.34	0.043	0.048

Table 5.14: Contribution of the several components of the full configuration on the model's resistance Three different Froude numbers are examined for draught T=0.125m

Froude	Total [kp]	Hull [kp]	Skegs [kp]	Wing [kp]
0.25	0.788	0.62	0.073	0.095
0.22	0.614	0.48	0.059	0.075
0.176	0.413	0.32	0.042	0.051

5.3.4 Effect of Foil Inclination in Calm Water Conditions

In order to investigate the utilization of the wing, trimming experimental have been performed and used here as reference for comparison. Measurements were conducted with the wing positioned at four different angles AoA= 3.1^o, 1.6^o, 0^o and -1.6^o, where the positive sign indicates nose–up foil inclination. The experiments were conducted considering the full configuration (skegs, wing and vane) at the nominal Fn=0.25 (V=1.42 m/s) for the heavy condition (T=0.135m).

Table 5.15: Experimental results for the static wing in various AoA. All results regard the nominal speed of the vessel ($Fn = 0.25$ or $= 1.42m/s$) in case of the heavier condition ($T = 0.135m$).

AoA [deg]	R_m [kp]	τ [deg]	σ [cm]
3.1	1.031	0.159	-0.198
1.6	1.007	0.039	-0.291
0	1.042	-0.132	-0.401
-1.6	1.028	-0.264	-0.494

It is evident that, with respect to the resistance when the wing is positioned at zero inclination (AoA= 0°), a change in the angle can have a beneficial effect. Indeed, for all the angles presented above there is a drop in the measured resistance, attributed to different dynamic trim and sinkage.

Contrary to the experimental setup, the CFD simulations were performed without the supporting skegs and the vane. The mesh considered in the previous simulations is used (wing at AoA=0°) and by employing the mesh deformation algorithm proposed by Zhao [128], which is described in Section 3.10.1, the angle of attack of the wing can be adjusted without changing the computational mesh. The measurements include the whole configuration. In order to compare them with the CFD predictions, the effect of the vane and the skegs is subtracted from the measured data. Regarding the vane, this is accomplished by using the experimental measurements with and without the vane (see Figure 5.31b). To quantify the effect of the skegs on the resistance, the CFD predictions of the hull, skeg and wing system are exploited (see Table 5.13). The skegs' resistance is normalized as percentage of the total resistance and by assuming that it remains constant for the various configurations, the experimental data are

corrected, enabling the direct comparison of measurements and the numerical CFD predictions as presented in Figure 5.32c.

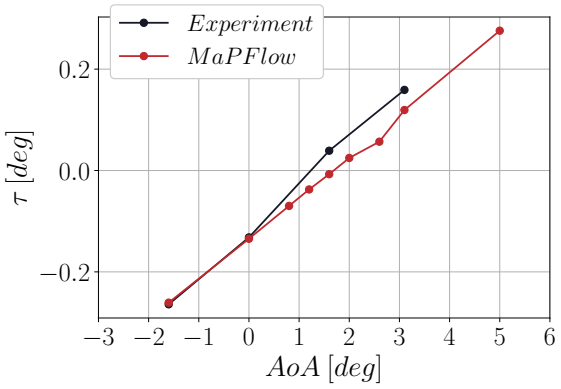

(a) Trim angle – τ

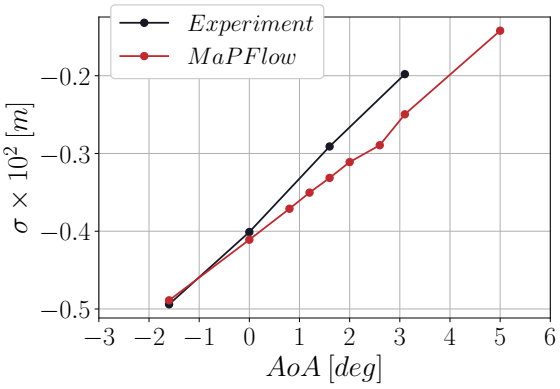

(b) Sinkage – σ

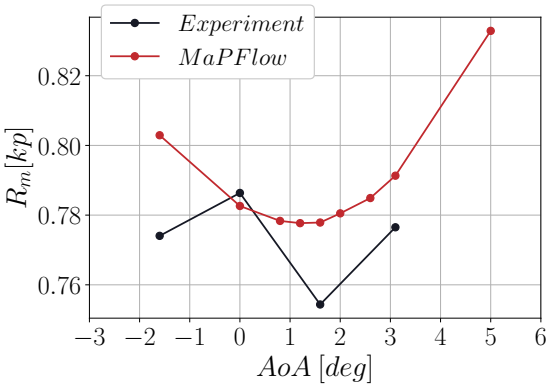

(c) Resistance – R_m

Figure 5.32: Comparison of the CFD data and experimental predicted for the two draughts for the ship resistance and the two degrees of freedom

The CFD simulations have been conducted for additional wing angles namely at 0.8°,1.2°, 2°, 2.6° and 5°. It is clear from Figure 5.32c that the reduction in resistance for an AoA ranging from [0.8° : 1.2°] is also predicted by the numerical simulations. When the wing is positioned below 2° the resistance increases. Compared to the measurement, the simulations predict smaller benefit in the total resistance, however, the follow the experimental trend at least for the positive angles. The larger deviation between the measurements and the simulations is noted when the wing is placed at AoA=-1.6° (negative implies nose down foil inclination).

Finally, the predicted and measured dynamic trim and sinkage values for the various AoA's are presented in Figure 5.32a and Figure 5.32b, respectively. As concerns the experimental data in these figures the original values are plotted (including the supporting skegs and vane), since is not feasible to decouple the contribution of each component to the dynamic behavior of the model. Despite, the different setup, the comparison between the two approximations is fairly good for a wide range of AoA. At 0° and -1.6° the predicted sinkage and trim almost coincide. Even though for negative AoA's the deviation between the CFD and the experiments increases, are still within acceptable limits, with largest difference being 0.05° for trim and 0.05cm for sinkage.

5.3.5 Effect of Wing in Presence of Regular Waves

In the last part of this study, the effect of a static wing on the model is investigated under the excitation of regular waves for the heavier condition (T=0.135m). Simulations with and without the foil are performed for four different head incident regular waves. The skegs are neglected in the latter case. In all cases, the configuration has two degrees of freedom; namely pitch (θ) and heave (z). Numerical predictions are compared with experiments that were conducted at the NTUA towing tank for the bare hull and static wing configuration. The frequencies of the incident waves are: f=0.55Hz, 0.65Hz, 0.67Hz and 0.75Hz. The corresponding ratios of wavelength over ship's length (λ/L_{pp}), using the linear theory of Airy, are: 1.66, 1.12, 1.20 and 0.87. In all cases the wave height is 0.06m. The frequencies selected is based on a particular sea state spectrum. An extended band around resonance (0.67Hz) is considered in order to obtain useful results also for the behavior in irregular waves characterized by this spectrum.

For the numerical setup the wave tank of Figure 5.25 is used. In order to account for the mesh motion, the grid deformation algorithm of Zhao is used [128]. Compared to the mesh used in the previous case, an extra refinement zones is defined upstream of the ship, for effective wave propagation. The refined mesh has a constant dx equals to $0.03m$ which corresponds to 90 cells in the shortest wavelength and 170 to the largest. In the vertical direction 20 cells are defined per wave height. The total mesh size for the bare is 4.56 million cells, while for the configuration with the foil 6.00 million cells are used. For the proper time discretization a sensitivity study is conducted, using as reference the main frequency ($f = 0.67Hz$). Three timesteps are considered and the results are summarized in Table 5.16. Convergence is noted for the two smaller timestep discretization. The smallest timestep is chosen for all simulations, to ensure consistency of the results in larger wave frequencies as well.

Table 5.16: Timestep sensitivity study for the case study in regular waves. The table presents mean value $\bar{\cdot}$ and amplitude A of the heave—z, pitch—θ and resistance— R_p

dt [s]	$\overline{z}$	$\overline{\theta}$	$\overline{R}_p$	A_z	A_θ	A_{R_p}
3.00E-03	1.93	2.27	1.18	1.93	2.27	1.18
2.00E-03	1.79	2.19	1.1	1.79	2.19	1.1
1.00E-03	1.75	2.14	1.08	1.75	2.14	1.08

For better understanding of the wing's influence under the excitation of the different waves, in Figure 5.33 the signals of resistance, ship trim and sinkage are plotted in one encounter period. All signals suggest better performance characteristics when a static foil is arranged in front of the bow. By examining the signal of the resistance in case of the bare hull configuration, a sudden increase of the loads, approximately at 0.4 of the encounter frequency, is noted for the two larger wave frequencies (see Figures 5.33c and 5.33e). At that instance, the pitch of the model is at its maximum negative value (negative pitch indicates bow down). The sudden increase is attributed to the slamming of the ship's bow at a wave crest. In case of the augmented configuration, a delay in the signal of the pitch is noted. This phase shift prevents the slamming of the bow, leading to smoother resistance signal. Regarding the effect of the static wing to the vessel's mean resistance in head wave conditions, Figures 5.33a, 5.33c and 5.33e, present, with dotted lines, the mean resistance over an encounter cycle. The mean (total) resistance of the vessel is reduced in all cases.

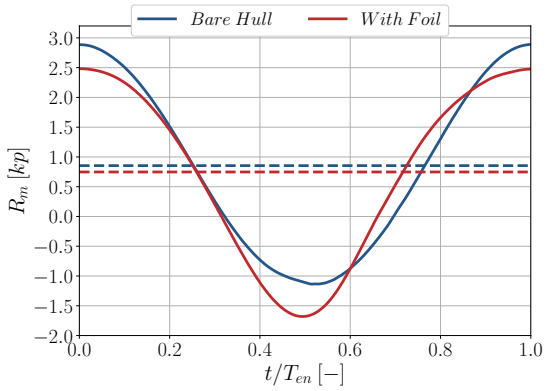

(a) Ship's resistance–R_m, the dotted line corresponds to the mean value.
$f = 0.55Hz$ and $\lambda/L_{PP} = 1.66$

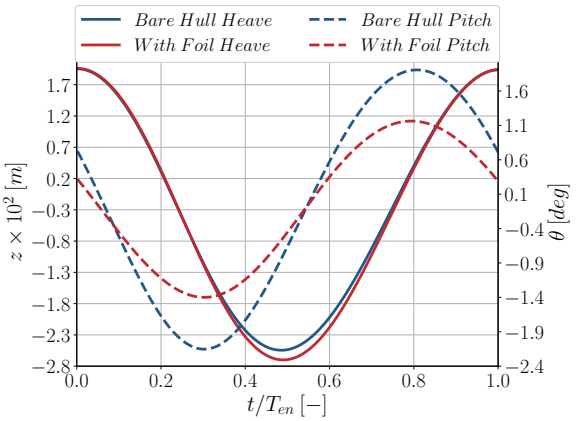

(b) Heave–z (left axis) and pitch-θ (right axis) motions.
$f = 0.55Hz$ and $\lambda/L_{PP} = 1.66$

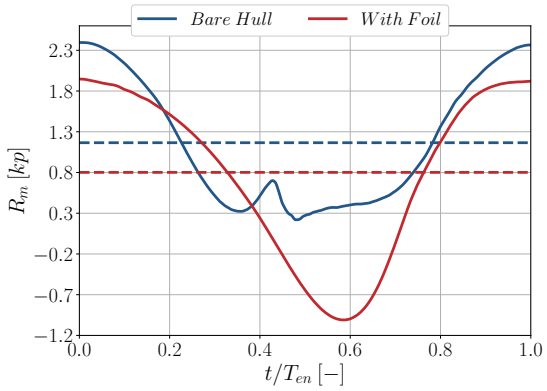

(c) Ship's resistance–R_m, the dotted line corresponds to the mean value.
$f = 0.67Hz$ and $\lambda/L_{PP} = 1.09$

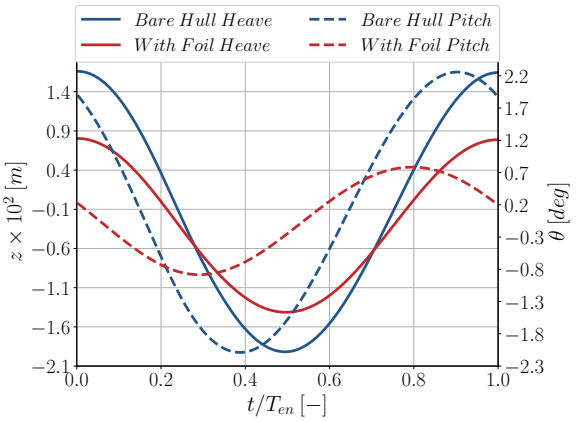

(d) Heave–z (left axis) and pitch–θ (right axis) motions.
$f = 0.67Hz$ and $\lambda/L_{PP} = 1.09$

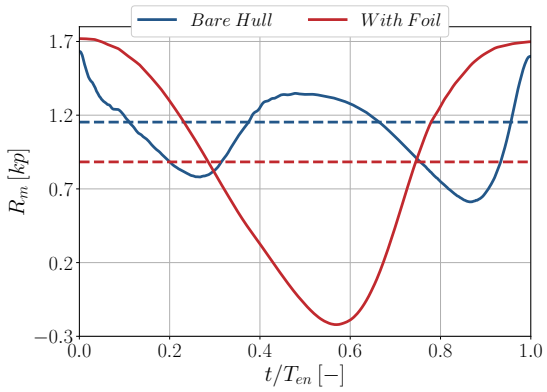

(e) Ship's resistance–R_m, the dotted line corresponds to the mean value.
$f = 0.75Hz$ and $\lambda/L_{PP} = 0.87$

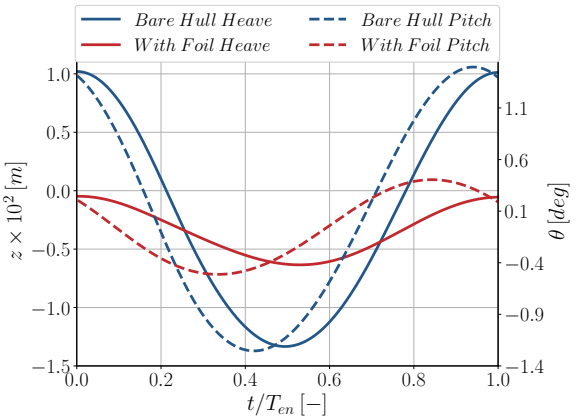

(f) Heave–z (left axis) and pitch-θ (right axis) motions.
$f = 0.75Hz$ and $\lambda/L_{PP} = 0.87$

Figure 5.33: Numerical results with and without the foil over one encounter period. From top to bottom, the results correspond to $f = 0.55Hz$, $f = 0.67Hz$ and $f = 0.75Hz$. The left figures present ship's resistance and the corresponding mean values (with dotted lines), while the right figures signals of heave (z) and pitch (θ).

The previous remarks can be further illustrated by examining the flow characteristics at the instance of the slamming for the two configurations. Flowfield comparisons with and without the foil are presented in Figures 5.34 and 5.35. The first figure illustrates an iso–surface of the VoF field for $a_l = 0.5$ colored by the vertical coordinate, in case of the heavier draught and incident wave frequency 0.67Hz. The two snapshots are taken the moment of the impact of the bare hull's bow to the free surface, which occurs approximately at the 0.4 of the encounter frequency (see Figure 5.33c). It can be seen the that at the same moment the pitch angle of the hull equipped with the foil is smaller and no impact occurs. This leads to a smoother resistance signal. This difference is further illustrated in Figure 5.35, where the pressure contours at the symmetry plane are given for the two configurations at the same instance. The increased pressure region in the bow of the bare hull configuration is clearly seen. At the same instant, the augmented configuration presents a pressure difference at the sides of the foil and thus a lift that effectively regulates the ship's motion.

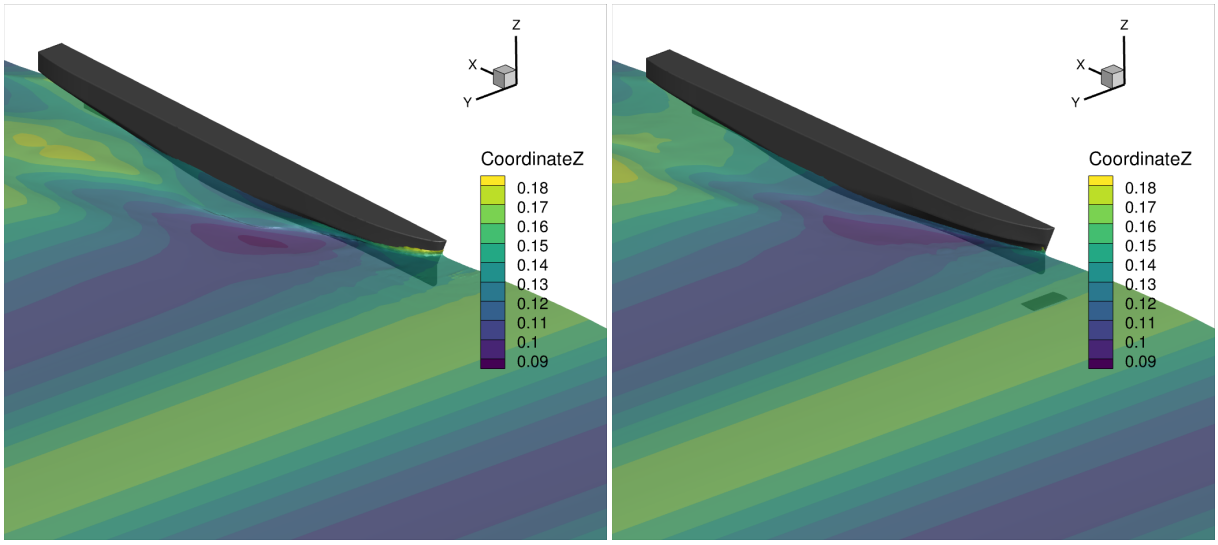

(a) Bare hull case **(b)** Hull equipped with the static foil

Figure 5.34: Iso–surface of the VoF field for $a_l = 0.5$ colored by the vertical coordinate. The two figures correspond to the heavier draught (T=0.135m) for incident wave frequency 0.67Hz

To summarize, it is evident that in all studied cases the foil has a positive effect. The foil successfully reduces the heave and pitch responses. This has a direct impact on the resistance showing reduction of up to 34% when the foil is present (in static condition). The reduction in resistance at all the wavelengths is summarized in Table 5.17.

Table 5.17: Mean Resistance per encounter cycle for the bare hull and with foil configurations at the considered wave excitation

Wavelength to ship's length λ/L_{pp}	Resistance [kp] Bare Hull	Resistance[kp] With Foil	Gain (%)
0.87	1.153	0.883	23.5
1.09	1.165	0.801	31.2
1.16	1.177	0.774	34.2
1.62	0.854	0.747	12.5

The effect of the wing can be further illustrated by the Response Amplitude Operators, which are presented in Figure 5.36. The figures present the response amplitude operators, for the non-dimensional heave (Fig.5.36a) and for the non–dimensional pitch (Fig. 5.36b). The heave is non–dimensionalized based on the wave amplitude (A), while pitch using wavenumber (k) times

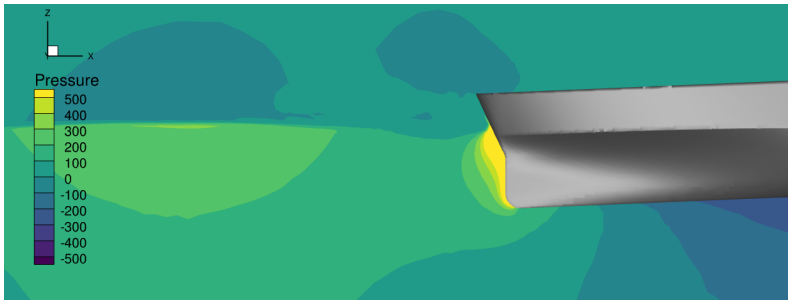

(a) Bare hull case

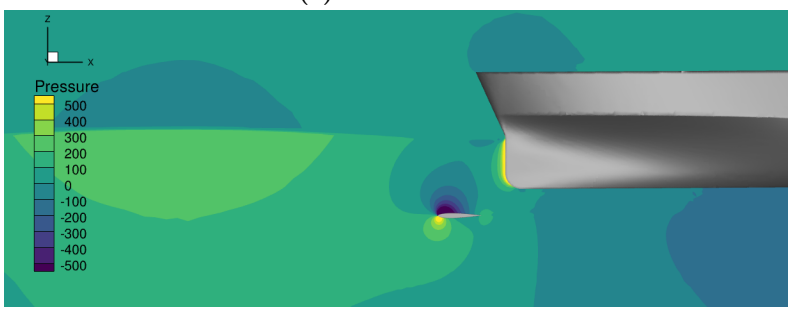

(b) Hull equipped with the static foil

Figure 5.35: Pressure field at the symmetry plane ($y = 0m$) for the two configurations. The two figures correspond to the heavier draught ($T = 0.135m$) for incident wave frequency $0.67Hz$

wave amplitude (A). The numerical results are also supported by experiments conducted in LMSH of NTUA, where the full configuration of hull–foil–skegs–vane is tested at the same wave frequencies.

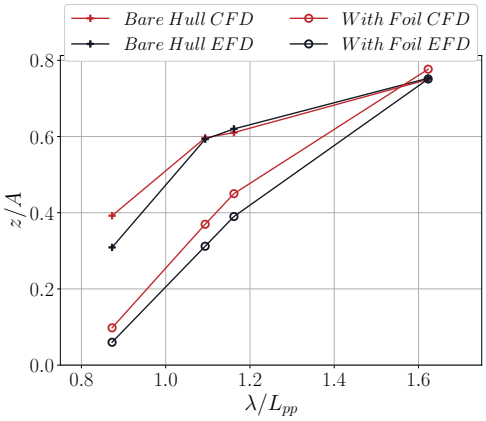

(a) Normalized heave motion

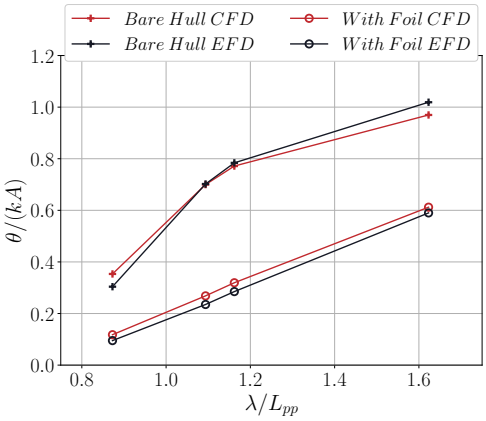

(b) Normalized pitch motion

Figure 5.36: Comparison between numerical (CFD) and experimental (EFD) results for regular waves with and without foil. The figures present the response amplitude operators for the two motions, non–dimensionalized. A is wave amplitude and k the wave number

Firstly, it is noted that the agreement between the computational results and the measurements is fair. The larger deviation can be seen in the heave amplitude for the shortest wavelength in case of the bare hull. Aside from that, the CFD calculations are in accordance with the experimental for the bare hull. Regarding, the comparison when the foil is present it is noted that although CFD results follow the experimental trends an almost constant deviation from the measurements appears. Part of this deviation could be due to the different way the wing appears in experiments and simulations where only the wing alone is modeled without the

supporting skegs.

From both the numerical simulations and the measurements the same qualitative conclusions can be drawn. The wing reduces significantly, the amplitude of the pitch motion. Heave is only reduced at smaller wavelengths, while at larger the differences are smaller.

5.4 Semi–Submersible Platform

On the direction of evaluating the coupled methodology of fluid structure interaction, the last test case focuses on the interaction of a floating platform, used as foundation for a wind turbine, with the surrounding fluid. Compared to the previous tests, in this case the motion in all 6 Degrees of Freedom (DoFs) is considered, a more complicated dynamic model is examined, and more detailed experimental data are available. All these, will help to enlight the particularities of the coupling of the flow and rigid body solver.

Floating offshore wind turbines (FOWT) have emerged as a promising solution for deploying wind turbines (WT) in deep water. Modeling of FOWT systems pose several challenges since we need to consider the complex hydrodynamic interactions between the turbine, the platform, the mooring system and the surrounding water. The results presented in this last section are part of the 1st FOWT Comparative Study [142]. Particularly, an experimental campaign has been carried out in the COAST Laboratory Ocean Basin at the University of Plymouth to investigate the hydrodynamic behavior of a semi–submersible platform without the effect of the wind turbine. The main scope of the 1st FOWT Comparative Study is to evaluate the accuracy and efficiency of various numerical approaches for modeling the wave interaction with a FOWT support structure.

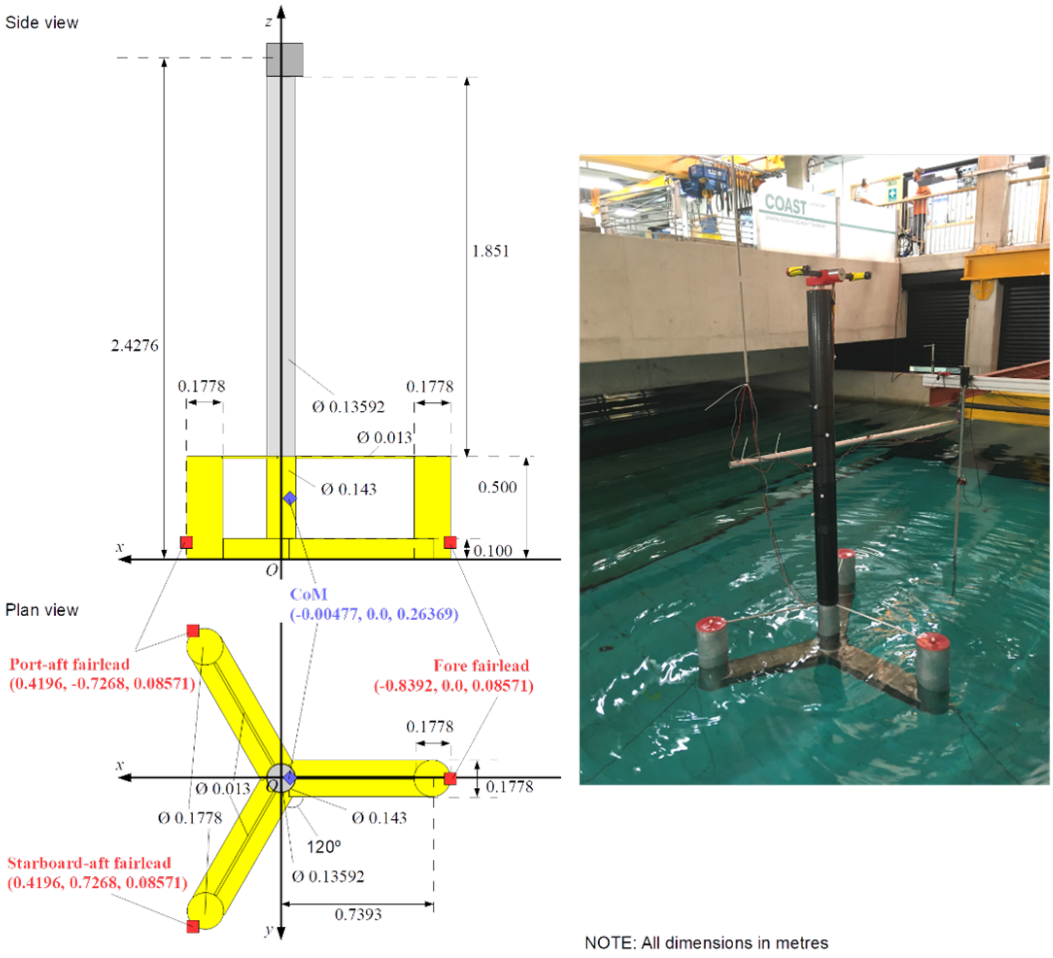

Figure 5.37: Model scaled UMain VolturnUS-S semi submersible platform. At the left a schematic representation of the floater is presented along the its dimension and the definition of the body fitted coordinate system. At the right a snapshot taken during experiments is shown. Figures taken from [141]

The floater selected for the measurements is a 1:70 scale model of the IEA 15MW reference

wind turbine (IEA-15-240-RWT) [164] and UMaine VolturnUS–S semi–submersible platform [1]. The model of the platform is depicted in Figure 5.37 along with its basic dimensions. The experimental campaign, includes static equilibrium load cases, free decay tests (in heave, surge and pitch) and the hydrodynamic response to two focused wave trains.

The floater consists of a main column on which the wind turbine is mounted and three cylinders arranged with 120^o offset forming a circle of $0.7393m$ in radius. The three peripheral cylinders are interconnected with the main column by orthogonal blocks (pontoons) at their bases. The center of mass (CoM) of the structure is displaced by $-4.77mm$ along the x–axis from its geometric center. Three fairleads positioned $8.571cm$ above the hull bottom, one on each external cylinder, are used as mounting points for the mooring lines. The positions of the three fairleads and of the CoM are also depicted in Figure 5.37 and also given in Table 5.18. The mass of the floater is 56.3kg and the moments of inertia with respect to the body fixed coordinate system, as illustrated in Figure 5.37, are $I_{xx} = 26.68kg\,m^2$, $I_{yy} = 26.68kg\,m^2$ and $I_{zz} = 14.18kg\,m^2$.

Table 5.18: Fairleads and CoM position with respect to the body fitted coordinate system

	x [m]	y [m]	z [m]
Fore fairlead	-0.8392	0.0	0.08571
Starboard-aft fairlead	0.4196	0.7268	0.08571
Port-aft fairlead	0.4196	-0.7268	0.08571
Center of Mass (CoM)	-0.00477	0.0	0.26369

Furthermore, in Figure 5.38 a sketch of the experimental setup is drawn. The global coordinate system is defined as follows, the x–axis is parallel to the wave propagation, the z–axis points upwards and the y–axis is placed accordingly to form a right-handed coordinate system. The origin of the coordinate system is placed on the cross point of the calm free surface and the vertical centerline of the structure.

The device is held in place using a 3–point mooring system constructed from 3mm long–link chain. The positions of the anchors can be seen in Figure 5.38 and also given in tabulated form in 5.19. The three mooring lines are of different length, the port and the starboard have lengths of $9.017m$, while the fore mooring line is longer with a length of $9.685m$. The mass properties of the mooring line are, its dry mass per meter length $0.144kg/m$ and its submerged mass $0.126kg/m$. The bar diameter of the chain is $0.00282m$ and the inner dimensions of the link are $0.0263m$ and $0.0065m$. Based on this geometric characteristics and for common steel the stiffness of the chain can be estimated [165].

Table 5.19: Anchors position with respect to the global coordinate system

	x [m]	y [m]	z [m]
Fore anchor	-9.525	0	-2.86
Starboard-aft anchor	4.412	7.655	-2.86
Port-aft anchor	4.412	-7.655	-2.86

The experimental campaign conducted three groups of test cases. The first test case aims to establish the equilibrium position with and without the mooring system attached. The floater is left free to balance and the final equilibrium position of the CoM is tracked. In case of the

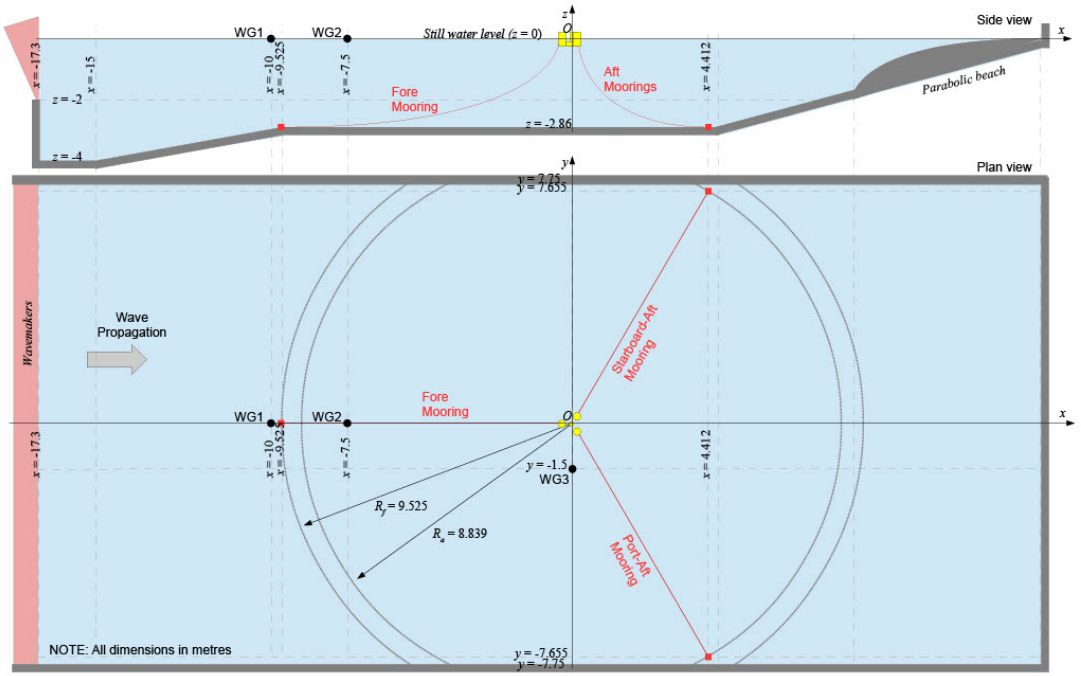

Figure 5.38: Schematic representation of the experimental setup for the VolturnUS–S semi–submersible platform and definition of the global coordinate system. Figure taken from [141]

unmoored equilibrium position only an estimation of the pitch angle and heave position can be made, since the other directions are not restrained. Apart from the final position experiments provide the tension on the mooring lines.

The second group of test cases includes decay tests for the moored floater. Three test cases are conducted with respect to the moored floater. In the first test, the floater is displaced in the surge direction (along the x–axis), in the second in the heave direction (along the z–axis) and at the last test case it is rotated around the pitch axis (y–axis). Although, the floater is displaced every time in one of the three directions, due to the coupling of the motions, small displacements or rotations occur in the other two directions. The initial displacements and rotation of the floater, as they were provided by the experiments, are given in Table 5.20. In the experimental dataset the decay history in the six degrees of freedom can be found, along with the tension on the mooring lines.

Table 5.20: Offsets of the floaters for the three decay tests

	Heavy Decay	Surge Decay	Pitch Decay
Initial z offset [m]	-0.1472	-0.0017	-0.0277
Initial x offset [m]	-0.0149	0.3825	-0.0031
Initial pitch offset [°]	0.4719	-0.7657	-9.798

The final group considers the wave structure interaction. To this end, two separate focused wave trains are created by a paddle wave maker located 17.3m upstream of the floater (see Figure 5.38). 112 wave fronts (components) evenly spaced between frequencies of 0.15 and 2Hz create a single wave front that impinges on the floater. The characteristics of the wave fronts were provided by the experiments for the comparative study. The description of the theoretical wave is crest–focused, which means that a zero phase occurs at the focus location x_{focus}, at time focus t_{focus}. The two wave trains have similar steepness but vary in terms of peak frequency, T_p, and of significant wave height, H_s. The first wave spectrum has theoretical $T_p = 1.3831s$,

theoretical $H_s = 0.069m$ and theoretical crest elevation at the focus location $A_{cr} = 0.064m$. The corresponding characteristics of the second wave group are, $T_p = 1.9380s$ and $H_s = 0.139m$ and $A_{cr} = 0.127m$. Due to the different crest elevations, the first wave train is hereafter denoted as *Benign* and the second one as *Extreme*. Both wave cases have a theoretical focus time at $t_{focus} = 50s$ and a theoretical focus location in the global coordinate system, $x_{focus} = 0m$, i.e. $17.3m$ downstream of the wave paddles. The experiments provided the free surface elevation in 9 wave gauges in case of empty wave tank (without the floater). Their coordinates are given in Table 5.21. In case of the floater–wave interaction, the experiments provide the free surface elevation at the first 3 wave gauges of Table 5.21, the coordinates of the CoM, the rotation around the axis that pass through the CoM and the tension on the three mooring lines.

Table 5.21: Position of wave gauges for the free surface elevation in case of the focused wave trains, for empty tank simulations. Coordinates are given with respect to the global coordinate system

	WG1	WG2	WG3	WG4	WG5	WG6	WG7	WG8	WG9
x [m]	-10	-7.5	0	-0.4	-0.2	0	0.2	0.4	0.75
y [m]	0.	0.	-1.5	0.	0	0	0	0	0

In this last section, the numerical results are obtained with the proposed AC methodology and FSI algorithm are presenting. This results have been also published and presented in the ISOPE conference 2023 as part of the NTUA's contribution to the comparative study [166]. Firstly, numerical setup is presented which includes the computational wave tank characteristics, mesh and timestep sensitivity studies. Moreover, in the numerical setup subsection the equilibrium position of the floater with and without the mooring lines is given. The following two sections include the decay characteristics in the three directions and finally, the response of the floater under the excitation of a single crested wave train. In all cases comparison is made between the CFD results and the results obtained from the experimental campaign. The discussion focuses on the principal degrees of freedom as they are defined by the excitation. Specifically, comparisons are made upon the surge displacement (x), the heave displacement (z) and pitch rotation (θ). Finally, it is noted that, every simulation has a specific time length which is specified for each group of tests by the experiments.

5.4.1 Numerical Setup

The basic computational setup for can be seen in Figure 5.39. The depth of the computational setup is constant at $2.86m$, as in the experiments. In the absence of incident waves are considered (static equilibrium or decay tests) a rectangular wave tank is used. In this case, its width spans for eight floater diameters and near the boundaries of the domain wave absorption zones are utilized to avoid undesired reflections. All boundaries are set to farfield in this case. For the focused wave trains tests, the domain upstream of the floater is extended to allow for wave generation. The inlet boundary is placed at $x = -17.3m$ with respect to the global coordinate system, while the floater at $x = 0m$ that matches the focus location of the wave trains. At the inlet boundary, a generation zone of one peak wave length is defined and it is used to create the wave spectrum. The inlet and the outlet boundaries, in this set of test cases, are set to farfield, while the lateral boundaries to symmetry.

In Figure 5.39 the mooring lines are also depicted. The dynamics of the mooring lines are solved by a separate computational module which was developed in the Laboratory of Aerodynamics of NTUA, as part of the dynamic solver *hGAST* [5]. The effect of the mooring line is accounted for implicitly, this means that mooring dynamics are an additional step in the iterative procedure described in Section 3.9. In every real computational timestep, an iterative procedure is followed between the rigid body solver, the mooring lines solver and the

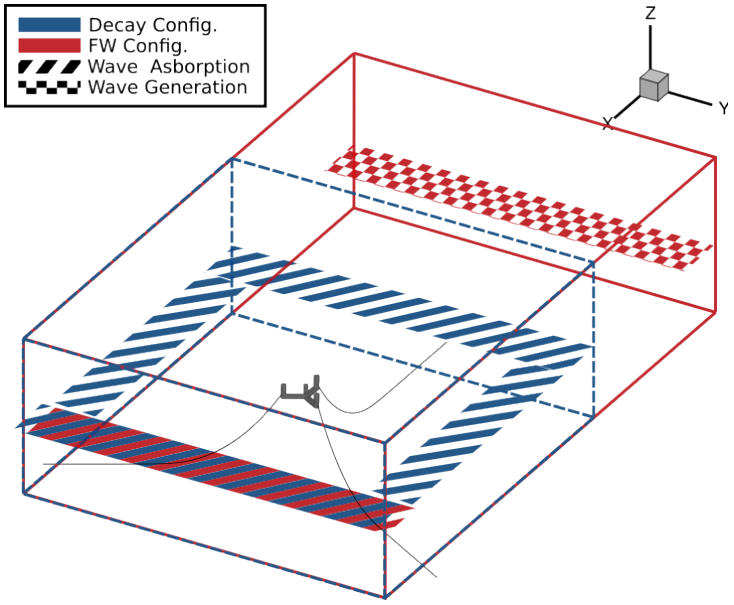

Figure 5.39: Simulation setup. The figure illustrates the two CFD domains used, in case of the decay test cases (blue color) and in case of the focused wave trains (red color). In the figure also the generation zones and the wave absorption zones are also depicted

hydrodynamic solver. The mooring line solver calculates the restoring forces and moments given the position, velocity and acceleration of the floater, based on the hydrodynamic loading and the tension of the mooring lines the new displacement and rotation of the floater is calculated by the dynamic solver. Afterwards, the 6 DoFs are communicated in the flow solver by moving the surface nodes of the mesh. As in the standard FSI procedure, an appropriate algorithm to calculate the deformation of the mesh is needed. In these series of test cases, due to the complexity of geometry, the RBF based algorithm, as described in Section 3.10.2 is used. Finally, the new flow characteristics are computed and the process is repeated until convergence.

Regarding the modeling of the mooring system, here only a brief analysis is presented and more details about the module can be found in the original publication [167]. Each mooring line is divided into a number of geometrically nonlinear truss elements. Such elements transfer only tensile forces while their compression stiffness is set approximately to zero. Application of the virtual work principle leads to the dynamic equations of a truss element in space. This requires that, for an arbitrary virtual displacement field $\delta\vec{x}$,

$$\int_{V_0} \sigma\delta\epsilon dV - \int_{L_o} \delta\vec{x}^T \left(\vec{q}_E - \vec{q}_I\right) dl = 0 \tag{5.4}$$

where $\vec{q}_I$ and $\vec{q}_E$ are the inertial and external (hydrodynamic, gravitational and buoyancy) forces per unit length, σ and $\delta\epsilon$ are the axial stress and the variation of the axial strain caused by the end nodes of the element, V_0 and L_0 are the volume and the length of the undeformed element.

The stress field is calculated using Hooke's law, by assuming a linear elastic material, $\sigma = E\epsilon$, with E being the Young's modulus. The hydrodynamic loads are calculated based in Morison's equation. The effect of the seabed is modeled through distributed stiffness and damping terms which are activated when the element approaches the seabed.

Prior to conducting the simulations, the equilibrium position of the floater needs to be specified. The floater is left free to move until it reaches an equilibrium position. As already mentioned the CoM of the floater is displaced by $4.77m$ towards the negative axis. This eccentricity of the CoM creates a non–zero pitch angle and a backwards displacement at the equilibrium state. In addition, it is expected to cause a stronger coupling between the DoFs as will be further discussed in the following test cases.

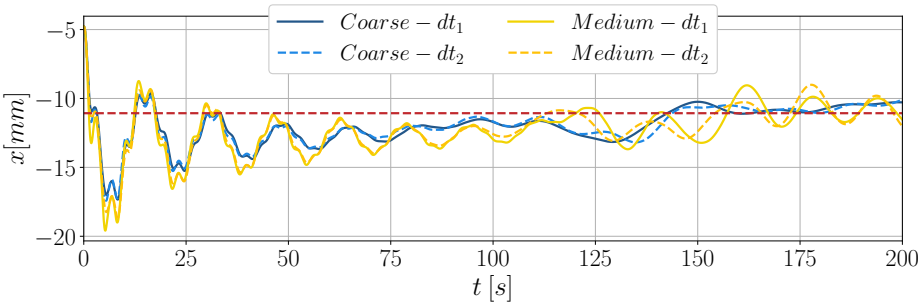

(a) Surge motion

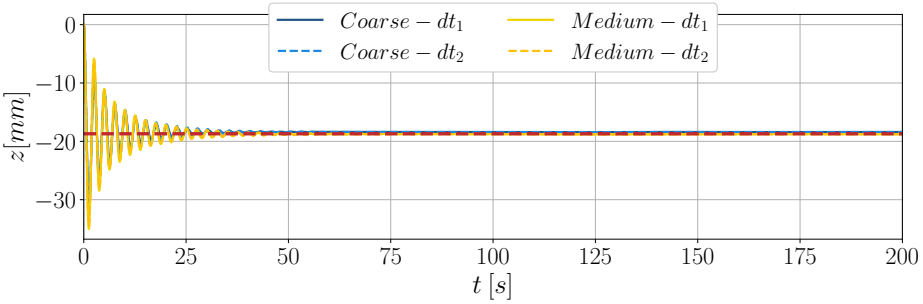

(b) Heave motion

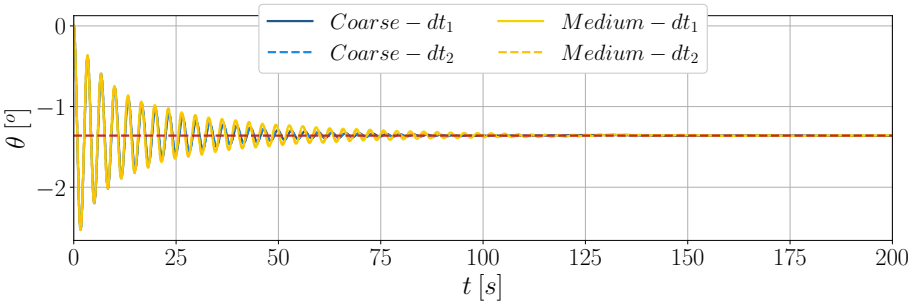

(c) Pitch motion

Figure 5.40: Mesh and time sensitivity studies. Two different mesh sizes and timesteps $dt_1 = 0.01s$ and $dt_2 = 0.005s$ are considered. The red dashed lines correspond to the final equilibrium position of CoM, $x_{CoM} = (-0.01177, 0, -0.0187)m$ and $\theta = -1.36^o$

In order to find the right numerical configuration, a mesh and a timestep sensitivity study is conducted. Since the radiating waves from the structure are expected to be negligible for this test case only two meshes are considered. The *Coarse* grid is consists of 1.28 million cells and the surface mesh is 50 thousand cells. The *Medium* mesh consists of 3.1 million cells and the surface mesh is 123 thousand cells. The first node in all meshes is placed $1mm$ normal to the wall. Two timesteps are also chosen, namely $dt_1 = 0.005s$ and $dt_2 = 0.01s$. All the results are presented in Figure 5.40 regarding surge, heave and pitch. It is evident that regardless of the mesh and timestep employed similar results are obtained. The final equilibrium position of the CoM, in terms of global coordinate system, are $(-0.01177, 0, -0.0187)$m and a pitch angle -1.36^o. In the experimental campaign, the equilibrium position is found at $(-0.02038, 0.0, -0.02386)m$ with a pitch angle of -1.502^o. The difference of the equilibrium position of the CoM between the simulations and the measurements is attributed to the mooring line modeling. Indeed, at the equilibrium position the simulation predict $7.35N$ tension at the fore mooring line and $7.36N$ tension in the port and starboard mooring line, while the corresponding measured tension forces are $7.6N$ and $7.2N$, respectively. Nevertheless, the comparison is considered fair.

Using the same grid and timestep, the equilibrium position of the floater without the mooring

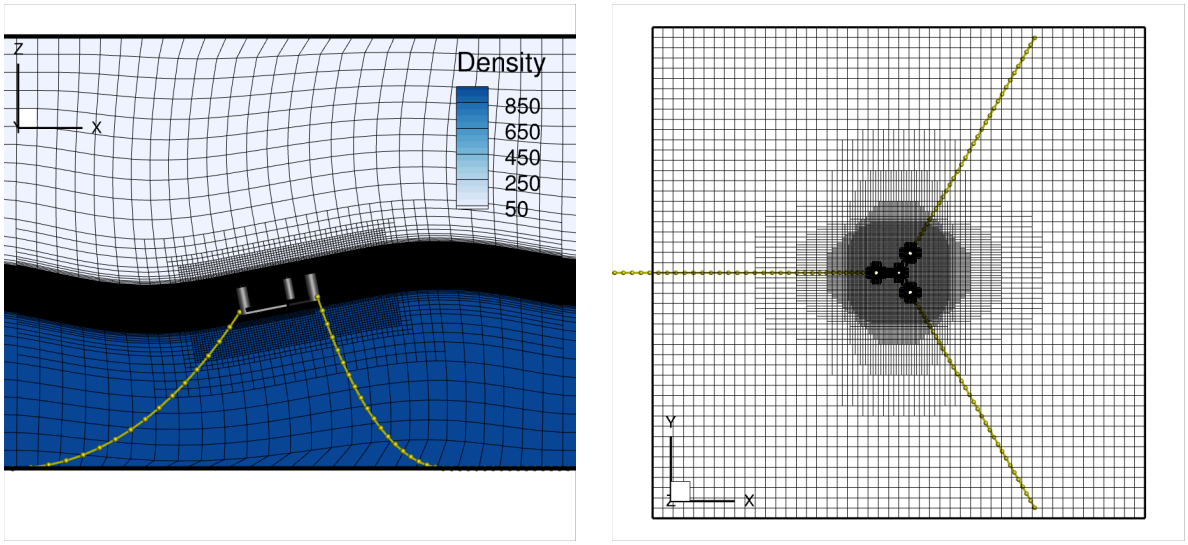

(a) Mesh slice along the y–axis. The free surface refinement zone is clear shown

(b) Mesh slice along the z–axis. The volume refinement around the floater is depicted

Figure 5.41: Snapshots of the computational mesh used for the decay tests. A large refinement zone near the free surface is defined to resolve the density discontinuity even at the maximum initial pitch angle

lines is computed. In order to perform this simulation, only two degrees of freedom have been considered, namely heave and pitch, and the rest have been deactivated. This choice has been made only for this test case because, since there is nothing to restrain the floater, any numerical instabilities introduced during convergence directly affect the motion of the floater. The final equilibrium position of CoM, after $200s$ of simulation, in the z–direction is $0.002m$ while its pitch angle is computed as -1.49^o. For the same test case, the experiments predict heave position $z = -0.00126m$ and pitch angle -1.729^o. This test case is primarily affected by the distribution of the hydrostatic pressure on the surface of the floater. The differences can only be attributed only to uncertainties introduced by either to numerical instabilities due to the free surface discontinuity or due to uncertainties in the measurements since the floater is not restraint. Either way, the differences are $3.25mm$ in heave and 0.24^o in pitch, which can be regarded as minor.

The results of the equilibrium test case are presented in tabulated form for both cases, with and without the mooring lines in Table 5.22.

Table 5.22: Comparison between experimental and CFD results for the equilibrium test cases, with and without the mooring lines

	Moored		Unmoored	
	Exp.	CFD	Exp.	CFD
x [mm]	-20.38	-11.77	–	–
z [mm]	-23.86	-18.70	-1.26	1.98
θ [^{o}]	-1.502	-1.36	-1.729	-1.490

Since the equilibrium position has been found, separate sensitivity studies are conducted for the decay tests. Taken as reference the pitch decay test, three grids are constructed using an unstructured trim mesher, denoted as *Coarse*, *Medium* and *Fine*. The *Coarse* grid which consists of 1.4 million cells and its surface mesh is 31 thousand, the *Medium* which has 3.3 million cells and 80 thousand cells on the surface of the structure and finally the *Fine* which consists of 5.3 million cells and the corresponding surface mesh has 150 thousand cells. The refinement strategy was based on the cell sizes of the surface mesh, the size at the sharp edges

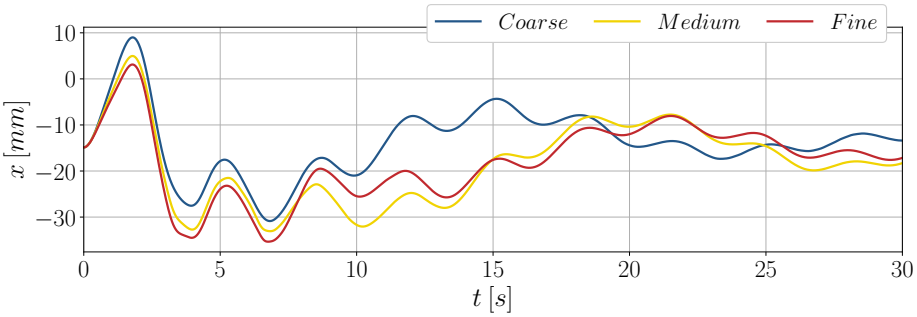

(a) Surge motion

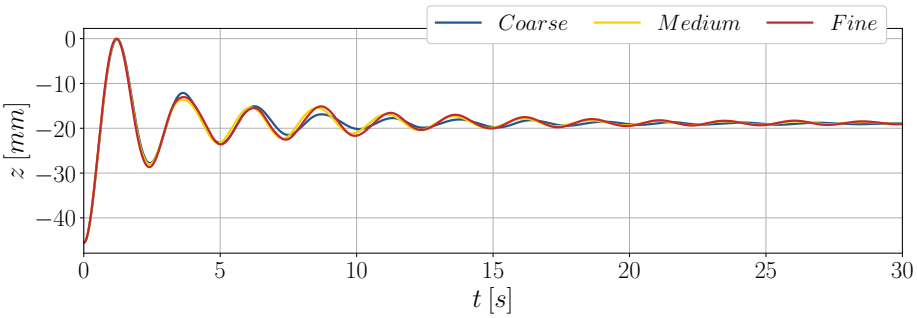

(b) Heave motion

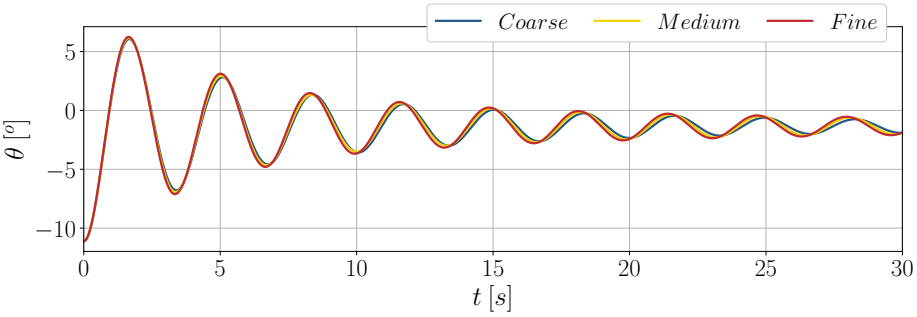

(c) Pitch motion

Figure 5.42: Mesh sensitivity study for the decay tests. The pitch decay study has been considered as reference. The timestep size is set to $dt = 0.0025s$. The *Medium* mesh is chosen for the decay simulations

of the structure, the vertical step in the vicinity of the free surface, and finally on the volume mesh which extends for two floater diameters around the body. The two latter refinement zones can be seen in Figure 5.41, where two mesh slices are presented. It needs to be noticed that, the free surface refinement box was large enough to account for the rotation of the mesh due to the pitching motion. Specifically the corresponding cell sizes are, for the *Coarse* (base) mesh, the surface mesh, the vertical step at the free surface, and the length close to the sharp edges, all were to 0.8cm, while the volumic refinement size to 1.2cm. Based on the previous mesh, for the *Medium* mesh the cell sizes at the vertical direction and the sharp edges, where reduced in half, 0.4cm while the rest were kept the same. Finally for the *Fine* mesh, the cell size at the edges was further refined to 0.2cm and the characteristic length of the volumic mesh was reduced 0.6cm. For the timestep sensitivity study three resolutions are selected, $dt = 0.008, 0.005$ and $0.0025s$. The results are compared in terms of surge, heave and pitch and can be seen in Figures 5.42 and 5.43. A fine agreement is noted between all configurations, especially in heave and pitch motions. In the surge direction, small deviations are noted that are considered insignificant as the surge motion is slightly excited in the pitch decay test and consequently the displacement values are small. Consequently, the *Medium* mesh is chosen for the rest of the study with a timestep of $dt = 0.005s$.

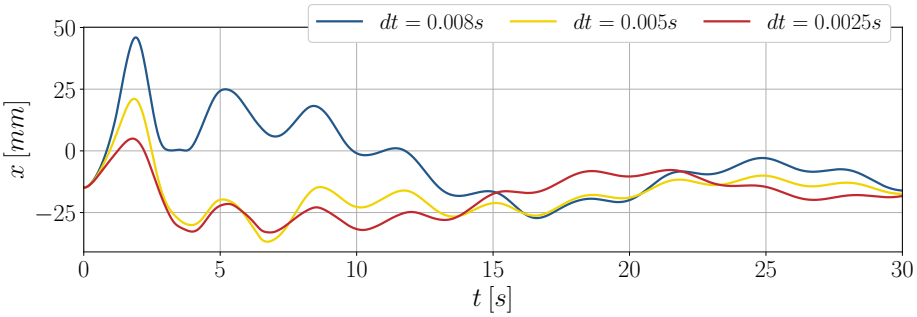

(a) Surge motion

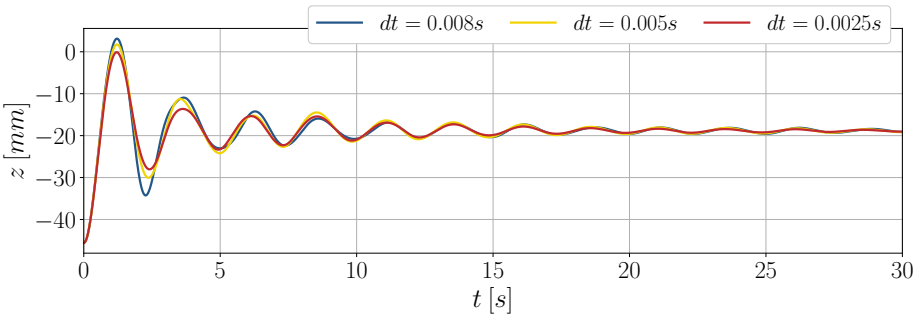

(b) Heave motion

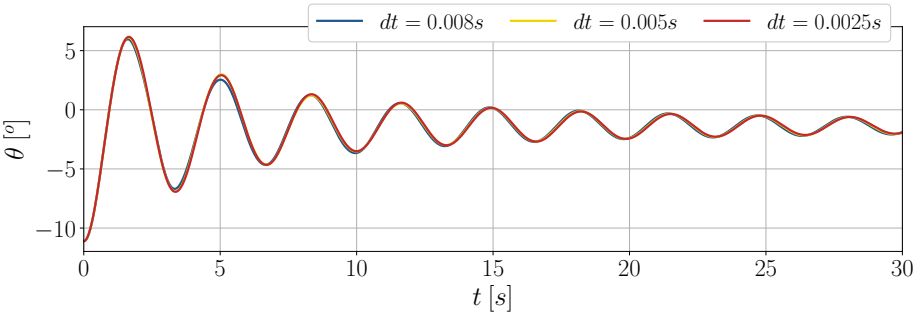

(c) Pitch motion

Figure 5.43: Timestep sensitivity study for the decay tests in case of the *Medium* mesh. The pitch decay study has been considered as reference. Timestep $dt = 0.005s$ is chosen for the decay simulations

Following up the decay tests, the incident wave cases are considered. The wave groups are generated as a superposition of the 112 waves given by the experimental description. Again, the parameters of timestep and grid should specified. The sensitivity studies regard only the numerical parameters for the accurate wave propagation of the two wave spectra in empty wave tank. For the floater wave interaction, the characteristics of the mesh near the structure are the same as in the case of the *Medium* mesh in the decay configuration. The characteristics of the mesh are based on the significant wave height and the peak wave length. More precisely, three meshes are considered. The vertical step near the free surface for the three grids, is 4, 8 and 16 cells per wave height, respectively, while the horizontal step is 300, 600 and 1200 per peak wave length. Furthermore, for the timestep resolution the peak wave period is selected as reference value. Three timesteps are considered with 400, 800 and 1600 timesteps per peak wave period. Convergence is accomplished for the medium timestep and mesh. The comparison is made upon the free surface elevation on the given wave gauges (see Table 5.21). Figures 5.44 and 5.45 present the results of the grid and time independence study for the benign test case. Two gauges are selected for comparison, firstly, the elevation recorded by WG1 is plotted and secondly the elevation recorded by WG2 is given. WG2 is placed at the focus location of the wave group which is the initial position of the floater, from where it was left free to balance.

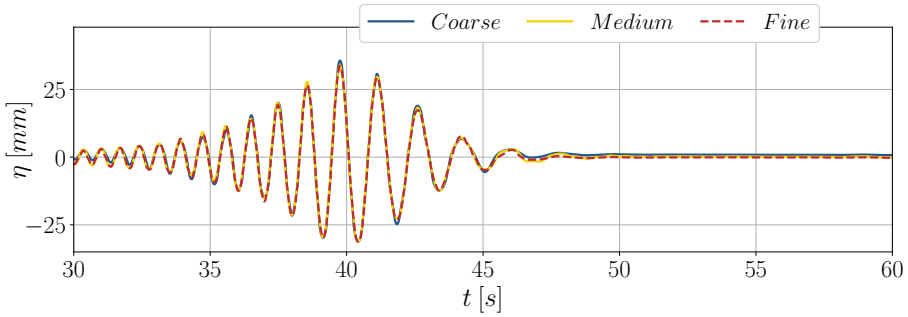

(a) Wave gauge position $x = -10m, y = 0$

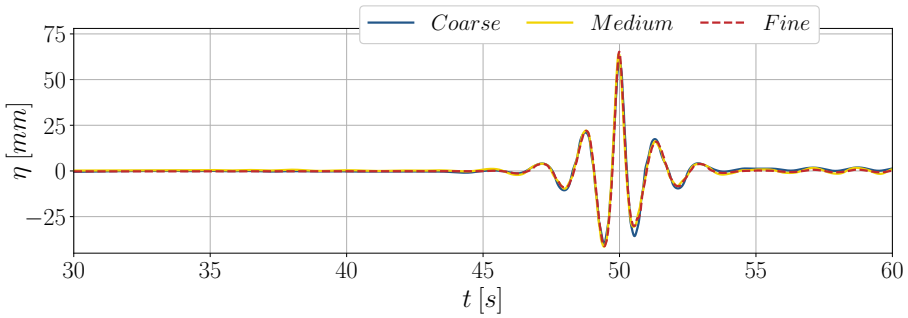

(b) Wave gauge position $x = 0m, y = 0$

Figure 5.44: Mesh sensitivity study for the *benign wave train test case* in an empty wave tank. In all cases the timestep size is $T_p/1600$. The *Medium* Mesh was selected for the simulations

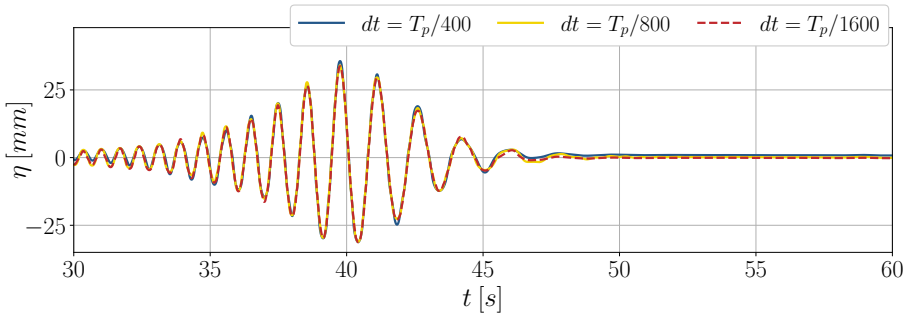

(a) Wave gauge position $x = -10m, y = 0$

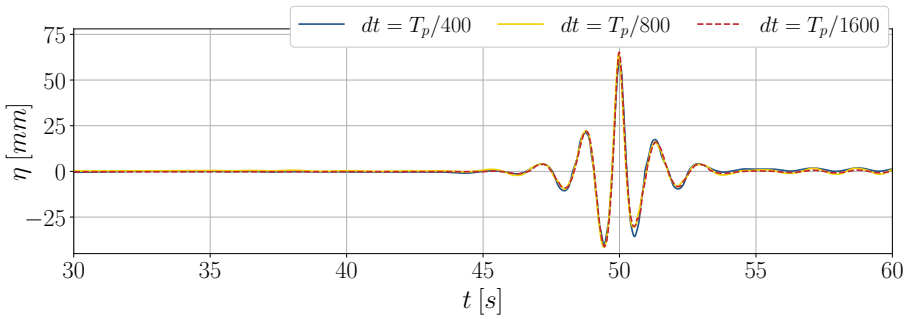

(b) Wave gauge position $x = 0m, y = 0$

Figure 5.45: Time sensitivity study for the benign wave train test case in an empty wave tank, in case of the *Medium* mesh. Timestep $T_p/1600$ was selected for the simulations

All configurations converge the same results and the differences are minor. For the wave floater interaction study the *Medium* configurations have been selected. Finally, for the extreme wave train case study, the same characteristics are chosen based on the corresponding wave of the peak frequency.

Table 5.23: Overview of the numerical parameters used in each series of test cases

	Equilibrium	Decay tests	Focused wavetrain (FW1)	Focused wavetrain (FW2)
Approx.	Laminar	Laminar	Laminar	Laminar
Mesh	1181248	3108816	6989404	4973113
dt	0.01s	0.005s	$T_p/800$	$T_p/800$
β	10	10	10	10
CFL_τ	20	20	20	20

5.4.2 Decay Tests

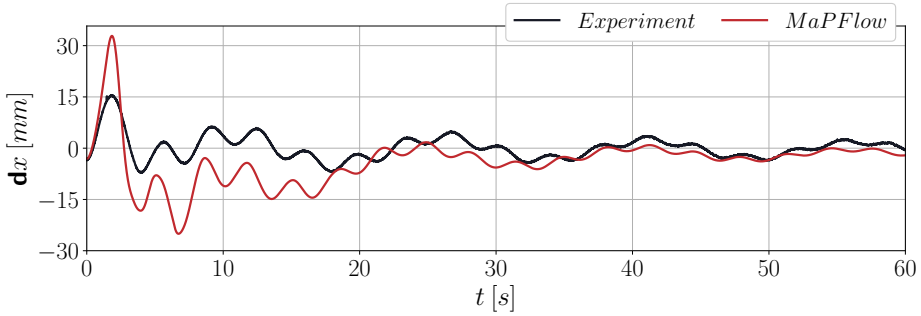

(a) Surge motion

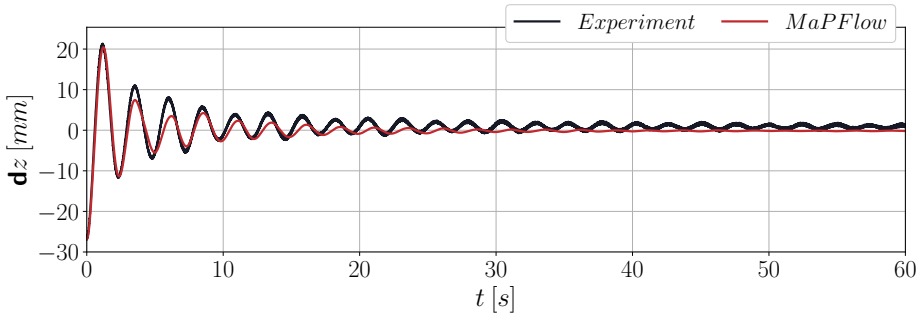

(b) Heave motion

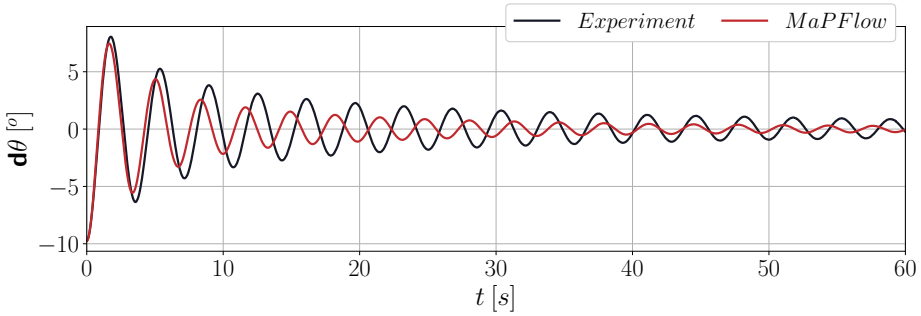

(c) Pitch motion

Figure 5.46: Comparison between computational and experimental results for the *pitch decay* test case. Offsets from the corresponding equilibrium positions.

Here the results of the three decay test cases are presented and a discussion is made upon the comparison with the experimental. At each case the floater is moved from its equilibrium position based on the offsets given by Table 5.20. The numerical equilibrium position of the CoM, as it was found in the previous subsection, is $(-0.01177, 0, -0.0187)m$ with a pitch angle of -1.36^o. At this point, it needs to be noticed that now tuning has been performed to match

the natural frequencies of the numerical model with the experimental ones. The whole duration of the numerical simulations is $180s$, however in the next figures only the first $60s$. This is done to better illustrate the results, since afterwards the motion amplitudes of the structure are relative small.

Starting the analysis from the pitch decay test and Figure 5.46, the floater is rotated by -9.7980^o around the y–axis. Due to the coupling of motions, apart from the initial pitch angle, the floater also submerges $2.77cm$ and moves by $-3.1mm$ in the x–axis. In order to be able to compare directly the numerical with the experimental results, the decay signals are presented in terms of difference $\mathbf{d}\cdot$, between the value of the corresponding DoF at time t and its initial value at the equilibrium position. Comparison of the decay time series indicates that the CFD results are able to adequately predict the amplitude of pitch motion for the first two periods. Afterwards, the pitch amplitude of the simulations decreases faster than the measurements. Moreover, a time lagging is also evident after the second decay period. This is also confirmed by Fourier analysis on the time signals presented in Figure 5.47. The decay frequency for the experiments is $0.28Hz$, while CFD calculations predict $0.30Hz$. This indicates that the numerical dynamic system differs with respect to measurements.

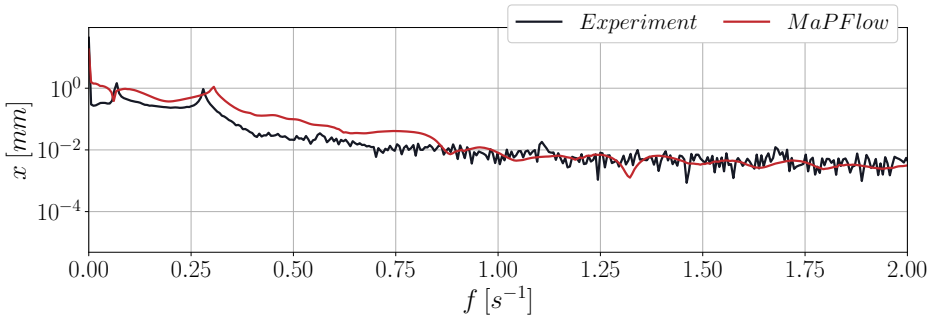

(a) Surge motion

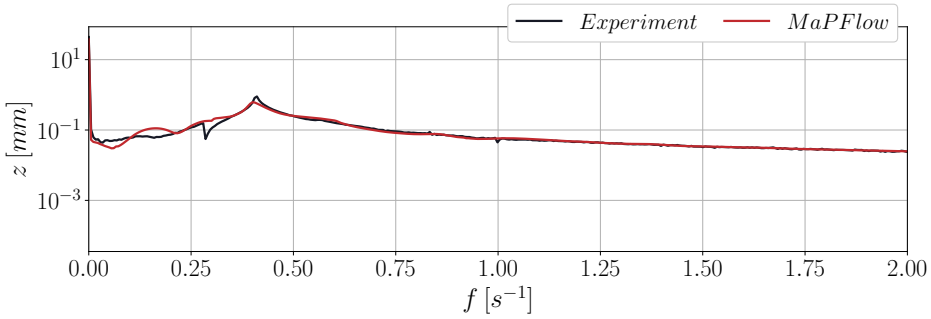

(b) Heave motion

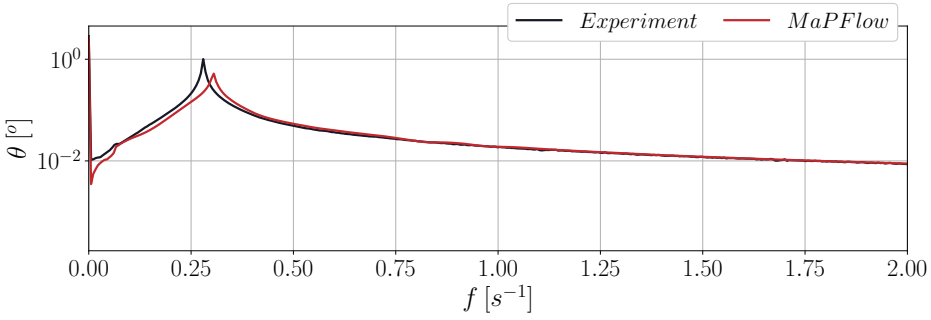

(c) Pitch motion

Figure 5.47: Fourier analysis of the *pitch decay* signals. Comparison between computational and experimental results. The vertical axis is in logarithmic scale

Regarding the other two degrees of freedom, the amplitude of the heave motion in the CFD

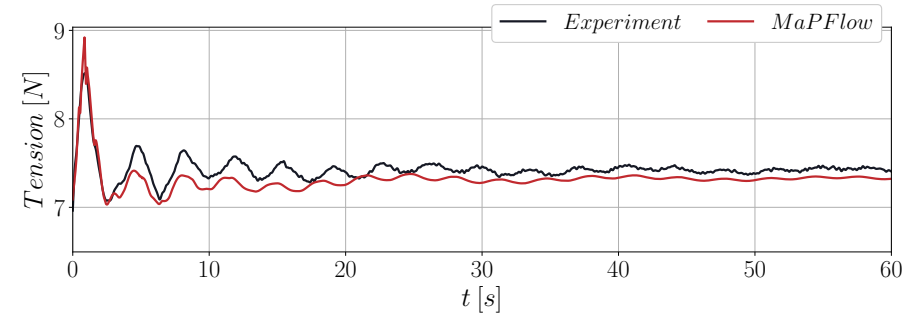

(a) Fore fairlead

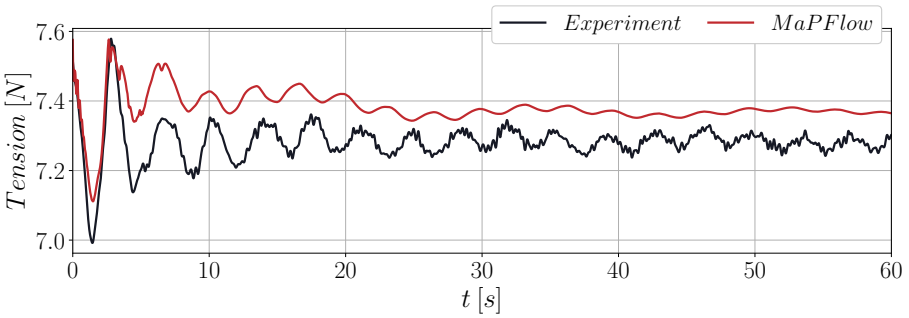

(b) Port fairlead

Figure 5.48: Comparison between computational and experimental results for the *pitch decay* test case. Tension on the mooring lines (a) at the fore fairlead and (b) at the port fairlead

results damps earlier than in experiments. In fact in case of the experiments, the amplitude of the motion remains almost constant for a time window of approximately $20s$ (from $t = 30s$ to $t = 50s$). This again indicates a difference between the dynamic model of the simulations and the experiments. In terms of of the oscillation frequency, the two approximations produce similar results as indicated by the Fourier analysis (Figure 5.47b). Finally, in the surge direction, in both setups the amplitude of motion is small and no safe conclusions can be drawn, however the numerical results seem to overestimate the first peak of the decay. Additionally, by conducting a Fourier analysis, two frequencies of motion are detected in the experimental results, as it can be seen in Figure 5.47a. The first that corresponds to the surge motion itself and a second one related to the pitch frequency. Conducting the same analysis in the numerical results it is noted that, the simulations does not present a peak in the surge frequency, however the comparison is fair for the larger frequency, caused by the pitch motion. The absence of the smaller frequency could be due to low grid or time resolution, nevertheless, since the amplitude values are small this can be neglected.

To further analyze the behavior of the structure during the pitch decay, the tensions of the mooring lines are presented in Figure 5.48. The tension at the starboard mooring is omitted due to symmetry. In the first seconds of the decay simulations and experiments are in close agreement. However, after the first 10s discrepancies are evident. Firstly, the tensions tend to converge in different levels, which is expected since different values are predicted in the equilibrium position. Additionally, the amplitude of the loading decays faster in case of the CFD results, which is in accordance with the previous remarks. In general, the figure indicates that the simulations are compared well with the experiments.

All in all, from the first decay test it can be concluded that, a similar behavior is noted between experiments and simulations. Nevertheless, differences between the modeled and the actual dynamic systems are evident. The numerical model seems to predict increased structural damping, thus a faster decay of the amplitudes is predicted. Additionally, the differences in the dynamic modeling lead to the prediction of a slightly greater natural frequency by the numerical

solver compared to the experiment.

The second decay test case regards the response of the structure to an initial displacement along the x–axis. The floater is moved in the x–direction by $0.3825m$, in the y–direction by $-0.0017m$ and it is rotated around the pitch axis that passes through the CoM by -0.76757^o. In this test case, the effect of the mooring lines is dominant for the response of the structure while the effect of the hydrodynamics is secondary. As Figure 5.49 suggests, the amplitude of the surge decay is predicted well by the numerical simulation, with a difference between the predicted periods. Regarding the other two degrees of freedom, the amplitudes of motions are negligible and a small difference is noted in the periods. Moreover, the numerical results predict a second higher frequency, which also appears in the experiments but it is damped during the first $10s$ of the simulation. In general the surge decay test is a standard validation test to assess the performance of the mooring lines dynamic solver and its parameters. This is attributed to the small amplitude of the secondary motions (pitch, heave) and to the insignificant height of the radiated waves. For this reason, it becomes clear from Figure 5.49 that the characteristics of the mooring lines are different in the experiments and the simulations and this affects all results including the final equilibrium position of the floater.

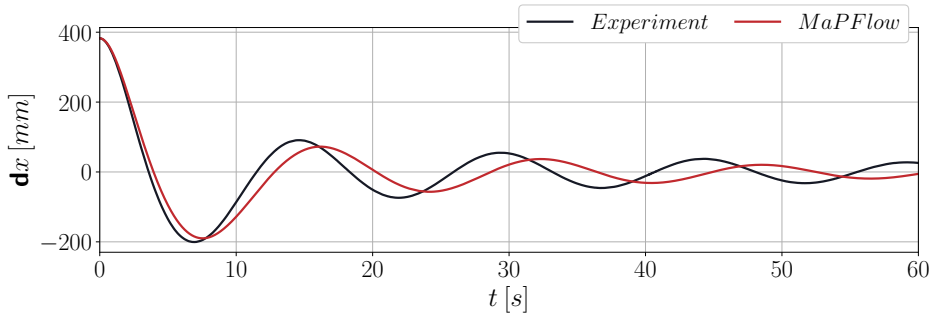

(a) Surge motion

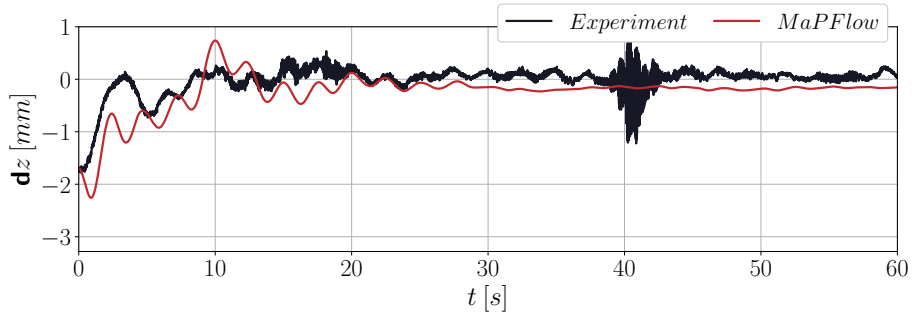

(b) Heave motion

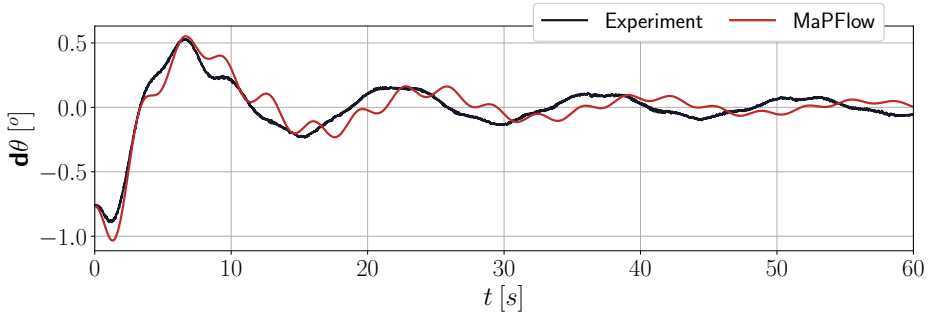

(c) Pitch motion

Figure 5.49: Comparison between computational and experimental results for the *surge decay* test case. Offsets from the corresponding equilibrium positions.

The last decay test examines the response of the floater if a downwards displacement is ap-

plied to the floater. Particularly, the floater is submerged for $14.72cm$ and due to the eccentricity of the CoM, the CoM moves for $-1.49cm$ in the x–axis and for 0.4719^o around the y–axis. In general, by examining the time histories of Figure 5.50, the remarks from the previous cases apply here as well. The amplitude of the principal motion is the same in the two approaches but it decays faster in the numerical simulation (see Figure 5.50b), as it was observed in the pitch decay test. Regarding the period of the motion, it can be seen that there is a relative agreement between the two. Furthermore, for the amplitudes of the surge and pitch motion, a slight difference between the two is noted and once again different frequencies are predicted. Their amplitudes of motion are rather small and the differences can be omitted. Finally, compared to the previous test cases, the frequency of the principal displacement is in agreement in experimental and numerical results.

As an overall comment, the analysis of the three decay tests revealed that the numerical modeling of the mooring lines did not replicate exactly the mooring lines used in the experimental setup. For the modeling of the mooring lines only geometric properties were available from the experiments. The stiffness of the mooring lines was computed based on an approximation for common steel was adopted and empirical relation for studless chains [165]. The natural frequencies in the surge and pitch directions do not coincide between the experiments and the simulations. A relative agreement is noted in the heave direction, where the restoring force originates primarily from the hydrostatic pressure. In spite of the differences, the numerical simulations have in general succeeded to replicate the experiments and similar dynamic characteristics have been obtained.

5.4.3 Response under Irregular Wave Excitation

The final group of simulations regards the response of the structure under the excitation of two focused wave trains. As already described in the introduction of this section, the two focused wave trains have focus location at the origin of the global coordinate system and focus time at $t_{focus} = 50s$. Their difference lies in the expected crest elevation at the focus location, the first one is smaller and thus it is attributed as *Benign* wave train with $A_{cr} = 0.064m$ and the second one *Extreme* wave train has $A_{cr} = 0.127m$. The 112 wave fronts (given from experiments) were specified as input for the wave spectrum generation. Their superposition resulted the desired wave spectrum. The total simulation time is $64s$, as it was dictated by the experimental campaign.

Firstly, the results for the *Benign* test case are considered. In Figure 5.51 the wave elevation in the first three gauges of Table 5.21, as predicted by *MaPFlow*, are compared against measurements. The results are practically identical and no major differences are noted.

Moving on to the comparison of the three principal DoFs, the next Figure (Fig. 5.52) depicts the offsets of CoM from the equilibrium position. As it can be seen in the figures, the floater is not moving for the first $47s$ seconds of the simulation, then the wave train impinges on the floater and it starts moving. After approximately $5s$, the wave train has passed through the floater and the damping of the excited motion begins. Firstly, it needs to be noticed that in the surge direction, a slight displacement is noted before the wave train hits the structure for both numerical and experimental data. For the numerical ones, this could be caused by numerical instabilities introduced either by the grid or by the wave generation process. Either way, this offset is relatively small (approx. 5mm) and it is constant during the whole simulation. Afterwards, the results for the time window where the floater is moving under the action of the wave. The two data sets practically coincide and now major differences are noted. As it is seen the offset of 5mm is not sufficient to create any phase difference between the experimental and numerical data. Afterwards, when the damping of the motion begins the same conclusions can be drawn as in the decay tests. Different frequencies between the two results are noted in the pitch direction and the heave amplitude damps out faster in the simulations than the experiments as before. Moreover, to further examine the behavior of the numerical modeling, in Figure

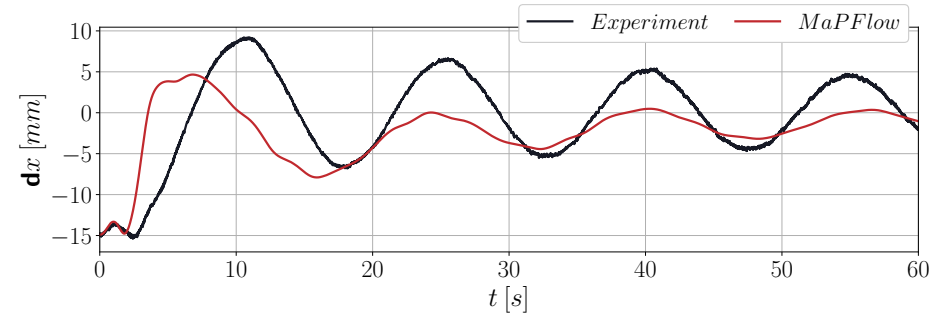

(a) Surge motion

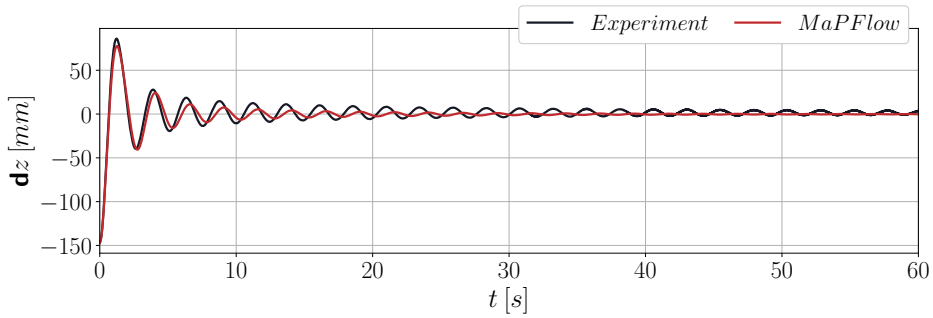

(b) Heave motion

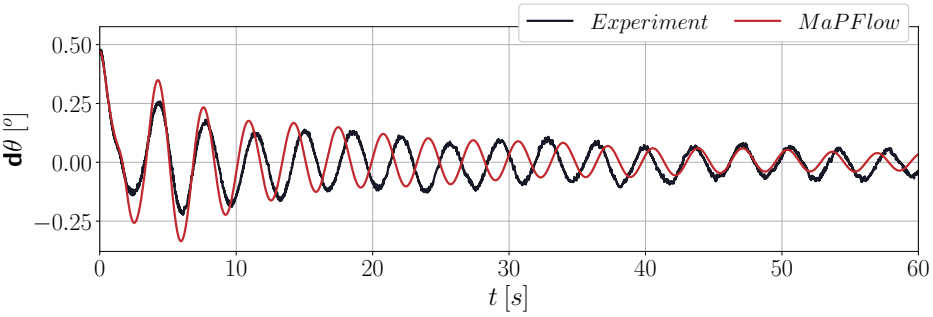

(c) Pitch motion

Figure 5.50: Comparison between computational and experimental results for the *heave decay* test case. Offsets from the corresponding equilibrium positions.

5.53 the tensions of the mooring lines are plotted for the experiment and the simulation. The mooring line tension is different in the equilibrium position, a constant offset is thus expected between the two (in agreement with Fig. 5.48) and this is further pronounced by the previously mentioned displacement in the x–direction. However, in terms of amplitude and frequency of the two signals, measurements and simulations predict similar characteristics.

Finally, the response of the moored floater excited by the higher amplitude (*Extreme*) wave train is examined. The displacement of the CoM in terms of surge, heave and pitch is presented in Figure 5.54. Simulations are in good agreement with the measurements in heave and pitch. Some differences are evident in case of the surge motion, as in the previous case of the benign wave train. Particularly, the numerical surge displacement presents a constant offset with respect to the measurements.

To sum up, for the time window where the motion of the structure is governed primarily by the hydrodynamic part, numerical results can be predict with great accuracy with the experimental ones. After the wave train passes through the floater, the decay of motion by the catenary mooring lines begins. Again differences are evident between the two approaches, originate primarily from the dynamic modeling, and the remarks that were discussed in the previous subsection apply here as well.

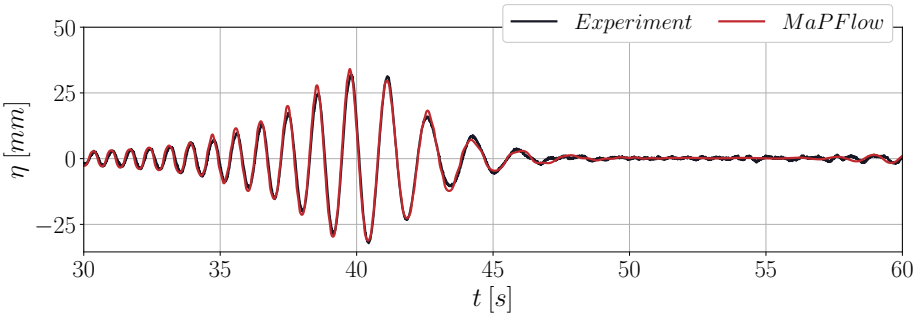

(a) Wave gauge position $x = -10m, y = 0$

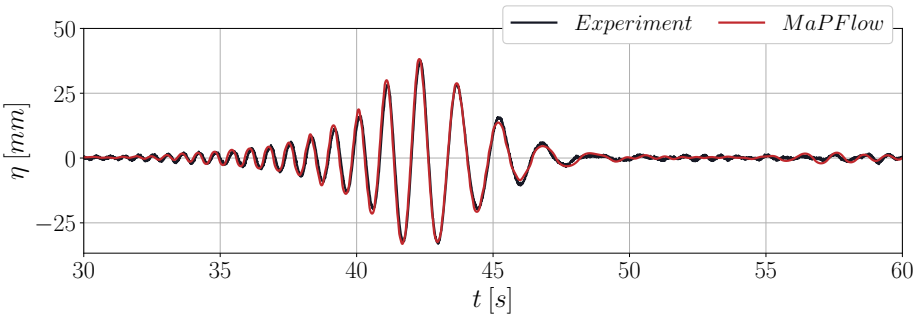

(b) Wave gauge position $x = -7.5m, y = 0$

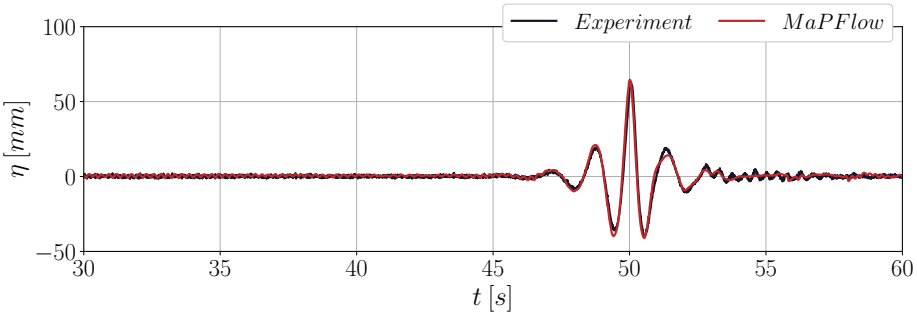

(c) Wave gauge position $x = 0, y = -1.5m$

Figure 5.51: Comparison between computational and experimental results for the *benign focused wave train* test case. Free surface elevation at various wave gauges

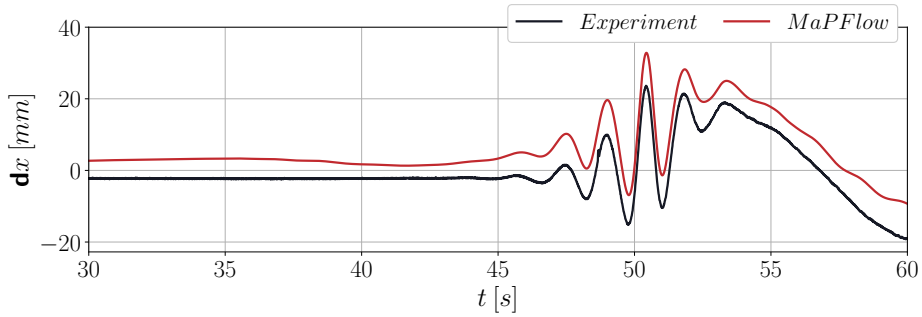

(a) Surge motion

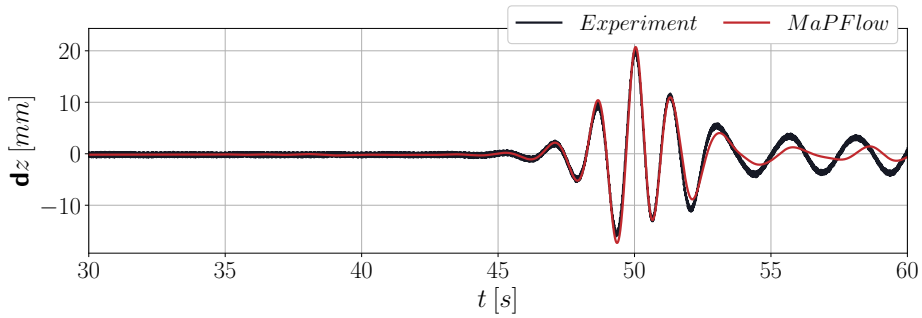

(b) Heave motion

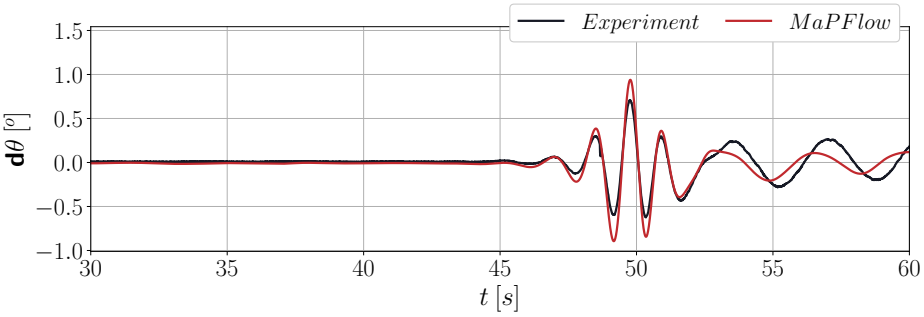

(c) Pitch motion

Figure 5.52: Comparison between computational and experimental results for the *benign wave train* test case. Offsets from the corresponding equilibrium positions.

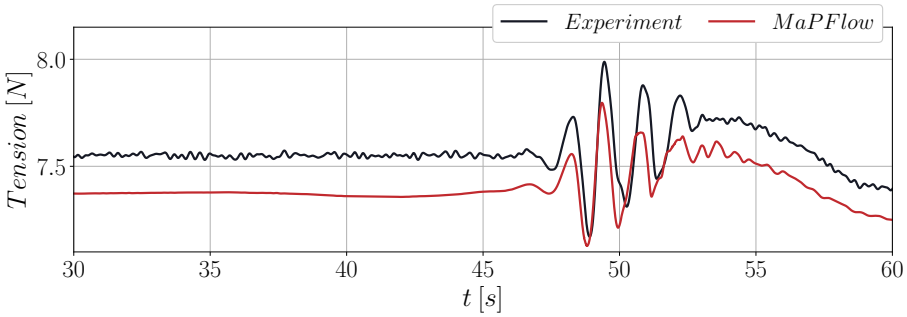

(a) Fore fairlead

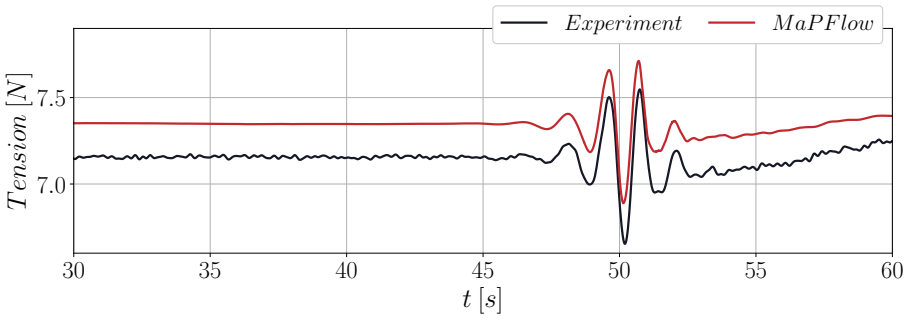

(b) Port fairlead

Figure 5.53: Comparison between computational and experimental results for the *benign wave train* test case. Tension on the mooring lines.

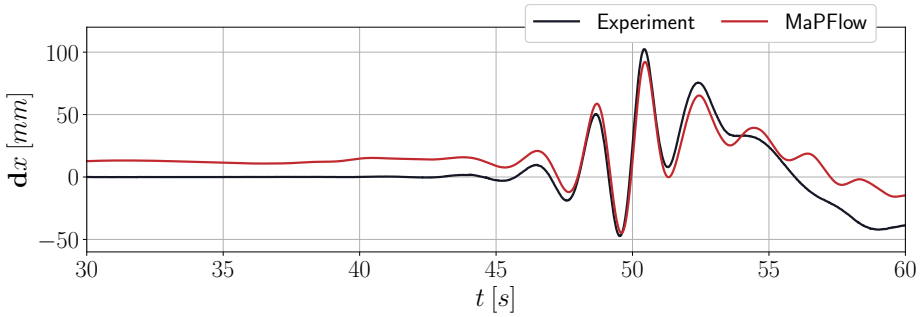

(a) Surge motion

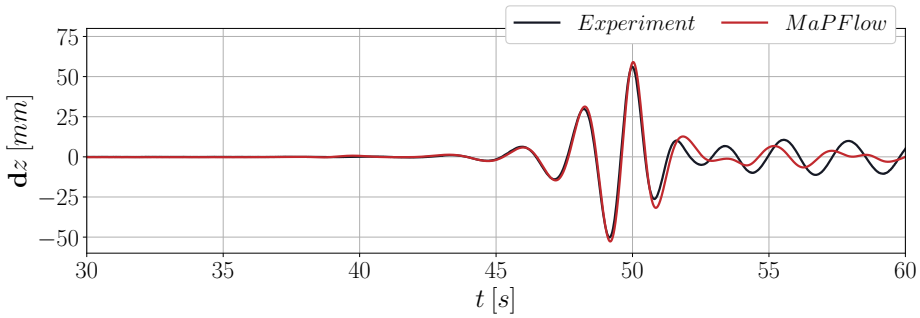

(b) Heave motion

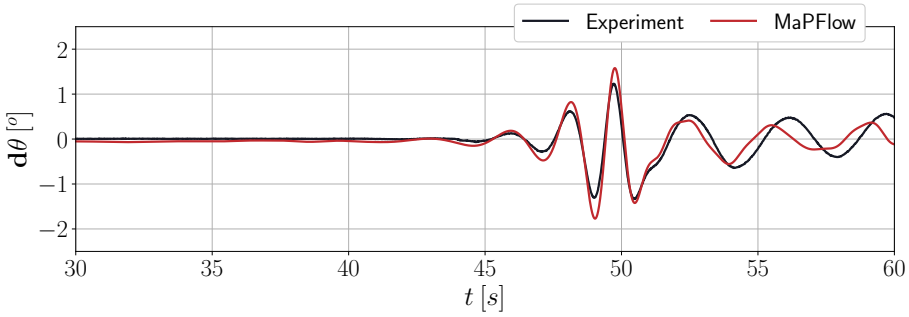

(c) Pitch motion

Figure 5.54: Comparison between computational and experimental results for the *extreme focused wave train* test case. Offsets from the corresponding equilibrium positions.

This page intentionally left blank

Chapter 6

Conclusions & Future Work

In this final chapter of the thesis, the basic conclusions of the work are drawn. The basic intermediate steps taken are summarized and finally, recommendations for future work are given.

6.1 Thesis Conclusions

The primary goals of the present work were, firstly to introduce a complete methodology for simulating Fluid–Structure Interaction (FSI) problems in the marine environment and secondly, to conduct a thorough validation in a plethora of numerical test cases. In order to accomplish the first goal, the theoretical formulation of the coupled AC/VoF for free surface flows was derived and guidelines for several aspects of the CFD modeling were given. Secondly, the test cases were carefully chosen based on either recommendation taken from literature or requirements that arise from modern engineering designs.

In order to accomplish the aforementioned goals, the following three steps were made

1. Development of an Artificial Compressibility formulation coupled with the Volume of Fluid method to account for free surface flows. The research gap of exploiting the AC method for free surface flows was successfully explored.
2. Development of a 6–DoF rigid body solver and of a FSI procedure for the coupling of the rigid body solver with the flow solver. In addition, mesh deformation algorithms were applied for the effective motion of the bodies inside a computational domain.
3. Validation of the above methodology in 7 test–cases, in which 4 of them considered the interaction of the studied structure with the surrounding flowfield.

In each step the following general remarks can be made. Initially, for the fluid solver,

- The present methodology was based on the work of Kunz *et al.* [61]. The numerical method was extended in arbitrarily polyhedral volumes that are able to move in space or experience deformation.
- The implicit source zones formulation was implemented for the wave generation and absorption inside a numerical wave tank
- The various challenges of field reconstruction have been efficiently tackled. High–order resolution schemes were used to prevent the smearing of the free surface, while for the pressure field, near the free surface, a density based interpolation scheme was utilized to account for the change of the pressure gradient.
- A flux–correction scheme was applied to maintain second order accuracy in case of non–planar vertices in 3D.

– The overproduction of turbulence near the free surface was successfully suppressed. Remedies proposed by literature were investigated and further guidelines were given.

Secondly, for the coupled FSI procedure,

– A standard 6–DoF rigid body solver was developed. The equations of motion are solved in the relative frame of reference. The non–linear terms are discretized using a δ–formulation and for the time integration the Newmark–β is utilized.
– An iterative process was formulated for the coupling of the flow and the rigid body solvers. The strong coupling of the solvers was enforced by combining them into an iterative procedure with appropriate termination criterion.
– For the motion of the structure, two mesh deformation algorithms were used. A simple, but efficient algorithm used for simple geometries, in which, deformation damps away from the solid boundary, based on an exponential function. Moreover, a more sophisticated method was implemented, which is based on the RBF interpolation method, supplemented with a point reduction algorithm, to reduce the computational cost.
– The implementation of the FSI procedure was greatly facilitated by the coupled AC/VoF approach. Since, no time lagging exists between the flow equations, no further limitations in the maximum allowed timestep occurred.

Finally, for the validation of the methodology and the applications discussed in the previous two chapters,

– Parametric studies conducted revealed a dependency of the method on the value of the AC parameter β. If extremely large or small values of β are chosen, the convergence of the may be affected. A relative familiarity of the user with the numerical method is required. However, as it was demonstrated, there is a wide range of values, where β value can be defined, and convergence would not be affected.
– Wave generation and absorption was performed using implicit source zones. For the generation of the waves, typically one wavelength of source zone was sufficient for accurate wave generation, and no major dependencies from numerical parameters of the method were found. More complications arise for the damping of the outgoing waves. Based on parametric studies, the damping of the waves was found to be sensitive on the corresponding the numerical parameters. Primarily, dependency was found on the length of the wave generation zone, which should extend for at least for 1.5 wavelengths.
– In case of the turbulent flows, the conventional turbulence models exhibit an overproduction of turbulent viscosity near the free surface. The conventional techniques proposed in literature manage to reduce overproduction, however they were unable to suppress it completely. This is more pronounced in flows which include surface–piercing structures, in absence of current. In this work, supplementary to the existing recommendations, the Kato–Launder method was employed and the turbulent viscosity levels near the free surface were drastically decreased.
– For the ship calculations, the calculated resistance and motion of the studied ship hulls were in accordance with the experimental and numerical results. The only major deviations from the experiments were noted, in low Froude numbers. However, these deviations where not larger than 0.008^o in trim and $1.3mm$ in sinkage (see Sec. 5.2.3). Additionally, all results seem to be within the same limits as other computational results (see Appendix E).
– For the floater calculations, the blind test comparison with the experiments was fair. All calculations predict a similar response characteristics as in the experiments. The deviations were primarily originated from the dynamic modeling of the mooring lines.

Tuning of the dynamic model, using the experimental data, might improve the numerical results.

– Lastly, it has to be noticed, that the method performed well, in all sensitivity analyses. An adequate convergence performance was noted in all timestep and grid independence studies.

6.2 Suggestions for Future Work

The recommendations for future research discussed here, concern two main topics. Firstly, extensions and improvements on the numerical methodology and secondly engineering investigations of various concepts and issues, that can use the present work as their starting point.

Starting from the extensions and improvements of the flow solver,

– The first family of improvements concerns the reconstruction of the VoF field. More accurate approximations can be adopted to restrain the numerical diffusion. In this direction, geometric approximations can be considered, or even coupling VoF method with the level–set function creating the hybrid formulation of CLSVOF [30].

– The inclusion of surface tension terms in the free surface modeling. This recommendation can be combined with the previous step. A more accurate representation of the free surface would facilitate the calculation of the geometric quantities, such as curvature.

– Investigation of cavitating flows. The mass transfer terms proposed by Kunz *et al.* [61] can be easily incorporated in the present methodology. A primary investigation in this direction has already been conducted in MaPFlow [168], however a more detailed investigation is required, including its application to more realistic engineering problems.

– In MaPFlow apart from the RANS approach for the turbulence modeling, higher fidelity models are also available [76]. Specifically, the Large Eddy Simulation (LES) [169] and the Detached Eddy Simulation (DES) [170] have been developed in the compressible version of the code. An immediate extension of the present work would be to incorporate these methods to the free surface framework.

– MaPFlow has the ability of predicting transition from laminar to turbulent flow [76]. Another possible extension would be to assess their performance and explore their capabilities in various marine applications. Among the implemented methods, models based on transport equations, such the Amplification Factor Transport (AFT) model [171] and the $\gamma - Re_\theta$ [172] model could be considered for the calculation of the ship's resistance in conditions of free transition, or for more accurate prediction of propeller thrust.

Since in the present thesis, a complete methodology for free surface flows was formulated, a natural follow–up is to be used as an assessment tool for engineering concepts. In this direction, some recommendations are,

– Investigation of full scaled structures. In the present work, only model scaled structures are considered. A possible extension of this work would be the investigations of full scale ships and platforms for real application. In these cases Reynolds number increases drastically along with the computational cost.

– Study of the interaction of vortical structures with the boundary layer of ship hulls. In literature, ongoing research is performed on the evaluation of vortical structures generated by parts of the ship hull (transom, fore–body, bilge keels) and their interaction with the boundary layer using numerical methods. These simulations require high fidelity approximations for turbulence and a fine spatial discretization. In literature, there are available data for comparison. For example in [173] experimental data on the 3D separation and

the progression of vortical structures are presented, in cases of the surface combatant 5512 in straight–ahead and drift conditions.

– Another class of engineering problems that can be faced based on the present work is the maneuvering test cases. Turning circle, zig–zig manoeuvre, stopping test, are few of the test cases proposed by the ITTC [174] to evaluate the manoeuvring characteristics of a vessel.

– Self–propulsion test cases are one of the most common procedures executed with CFD softwares in industrial level. MaPFlow, recently has been extended to include more than one meshes that can overlap with each other [175]. This approximation, commonly referred to as overset–grids, can be used to resolve the rotation of the propeller inside a background grid fitted to the ship hull. Alternatively, the Actuator Disk method can utilized to reduce the computational cost.

– Another idea for possible extension of the present work stems from the concluding remarks of the EU founded project SEATECH. Both numerical and experimental results (see Sec. 5.3) indicated that, in presence of waves, a fully submerged horizontal foil can be used to reduce the motions (especially in the heave direction) of a ship, and as a result its resistance. In this direction, already some steps have been made in experimental level. A preliminary experimental campaign has been conducted to study an alternative design of submerged wing placed at the bow of the ship. A reverse T–shaped foil with a sweep angle was constructed and placed beneath the bow of a model ferry ship. Pictures of the experimental model and the T–foil arrangement are presented in Figure 6.1. In the numerical level, the methodology developed in the present thesis can be used to obtain predictions and detailed flowfield patterns for the effect of the foil in presence of waves, as well as, for conducting a parametric study for trim optimization by regulating the Angle of Attack (AoA) of the foil.

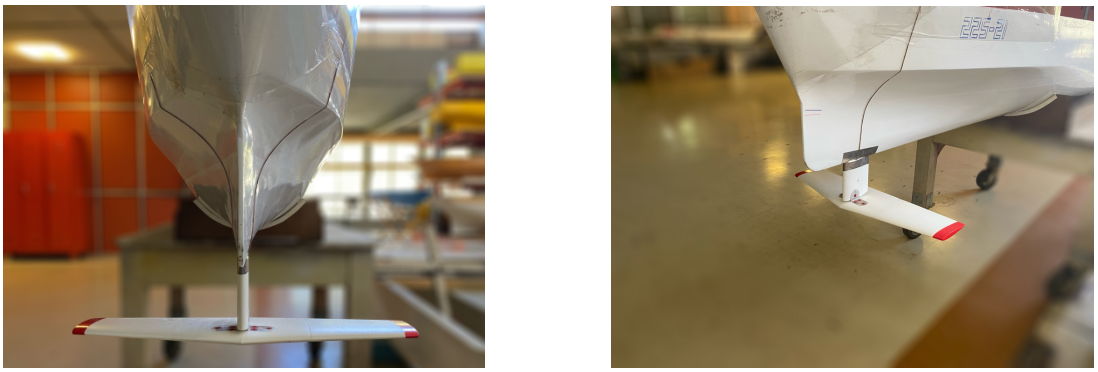

(a) Front view **(b)** Side view

Figure 6.1: Pictures of the experimental arrangement of a reverse T–foil placed in under the bow of scaled ferry ship. Ship dimensions: length L=3.3m, breadth B=0.43 and draught T=0.135m. Foil dimensions: span s=0.5m, sweep angle $\theta = 12^o$

6.3 Publications

Within the context of the present thesis the following publications have been made, in international journals and in proceedings of corresponding conferences.

6.3.1 Journal Papers

1. **D. Ntouras**, G. Papadakis, K. Belibassakis. (2022). Ship Bow Wings with Application to Trim and Resistance Control in Calm Water and in Waves. *Journal of Marine Science and Engineering.* 10. 10.3390/jmse10040492.

2. **D. Ntouras** and G. Papadakis. (2020). A coupled artificial compressibility method for free surface flows. *Journal of Marine Science and Engineering.* 8(8). 590 10.3390/jmse8080590.

3. A. Mavrakos, D. Konispoliatis, **D. Ntouras**, G. Papadakis and S. Mavrakos. (2023). Hydrodynamic coefficients in heave of a moonpool-type floater using theoretical, numerical and CFD methodologies. *Ocean Engineering.* 279. 10.1016/j.oceaneng.2023.114519.

4. M. Manolesos, L. Chng, N. Kaufmann, P. Ouro, **D. Ntouras** and G. Papadakis. (2023). Using vortex generators for flow separation control on tidal turbine profiles and blades. *Renewable Energy.* 205. 10.1016/j.renene.2023.02.009.

5. A. Mavrakos, D. Konispoliatis, **D. Ntouras**, G. Papadakis and S. Mavrakos. (2022). Hydrodynamics of Moonpool-Type Floaters: A Theoretical and a CFD Formulation. *Energies.* 15. 570. 10.3390/en15020570.

6. A. Dermatis, **D. Ntouras**, G. Papadakis. (2022). Numerical Simulation of Irregular Breaking Waves Using a Coupled Artificial Compressibility Method. *Fluids.* 10.3390/fluids7070235.

7. K. Theodorakis, **D. Ntouras** and G. Papadakis. (2022). Investigation of a submerged fully passive energy-extracting flapping foil operating in sheared inflow. *Journal of Fluids and Structures.* 113. 10.1016/j.jfluidstructs.2022.103674.

8. G. Grigoropoulos, C. Bakirtzoglou, G. Papadakis and **D. Ntouras.** (2021). Mixed-Fidelity Design Optimization of Hull Form Using CFD and Potential Flow Solvers. *Journal of Marine Science and Engineering.* 9. 1234. 10.3390/jmse9111234.

6.3.2 Conference Papers

1. **D. Ntouras**, D. Manolas, G. Papadakis and V. Riziotis. (2023). Hydrodynamic response of a floating offshore wind turbine using an artificial compressibility finite volume method. *33rd International Society of Offshore and Polar Engineers*, Ottawa, Canada

2. **D. Ntouras**, G. Papadakis, D. Liarokapis, G. Trachanas and G. Tzabiras. (2022). Numerical and experimental investigation of a model scaled propeller. *MARTECH 2022*, Lisbon, Portugal, li10.1201/9781003320272-45.

3. **D. Ntouras**, D.Manolas, G. Papadakis and V. Riziotis. (2020). Exploiting the limit of BEM solvers in moonpool type floaters. *TORQUE Conference*, Delft, Netherlands, September 2020.

4. L. Chng, J. Alber, **D. Ntouras**, G. Papadakis, N. Kaufmann, P. Ouro and M. Manolesos. (2022). On the combined use of Vortex Generators and Gurney Flaps for turbine airfoils. *Journal of Physics: Conference Series.* 2265. 032040. 10.1088/1742-6596/2265/3/032040.

5. G. Papadakis, E. Filippas, **D. Ntouras** and K. Belibassakis. (2019) Effects of viscosity and nonlinearity on 3D flapping-foil thruster for marine applications. *OCEANS 2019 - Marseille*, Marseille, France, 10.1109/OCEANSE.2019.8867084.

This page intentionally left blank

Appendix A

δ–formulation of Rigid Body Equations

The motion of a rigid body vehicle is governed by the Newton's second law of motion for its linear acceleration and by the relation between moments and angular momentum for its orientation. If m is the body mass, that is subjected to external forcing $\overrightarrow{F}$, which creates moment $\overrightarrow{G}$ with respect to its center of mass, $\overline{I}$ is the symmetric inertia tensor, $\vec{u}$ the velocity of the body fixed frame with components u, v, w, $\vec{\omega}$ the rotational speed of the relative frame with components p, q, r and $\vec{h} = \overline{I}\vec{\omega}$ the angular momentum, then the equations of motions are written as

$$\begin{aligned} \overrightarrow{F} &= m\left(\dot{\vec{u}} + \vec{\omega} \times \vec{u}\right) \\ \overrightarrow{G} &= \dot{\vec{h}} + \vec{\omega} \times \vec{h} \end{aligned} \tag{A.1}$$

This is a non–linear system of equations due to the cross product terms that involve the unknown translational and rotational velocities. The non–linear terms arose from the coordinate system transformation and in order to take them into account an iterative process is followed. In every iteration l of the FSI algorithm, as described in Section, 3.9, small variations of the unknown variables $\delta\vec{u}, \delta\vec{\omega}$ are assumed between the known level l and the next unknown $l+1$. This δ formulation implies

$$\begin{aligned} \vec{u}_{l+1}^{n+1} &= \vec{u}_{l}^{n+1} + \delta\vec{u} \\ \vec{\omega}_{l+1}^{n+1} &= \vec{\omega}_{l}^{n+1} + \delta\vec{\omega} \end{aligned} \tag{A.2}$$

with $n+1$ being the next unknown timestep. The iterative process terminates once variations tend to zero.

By inserting Equation (A.2) into Equation (A.1) the following expression is obtained

$$\begin{aligned} \delta\vec{F} &= m\left(\delta\dot{\vec{u}} + \left(\vec{\omega}_{l}^{n+1} \times \delta\vec{u}\right) - \left(\vec{u}_{l}^{n+1} \times \delta\vec{\omega}\right)\right) \\ \delta\vec{G} &= \delta\dot{\vec{h}} + \left(\vec{\omega}_{l}^{n+1} \times \delta\vec{h}\right) - \left(\vec{h}_{l}^{n+1} \times \delta\vec{\omega}\right) \end{aligned} \tag{A.3}$$

where the quadratic terms have been ignored. The forcing on the left hand side of the equations is corrected by the acceleration term on the known time level l, meaning $\delta\vec{F} = \vec{F}_{l}^{n+1} - m\left(\dot{\vec{u}}_{l}^{n+1} + \left(\vec{\omega}_{l}^{n+1} \times \vec{u}_{l}^{n+1}\right)\right)$ and $\delta\vec{G} = \vec{G}_{l}^{n+1} - \left(\dot{\vec{h}}_{l}^{n+1} + \vec{\omega}_{l}^{n+1} \times \vec{h}_{l}^{n+1}\right)$.

Equations (A.3) can be further simplified by expressing the cross products as skew symmetric

tensors[1]. Starting from the expression for the translational motion

$$\omega_l^{n+1} \times \delta\vec{u} = \omega_{l,\times}^{n+1}\delta\vec{u} = \begin{bmatrix} 0 & -r & q \\ r & 0 & -p \\ -q & p & 0 \end{bmatrix} \delta\vec{u} = \overline{C}_{nl,1}\delta\vec{u} \tag{A.4}$$

and

$$-u_l^{n+1} \times \delta\vec{\omega} = -u_{l,\times}^{n+1}\delta\vec{\omega} = \begin{bmatrix} 0 & w & -v \\ -w & 0 & u \\ v & -u & 0 \end{bmatrix} \delta\vec{\omega} = \overline{C}_{nl,2}\delta\vec{\omega} \tag{A.5}$$

Similarly, for the rotational motion

$$\vec{\omega}_l^{n+1} \times \delta\vec{h} - \vec{h}_l^{n+1} \times \delta\vec{\omega} = \left(\omega_{l,\times}^{n+1}\overline{I} - h_{l,\times}^{n+1}\right)\delta\vec{\omega} =$$
$$\begin{bmatrix} I_{xz}q - I_{xy}r & I_{xz}p + (I_{zz} - I_{yy})\,r + 2I_{yz}q & -I_{xy}p + (I_{zz} - I_{yy})\,q - 2I_{yz}r \\ -I_{yz}q + (I_{xx} - I_{zz})\,r - 2I_{xz}p & I_{xy}r - I_{yz}p & I_{xy}q + (I_{xx} - I_{zz})\,p + 2I_{xz}r \\ I_{yz}r + (I_{yy} - I_{xx})\,q + 2I_{xy}p & -I_{xz}r + (I_{yy} - I_{xx})\,p - 2I_{xy}q & I_{yz}p - I_{xz}q \end{bmatrix} \delta\vec{\omega}$$
$$= \overline{C}_{nl,3}\delta\vec{\omega} \tag{A.6}$$

Once the previous definitions have been given the following vector equation can be defined

$$\delta\overrightarrow{Q} = \overline{M}\delta\ddot{\overrightarrow{U}} + \overline{C}_{nl}\delta\overrightarrow{U} \tag{A.7}$$

where $\overrightarrow{Q}$ is a generalized vector that includes both forces and moments, vector $\overrightarrow{U} = [u, v, q, p, q, r]^T$ contains the unknown translational and rotational velocities, $\overline{M}$ is the mass matrix and $\overline{C}_{nl}$ the damping matrix that includes the coupling between the equations of motion. The damping matrix is a block matrix with submatrices according to definitions (A.4),(A.5) and (A.6)

$$\overline{C}_{nl} = \begin{bmatrix} m\overline{C}_{nl,1} & m\overline{C}_{nl,2} \\ 0 & \overline{C}_{nl,3} \end{bmatrix} \tag{A.8}$$

Typically Equation (A.7) is expressed in terms of the three translations surge–x, sway–y and heave–z and the three rotations roll–ϕ, pitch–θ and yaw θ leading to the following expression

$$\delta\overrightarrow{Q} = \overline{M}\delta\ddot{\overrightarrow{x}} + \overline{C}_{nl}\delta\dot{\overrightarrow{x}} \tag{A.9}$$

with $\overrightarrow{x}$ being a generalized vector that includes both translations and rotations, $\vec{x} = [x, y, z, \phi, \theta, \psi]^T$.

[1] $\vec{a} \times \vec{b} = a_\times \vec{b} = \begin{bmatrix} 0 & -a_z & a_y \\ a_z & 0 & -a_z \\ -a_y & a_x & 0 \end{bmatrix} \begin{bmatrix} b_x \\ b_y \\ b_z \end{bmatrix}$

Appendix B

Numerical Solution of Dynamic System of Equations

In general, the response of a dynamic system can be expressed as a second order differential equation of the form

$$\overline{M}\ddot{\vec{x}} + \overline{C}\dot{\vec{x}} + \overline{K}\vec{x} = \overrightarrow{Q}(\vec{x}, \dot{\vec{x}}) \tag{B.1}$$

where $\overline{M}$ is the mass matrix, $\overline{C}$ is the damping matrix, $\overline{K}$ is the stiffness matrix and $\overrightarrow{Q}$ is the vector of external dynamic loads (e.g. hydrodynamic forces, gravity, etc).

Equation (B.1) is a non–linear system of equation, since the forcing on the right hand side depends on the unknown displacements and velocities of the problem. At any point in time $t^{n+1} = (n+1)\Delta t$ an in initial value problem is solved

$$\overline{M}\ddot{\vec{x}}^{n+1} + \overline{C}\dot{\vec{x}}^{n+1} + \overline{K}\vec{x}^{n+1} = \overrightarrow{Q}(\vec{x}^{n+1}, \dot{\vec{x}}^{n+1}) \tag{B.2}$$

with initial data $\vec{x}(t^0) = \vec{x}^0$, $\dot{\vec{x}}(t^0) = \dot{\vec{x}}^0$.

For the solution of the non–linear equations, a δ–formulation is adopted

$$\begin{aligned} \vec{x}_{l+1}^{n+1} &= \vec{x}_l^{n+1} + \delta\vec{x} \\ \dot{\vec{x}}_{l+1}^{n+1} &= \dot{\vec{x}}_l^{n+1} + \delta\dot{\vec{x}} \\ \ddot{\vec{x}}_{l+1}^{n+1} &= \ddot{\vec{x}}_l^{n+1} + \delta\ddot{\vec{x}} \end{aligned} \tag{B.3}$$

The above equations formulate an iterative process, which aims to drive perturbations $\delta\vec{x}$,$\delta\dot{\vec{x}}$ and $\delta\ddot{\vec{x}}$ to zero. For $l = 0$ the iterative procedure is initiated with $\vec{x}_l^{n+1} = \vec{x}^n$ and upon convergence the new positions are retrieved $\vec{x}^{n+1} = \vec{x}_{l+1}^{n+1}$ (similarly for $\dot{\vec{x}}^{n+1}$, $\ddot{\vec{x}}^{n+1}$).

Plugging Equation (B.3) in (B.1) the following expression occurs

$$\begin{gathered} \overline{M}\left(\ddot{\vec{x}}_l^{n+1} + \delta\ddot{\vec{x}}\right) + \overline{C}\left(\dot{\vec{x}}_l^{n+1} + \delta\dot{\vec{x}}\right) + \overline{K}\left(\vec{x}_l^{n+1} + \delta\vec{x}\right) = \overrightarrow{Q} \Rightarrow \\ \overline{M}\delta\ddot{\vec{x}} + \overline{C}\delta\dot{\vec{x}} + \overline{K}\delta\vec{x} = \delta\overrightarrow{Q} \end{gathered} \tag{B.4}$$

where $\delta\overrightarrow{Q} = \overrightarrow{Q}_l^{n+1} - \overline{M}\ddot{\vec{x}}_l^{n+1} - \overline{C}\dot{\vec{x}}_l^{n+1} - \overline{K}\vec{x}_l^{n+1}$, with $\vec{Q}_l^{n+1} = \overrightarrow{Q}(\vec{x}_l^{n+1}, \dot{\vec{x}}_l^{n+1})$.

In FSI problems, with l being the iteration index, the hydrodynamic components of the forcing term $\vec{Q}_l^{n+1}$ is calculated by the hydrodynamic solver (see Sec. 3.9).

For the time integration of the non–linear system the Newmark–β method is used. The method expresses the unknown displacements and velocities of Equation (B.2) of the time level $n+1$ as a Taylor expansion, with two regulation parameters β, γ. Specifically

$$\begin{aligned} \vec{x}^{n+1} &= \vec{x}^n + dt\dot{\vec{x}}^n + dt^2\left((0.5-\beta)\ddot{\vec{x}}^n + \beta\ddot{\vec{x}}^{n+1}\right) = \vec{x}_{pre} + dt^2\beta\ddot{\vec{x}}^{n+1} \\ \dot{\vec{x}}^{n+1} &= \dot{\vec{x}}^n + dt\left((1-\gamma)\ddot{\vec{x}}^n + \gamma\ddot{\vec{x}}^{n+1}\right) = \dot{\vec{x}}^{pre} + dt\gamma\ddot{\vec{x}}^{n+1} \end{aligned} \tag{B.5}$$

In the above equations $\vec{x}_{pre}$ and $\vec{\dot{x}}_{pre}$ contain the known contribution from the previous timestep. Again, the δ–formulation as defined in Equation (B.3), is introduced into both equations. Starting from the expression for the displacements $\vec{x}^{n+1}$

$$\begin{aligned} \vec{x}_l^{n+1} + \delta\vec{x} &= \vec{x}_{pre} + \beta dt^2 \left(\vec{\ddot{x}}_l^{n+1} + \delta\vec{\ddot{x}}\right) \Rightarrow \\ \delta\vec{\ddot{x}} &= \frac{\vec{x}_l^{n+1} - \vec{x}_{pre}}{\beta dt^2} - \vec{\ddot{x}}_l^{n+1} + \frac{\delta\vec{x}}{\beta dt^2} \Rightarrow \\ \delta\vec{\ddot{x}} &= \vec{\ddot{x}}_M + \frac{\delta\vec{x}}{\beta dt} \end{aligned} \tag{B.6}$$

where $\vec{\ddot{x}}_M = \frac{\vec{x}_l^{n+1} - \vec{x}_{pre}}{\beta dt^2} - \vec{\ddot{x}}_l^{n+1}$.

Similarly for the velocities

$$\begin{aligned} \vec{\dot{x}}_l^{n+1} + \delta\vec{\dot{x}} &= \vec{\dot{x}}_{pre} + \gamma dt\vec{\ddot{x}}_l^{n+1} + \gamma dt\delta\vec{\ddot{x}} \Rightarrow \\ \delta\vec{\dot{x}} &= \vec{\dot{x}}_{pre} - \vec{\dot{x}}_l^{n+1} + \cancel{\gamma dt\vec{\ddot{x}}_l^{n+1}} + \gamma dt \left(\frac{\vec{x}_l^{n+1} - \vec{x}_{pre}}{\beta dt^2} - \cancel{\vec{\ddot{x}}_l^{n+1}} + \frac{\delta\vec{x}}{\beta dt^2}\right) \Rightarrow \\ \delta\vec{\dot{x}} &= \vec{\dot{x}}_C + \frac{\gamma}{\beta dt}\delta\vec{x} \end{aligned} \tag{B.7}$$

where $\vec{\dot{x}}_c = \dot{x}_{pre} - \vec{\dot{x}}_l^{n+1} + \frac{\gamma}{\beta dt}\left(\vec{x}_l^{n+1} - \vec{x}_{pre}\right)$.

Equations (B.6) and (B.4) are introduced into (B.7) resulting in a linear system of equations

$$\left(\frac{1}{\beta dt^2}\overline{M} + \frac{\gamma}{\beta dt}\overline{C} + \overline{K}\right)\delta\vec{x} = \delta\overrightarrow{Q} - \overline{M}\vec{\ddot{x}}_M - \overline{C}\vec{\dot{x}}_C \tag{B.8}$$

The system is solved with LU decomposition. The last step of the procedure is to update all variables

$$\begin{aligned} \vec{x}_{l+1}^{n+1} &= \vec{x}_l^{n+1} + \delta\vec{x} \\ \vec{\ddot{x}}_{l+1}^{n+1} &= \frac{\vec{x}_l^{n+1} - \vec{x}_{pre}}{\beta dt^2} \\ \vec{\dot{x}}_{l+1}^{n+1} &= \vec{\dot{x}}_{pre} + \gamma dt\vec{\ddot{x}}_{l+1}^{n+1} \end{aligned} \tag{B.9}$$

Appendix C

Eigenstructure of the Hyperbolic Two–Phase Problem

One main advantage of employing the Artificial Compressibility method in two–phase flows is the formation of a hyperbolic system of equations in pseudo–time. Let $\overrightarrow{Q} = [p, \vec{v}, a]^T$, be the vector of unknown primitive variables, then by introducing the AC method the following system is obtained.

$$\overline{\Gamma}\frac{\partial \overrightarrow{Q}}{\partial \tau} + \overline{A}_c \frac{\partial \overrightarrow{Q}}{\partial \vec{x}} = 0 \tag{C.1}$$

where $\overline{A}_c$ is the convective jacobian

$$\overline{A}_c = \frac{\partial \overrightarrow{F}}{\partial \overrightarrow{Q}} \tag{C.2}$$

and $\overrightarrow{F} = \left(\vec{f}, \vec{g}, \vec{h}\right)$ is a generalized vector that contains the inviscid fluxes in the x,y and z direction [99]. The preconditioner $\overline{\Gamma}$ of Kunz [61], is used to facilitate convergence

$$\overline{A}_c = \overline{\Gamma}\overline{\Gamma}^{-1}\overline{A}_c = \overline{\Gamma}\tilde{A}_c \tag{C.3}$$

The scaled jacobian matrix $\tilde{A}_c$ is used to solve the hyperbolic system, which has real and distinct eigenvalues. The matrix is given by the following expression

$$\tilde{A}_c = \begin{bmatrix} 0 & n_x & n_y & n_z & 0 \\ n_x & \rho_m\left(n_x u + \Delta V\right) & \rho_m n_y u & \rho_m n_z u & u\Delta V \Delta\rho \\ n_y & \rho_m n_x v & \rho_m\left(n_y v + \Delta V\right) & \rho_m n_z v & v\Delta V \Delta\rho \\ n_z & \rho_m n_x w & \rho_m n_y w & \rho_m\left(n_z w + \Delta V\right) & w\Delta V \Delta\rho \\ 0 & \alpha_l n_x & \alpha_l n_y & \alpha_l n_z & \Delta V \end{bmatrix} \tag{C.4}$$

A diagonalization of matrix $\tilde{A}_c$ implies that

$$\left|\tilde{A}_c\right| = \tilde{R}^{-1}\left|\tilde{\Lambda}\right|\tilde{R} \tag{C.5}$$

where matrix $\tilde{R}$ contains the right eigenvectors of the jacobian matrix arranged in row wise order, $\tilde{R}^{-1}$ is the matrix of the left eigenvectors arranged in column wise order and $\tilde{\Lambda}$ is a diagonal matrix containing the absolute values of the system eigenvalues. The eigenvalues are computed as

$$\begin{aligned} \lambda_{1,2,5} &= V_n - V_g \\ \lambda_3 &= V_n - c - \frac{V_g}{2} \\ \lambda_4 &= V_n + c - \frac{V_g}{2} \end{aligned} \tag{C.6}$$

where $V_n = \vec{v} \cdot \vec{n}$, $V_g = \vec{v}_{vol} \cdot \vec{n}$ and the artificial sound speed is computed as

$$c = \sqrt{\beta + \left(V_n - \frac{V_g}{2}\right)^2} \tag{C.7}$$

Finally, the eigenvectors of the Jacobian (C.3) are given by Equations (C.8) and (C.9).

$$\tilde{R} = \begin{bmatrix} 0 & 0 & -\rho_m c_m & \rho_m c_p & 0 \\ x_1 & x_2 & n_x + \dfrac{u\lambda_3}{\beta} & n_x + \dfrac{u\lambda_4}{\beta} & 0 \\ y_1 & y_2 & n_y + \dfrac{v\lambda_3}{\beta} & n_y + \dfrac{v\lambda_4}{\beta} & 0 \\ z_1 & z_2 & n_z + \dfrac{w\lambda_3}{\beta} & n_z + \dfrac{w\lambda_4}{\beta} & 0 \\ 0 & 0 & 0 & 0 & 1 \end{bmatrix} \tag{C.8}$$

$$\tilde{R}^{-1} = \begin{bmatrix} \dfrac{1}{\rho_m c_g}\left[n_x\left(wy_2 - vz_2\right) + n_y\left(uz_2 - wx_2\right) + n_z\left(vx_2 - uy_2\right)\right] & \dfrac{1}{c_g}\left[\beta\left(n_z y_2 - n_y z_2\right) + \Delta V\left(wy_2 - vz_2\right)\right] & \dfrac{1}{c_g}\left[\beta\left(n_x z_2 - n_z x_2\right) + \Delta V\left(uz_2 - wx_2\right)\right] & \dfrac{1}{c_g}\left[\beta\left(n_y x_2 - n_x y_2\right) + \Delta V\left(vx_2 - uy_2\right)\right] & 0 \\ \dfrac{1}{\rho_m c_g}\left[n_x\left(vz_1 - wy_1\right) + n_y\left(wx_1 - uz_1\right) + n_z\left(uy_1 - vx_1\right)\right] & \dfrac{1}{c_g}\left[\beta\left(n_y z_1 - n_z y_1\right) + \Delta V\left(wy_1 - vz_1\right)\right] & \dfrac{1}{c_g}\left[\beta\left(n_z x_1 - n_x z_1\right) + \Delta V\left(wx_1 - uz_1\right)\right] & \dfrac{1}{c_g}\left[\beta\left(n_x y_1 - n_y x_1\right) + \Delta V\left(vx_1 - uy_1\right)\right] & 0 \\ -\dfrac{1}{\rho_m\, 2c\, c_g}\left(\beta + \lambda_4 V_n\right) & \dfrac{1}{2c\, c_g}\beta c_p n_x & \dfrac{1}{2c\, c_g}\beta c_p n_y & \dfrac{1}{2c\, c_g}\beta c_p n_z & 0 \\ \dfrac{1}{\rho_m\, 2c\, c_g}\left(\beta + \lambda_3 V_n\right) & \dfrac{1}{2c\, c_g}\beta c_m n_x & \dfrac{1}{2c\, c_g}\beta c_m n_y & \dfrac{1}{2c\, c_g}\beta c_m n_z & 0 \\ 0 & 0 & 0 & 0 & 1 \end{bmatrix} \tag{C.9}$$

In the preceding equations c_m, c_p and c_g are expressed as

$$c_m = c - \frac{V_g}{2}, \quad c_p = c + \frac{V_g}{2}, \quad c_g = \beta + V_n \Delta V \tag{C.10}$$

ΔV is equal to $V_n - V_g$, while for the unit vectors $\vec{x}_1 = (x_1, y_1, z_1)$ and $\vec{x}_2 = (x_2, y_2, z_2)$ should hold $\vec{x}_1 \cdot \vec{n} = \vec{x}_2 \cdot \vec{n} = 0$.

Appendix D

Characteristic Boundary Conditions

For better approximation of the boundary conditions at farfield, the characteristic formulation of the hyperbolic problem can be exploited. Since the problem is hyperbolic, information propagates either inwards or outwards of the domain based on the local eigenvalues of the problem.

The characteristic formulation begins with the definition of the linearised one–dimensional Euler equations along direction x_n normal to the boundary, according to Equation (D.1).

$$\overline{\Gamma}\frac{\partial \vec{Q}}{\partial \tau} + \overline{A}_o \frac{\partial \vec{Q}}{\partial x_n} = 0 \tag{D.1}$$

The matrix $\overline{A}_o$ is the averaged jacobian between the states at farfield $\vec{Q}_\infty$, which are known and constant, and the interior values $\vec{Q}_I$ of the boundary cell. By multiplying with the inverse preconditioner matrix $\overline{\Gamma}^{-1}$ the preconditioned averaged jacobian, $\tilde{A}_o = \overline{\Gamma}^{-1} A_o$ is introduced

$$\frac{\partial \vec{Q}}{\partial \tau} + \tilde{A}_o \frac{\partial \vec{Q}}{\partial x_n} = 0 \tag{D.2}$$

The diagonalization of $\tilde{A}_o$ implies

$$\tilde{A}_o = \tilde{R}_o \tilde{\Lambda}_o \tilde{R}_o^{-1} \quad \Rightarrow \quad \tilde{\Lambda} = \tilde{R}_o^{-1} \tilde{A}_o \tilde{R}_o \tag{D.3}$$

where $\tilde{R}_o, \tilde{R}_o^{-1}$ are the right and left eigenvectors of the matrix $\tilde{A}_o$ and $\tilde{\Lambda}_o$ is a diagonal matrix which contains the eigenvalues of matrix $\tilde{A}_o$.

Multiplying Equation (D.2) with R_o^{-1} and applying the definition (D.3) leads to,

$$\tilde{R}_o^{-1}\frac{\partial \vec{Q}}{\partial \tau} + \tilde{R}_o^{-1}\tilde{R}_o\tilde{\Lambda}\tilde{R}_o^{-1}\frac{\partial \vec{Q}}{\partial x_n} = 0 \quad \Rightarrow \tilde{R}_o^{-1}\frac{\partial \vec{Q}}{\partial \tau} + \tilde{\Lambda}\tilde{R}_o^{-1}\frac{\partial \vec{Q}}{\partial x_n} = 0 \tag{D.4}$$

Let $\vec{W}$ be the characteristic variables which are defined as

$$\partial \vec{W} = \tilde{R}_o^{-1} \partial \vec{Q} \tag{D.5}$$

the system of equations in (D.4) can now be written in a decoupled form given by Equation (D.6) and can be solved exact

$$\frac{\partial w_i}{\partial t} + \lambda_i \frac{\partial w_i}{\partial x_n} = 0, \;\; i = 1, \ldots, m \tag{D.6}$$

where m is the degree of the system.

Equation (D.6) implies that w_i are information carried by the characteristic lines on the curves $dx = \lambda_i dt$ with wave speeds λ_i [115]. This means that,

$$dw_i = 0 \;\text{ for }\; \frac{dx}{d\tau} = \lambda_i \tag{D.7}$$

The values characteristic variables w_i should be specified. Integrating equation (D.6) and since $\tilde{R}_o^{-1}$ is constant

$$\int \partial w_i = \sum_{j=1}^{n} \tilde{R}_o^{-1}[i,j] \int \partial q_j \tag{D.8}$$

The above equations for $i = 1$ can be written as

$$\int \partial w_1 = \tilde{R}_o^{-1}[1,1] \int \partial p + \tilde{R}_o^{-1}[1,2] \int \partial u + \tilde{R}_o^{-1}[1,3] \int \partial v + \tilde{R}_o^{-1}[1,4] \int \partial w + \tilde{R}_o^{-1}[1,5] \int \partial \alpha_l \tag{D.9}$$

or in discrete form

$$\delta w_1 = \tilde{R}_o^{-1}[1,1]\,\delta p + \tilde{R}_o^{-1}[1,2]\,\delta u + \tilde{R}_o^{-1}[1,3]\,\delta v + \tilde{R}_o^{-1}[1,4]\,\delta w + \tilde{R}_o^{-1}[1,5]\,\delta \alpha_l \tag{D.10}$$

where $\delta\{\cdot\} = \{\cdot\}_r - \{\cdot\}_b$, with the subscript r referring to a reference state and subscript b to the unknown values at the boundary.

The reference state r depends on the sign of the eigenvalues λ_i, it can be either the interior computational values or the physical exterior values at farfield. Adopting the convention that the normal vector on the boundary points always outside of the computational domain, and since $c > V_n$, λ_3 is always negative and λ_4 is always positive. This implies that for $i = 3$ the reference state corresponds to the exterior values while for $i = 4$ to the interior values. Furthermore, the sign of the eigenvalues, $\lambda_{1,2,5}$ depends of the sign of the velocity V_n. In the case of inflow, V_n is negative and thus the reference values is computed based on the farfield values and on the opposite case where V_n is positive, information is propagating outwards of the domain, indicating an outflow boundary, and the reference state is the interior values.

Before formulating the system of equations some algebraic operations are performed. Firstly, for the multiplication of the first row of matrix R_o^{-1} with the vector of $\delta\vec{Q}$, it can be written that

$$\begin{aligned} R_o^{-1}[1,1]\,\delta p &= \left[\frac{1}{c_{g,o}\rho_{m,o}}\left[n_x\left(w_o y_2 - u_o z_2\right) + n_y\left(u_o z_2 - w_o x_2\right) + n_z\left(v_o z_2 - u_o y_2\right)\right]\right]\delta p \Rightarrow \\ R_o^{-1}[1,1]\,\delta p &= \frac{\vec{v}_o \cdot (\vec{n} \times \vec{n}_2)}{c_{g,o}\rho_{m,o}}\delta p = -\frac{\vec{v}_o \cdot \vec{n}_1}{c_{g,o}\rho_{m,o}}\delta p = -\frac{V_{n_1,o}}{c_{g,o}\rho_{m,o}}\delta p \end{aligned} \tag{D.11}$$

and

$$\begin{aligned} &R_o^{-1}[1,2]\,\delta u + R_o^{-1}[1,3]\,\delta v + R_o^{-1}[1,4]\,\delta w = \\ &\frac{1}{c_{g,o}}\left[\beta_o\left(n_z y_2 - n_y z_2\right) + \left(V_{n,o} - V_g\right)\right]\delta u + \frac{1}{c_{g,o}}\left[\beta_o\left(n_x z_2 - n_z x_2\right) + \left(V_{n,o} - V_g\right)\right]\delta v + \\ &\frac{1}{c_{g,o}}\left[\beta_o\left(n_y x_2 - n_x y_2\right) + \left(V_{n,o} - V_g\right)\right]\delta w = \\ &\frac{1}{c_{g,o}}\left[\beta_o \delta\vec{v} \cdot (\vec{n}_2 \times \vec{n}) + (\vec{v}_o - \vec{v}_{vol}) \cdot \vec{n} \cdot \delta\vec{v} \cdot (\vec{n}_2 \times \vec{v}_o)\right] \overset{\vec{n}\cdot\vec{n}_2=0}{\Rightarrow} \\ &R_o^{-1}[1,2]\,\delta u + R_o^{-1}[1,3]\,\delta v + R_o^{-1}[1,4]\,\delta w = \frac{1}{c_{g,o}}\beta_o \delta\vec{v} \cdot \vec{n}_1 = \frac{1}{c_{g,o}}\beta_o \delta V_{n_1} \end{aligned} \tag{D.12}$$

and,

$$R_o^{-1}[1,5]\,\delta\alpha_l = 0 \tag{D.13}$$

which leads to

$$\delta w_1 = -\frac{V_{n_1,o}}{c_{g,o}\rho_{m,o}}\delta p + \frac{\beta_o}{c_{g,o}}\delta V_{n_1} \tag{D.14}$$

Similarly for the other rows

$$\delta w_2 = -\frac{V_{n_2,o}}{c_{g,o}\rho_{m,o}}\delta p + \frac{\beta_o}{c_{g,o}}\delta V_{n_2} \tag{D.15}$$

$$\delta w_3 = -\frac{\beta_o + \lambda_{4,o}V_{n,o}}{2c_o c_{g,o}\rho_{m,o}}\delta p + \frac{\beta_o c_{p,o}}{2c_o c_{g,o}}\delta V_n \tag{D.16}$$

$$\delta w_4 = \frac{\beta_o + \lambda_{3,o}V_{n,o}}{2c_o c_{g,o}\rho_{m,o}}\delta p + \frac{\beta_o c_{m,o}}{2c_o c_{g,o}}\delta V_n \tag{D.17}$$

$$\delta w_5 = \delta\alpha_l \tag{D.18}$$

Since w_i are constant in each characteristic line and using the reference states depending on the signs of λ_i, the following system of equations is obtained

$$\begin{aligned}
w_{1,r} = w_{1,b} \quad &\Rightarrow \quad -\frac{V_{n_1,o}}{\rho_{m,o}}p_r + \beta_o V_{n_1,r} = -\frac{V_{n_1,o}}{\rho_{m,o}}p_b + \beta_o V_{n_1,b} \\
w_{2,r} = w_{2,b} \quad &\Rightarrow \quad -\frac{V_{n_2,o}}{\rho_{m,o}}p_r + \beta_o V_{n_2,r} = -\frac{V_{n_2,o}}{\rho_{m,o}}p_b + \beta_o V_{n_2,b} \\
w_{3,\infty} = w_{3,b} \quad &\Rightarrow \quad -\frac{\beta_o + \lambda_{4,o}V_{n,o}}{\rho_{m,o}}p_\infty + \beta_o c_{p,o}V_{n,\infty} = -\frac{\beta_o + \lambda_{4,o}V_{n,o}}{\rho_{m,o}}p_b + \beta_o c_{p,o}V_{n,b} \\
w_{4,i} = w_{4,b} \quad &\Rightarrow \quad \frac{\beta_o + \lambda_{3,o}V_{n,o}}{\rho_{m,o}}p_i + \beta_o c_{m,o}V_{n,i} = \frac{\beta_o + \lambda_{3,o}V_{n,o}}{\rho_{m,o}}p_b + \beta_o c_{m,o}V_{n,b} \\
w_{5,r} = w_{4,b} \quad &\Rightarrow \quad \alpha_{l,r} = \alpha_{r,b}
\end{aligned} \tag{D.19}$$

where once again the subscript ∞ denotes the state at infinite, i the state at the interior of the computational domain and r the state at infinite or in the interior depending on the sign of the corresponding eigenvalue.

The matrix form of the previous system of equations is

$$\begin{bmatrix}
-\frac{V_{1,o}}{\rho_{m,o}} & 0 & \beta_o & 0 & 0 \\
-\frac{V_{1,o}}{\rho_{m,o}} & 0 & 0 & \beta_o & 0 \\
-\frac{\beta_o + \lambda_{4,o}V_{n.o}}{\rho_{m,o}} & \beta_o c_{p,o} & 0 & 0 & 0 \\
\frac{\beta_o + \lambda_{3,o}V_{n.o}}{\rho_{m,o}} & \beta_o c_{m,o} & 0 & 0 & 0 \\
0 & 0 & 0 & 0 & 1
\end{bmatrix}
\begin{bmatrix} p_b \\ V_{n,b} \\ V_{n_1,b} \\ V_{n_2,b} \\ \alpha_{l,b} \end{bmatrix} =
\begin{bmatrix}
-\frac{V_{n_1,o}}{\rho_{m,o}}p_r + \beta_o V_{n_1,r} \\
-\frac{V_{n_2,o}}{\rho_{m,o}}p_r + \beta_o V_{n_2,r} \\
-\frac{\beta_o + \lambda_{4,o}V_{n,o}}{\rho_{m,o}}p_\infty + \beta_o c_{p,o}V_{n,\infty} \\
\frac{\beta_o + \lambda_{3,o}V_{n,o}}{\rho_{m,o}}p_i + \beta_o c_{m,o}V_{n,i} \\
\alpha_{l,r}
\end{bmatrix} \tag{D.20}$$

The solution of the system gives

$$
\begin{aligned}
p_b &= \left(\frac{c_p\left(\beta+\lambda_3 V_n\right)}{2cc_g}\right)_o p_i + \left(\frac{c_m\left(\beta+\lambda_4 V_n\right)}{2cc_g}\right)_o p_\infty + \left(\frac{\beta c_m c_p \rho_m}{2cc_g}\right)_o \left(V_{n,i}-V_{n,\infty}\right) \\
V_{n,b} &= \left(\frac{c_p\left(\beta+\lambda_3 V_n\right)}{2cc_g}\right)_o V_{n,\infty} + \left(\frac{c_m\left(\beta+\lambda_4 V_n\right)}{2cc_g}\right)_o V_{n,i} + \left(\frac{\left(\beta+\lambda_3 V_n\right)\left(\beta+\lambda_4 V_n\right)}{2\beta cc_g\rho_m}\right)_o \left(p_i-p_\infty\right) \\
V_{n_1,b} &= V_{n_1,r} + \left(\frac{V_{n_1}}{2cc_g\rho_m}\right)_o \left(c_{m,o}\left(p_\infty-p_r\right)+c_{p,o}\left(p_i-p_r\right)\right) + \\
&\quad + \left(\frac{V_{n_1}V_n}{2\beta cc_g\rho_m}\right)_o \left(c_{m,o}\lambda_{4,o}\left(p_\infty-p_r\right)+c_{p,o}\lambda_{3,o}\left(p_i-p_r\right)\right) + \left(\frac{c_m c_p V_{n_1}}{2cc_g}\right)_o \left(V_{n,i}-V_{n,\infty}\right) \\
V_{n_2,b} &= V_{n_2,r} + \left(\frac{V_{n_2}}{2cc_g\rho_m}\right)_o \left(c_{m,o}\left(p_\infty-p_r\right)+c_{p,o}\left(p_i-p_r\right)\right) + \\
&\quad + \left(\frac{V_{n_2}V_n}{2\beta cc_g\rho_m}\right)_o \left(c_{m,o}\lambda_{4,o}\left(p_\infty-p_r\right)+c_{p,o}\lambda_{3,o}\left(p_i-p_r\right)\right) + \left(\frac{c_m c_p V_{n_2}}{2cc_g}\right)_o \left(V_{n,i}-V_{n,\infty}\right) \\
\alpha_{l,b} &= \alpha_{l,r}
\end{aligned}
\tag{D.21}
$$

where now the velocities at the boundary can be computed as

$$
\begin{aligned}
u_b = &\; V_{n,b}\left(y_1z_2-y_2z_1\right)+V_{n_1,b}\left(n_zy_2-n_yz_2\right)+V_{n_2,b}\left(n_yz_1-n_zy_1\right) \\
v_b = &\; V_{n,b}\left(z_1x_2-z_2x_1\right)+V_{n_1,b}\left(n_xz_2-n_zx_2\right)+V_{n_2,b}\left(n_zx_1-n_xz_1\right) \\
w_b = &\; V_{n,b}\left(x_1y_2-x_2y_1\right)+V_{n_1,b}\left(n_yx_2-n_xy_2\right)+V_{n_2,b}\left(n_xy_1-n_yx_1\right)
\end{aligned}
\tag{D.22}
$$

Appendix E

KCS – Comparison with Other Numerical Codes

In 2015, in Tokyo, the 7th CFD Workshop was organized for the assessment of the state of the art numerical hydrodynamics tools. The 2015 Workshop offered 16 test cases for three ship hulls. For the validation of the presented coupled methodology, two test cases of the Tokyo 2015 workshop have been used as reference. The first case regards the evaluation of KRISO Container Ship (KCS) in calm water conditions for 6 different Froude numbers, while the second considers the same hull in regular head waves at Froude 0.26. In both cases, the ship hull has two degrees of freedom being able to move in the heave and pitch directions.

In this section, the numerical results presented in Section 5.2.4, are contrasted with the numerical results submitted by the participants of the workshop. The first case, titled as Case 2.1, received 13 submissions in total. A variety of numerical tool were used, for example commercial codes, such as Fluent and Star–CCm, open–source tools, such as OpenFOAM, and other in–house solvers. The majority of the participants used a finite volume approximation on unstructured grids, with VoF modeling for the free surface, two equations turbulence models, while the motion of the hull was accounted for by using either deforming or overset grids. Grid sizes varied from 1.1 to 6.6M. Noteworthy, all solvers are based on pressure–correction algorithms and none of them use an Artificial Compressibility (AC) approach. All results are plotted in Figure E.1, which includes the trim–τ, the sinkage–σ and the resistance coefficient–C_T of the hull. In addition to the 13 results and the experimental data, the average of all CFD approximations is also plotted in Figure E.1. The results obtained with MaPFlow are, in all cases, within the limits of the other approximations and are especially close to the average results. MaPFlow's results deviate from the average results only in case of the resistance coefficient at the two smaller speeds. Nevertheless, in this region, a scattering of all results is noted.

The corresponding results of the second test case, labeled as 2.10 in the workshop's proceedings, are presented from Figure E.2 to E.6. Figures show the input wave elevation–ζ, resistance coefficient–C_T, heave–z and pitch–θ motion over a time window of ten periods. For this test case, 10 evaluations have been submitted using 9 different CFD codes. Results, however, are reported only for 7 submissions. All codes use pressure–correction algorithms to solve the incompressible equations. Four of them use the VoF approach for the two–phase modeling, while the other three a Level Set approach. The motion of the ship is accounted for by deforming grids (2 participants) or overset grids (2 participants) or dynamic grids (4 participants). Grid sizes varied from 0.6 to 29M cells with an average of 9.8M cells. All reported results using the $k-\omega$ SST model, except for 1, which used the Explicit Algebraic Stress k$-\omega$. Lastly, it has to be noticed that 8 of the participants used wall functions and only 2 have chosen near wall approximation, as in the case of MaPFlow's results. Unfortunately, the report does not state which results correspond to wall functions and which to near wall treatment.

As in the previous case, the numerical data are supplemented with the experimental results. Specifically, the FORCE[2] experiments are presented and denoted as "D" in the legends. FORCE reported that the mount natural frequency was close to the heave and pitch resonance condition. This is most clearly seen in C_T for λ/L equal to 0.85 and 1.15 in Figures E.3c and E.4c. Regarding the comparison of the results, all predictions converge to the same results for the longer waves. In the case of the shorter waves, starting from $\lambda/L = 0.85$, deviations are noted between numerical results and experiments, especially in heave and pitch motion plots (see Figs. E.3d and E.3e). Moreover, for $\lambda/L = 0.65$ large scattering of the results is noted. All approximations seem to predict similar amplitudes of the primary frequency, but differences are noted for the characteristics of the secondary frequency. MaPFlow predict smaller frequency and larger amplitude, which is not in agreement with the majority of the results. However, two of the results, IIHR and NUMECA, produce similar results with MaPFlow. This is especially pronounced in Figure E.2e. Since only two submissions use near wall treatment, it is safe to assume that the near wall treatment may be responsible for this difference. In all calm water results presented here, small oscillations around the mean values are noted (see for example Sec. 5.2.3 and 5.3.2). Naturally, by fully resolving the boundary layer will result the simulations will become more stiff and so numerical instabilities are more likely to emerge.

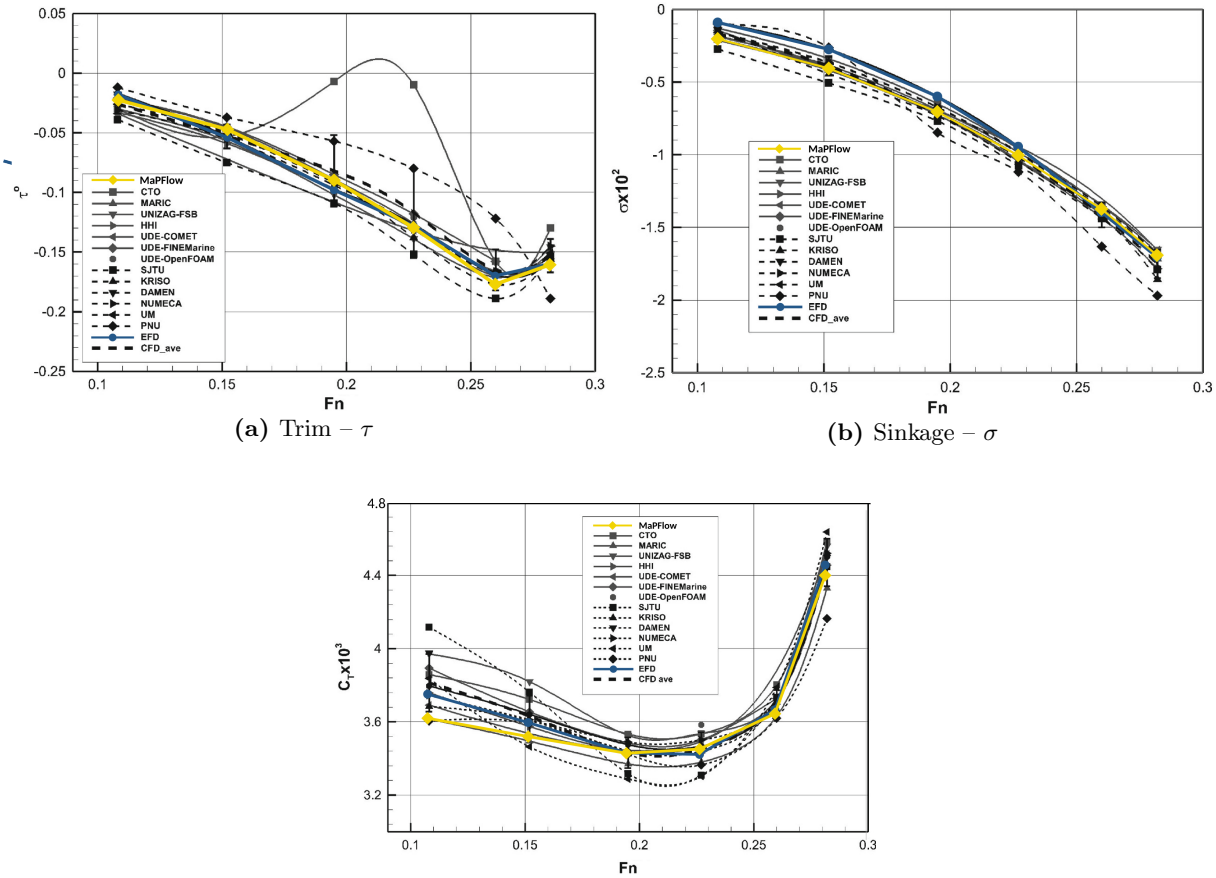

(a) Trim – τ

(b) Sinkage – σ

(c) Resistance Coefficient – C_T

Figure E.1: KCS in calm water conditions. Plots for trim–τ, sinkage–σ and Resistance coefficient–C_T in six Froude Numbers. Plots include experimental data (EFD), the results from the 13 contributions of the 2015 Tokyo Hydrodynamics Workshop [150] the average results of the CFD contributions (CFD_aver) and the results obtained with the presented methodology (MaPFlow)

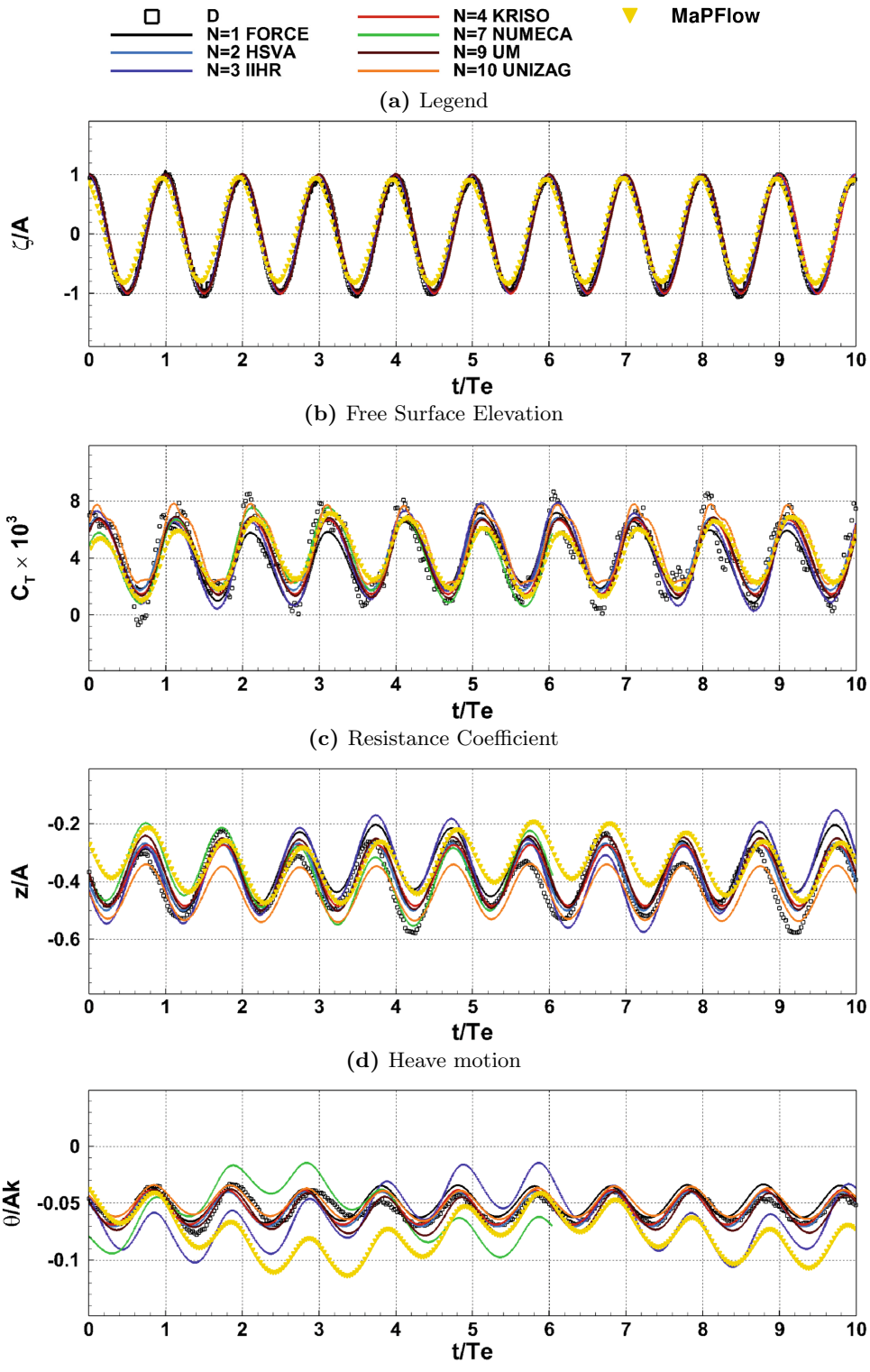

(a) Legend

(b) Free Surface Elevation

(c) Resistance Coefficient

(d) Heave motion

(e) Pitch motion

Figure E.2: KCS in regular head waves conditions with $Fn = 0.26$. Results for $\lambda/L = 0.65$ in a ten–period segment. Plots for wave elevation–ζ, resistance coefficient–C_T, heave z and pitch motion θ. Plots include experimental data (D), results from the 10 contributions of the 2015 Tokyo Hydrodynamics Workshop [150] and the results obtained with the presented methodology (MaPFlow)

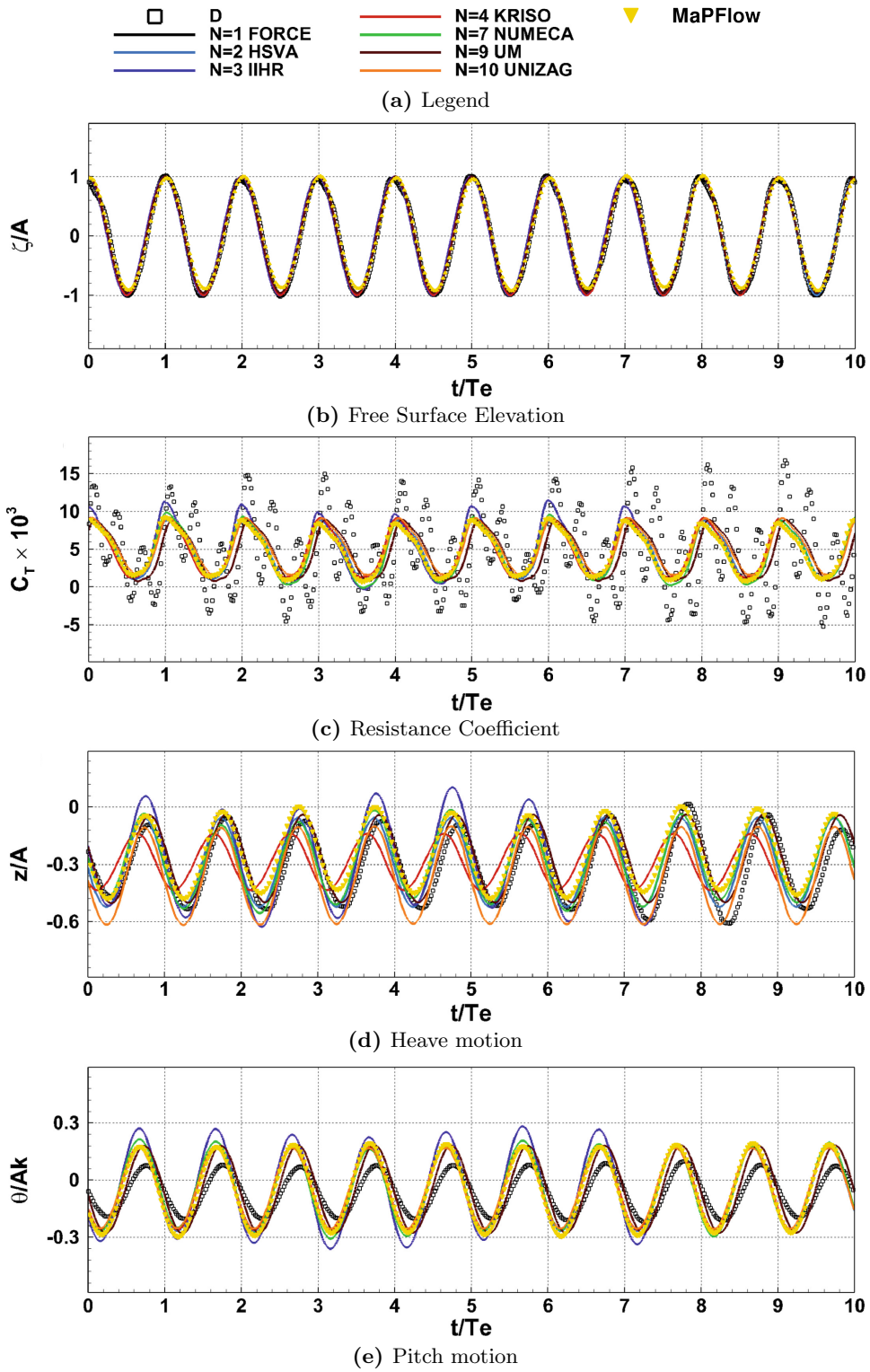

(a) Legend

(b) Free Surface Elevation

(c) Resistance Coefficient

(d) Heave motion

(e) Pitch motion

Figure E.3: KCS in regular head waves conditions with $Fn = 0.26$. Results for $\lambda/L = 0.85$ in a ten–period segment. Plots for wave elevation–ζ, resistance coefficient–C_T, heave z and pitch motion θ. Plots include experimental data (D), results from the 10 contributions of the 2015 Tokyo Hydrodynamics Workshop [150] and the results obtained with the presented methodology (MaPFlow)

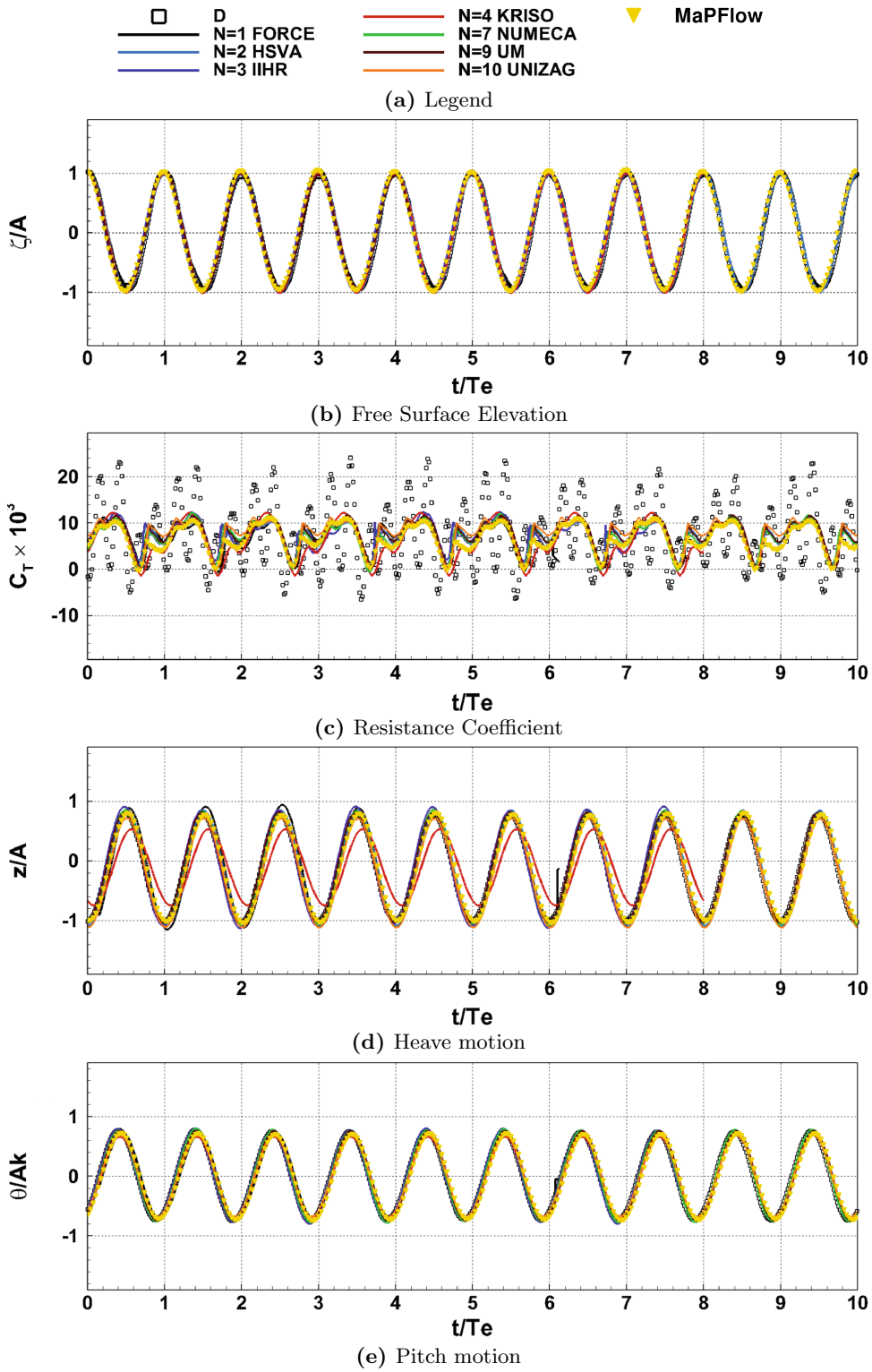

(a) Legend

(b) Free Surface Elevation

(c) Resistance Coefficient

(d) Heave motion

(e) Pitch motion

Figure E.4: KCS in regular head waves conditions with $Fn = 0.26$. Results for $\lambda/L = 1.15$ in a ten–period segment. Plots for wave elevation–ζ, resistance coefficient–C_T, heave z and pitch motion θ. Plots include experimental data (D), results from the 10 contributions of the 2015 Tokyo Hydrodynamics Workshop [150] and the results obtained with the presented methodology (MaPFlow)

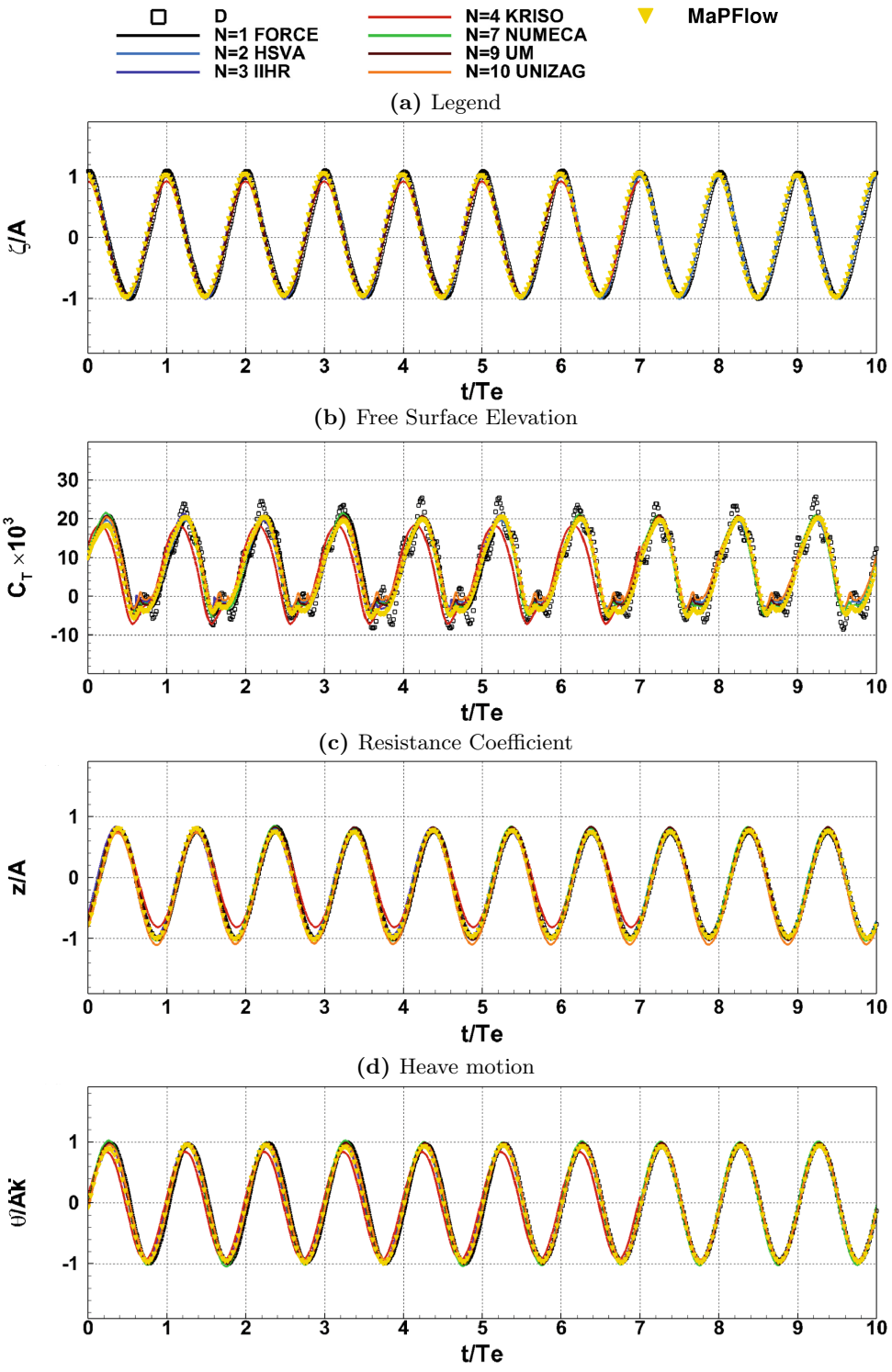

(a) Legend

(b) Free Surface Elevation

(c) Resistance Coefficient

(d) Heave motion

(e) Pitch motion

Figure E.5: KCS in regular head waves conditions with $Fn = 0.26$. Results for $\lambda/L = 1.37$ in a ten–period segment. Plots for wave elevation–ζ, resistance coefficient–C_T, heave z and pitch motion θ. Plots include experimental data (D), results from the 10 contributions of the 2015 Tokyo Hydrodynamics Workshop [150] and the results obtained with the presented methodology (MaPFlow)

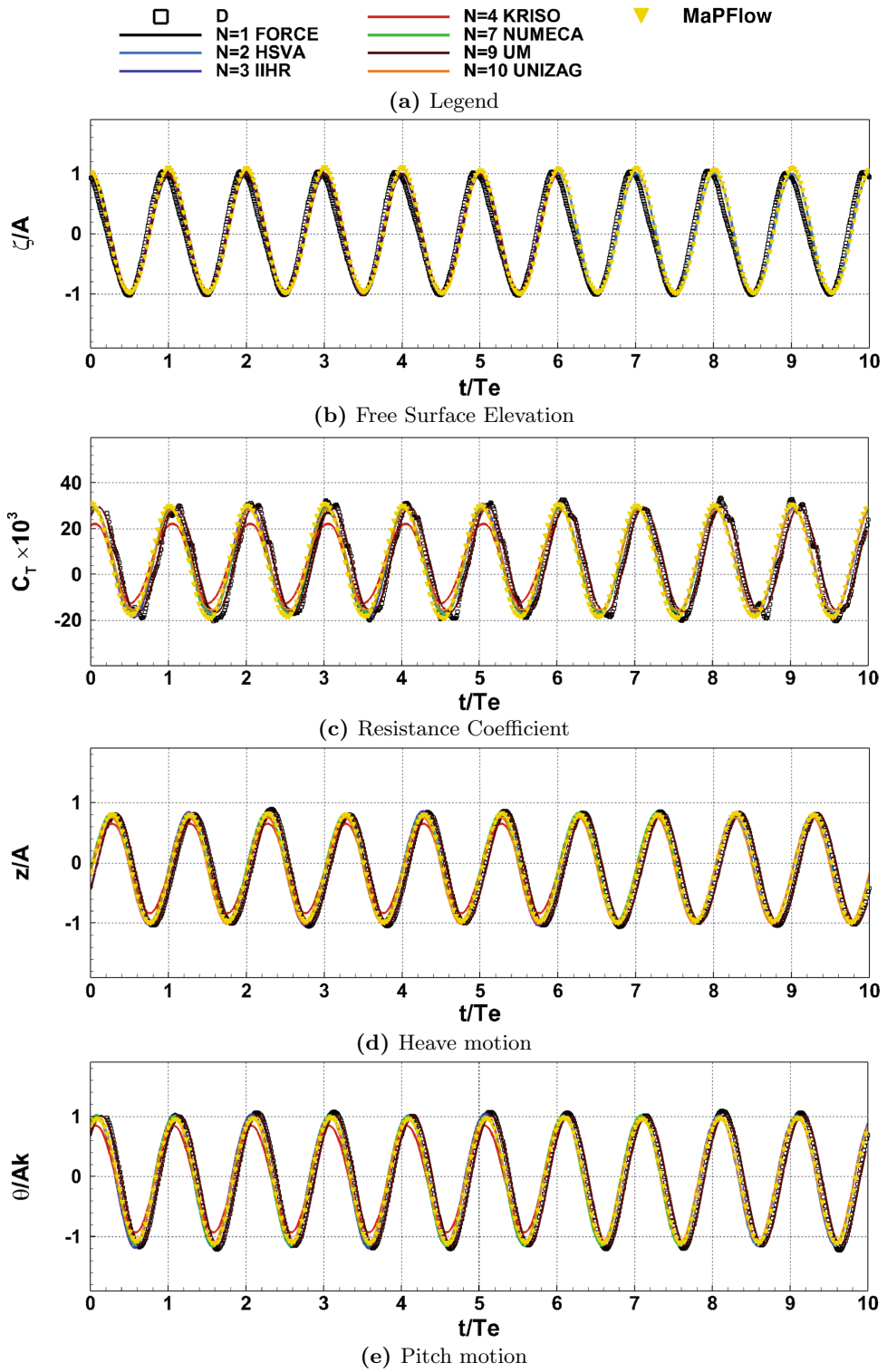

(a) Legend

(b) Free Surface Elevation

(c) Resistance Coefficient

(d) Heave motion

(e) Pitch motion

Figure E.6: KCS in regular head waves conditions with $Fn = 0.26$. Results for $\lambda/L = 1.95$ in a ten–period segment. Plots for wave elevation–ζ, resistance coefficient–C_T, heave z and pitch motion θ. Plots include experimental data (D), results from the 10 contributions of the 2015 Tokyo Hydrodynamics Workshop [150] and the results obtained with the presented methodology (MaPFlow)

This page intentionally left blank

Bibliography

[1] C. Allen *et al.*, "Definition of the umaine volturnus–s reference platform developed for the iea wind 15-megawatt offshore reference wind turbine", Golden, CO: National Renewable Energy Laboratory. NREL/TP-5000-76773, Tech. Rep., 2020. [Online]. Available: https://www.nrel.gov/docs/fy20osti/76773.pdf.

[2] S. Grilli, "Fully nonlinear potential flow models used for long wave runup prediction", *Chapter in Long-Wave Runup Models,(eds. H. Yeh, P. Liu, and C. Synolakis)*, pp. 116–180, 1997.

[3] E. Filippas, "Hydrodynamic analysis of ship and marine biomimetic systems in waves using gpgpu programming", Ph.D. dissertation, School of Naval Architecture & Marine Engineering, National Technical University of Athens, 2019.

[4] D. E. Anevlavi, E. S. Filippas, A. E. Karperaki, and K. A. Belibassakis, "A non-linear bem-fem coupled scheme for the performance of flexible flapping-foil thrusters", *Journal of Marine Science and Engineering*, vol. 8, 1 Jan. 2020, ISSN: 20771312. DOI: 10.3390/JMSE8010056.

[5] D. Manolas, "Hydro-aero-elastic analysis of offshore wind turbines", Ph.D. dissertation, School of Mechanical Engineering, National Technical University of Athens, 2015.

[6] C. Papoutsellis and G. Athanassoulis, *A new efficient hamiltonian approach to the nonlinear water-wave problem over arbitrary bathymetry*, 2017. arXiv: 1704.03276 [physics.flu-dyn].

[7] E. S. Filippas, G. P. Papadakis, and K. A. Belibassakis, "Free-Surface Effects on the Performance of Flapping-Foil Thruster for Augmenting Ship Propulsion in Waves", *Journal of Marine Science & Engineering*, no. 5, 2020. DOI: 10.3390/jmse8050357.

[8] V. Vukcevic, "Numerical Modelling of Coupled Potential and Viscous Flow for Marine Applications", Ph.D. dissertation, Faculty of Mechanical Engineering and Naval Architecture, University of Zagreb, 2017. DOI: 10.13140/RG.2.2.23080.57605.

[9] L. Plumerault, D. Astruc, P. Villedieu, and P. Maron, "A numerical model for aerated-water wave breaking", *International Journal for Numerical Methods in Fluids*, vol. 69, no. 12, pp. 1851–1871, Aug. 2012, ISSN: 02712091. DOI: 10.1002/fld.2667.

[10] S. Liu, I. Gatin, C. Obhrai, M. C. Ong, and H. Jasak, "CFD simulations of violent breaking wave impacts on a vertical wall using a two-phase compressible solver", *Coastal Engineering*, 2019, ISSN: 03783839. DOI: 10.1016/j.coastaleng.2019.103564.

[11] G. Tryggvason, R. Scardovelli, and S. Zaleski, *Direct Numerical Simulations of Gas–Liquid Multiphase Flows*. Cambridge University Press, 2011. DOI: 10.1017/CBO9780511975264.

[12] J. H. Ferziger and M. Perić, *Computational Methods for Fluid Dynamics*, Third. Berlin: Springer, 2002, ISBN: 978-3-540-42074-3. DOI: 10.1007/978-3-642-56026-2.

[13] A. Jafari and N. Ashgriz, "Numerical techniques for free surface flows: Interface capturing and interface tracking", in Springer US, 2014, pp. 1–27. DOI: 10.1007/978-3-642-27758-0_1139-2. [Online]. Available: https://link.springer.com/10.1007/978-3-642-27758-0_1139-2.

[14] A. Takizawa, S. Koshizuka, and S. Kondo, "Generalization of physical component boundary fitted co-ordinate (PCBFC) method for the analysis of free-surface flow", *International Journal for Numerical Methods in Fluids*, vol. 15, no. 10, pp. 1213–1237, 1992, ISSN: 10970363. DOI: 10.1002/fld.1650151005.

[15] G. D. Tzabiras, "Resistance and Self-Propulsion Simulations for a Series-60, CB = 0.6 Hull at Model and Full Scale", *Ship Technology Research*, vol. 51, no. 1, pp. 21–34, 2004, ISSN: 0937-7255. DOI: 10.1179/str.2004.51.1.004. [Online]. Available: http://www.tandfonline.com/doi/full/10.1179/str.2004.51.1.004.

[16] M. Sussman, P. Smereka, and S. Osher, "A level set approach for computing solutions to incompressible two-phase flow", *Journal of Computational Physics*, vol. 114, no. 1, pp. 146–159, 1994, ISSN: 00219991. DOI: 10.1006/jcph.1994.1155. arXiv: 1994.

[17] D. Hartmann, M. Meinke, and W. Schröder, "The constrained reinitialization equation for level set methods", *Journal of Computational Physics*, vol. 229, pp. 1514–1535, 5 Mar. 2010, ISSN: 10902716. DOI: 10.1016/j.jcp.2009.10.042.

[18] S. O. Unverdi and G. Tryggvason, "A front-tracking method for viscous, incompressible, multi-fluid flows", *Journal of Computational Physics*, vol. 100, pp. 25–37, 1 May 1992, ISSN: 00219991. DOI: 10.1016/0021-9991(92)90307-K. [Online]. Available: https://linkinghub.elsevier.com/retrieve/pii/002199919290307K.

[19] F. H. Harlow and J. E. Welch, "Numerical calculation of time-dependent viscous incompressible flow of fluid with free surface", *Physics of Fluids*, vol. 8, no. 12, pp. 2182–2189, 1965, ISSN: 10706631. DOI: 10.1063/1.1761178.

[20] G. W. Cowles, "A parallel viscous multiblock flow solver for free surface flows past complex geometries", Ph.D. dissertation, Department of Mechanical and Aerospace Engineering, Princeton University, 2001.

[21] D. Jacqmin, "Calculation of two-phase navier–stokes flows using phase-field modeling", *Journal of Computational Physics*, vol. 155, pp. 96–127, 1 Oct. 1999, ISSN: 00219991. DOI: 10.1006/jcph.1999.6332. [Online]. Available: https://linkinghub.elsevier.com/retrieve/pii/S0021999199963325.

[22] S. Mirjalili, S. Jain, and M. Dodd, "Interface-capturing methods for two-phase flows: An overview and recent developments", *Center for Turbulence Research - Annual research brief*, pp. 117–135, Dec. 2017.

[23] C. Hirt and B. Nichols, "Volume of Fluid (VOF) Method for the Dynamics of Free Boundaries", *Journal of Computational Physics*, vol. 39, pp. 201–225, 1981.

[24] H. Weller, "A new approach to vof–based interface capturing methods for incompressible, compressible and cavitating flow", in *Technical Report*, OpenCFD Limited, 2006.

[25] S. S. Deshpande, L. Anumolu, and M. F. Trujillo, "Evaluating the performance of the two-phase flow solver interfoam", *Computational Science and Discovery*, vol. 5, 1 Jan. 2012, ISSN: 17494680. DOI: 10.1088/1749-4699/5/1/014016.

[26] O. Ubbink and R. I. Issa, "A method for capturing sharp fluid interfaces on arbitrary meshes", *Journal of Computational Physics*, vol. 153, pp. 26–50, 1999.

[27] S. Muzaferija, "A two-fluid navier-stokes solver to simulate water entry", *Proceeding of the 22nd symposium of naval hydrodynamics. Washington, DC, 1998*, 1998. [Online]. Available: https://cir.nii.ac.jp/crid/1574231875213519872.

[28] R. DeBar, "Method in two-d eulerian hydrodynamics", Lawrence Livermore National Lab., CA (USA), Tech. Rep., 1974.

[29] J. Roenby, H. Bredmose, and H. Jasak, "A computational method for sharp interface advection", *Royal Society Open Science*, vol. 3, 11 2016, ISSN: 20545703. DOI: 10.1098/rsos.160405.

[30] M. Sussman and E. G. Puckett, "A coupled level set and volume-of-fluid method for computing 3d and axisymmetric incompressible two-phase flows", *Journal of Computational Physics*, vol. 162, no. 2, pp. 301–337, 2000, ISSN: 0021-9991. DOI: https://doi.org/10.1006/jcph.2000.6537.

[31] Y. Liu and X. Yu, "A coupled phase–field and volume-of-fluid method for accurate representation of limiting water wave deformation", *Journal of Computational Physics*, vol. 321, pp. 459–475, 2016, ISSN: 0021-9991. DOI: https://doi.org/10.1016/j.jcp.2016.05.059.

[32] D. Drikakis and R. WJ, *High-Resolution Methods for Incompressible and Low-Speed Flows*. Springer, Jan. 2005.

[33] C. M. Rhie and W. L. Chow, "Numerical study of the turbulent flow past an airfoil with trailing edge separation", *AIAA Journal*, vol. 21, no. 11, pp. 1525–1532, 1983, ISSN: 00011452. DOI: 10.2514/3.8284.

[34] S. Patankar and D. Spalding, "A calculation procedure for heat, mass and momentum transfer in three-dimensional parabolic flows", *International Journal of Heat and Mass Transfer*, vol. 15, pp. 1787–1806, 10 Oct. 1972, ISSN: 00179310. DOI: 10.1016/0017-9310(72)90054-3.

[35] S. V. Patankar, *Numerical heat transfer and fluid flow* (Series on Computational Methods in Mechanics and Thermal Science). Hemisphere Publishing Corporation (CRC Press, Taylor & Francis Group), 1980, ISBN: 978-0891165224.

[36] J. P. V. Doormaal and G. D. Raithby, "Enhancements of the simple method for predicting incompressible fluid flows", *Numerical Heat Transfer*, vol. 7, no. 2, pp. 147–163, 1984. DOI: 10.1080/01495728408961817.

[37] R. I. Issa, "Solution of the Implicitly Fluid Flow Equations by Operator-Splitting", *Journal of Computational Physics*, vol. 62, pp. 40–65, 1985, ISSN: 15210634. DOI: 10.1080/10407782.2016.1173467.

[38] A. J. Chorin, "Numerical solution of the navier-stokes equations", *Mathematics of Computation*, vol. 22, pp. 745–762, 104 1968, ISSN: 0025-5718. DOI: 10.1090/S0025-5718-1968-0242392-2.

[39] J. Kim and P. Moin, "Application of a Fractional-Step Method to Incompressible Navier-Stokes Equations", *Jouranl of Computational Physics*, vol. 59, pp. 308–323, 1985, ISSN: 00413771.

[40] J. E. Fromm and F. H. Harlow, "Numerical solution of the problem of vortex street development", *Physics of Fluids*, vol. 6, pp. 975–982, 7 1963, ISSN: 10706631. DOI: 10.1063/1.1706854.

[41] A. J. Chorin, "A Numerical Method for Solving Incompressible Visous Flow Problems", pp. 12–26, 1967, ISSN: 00219991. DOI: 10.1109/ET2ECN.2012.6470106.

[42] C. Merkle and P. Tsai, "Application of Runge-Kutta Schemes to Incompressible Flows", in *AIAA 24th Aerospace Sciences Meeting, Reno, Nevada*, 1986.

[43] A. Harten, P. D. Lax, and B. v. Leer, "On upstream differencing and godunov-type schemes for hyperbolic conservation laws", *SIAM Review*, vol. 25, no. 1, pp. 35–61, 1983. DOI: 10.1137/1025002. eprint: https://doi.org/10.1137/1025002.

[44] S. Osher and F. Solomon, "Upwind difference schemes for hyperbolic systems of conservation laws", *Mathematics of Computation*, vol. 38, no. 158, pp. 339–374, 1982, ISSN: 00255718, 10886842. [Online]. Available: http://www.jstor.org/stable/2007275 (visited on 07/15/2023).

[45] P. L. Roe, "Approximate Riemann solvers, parameter vectors, and difference schemes", *Journal of Computational Physics*, vol. 43, no. 2, pp. 357–372, 1981. DOI: 10.1016/0021-9991(81)90128-5. arXiv: arXiv:1011.1669v3.

[46] P. Tamamidis, G. Zhang, and D. N. Assanis, "Comparison of pressure-based and artificial compressibility methods for solving 3d steady incompressible viscous flows", *Journal of Computational Physics*, vol. 124, pp. 1–13, 1 1996, ISSN: 00219991. DOI: 10.1006/jcph.1996.0041.

[47] P. Queutey and M. Visonneau, "An interface capturing method for free-surface hydrodynamic flows", *Computers and Fluids*, vol. 36, no. 9, pp. 1481–1510, 2007. DOI: 10.1016/j.compfluid.2006.11.007.

[48] P. Higuera, J. L. Lara, and I. J. Losada, "Realistic wave generation and active wave absorption for Navier-Stokes models. Application to OpenFOAM®.", *Coastal Engineering*, 2013, ISSN: 03783839. DOI: 10.1016/j.coastaleng.2012.07.002.

[49] D. Angelidis, S. Chawdhary, and F. Sotiropoulos, "Unstructured Cartesian refinement with sharp interface immersed boundary method for 3D unsteady incompressible flows", *Journal of Computational Physics*, vol. 325, pp. 272–300, 2016, ISSN: 10902716. DOI: 10.1016/j.jcp.2016.08.028.

[50] P. Nithiarasu, "An efficient artificial compressibility (ac) scheme based on the characteristic based split (cbs) method for incompressible flows", *International Journal for Numerical Methods in Engineering*, vol. 56, no. 13, pp. 1815–1845, 2003.

[51] O. F. Oxtoby and A. G. Malan, "A matrix-free, implicit, incompressible fractional-step algorithm for fluid–structure interaction applications", *Journal of Computational Physics*, vol. 231, no. 16, pp. 5389–5405, 2012.

[52] C. Merkle, "Time-accurate unsteady incompressible flow algorithms based on artificial compressibility", American Institute of Aeronautics and Astronautics, Jun. 1987. DOI: 10.2514/6.1987-1137. [Online]. Available: https://arc.aiaa.org/doi/10.2514/6.1987-1137.

[53] E. Turkel, "Preconditioned methods for solving the incompressible and low speed compressible equations", *Journal of Computational Physics*, vol. 72, no. 2, pp. 277–298, Oct. 1987, ISSN: 0021-9991. DOI: 10.1016/0021-9991(87)90084-2.

[54] A. Malan, R. Lewis, and P. Nithiarasu, "An improved unsteady, unstructured, artificial compressibility, finite volume scheme for viscous incompressible flows: Part i. theory and implementation", *International Journal for Numerical Methods in Engineering*, vol. 54, no. 5, pp. 695–714, 2002.

[55] J. M. Weiss and W. A. Smith, "Preconditioning applied to variable and constant density flows", *AIAA Journal*, vol. 33, pp. 2050–2057, 11 1995, ISSN: 0001-1452. DOI: 10.2514/3.12946.

[56] S. Vrahliotis, "Development of an artificial compressibility methodology for unsteady 3d aerodynamic flows", in Greek, Ph.D. dissertation, School of Mechanical Engineering, National Technical University of Athens, 2012.

[57] S. Sarakinos, "On the simulation of steady and unsteady incompressible flows using the finite volume approach and artificial compressibility concept on hybrid unstructured grids", Ph.D. dissertation, School of Production Engineering & Management, Technical University of Crete, 2016.

[58] K. Tsiakas, "Development of shape parameterization techniques, a flow solver and its adjoint, for optimization on gpus. turbomachinery and external aerodynamics applications", Ph.D. dissertation, School of Mechanical Engineering, National Technical University of Athens, 2019.

[59] F. Bassi, A. Crivellini, D. A. D. Pietro, and S. Rebay, "An artificial compressibility flux for the discontinuous galerkin solution of the incompressible navier-stokes equations", *Journal of Computational Physics*, vol. 218, pp. 794–815, 2 Nov. 2006, ISSN: 10902716. DOI: 10.1016/j.jcp.2006.03.006.

[60] C. Cox, C. Liang, and M. W. Plesniak, "A high-order solver for unsteady incompressible navier-stokes equations using the flux reconstruction method on unstructured grids with implicit dual time stepping", *Journal of Computational Physics*, vol. 314, pp. 414–435, Jun. 2016, ISSN: 10902716. DOI: 10.1016/j.jcp.2016.03.016.

[61] R. F. Kunz *et al.*, "A preconditioned Navier-Stokes method for two-phase flows with application to cavitation prediction", *Computers and Fluids*, vol. 29, no. 8, pp. 849–875, 2000.

[62] P. Y. Vrionis, "Shape and topology optimization using the cut-cell method and its continuous adjoint for single– and two–phase turbulent flows, in a multiprocessor environment", Ph.D. dissertation, National Technical University of Athens, 2022.

[63] K. Hejranfar, E. Ezzatneshan, and K. Hesary, "A dual-time implicit preconditioned navier-stokes method for solving 2d steady/unsteady laminar cavitating/noncavitating flows using a barotropic model", *7th International Symposium on Cavitation*, pp. 1–10, 138 2009. [Online]. Available: http://141.213.232.243/handle/2027.42/84312.

[64] J. s. Yue and S. p. Wu, "An improvement to the kunz preconditioner and numerical investigation of hydrofoil interactions in tandem", *International Journal of Computational Fluid Dynamics*, vol. 32, no. 4-5, pp. 167–185, 2018. DOI: 10.1080/10618562.2018.1508655.

[65] S. Venkateswaran, J. Lindau, R. Kunz, and C. Merkle, "Preconditioning algorithms for the computation of multi-phase mixture flows", in *39th Aerospace Sciences Meeting and Exhibit*, 2001, p. 279.

[66] F. J. Kelecy and R. H. Pletcher, "The development of a free surface capturing approach for multidimensional free surface flows in closed containers", *Journal of Computational Physics*, vol. 138, no. 2, pp. 939–980, 1997, ISSN: 00219991. DOI: 10.1006/jcph.1997.5847.

[67] V. T. Nguyen and W. G. Park, "A free surface flow solver for complex three-dimensional water impact problems based on the vof method", *International Journal for Numerical Methods in Fluids*, vol. 82, pp. 3–34, 1 Sep. 2016, ISSN: 10970363. DOI: 10.1002/fld.4203.

[68] S. Bhat and J. C. Mandal, "Contact preserving riemann solver for incompressible two-phase flows", *Journal of Computational Physics*, vol. 379, pp. 173–191, Feb. 2019, ISSN: 10902716. DOI: 10.1016/j.jcp.2018.10.039.

[69] S. Leakey, V. Glenis, and C. J. M. Hewett, "Riemann solvers and pressure gradients in godunov-type schemes for variable density incompressible flows", pp. 1–36, Aug. 2021. [Online]. Available: http://arxiv.org/abs/2108.08769.

[70] V. T. Nguyen and W. G. Park, "A review of preconditioning and artificial compressibility dual-time navier–stokes solvers for multiphase flows", *Fluids*, vol. 8, 3 Mar. 2023, ISSN: 23115521. DOI: 10.3390/fluids8030100.

[71] T. Hino, "An interface capturing method for free surface flow computations on unstructured grids", *Journal of the Society of Naval Architects of Japan*, vol. 1999, pp. 177–183, 186 1999, ISSN: 1884-2070. DOI: 10.2534/jjasnaoe1968.1999.186_177.

[72] L. Qian, D. M. Causon, C. G. Mingham, and D. M. Ingram, "A free-surface capturing method for two fluid flows with moving bodies", *Proceedings of the Royal Society A: Mathematical, Physical and Engineering Sciences*, vol. 462, pp. 21–42, 2065 2006, ISSN: 14712946. DOI: 10.1098/rspa.2005.1528.

[73] J. Wackers and B. Koren, "Efficient computation of steady water flow with waves", *International Journal for Numerical Methods in Fluids*, vol. 56, no. 8, pp. 1567–1574, Mar. 2008, ISSN: 02712091. DOI: 10.1002/fld.1596.

[74] D. S. Nichols, "Development of a free surface method utilizing an incompressible multiphase algorithm to study the flow about surface ships and underwater vehicles", Ph.D. dissertation, Department of Aerospace Engineering, Faculty of Mississippi State University, 2002.

[75] G. Papadakis, "Development of a hybrid compressible vortex particle method and application to external problems including helicopter flows", Ph.D. dissertation, School of Mechanincal Engineering, National Technical University of Athens, 2014.

[76] K. Diakakis, "Computational analysis of transitional and massively separated flows with application to wind turbines", Ph.D. dissertation, School of Mechanical Engineering, National Technical University of Athens.

[77] G. Karypis, "METIS A Software Package for Partitioning Unstructured Graphs, Partitioning Meshes, and Computing Fill-Reducing Orderings of Sparse Matrices Version", Tech. Rep., 2013, pp. 1–44.

[78] H. T. Ahn and Y. Kallinderis, "Strongly coupled flow/structure interactions with a geometrically conservative ALE scheme on general hybrid meshes", *Journal of Computational Physics*, vol. 219, pp. 671–696, 2006. DOI: 10.1016/j.jcp.2006.04.011.

[79] R. Biedron and J. Thomas, "Recent enhancements to the fun3d flow solver for moving-mesh applications", American Institute of Aeronautics and Astronautics, Jan. 2009, ISBN: 978-1-60086-973-0. DOI: 10.2514/6.2009-1360. [Online]. Available: https://arc.aiaa.org/doi/10.2514/6.2009-1360.

[80] R. K. Agarwal and J. E. Deese, "Euler calculations for flowfield of a helicopter rotor in hover", *Journal of Aircraft*, vol. 24, no. 4, pp. 231–238, 1987. DOI: 10.2514/3.45431.

[81] J. Blazek, *Computational Fluid Dynamics: Principles and Applications*, 2nd ed. Elsevier, 2005.

[82] F. R. Menter, "Two-equation eddy-viscosity turbulence models for engineering applications", *AIAA Journal*, vol. 32, no. 8, pp. 1598–1605, 1994. DOI: 10.2514/3.12149.

[83] B. Devolder, P. Rauwoens, and P. Troch, "Application of a buoyancy-modified k-ω SST turbulence model to simulate wave run-up around a monopile subjected to regular waves using OpenFOAM®", *Coastal Engineering*, vol. 125, no. April, pp. 81–94, 2017, ISSN: 03783839. DOI: 10.1016/j.coastaleng.2017.04.004.

[84] B. Devolder, P. Troch, and P. Rauwoens, "Performance of a buoyancy-modified k–ω and k–*omega* sst turbulence model for simulating wave breaking under regular waves using openfoam", *Coastal Engineering*, vol. 138, pp. 49–65, 2018, ISSN: 0378-3839.

[85] B. E. Larsen and D. R. Fuhrman, "On the over-production of turbulence beneath surface waves in Reynolds-averaged Navier–Stokes models", *Journal of Fluid Mechanics*, vol. 853, pp. 419–460, 2018, ISSN: 0022-1120. DOI: 10.1017/jfm.2018.577.

[86] A. Dermatis, D. Ntouras, and G. Papadakis, "Numerical simulation of irregular breaking waves using a coupled artificial compressibility method", *Fluids*, vol. 7, no. 7, 2022, ISSN: 2311-5521. DOI: 10.3390/fluids7070235.

[87] M. Kato and B. Launder, "The modeling of turbulent flow around stationary and vibrating square cylinders", *Ninth Symposium on Turbulent Shear Flows*, no. January 1993, pp. 10.4.1–10.4.6, 1993, ISSN: 0717-6163. DOI: 10.1007/s13398-014-0173-7.2. arXiv: arXiv:1011.1669v3.

[88] R. G. Dean and R. A. Dalrymple, *Water Wave Mechanics for Engineers and Scientists*. World Scientific, 1991, vol. Advanced Series on Ocean Engineering – Volume 2.

[89] M. W. Dingenmas, *Water Wave Propagation Over Uneven Bottoms*. World Scientific, 1997, vol. Advanced Series on Ocean Engineering – Volume 13.

[90] J. D. Fenton, "Nonlinear Wave Theories", in *The Sea - Ocean Engineering Science*, ser. A, B. L. Méhauté and D. M. Hanes, Eds., vol. 9, Wiley, New Work, 2010, pp. 3–25. [Online]. Available: http://johndfenton.com/Papers/Fenton90b-Nonlinear-wave-theories.pdf.

[91] M. M. Rienecker and J. D. Fenton, "Approximation for steady water waves.", *J Fluid Mech Vol pp*, vol. 104 SRC -, pp. 119–137, 1981.

[92] J. D. Fenton, "The numerical solution of steady water wave problems", *Computers & Geosciences*, vol. 14, no. 3, pp. 357–368, Sep. 1988, ISSN: 00983004. DOI: 10.1016/0098-3004(88)90066-0.

[93] B. Clayton and R. Bishop, *Mechanics of Marine Vehicles*. Gulf Publishing Company, 1982.

[94] E. M. Lewandowski, *The Dynamics of Marine Craft*. World Scientific, 2004, Advanced Series on Ocean Engineering: Volume 22. DOI: 10.1142/4815.

[95] H. Goldstein, C. Poole, and J. Safko, *Classical Mechanics*, 3rd ed. Addison-Wesley, 2001.

[96] N. M. Newmark, "A method of computation for structural dynamics", *Journal of the Engineering Mechanics Division*, vol. 85, pp. 67–94, 3 Jul. 1959, ISSN: 0044-7951. DOI: 10.1061/JMCEA3.0000098.

[97] E. Sozer, C. Brehm, and C. C. Kiris, "Gradient calculation methods on arbitrary polyhedral unstructured meshes for cell-centered cfd solvers", *52nd AIAA Aerospace Sciences Meeting - AIAA Science and Technology Forum and Exposition, SciTech 2014*, pp. 1–24, January 2014. DOI: 10.2514/6.2014-1440.

[98] F. Moukalled, L. Mangani, and M. Darwish, *The Finite Volume Method in Computational Fluid Dynamics: An Advanced Introduction with OpenFOAM® and Matlab®*. Oct. 2015, vol. 113, ISBN: 978-3-319-16873-9. DOI: 10.1007/978-3-319-16874-6.

[99] C. Hirsch, *Numerical Computation of Internal and External Flows, Volume 2: Computational Methods for Inviscid and Viscous Flows*. Elsevier Science, 2019, ISBN: 9780080940519.

[100] B. van Leer, "Towards the ultimate conservative difference scheme. V. A second-order sequel to Godunov's method", *Journal of Computational Physics*, vol. 32, no. 1, pp. 101–136, 1979, ISSN: 10902716. DOI: 10.1016/0021-9991(79)90145-1.

[101] H. Jasak, "Error analysis and estimation for the finite volume method with applications to fluid flows", Ph.D. dissertation, Department of Mechanical Engineering Imperial College of Science, Technology and Medicine, 1996.

[102] B. P. Leonard, "Simple high-accuracy resolution program for convective modelling of discontinuities", *International Journal for Numerical Methods in Fluids*, vol. 8, no. 10, pp. 1291–1318, 1988. DOI: 10.1002/fld.1650081013.

[103] B. P. Leonard, "The ultimate conservative difference scheme applied to unsteady one-dimensional advection", *Computer Methods in Applied Mechanics and Engineering*, vol. 88, no. 1, pp. 17–74, 1991. DOI: 10.1016/0045-7825(91)90232-U.

[104] P. H. Gaskell and A. K. C. Lau, "Curvature-compensated convective transport: Smart, a new boundedness-preserving transport algorithm", 1988, pp. 617–641.

[105] M. Darwish and F. Moulkaled, "Convective Schemes for Capturing Interfaces of Free-Surface Flows on Unstructured Grids", *Numerical Heat Transfer*, vol. 49, no. Part B, pp. 19–42, 2006. DOI: 10.1080/10407790500272137.

[106] S. Muzaferija and M. Perić, "Computation of free-surface flows using interface-tracking and interface-capturing methods.", in Jan. 1999, pp. 59–100.

[107] J. Wackers *et al.*, "Free-Surface Viscous Flow Solution Methods for Ship Hydrodynamics", *Archives of Computational Methods in Engineering*, vol. 18, no. 1, pp. 1–41, Apr. 2011.

[108] J. Wackers and B. Koren, "A surface capturing method for the efficient computation of steady water waves", *Journal of Computational and Applied Mathematics*, vol. 215, pp. 618–625, 2008. DOI: 10.1016/j.cam.2006.03.056. [Online]. Available: www.elsevier.com/locate/cam.

[109] D. S. Bale, R. J. Leveque, S. Mitran, and J. A. Rossmanith, "A wave propagation method for conservation laws and balance laws with spatially varying flux functions", *SIAM Journal on Scientific Computing*, vol. 24, pp. 955–978, 3 2003, ISSN: 10648275. DOI: 10.1137/S106482750139738X.

[110] E. Audusse, F. Bouchut, M.-O. Bristeau, R. Klein, and B. Perthame, "A fast and stable well-balanced scheme with hydrostatic reconstruction for shallow water flows", *SIAM Journal on Scientific Computing*, vol. 25, pp. 2050–2065, 6 Jan. 2004, ISSN: 1064-8275. DOI: 10.1137/S1064827503431090.

[111] J. A. Heyns, A. G. Malan, T. M. Harms, and O. F. Oxtoby, "A weakly compressible free-surface flow solver for liquid-gas systems using the volume-of-fluid approach", *Journal of Computational Physics*, vol. 240, pp. 145–157, 2013, ISSN: 10902716. DOI: 10.1016/j.jcp.2013.01.022. [Online]. Available: http://dx.doi.org/10.1016/j.jcp.2013.01.022.

[112] G. Krause, "Hydrostatic equilibrium preservation in mhd numerical simulation with stratified atmospheres: Explicit godunov-type schemes with muscl reconstruction", *Astronomy and Astrophysics*, vol. 631, pp. 1–15, 2019, ISSN: 14320746. DOI: 10.1051/0004-6361/201936387.

[113] H. Nishikawa, "A flux correction for finite-volume discretizations: Achieving second-order accuracy on arbitrary polyhedral grids", *Journal of Computational Physics*, vol. 468, Nov. 2022, ISSN: 10902716. DOI: 10.1016/j.jcp.2022.111481.

[114] R. Biedron, V. Vatsa, and H. Atkins, "Simulation of Unsteady Flows Using an Unstructured Navier-Stokes Solver on Moving and Stationary Grids", *23rd AIAA Applied Aerodynamics Conference*, pp. 1–17, 2005. DOI: 10.2514/6.2005-5093. [Online]. Available: http://arc.aiaa.org/doi/10.2514/6.2005-5093.

[115] C. B. Laney, *Computational Gas Dynamics*. Cambridge University Press, 1998. DOI: 10.1017/CBO9780511605604.

[116] Y. Saad, *Iterative Methods for Sparse Linear Systems*, 2nd ed. SIAM, 2003, ISBN: 978-0-89871-534-7.

[117] E. Bueler, *PETSc for Partial Differential Equations: Numerical Solutions in C and Python*. SIAM, 2020, p. 391, ISBN: 978-1-611976-30-4.

[118] M. B. Kennel, "Kdtree 2: Fortran 95 and c++ software to efficiently search for near neighbors in a multi-dimensional euclidean space", Aug. 2004. [Online]. Available: http://arxiv.org/abs/physics/0408067.

[119] C. Windt, J. Davidson, P. Schmitt, and J. Ringwood, "Assessment of Numerical Wave Makers", in *Proceedings of the 12th European Wave and Tidal Energy Conference*, 2017, pp. 707-1 - 707–10.

[120] P. Lin and P. L.-F. Liu, "Internal Wave-Maker for Navier-Stokes Equations Models", *Journal of Waterway, Port, Coastal, and Ocean Engineering*, vol. 125, no. 4, pp. 207–215, 1999. DOI: 10.1061/(ASCE)0733-950X(1999)125:4(207).

[121] R. Perić and M. Abdel-Maksoud, "Generation of free-surface waves by localized source terms in the continuity equation", *Ocean Engineering*, vol. 109, pp. 567–579, Nov. 2015, ISSN: 0029-8018. DOI: 10.1016/J.OCEANENG.2015.08.030.

[122] J. Choi and S. B. Yoon, "Numerical simulations using momentum source wave-maker applied to rans equation model", *Coastal Engineering*, vol. 56, pp. 1043–1060, 10 2009, ISSN: 03783839. DOI: 10.1016/j.coastaleng.2009.06.009. [Online]. Available: http://dx.doi.org/10.1016/j.coastaleng.2009.06.009.

[123] N. G. Jacobsen, D. R. Fuhrman, and J. Fredsøe, "A wave generation toolbox for the open-source CFD library: OpenFoam®", *International Journal for Numerical Methods in Fluids*, vol. 70, no. 9, pp. 1073–1088, Nov. 2012. DOI: 10.1002/fld.2726. arXiv: fld.1 [DOI: 10.1002].

[124] R. Perić, V. Vukčević, M. Abdel-Maksoud, and H. Jasak, "Optimizing wave generation and wave damping in 3d-flow simulations with implicit relaxation zones", *Coastal Engineering*, vol. 171, p. 104 035, 2022, ISSN: 0378-3839. DOI: https://doi.org/10.1016/j.coastaleng.2021.104035. [Online]. Available: https://www.sciencedirect.com/science/article/pii/S0378383921001794.

[125] R. Perić and M. Abdel-Maksoud, "Analytical prediction of reflection coefficients for wave absorbing layers in flow simulations of regular free-surface waves", *Ocean Engineering*, vol. 147, pp. 132–147, May 2017 2018, ISSN: 00298018. DOI: 10.1016/j.oceaneng.2017.10.009.

[126] G. Wei and J. T. Kirby, "Time-dependent numerical code for extended boussinesq equations", *Journal of Waterway, Port, Coastal, and Ocean Engineering*, vol. 121, pp. 251–261, 5 Sep. 1995, ISSN: 0733-950X. DOI: 10.1061/(ASCE)0733-950X(1995)121:5(251).

[127] M. Selim and R. Koomullil, "Mesh deformation approaches – a survey", *Journal of Physical Mathematics*, vol. 7, 2 2016. DOI: 10.4172/2090-0902.1000181.

[128] Y. Zhao, J. Tai, and F. Ahmed, "Simulation of micro flows with moving boundaries using high-order upwind fv method on unstructured grids", *Computational Mechanics*, vol. 28, pp. 66–75, 1 2001, ISSN: 01787675. DOI: 10.1007/s00466-001-0271-1.

[129] A. de Boer, M. S. van der Schoot, and H. Bijl, "Mesh deformation based on radial basis function interpolation", *Computers and Structures*, vol. 85, pp. 784–795, 11-14 Jun. 2007, ISSN: 00457949. DOI: 10.1016/j.compstruc.2007.01.013.

[130] T. C. Rendall and C. B. Allen, "Unified fluid-structure interpolation and mesh motion using radial basis functions", *International Journal for Numerical Methods in Engineering*, vol. 74, pp. 1519–1559, 10 Jun. 2008, ISSN: 00295981. DOI: 10.1002/nme.2219.

[131] H. Wendland, "Piecewise polynomial, positive definite and compactly supported radial functions of minimal degree", 1995, pp. 389–396.

[132] A. Beckert and H. Wendland, "Multivariate interpolation for fluid-structure-interaction problems using radial basis functions", 2001, pp. 125–134.

[133] T. C. S. Rendall and C. B. Allen, "Reduced surface point selection options for efficient mesh deformation using radial basis functions", *Journal of Computational Physics*, vol. 229, pp. 2810–2820, 8 2010, ISSN: 0021-9991. DOI: 10.1016/j.jcp.2009.12.006. [Online]. Available: http://dx.doi.org/10.1016/j.jcp.2009.12.006.

[134] B. Le Méhauté, *An Introduction to Hydrodynamics and Water Waves*. Springer, 1976.

[135] S. Beji and J. A. Battjes, "Experimental investigation of wave propagation over a bar", *Coastal Engineering*, vol. 19, no. 1-2, pp. 151–162, 1993, ISSN: 03783839. DOI: 10.1016/0378-3839(93)90022-Z.

[136] M. Dingemans, "Comparison of computations with Boussinesq-like models and laboratory", Delft Hydralics, Tech. Rep., 1994, pp. 1–16.

[137] A. G. Fredriksen, T. Kristiansen, and O. M. Faltinsen, "Wave-induced response of a floating two-dimensional body with a moonpool", *Philosophical Transactions of the Royal Society A: Mathematical, Physical and Engineering Sciences*, vol. 373, no. 2033, 2015, ISSN: 1364503X. DOI: 10.1098/rsta.2014.0109.

[138] A. G. Fredriksen, "A numerical and experimental study of a two-dimensional body with moonpool in waves and current", Ph.D. dissertation, Norwegian University of Science and Technology, 2015.

[139] D. Ntouras, D. Manolas, G. Papadakis, and V. Riziotis, "Exploiting the limit of bem solvers in moonpool type floaters", *Journal of Physics: Conference Series*, vol. 1618, p. 052 059, 5 Sep. 2020, ISSN: 1742-6588. DOI: 10.1088/1742-6596/1618/5/052059.

[140] D. Ntouras, G. Papadakis, and K. Belibassakis, "Ship bow wings with application to trim and resistance control in calm water and in waves", *Journal of Marine Science and Engineering*, vol. 10, 4 Apr. 2022, ISSN: 20771312. DOI: 10.3390/jmse10040492.

[141] "A collaborative computation project in wave structure interaction". (2022), [Online]. Available: https://www.ccp-wsi.ac.uk/data_repository/test_cases/test_case_015. (Accessed: 06.06.2023).

[142] E. Ransley *et al.*, "Hydrodynamic response of a floating offshore wind turbine (1st fowt comparative study dataset)", PEARL Research Repository, Tech. Rep., 2022. DOI: https://doi.org/10.24382/71J2-3385.

[143] D. Liarokapis, Private Communication, Laboratory of Ship and Marine Engineering, School of Naval Architecture & Marine Engineering, NTUA, 2022.

[144] BETA CAE systems, *Ansa*, version 23.0.2, https://www.beta-cae.com/ansa.htm, Accessed: 2023-04-25.

[145] M. Oosterveld and P. van Oossanen, "Further computer-analyzed data of the wageningen b-screw series", *International Shipbuilding Progress*, vol. 22, pp. 251–262, 251 Jul. 1975, ISSN: 15662829. DOI: 10.3233/ISP-1975-2225102.

[146] J. Jeong and F. Hussain, "On the identification of a vortex", *Journal of Fluid Mechanics*, vol. 285, pp. 69–94, February Feb. 1995, ISSN: 0022-1120. DOI: 10.1017/S0022112095000462.

[147] P. Queutey, E. Guilmineau, G. Deng, and M. Visonneau, "Ship flow simulations with the isis-cfd code", Jan. 2005.

[148] *Verification and Validation for the Resistance of a KRISO Container Ship in Calm Water*, International Ocean and Polar Engineering Conference, ISOPE-I-19-029, Jun. 2019.

[149] L. Larsson, F. Stern, and M. Visonneau, Eds., *Numerical Ship Hydrodynamics An assessment of the Gothenburg 2010 Workshop*, Springer, 2014.

[150] T. Hino, F. Stern, L. Larsson, M. Visonneau, N. Hirata, and J. Kim, Eds., *Numerical Ship Hydrodynamics An assessment of the Tokyo 2015 Workshop*, Springer, 2021.

[151] S. Van, W. Kin, G. Yim, D. Kim, and C. Lee, "Experimental investigation of the flow characteristics around practical hull forms", presented at the Proceedings 3rd Osaka Colloquium on Advanced CFD Applications to Ship Flow and Hull Form Design, Osaka,Japan, 1998.

[152] W. J. Kim, S. H. Van, and D. H. Kim, "Measurement of flows around modern commercial ship models", *Experiments in Fluids*, vol. 31, pp. 567–578, 5 Nov. 2001, ISSN: 0723-4864. DOI: 10.1007/s003480100332.

[153] Numeca, *Hexpress*, version 10.1, https://www.numeca.com/product/omnis-hexpress, Accessed: 25.04.2023.

[154] L. Kerner. "Kcs resistance calculation". (2014), [Online]. Available: https://www.numeca.com/docs/finemarine_kcs_g2010_2-1-2-3_18092014.pdf. (Accessed: 25.03.2023).

[155] C. Simonsen, J. Otzen, C. Nielson, and F. Stern, "Cfd prediction of added resistance of the kcs in regular head and oblique waves", presented at the 30th SNH, Hobart, Australia, Nov. 2014.

[156] "Fourth imo ghg study 2020", International Maritime Organization, Tech. Rep., 2021. [Online]. Available: https://wwwcdn.imo.org/localresources/en/OurWork/Environment/Documents/Fourth%20IMO%20GHG%20Study%202020%20-%20Full%20report%20and%20annexes.pdf.

[157] "Adoption of the initial imo strategy on reduction of ghg emissions from ships and existing imo activity related to reducing ghg emissions in the shipping sector", International Maritime Organization, Tech. Rep., 2018. [Online]. Available: https://unfccc.int/sites/default/files/resource/250_IMO%20submission_Talanoa%20Dialogue_April%202018.pdf.

[158] M. S. Triantafyllou, G. S. Triantafyllou, and D. K. P. Yue, "Hydrodynamics of fishlike swimming", *Annual Review of Fluid Mechanics*, vol. 32, pp. 33–53, 1 Jan. 2000, ISSN: 0066-4189. DOI: 10.1146/annurev.fluid.32.1.33.

[159] K. Theodorakis, D. Ntouras, and G. Papadakis, "Investigation of a submerged fully passive energy-extracting flapping foil operating in sheared inflow", *Journal of Fluids and Structures*, vol. 113, p. 103 674, 2022, ISSN: 0889-9746. DOI: https://doi.org/10.1016/j.jfluidstructs.2022.103674.

[160] K. Belibassakis, S. Bleuanus, J. Vermeiden, and N. Townsend, "Combined performance of innovative biomimetic ship propulsion system in waves with dual fuel ship engine and application to short-sea shipping", in *Proceedings of the 31st International Ocean and Polar Engineering Conference, ISOPE 2021*, International Society of Offshore and Polar Engineers, Jun. 2021, pp. 2815–2822.

[161] K. Belibassakis, J. Vermeiden, and A. Öster, "Development and testing of biomimetic dynamic-foil thruster for augmenting ship propulsion in waves", in *OCEANS 2021: San Diego – Porto*, 2021, pp. 1–6. DOI: 10.23919/OCEANS44145.2021.9705857.

[162] G. Papadakis, E. Filippas, D. Ntouras, and K. Belibassakis, "Effects of viscosity and nonlinearity on 3d flapping-foil thruster for marine applications", *OCEANS 2019 - Marseille*, pp. 1–10, 2019. DOI: 10.1109/oceanse.2019.8867084.

[163] K. Belibassakis, E. Filippas, and G. Papadakis, "Numerical and experimental investigation of the performance of dynamic wing for augmenting ship propulsion in head and quartering seas", *Journal of Marine Science and Engineering*, vol. 10, 1 2022, ISSN: 20771312. DOI: 10.3390/jmse10010024.

[164] E. Gaertner *et al.*, "Definition of the iea 15–megawatt offshore reference wind", Golden, CO: National Renewable Energy Laboratory. NREL/TP- 5000-75698, Tech. Rep., 2020. [Online]. Available: https://www.nrel.gov/docs/fy20osti/75698.pdf.

[165] Orcina. "Chain: Axial and bending stiffness". (), [Online]. Available: https://www.orcina.com/webhelp/OrcaFlex/Content/html/Chain,Axialandbendingstiffness.htm. (Accessed: 25.07.2023).

[166] D. Ntouras, D. Manolas, G. Papadakis, and V. Riziotis, "Hydrodynamic response of a floating offshore wind turbine using an artificial compressibility finite volume method", to be published, ISOPE, 2023.

[167] D. I. Manolas, V. A. Riziotis, G. P. Papadakis, and S. G. Voutsinas, "Hydro-servo-aero-elastic analysis of floating offshore wind turbines", *Fluids*, vol. 5, no. 4, 2020, ISSN: 2311-5521. DOI: 10.3390/fluids5040200.

[168] G. Anastasopoulos, "Implementation of algorithm for modeling of cavitation in marine applications using computational fluid dynamics", M.S. thesis, School of Naval Architecture & Marine Engineering, National Technical University of Athens, 2022.

[169] J. Smagorinsky, "General circulation experiments with the primitive equations", *Monthly Weather Review*, vol. 91, pp. 99–164, 3 Mar. 1963, ISSN: 0027-0644.

[170] F. R. Menter and M. Kuntz, "Adaptation of eddy-viscosity turbulence models to unsteady separated flow behind vehicles", pp. 339–352, 2004. DOI: 10.1007/978-3-540-44419-0_30.

[171] J. G. Coder and M. D. Maughmer, "Computational fluid dynamics compatible transition modeling using an amplification factor transport equation", *AIAA Journal*, vol. 52, pp. 2506–2512, 11 Nov. 2014, ISSN: 1533385X. DOI: 10.2514/1.J052905.

[172] F. R. Menter, P. E. Smirnov, T. Liu, and R. Avancha, "A one-equation local correlation-based transition model", *Flow, Turbulence and Combustion*, vol. 95, pp. 583–619, 4 Dec. 2015, ISSN: 15731987. DOI: 10.1007/s10494-015-9622-4.

[173] S. Bhushan *et al.*, "Verification and validation of cfd for surface combatant 5415 for straight ahead and 20 degree static drift conditions", Society of Naval Architects and Marine Engineers, 2015. DOI: 10.5957/WMTC-2015-124.

[174] "Full scale manoeuvring trials", ITTC – Recommended Procedures and Guidelines, Tech. Rep., 2017.

[175] S. Zafeiris, "The overset grid assembly (chimera) of unstructured partitioned grids coupled with the artificial compressibility roe solver and applications in marine hydrodynamics", M.S. thesis, School of Naval Architecture & Marine Engineering, National Technical University of Athens, 2023.